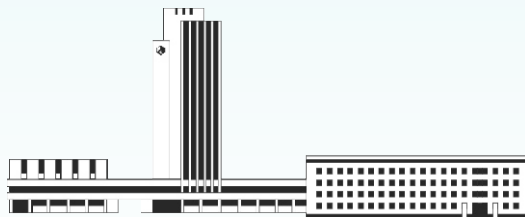


НАНОСИСТЕМИ, НАНОМАТЕРІАЛИ, НАНОТЕХНОЛОГІЇ

**Nanosistemi,
Nanomateriali,
Nanotehnologii**

ЗБІРНИК НАУКОВИХ ПРАЦЬ

ТОМ 22, ВИПУСК 1, 2024



НАЦІОНАЛЬНА АКАДЕМІЯ НАУК УКРАЇНИ



НАНОСИСТЕМИ
НАНОМАТЕРІАЛИ
НАНОТЕХНОЛОГІЇ

NANOSYSTEMS
NANOMATERIALS
NANOTECHNOLOGIES

Засновник: ІНСТИТУТ МЕТАЛОФІЗИКИ ІМ. Г. В. КУРДЮМОВА НАН УКРАЇНИ
Видавець: ІНСТИТУТ МЕТАЛОФІЗИКИ ІМ. Г. В. КУРДЮМОВА НАН УКРАЇНИ

«НАНОСИСТЕМИ, НАНОМАТЕРИАЛИ, НАНОТЕХНОЛОГІЇ» ♦ ‘NANOSISTEMI, NANOMATERIALI, NANOTECHNOLOGII’
Щоквартальний збірник наукових праць ♦ Quarterly Collected Scientific Transactions

РЕДАКЦІЙНА КОЛЕГІЯ

B. A. Татаренко	головний редактор, чл.-кор. НАН України, д.ф.-м.н., проф., Ін-т металофізики ім. Г. В. Курдюмова НАН України	V. A. Tatarenko	<i>Editor-in-Chief,</i> Cor. Mem. of the N.A.S. of Ukraine, Dr. Sci. (Phys.-Math.), Prof., G. V. Kurdymov Inst. for Metal Physics of the N.A.S. of Ukraine
B. M. Мордюк	заступник головного редактора, д.ф.-м.н., с.н.с., Ін-т металофізики ім. Г. В. Курдюмова НАН України	B. M. Morduk	<i>Associate Editor,</i> Dr. Sci. (Phys.-Math.), Sr. Researcher, G. V. Kurdymov Inst. for Metal Physics of the N.A.S. of Ukraine
B. V. Лізунов	відповідальний секретар редакції, д.ф.-м.н., проф., Ін-т металофізики ім. Г. В. Курдюмова НАН України	V. V. Lizunov	<i>Executive Managing Editor,</i> Dr. Sci. (Phys.-Math.), Prof., G. V. Kurdymov Inst. for Metal Physics of the N.A.S. of Ukraine
C. А. Беспалов	д.т.н., с.н.с., СФТМН НОВ Президії НАН України	S. A. Bespalov	Dr. Sci. (Tech.), Sr. Researcher, SPhTMS of Sci.-Org. Dept. of Presidium of the N.A.S. of Ukraine
M. Я. Валах	чл.-кор. НАН України, д.ф.-м.н., проф., Ін-т фізикій напівпровідників ім. В. С. Лашкарьова НАН України	M. Ya. Valakh	Cor. Mem. of the N.A.S. of Ukraine, Dr. Sci. (Phys.-Math.), Prof., V. Ye. Lashkaryov Inst. of Semiconductor Physics of the N.A.S. of Ukraine
P. В. Вовк	акад. НАН України, д.ф.-м.н., проф., Харківський національний університет імені В. Н. Каразіна МОН України	R. V. Vovk	Mem. of the N.A.S. of Ukraine, Dr. Sci. (Phys.- Math.), Prof., V. N. Karazin Kharkiv Natl. Univ. of the Ministry of Education and Science of Ukraine
П. П. Горбик	чл.-кор. НАН України, д.ф.-м.н., проф., Ін-т хімії поверхні ім. О. О. Чуїка НАН України	P. P. Gorbyk	Cor. Mem. of the N.A.S. of Ukraine, Dr. Sci. (Phys.-Math.), Prof., O. O. Chuiko Inst. of Surface Chemistry of the N.A.S. of Ukraine
B. О. Зажигалов	чл.-кор. НАН України, д.х.н., проф., Ін-т коробії та проблем ендокеології НАН України	V. O. Zazhigalov	Cor. Mem. of the N.A.S. of Ukraine, Dr. Sci. (Chem.), Prof., Inst. of Sorption and Problems of the Endocology of the N.A.S. of Ukraine
Б. Зайді	кандидат фізичних наук, факультет наук про матеріали, Ін-т Батна 1 Хаджар Батна, Алжир	Beddiah Zaidi	Docteur en Physique, Faculté des sciences de la matière, Université Batna 1 Hadj Lakhdar, Batna, Algérie
B. І. Карбієвський	д.ф.-м.н., проф., Ін-т металофізики ім. Г. В. Курдюмова НАН України	V. L. Karbivskyj	Dr. Sci. (Phys.-Math.), Prof., G. V. Kurdymov Inst. for Metal Physics of the N.A.S. of Ukraine
O. А. Кордюк	акад. НАН України, д.ф.-м.н., проф., Київський академічний університет	O. A. Kordyuk	Mem. of the N.A.S. of Ukraine, Dr. Sci. (Phys.- Math.), Prof., Kyiv Academic Univ.
C. О. Котречко	чл.-кор. НАН України, д.ф.-м.н., проф., Ін-т металофізики ім. Г. В. Курдюмова НАН України	S. O. Kotrechko	Cor. Mem. of the N.A.S. of Ukraine, Dr. Sci. (Phys.- Math.), Prof., G. V. Kurdymov Inst. for Metal Physics of the N.A.S. of Ukraine
M. П. Куліш	чл.-кор. НАН України, д.ф.-м.н., проф., Київський національний університет імені Тараса Шевченка МОН України	M. P. Kulish	Cor. Mem. of the N.A.S. of Ukraine, Dr. Sci. (Phys.- Math.), Prof., Taras Shevchenko Natl. Univ. of Kyiv of the Ministry of Education and Science of Ukraine
B. I. Лев	акад. НАН України, д.ф.-м.н., проф., Ін-т теоретичної фізики	B. I. Lev	Mem. of the N.A.S. of Ukraine, Dr. Sci. (Phys.- Math.), Prof., M. M. Bogolyubov Inst.
C. Г. Лен	д.ф.-м.н., проф., Ін-т металофізики ім. Г. В. Курдюмова НАН України	E. G. Len	for Theoretical Physics of the N.A.S. of Ukraine Dr. Sci. (Phys.-Math.), Prof., G. V. Kurdymov Inst. for Metal Physics of the N.A.S. of Ukraine
Ю. А. Малетін	чл.-кор. НАН України, д.х.н., с.н.с., Ін-т коробії та проблем ендокеології НАН України	Yu. A. Maletin	Cor. Mem. of the N.A.S. of Ukraine, Dr. Sci. (Chem.), Sr. Researcher, Inst. of Sorption and Problems of Endocology of the N.A.S. of Ukraine
C. I. Оковитий	чл.-кор. НАН України, д.х.н., проф., Дніпровський національний університет імені Олеся Гончара МОН України	S. I. Okovytuy	Cor. Mem. of the N.A.S. of Ukraine, Dr. Sci. (Chem.), Prof., Oles Honchar Dnipro Natl. Univ. of the Ministry of Education and Science of Ukraine
B. С. Панарін	д.т.н., с.н.с., Ін-т металофізики ім. Г. В. Курдюмова НАН України	V. Ye. Panarin	Dr. Sci. (Tech.), Sr. Researcher, G. V. Kurdymov Inst. for Metal Physics of the N.A.S. of Ukraine
P. Р. Панчук	д.б.н., Ін-т біології клітини НАН України	R. R. Panchuk	Dr. Sci. (Biol.), Inst. of Cell Biology of the N.A.S. of Ukraine
О. Д. Погребняк	д.ф.-м.н., проф., Сумський державний університет	O. D. Pogrebnyak	Dr. Sci. (Phys.-Math.), Prof., Sumy State Univ. of the Ministry of Education and Science of Ukraine
Ю. І. Прилуцький	д.ф.-м.н., проф., ННЦ «Ін-т біології та медицини» Київського національного університету імені Тараса Шевченка МОН України	Yu. I. Prylutskyy	Dr. Sci. (Phys.-Math.), Prof., NSC Inst. of Biology and Medicine of the Taras Shevchenko Natl. Univ. of Kyiv of the Ministry of Education and Science of Ukraine
B. А. Прокопенко	д.т.н., с.н.с., Ін-т біоколоїдної хімії ім. Ф. Д. Овчаренка НАН України	V. A. Prokopenko	Dr. Sci. (Tech.), Sr. Researcher, F. D. Ovcharenko Inst. of Biocolloidal Chemistry of the N.A.S. of Ukraine
O. А. Пуд	д.х.н., проф., Ін-т біоорганічної хімії та нафтотімії ім. В. П. Кухари НАН України	O. A. Pud	Dr. Sci. (Chem.), Prof., V. P. Kukhar Inst. of Bioorganic Chemistry and Petrochemistry of the N.A.S. of Ukraine
T. М. Радченко	д.ф.-м.н., с.н.с., Ін-т металофізики ім. Г. В. Курдюмова НАН України	T. M. Radchenko	Dr. Sci. (Phys.-Math.), Sr. Researcher, G. V. Kurdymov Inst. for Metal Physics of the N.A.S. of Ukraine
П. Е. Стрижак	акад. НАН України, д.х.н., проф., Ін-т фізичної хімії ім. Л. В. Писаржевського НАН України	P. Ye. Strizhak	Mem. of the N.A.S. of Ukraine, Dr. Sci. (Chem.), Prof., L. V. Pisarhevsky Inst. of Physical Chemistry of the N.A.S. of Ukraine
В. Й. Сугаков	чл.-кор. НАН України, д.ф.-м.н., проф., Ін-т ядерних досліджень НАН України	V. J. Sugakov	Cor. Mem. of the N.A.S. of Ukraine, Dr. Sci. (Phys.-Math.), Prof., Inst. of Nuclear Research of the N.A.S. of Ukraine
Л. Ф. Суходуб	чл.-кор. НАН України, д.ф.-м.н., проф., Сумський державний університет МОН України	L. F. Sukhodub	Cor. Mem. of the N.A.S. of Ukraine, Dr. Sci. (Phys.-Math.), Prof., Sumy State Univ. of the Ministry of Education and Science of Ukraine
В. М. Уваров	чл.-кор. НАН України, д.ф.-м.н., проф., Ін-т металофізики ім. Г. В. Курдюмова НАН України	V. M. Uvarov	Cor. Mem. of the N.A.S. of Ukraine, Dr. Sci. (Phys.- Math.), Prof., G. V. Kurdymov Inst. for Metal Physics of the N.A.S. of Ukraine
О. М. Файнлейб	чл.-кор. НАН України, д.х.н., проф., Ін-т високомолекулярних сполук НАН України	O. M. Fainleib	Cor. Mem. of the N.A.S. of Ukraine, Dr. Sci. (Chem.), Prof., Inst. of Chemistry of Macromolecular Compounds of the N.A.S. of Ukraine
Д. О. Харченко	д.ф.-м.н., проф., Ін-т прикладної фізики НАН України	D. O. Kharchenko	Dr. Sci. (Phys.-Math.), Prof., Inst. of Applied Physics of the N.A.S. of Ukraine
О. В. Хоменко	д.ф.-м.н., проф., Сумський державний університет МОН України	O. V. Khomenko	Dr. Sci. (Phys.-Math.), Prof., Sumy State Univ. of the Ministry of Education and Science of Ukraine

© Інститут металофізики ім. Г. В. Курдюмова НАН України (Київ), 2024

НАЦІОНАЛЬНА АКАДЕМІЯ НАУК УКРАЇНИ
Інститут металофізики ім. Г. В. Курдюмова

НАНОСИСТЕМИ, НАНОМАТЕРІАЛИ, НАНОТЕХНОЛОГІЇ

ЗБІРНИК НАУКОВИХ ПРАЦЬ
ТОМ 22, ВИПУСК 1



РВВ ІМФ
КИЇВ — 2024

УДК 536:669

НАНОСИСТЕМИ, НАНОМАТЕРІАЛИ, НАНОТЕХНОЛОГІЇ / Щоквартальний збірник наукових праць / Том 22, вип. 1. — Київ: РВВ ІМФ, 2024. — XVIII с. + 228 с.

У збірнику наведено оригінальні й оглядові статті за результатами робіт, виконаних у рамках досліджень за напрямом «Перспективні фундаментальні дослідження та інноваційні розробки наноматеріалів і нанотехнологій для потреб промисловості, охорони здоров'я та сільського господарства». Основну увагу приділено розгляду проблемних питань нанофізики, наноелектроніки, особливостей будови наноструктурованих матеріалів, з'ясуванню їхніх електричних, термічних, механічних, реологічних і хемічних властивостей, поверхневих явищ і самоорганізації. Представлено результати фабрикації, оброблення, тестування й аналізування нанорозмірних частинок, наномасштабних структур і багатофункціональних наноматеріалів технічного та біомедичного призначення в умовах впливу зовнішніх чинників. Розглянуто особливості технологій одержання, діагностики та характеризації наносистем.

Статті друкуються мовами оригіналів.

Збірник розраховано на наукових працівників, інженерів, викладачів ЗВО, аспірантів і студентів відповідних спеціальностей.

РЕДАКЦІЙНА КОЛЕГІЯ:

С. А. Беспалов, М. Я. Валах, Р. В. Вовк, П. П. Горбик, В. О. Зажигалов,
Б. Зайді, В. Л. Карбівський, О. А. Кордюк, С. О. Котречко, М. П. Кулиш,
Б. І. Лев, Є. Г. Лень, В. В. Лізунов (відповідальний секретар),
Ю. А. Малетін, Б. М. Мордюк (заступник головного редактора),
С. І. Оковитий, В. Є. Панаїн, Р. Р. Панчук, О. Д. Погребняк,
Ю. І. Прилуцький, В. А. Прокопенко, О. А. Пуд, Т. М. Радченко,
П. Є. Стрижак, В. Й. Сугаков, Л. Ф. Суходуб,
В. А. Татаренко (головний редактор), В. М. Уваров,
О. М. Файнлейб, Д. О. Харченко, О. В. Хоменко

НАНОСИСТЕМИ, НАНОМАТЕРІАЛИ, НАНОТЕХНОЛОГІЇ

ЗБІРНИК НАУКОВИХ ПРАЦЬ
ЗАСНОВАНИЙ У ЖОВТНІ 2003 р.

Том 22, вип. 1; 2024 р.

ЗМІСТ

Редакційні повідомлення	Інформація для передплатників	IX
	Інформація для авторів	XI
	Видавнича етика	XV
	Surface Morphology of Thin Films of $(Y_{0.06}Ga_{0.94})_2O_3$ Activated by Cr^{3+} <i>O. M. BORDUN, B. O. BORDUN, I. I. MEDVID, M. V. PROTSAK, I. Yo. KUKHARSKYY, K. L. BILIAK, D. M. MAKSYMCHUK, I. M. KOFLIUK, and D. S. LEONOV</i>	1
	Predicting the Thermodynamic Stability of $(Gd_{1-x}Ln_x)_2SiO_5$ and $(Lu_{1-x}Ln_x)_2SiO_5$ Solid Solutions of the $P2_1/c$ Space Group <i>E. I. GET'MAN, O. Yu. MARIICHAK, L. I. ARDANOVA, and S. V. RADIO</i>	13
	Machine Learning of the Physicothermal Properties of Graphene <i>Mohammad IMRAN AZIZ</i>	31
	Laser-Assisted Electrodeposition of Composite Carbon-Containing Nickel Coatings <i>V. V. TYTARENKO, V. A. ZABLUDOVSKY, and I. V. TYTARENKO</i>	41
	Формування нанопор в анодно-окисненому алюмінії під впливом вуглецевих наночастинок <i>К. О. КУДЕЛКО, О. Г. ДЗЯЗЬКО, Л. М. РОЖДЕСТВЕНСЬКА, <u>Л. Б. ХАРЬКОВА</u>, В. М. ОГЕНКО</i>	53
	Структурні та фотохемічні характеристики гібридних каталізаторів TiO_2/SiO_2 /мікроволастоніт, одержаних золь-гель-методом <i>O. В. ЗІНЧЕНКО, В. Д. ЄЖОВА, О. Л. ТОЛСТОВ</i>	67
	SBR Capped ZnS Quantum Dots as Nanoelectronic Filter <i>Abhigyan GANGULY, Saradindu PANDA, Siddhartha Sankar NATH, and Gautam GOPE</i>	85

Features of Relationship Between Rheological and Photogeneration Characteristics of PEPC + C ₆₀ Composites <i>M. A. ZABOLOTNYY, L. I. ASLAMOVA, V. P. VASHCHYN, D. O. GRYNKO, A. A. KOLESNICHENKO, D. S. LEONOV, D. O. KRASNOVYD, V. V. VOVK, M. M. PETRYSHYN, R. V. LYTVYN, S. O. RUDENKYI, and M. Yu. BARABASH</i>	93
Synthesis, Characterization and Application of PVA-CMC/SiO ₂ -Cr ₂ O ₃ Nanostructures <i>Rehab Shather ABDUL HAMZA and Majeed Ali HABEEB</i>	107
Metamaterial Sensors in Liquid Detection: An Illustrious Review <i>N. V. KRISHNA PRASAD and N. MADHAVI</i>	119
MXenes-Based Supercapacitors: A Review on Energy Storage Devices <i>N. V. KRISHNA PRASAD and N. MADHAVI</i>	133
Synthesis and Improved Dielectric Properties of PVP/TiN/Si ₃ N ₄ Nanocomposites <i>Ahmed HASHIM, Aseel HADI, and M. H. ABBAS</i>	147
Augmented Dielectric Properties of PVP/Si ₃ N ₄ /Al ₂ O ₃ Nanostructures <i>Ahmed HASHIM and Aseel HADI</i>	157
Boosting the Dielectric Properties of PVA/In ₂ O ₃ /SiC Nanostructures for Electronics Nanodevices <i>Ahmed HASHIM and M. H. ABBAS</i>	167
Tailoring the Dielectric Properties of PS/In ₂ O ₃ /SiC Nanocomposites for Nanoelectronics Fields <i>Ahmed HASHIM and Aseel HADI</i>	177
Exploring the Dielectric Properties of PVP/Ag/SiC Nanostructures to Use in Various Electronics Fields <i>Ahmed HASHIM and M. H. ABBAS</i>	187
Preparation and Characterization of Nanofilm-Coated Modified Electrodes and Their Use in Valsartan Drug Analysis <i>Ahmed Filayih HASSAN</i>	197
Characterization and Evaluation of the Antimicrobial Activity of CuO Nanoparticles Prepared by Pulse Laser Ablation in Double-Distilled Water <i>Khalaif AJAJ, Abdullah M. ALI, and Mushtaq Abed AL-JUBBORI</i>	209

Науковий редактор випуску — *В. А. Татаренко*
Відповідальний секретар редакційної колегії — *В. В. Лізунов*
Редактори-коректори: *І. О. Головащич, Д. С. Леонов, Н. А. Леонова*
Технічний редактор — *Д. С. Леонов*
Оригінал-макет для прямого репродукування виготовлено комп'ютеризованою групою РВВ
Інституту металофізики ім. Г. В. Курдюмова НАН України
Друкується за постановою редакційної колегії збірника англійською або українською мовами
Затверджено до друку вченю радою ІМФ ім. Г. В. Курдюмова НАН України
Свідоцтво суб'єкта видавничої справи серії ДК № 5875 від 13.12.2017 р.
Свідоцтво про державну реєстрацію ДЗМІ серії КВ № 23231-13071ПР від 22.03.2018 р.
Підп. до друку 30.04.2024 р. Формат 70×100/16. Гарн. SchoolBookC. Папір офсет. № 1. Друк різограф.

Адреса редакції «ННН»: Інститут металофізики ім. Г. В. Курдюмова НАН України,
бульв. Акад. Вернадського, 36, каб. 210; 03142 Київ, Україна
Тел.: +380 44 4241221, +380 44 4249042; факс: +380 44 4242561
Ел. пошта: tatar@imp.kiev.ua, dsleonov@gmail.com

Надруковано в РВВ ІМФ ім. Г. В. Курдюмова НАН України.
бульв. Акад. Вернадського, 36; 03142 Київ, Україна. Тел.: +380 44 4240236

Зав. поліграфічно-розмножувальної групи — *Л. І. Малініна*

NANOSISTEMI, NANOMATERIALI, NANOTEHNOLOGII

FOUNDED IN OCTOBER, 2003

Volume 22, Issue 1 (2024)

CONTENTS

Editorial Announcements	Information for Subscribers	X
	Information for Contributors	XIII
	Publication Ethics	XVI
	Surface Morphology of Thin Films of $(Y_{0.06}Ga_{0.94})_2O_3$ Activated by Cr^{3+} <i>O. M. BORDUN, B. O. BORDUN, I. I. MEDVID, M. V. PROTSAK, I. Yo. KUKHARSKYY, K. L. BILIAK, D. M. MAKSYMCHUK, I. M. KOFLIUK, and D. S. LEONOV</i>	1
	Predicting the Thermodynamic Stability of $(Gd_{1-x}Ln_x)_2SiO_5$ and $(Lu_{1-x}Ln_x)_2SiO_5$ Solid Solutions of the $P2_1/c$ Space Group <i>E. I. GET'MAN, O. Yu. MARIICHAK, L. I. ARDANOVA, and S. V. RADIO</i>	13
	Machine Learning of the Physicothermal Properties of Graphene <i>Mohammad IMRAN AZIZ</i>	31
	Laser-Assisted Electrodeposition of Composite Carbon-Containing Nickel Coatings <i>V. V. TYTARENKO, V. A. ZABLUDOVSKY, and I. V. TYTARENKO</i>	41
	Formation of Nanopores in Anodic Oxidized Aluminium under the Influence of Carbon Nanoparticles <i>K. O. KUDELKO, O. H. DZIAZ'KO, L. M. ROZHDESTVENS'KA, [L. B. KHAR'KOVA], and V. M. OGENKO</i>	53
	Structure and Photochemical Characteristics of Hybrid TiO_2/SiO_2 /Wollastonite Catalysts Prepared via Sol-Gel Approach <i>O. V. ZINCHENKO, V. D. EZHOVA, and A. L. TOLSTOV</i>	67
	SBR Capped ZnS Quantum Dots as Nanoelectronic Filter <i>Abhigyan GANGULY, Saradindu PANDA, Siddhartha</i>	

<i>Sankar NATH, and Gautam GOPE</i>	85
Features of Relationship Between Rheological and Photogeneration Characteristics of PEPC + C ₆₀ Composites	
<i>M. A. ZABOLOTNYY, L. I. ASLAMOVA, V. P. VASHCHYN, D. O. GRYNKO, A. A. KOLESNICHENKO, D. S. LEONOV, D. O. KRASNOVYD, V. V. VOVK, M. M. PETRYSHYN, R. V. LYTVYN, S. O. RUDENKYI, and M. Yu. BARABASH</i>	93
Synthesis, Characterization and Application of PVA–CMC/SiO ₂ –Cr ₂ O ₃ Nanostructures	
<i>Rehab Shather ABDUL HAMZA and Majeed Ali HABEEB</i>	107
Metamaterial Sensors in Liquid Detection: An Illustrious Review	
<i>N. V. KRISHNA PRASAD and N. MADHAVI</i>	119
MXenes-Based Supercapacitors: A Review on Energy Storage Devices	
<i>N. V. KRISHNA PRASAD and N. MADHAVI</i>	133
Synthesis and Improved Dielectric Properties of PVP/TiN/Si ₃ N ₄ Nanocomposites	
<i>Ahmed HASHIM, Aseel HADI, and M. H. ABBAS</i>	147
Augmented Dielectric Properties of PVP/Si ₃ N ₄ /Al ₂ O ₃ Nanostructures	
<i>Ahmed HASHIM and Aseel HADI</i>	157
Boosting the Dielectric Properties of PVA/In ₂ O ₃ /SiC Nanostructures for Electronics Nanodevices	
<i>Ahmed HASHIM and M. H. ABBAS</i>	167
Tailoring the Dielectric Properties of PS/In ₂ O ₃ /SiC Nanocomposites for Nanoelectronics Fields	
<i>Ahmed HASHIM and Aseel HADI</i>	177
Exploring the Dielectric Properties of PVP/Ag/SiC Nanostructures to Use in Various Electronics Fields	
<i>Ahmed HASHIM and M. H. ABBAS</i>	187
Preparation and Characterization of Nanofilm-Coated Modified Electrodes and Their Use in Valsartan Drug Analysis	
<i>Ahmed Filayih HASSAN</i>	197
Characterization and Evaluation of the Antimicrobial Activity of CuO Nanoparticles Prepared by Pulse Laser Ablation in Double-Distilled Water	
<i>Khalaf AJAJ, Abdullah M. ALI, and Mushtaq Abed AL-JUBBORI</i>	209

CONTENTS, Iss. 1 (Vol. 22)

Scientific Editor of the Issue—*V. A. Tatarenko*

Executive Managing Editor—*V. V. Lizunov*

Technical Editor—*D. S. Leonov*

Editorial-Publishing Department, G. V. Kurdyumov Institute for Metal Physics, N.A.S. of Ukraine

Editorial Office: 36 Academician Vernadsky Boulevard, UA-03142 Kyyiv, Ukraine

Telephone: +380 44 4241221, +380 44 4249042. Fax: +380 44 4242561

E-mail: tatar@imp.kiev.ua, dsleonov@gmail.com

ІНФОРМАЦІЯ ДЛЯ ПЕРЕДПЛАТНИКІВ І АВТОРІВ

ІНФОРМАЦІЯ ДЛЯ ПЕРЕДПЛАТНИКІВ

Редакція щоквартального збірника наукових праць

«НАНОСИСТЕМИ, НАНОМАТЕРІАЛИ, НАНОТЕХНОЛОГІЇ»

(CODEN: NNNAAAT; ISSN (Print): 1816-5230, ISSN (Online): 2617-3794;

у «Каталозі медіа України «Преса поштою» передплатний індекс: 94919)

повідомляє про передплату (починаючи з поточного кварталу випуску).

Рекомендуємо оформити передплату безпосередньо перерахуванням оплати

у гривнях:

«ОТРИМУВАЧУ»: Інститут металофізики ім. Г. В. Курдюмова НАН України на розрахунковий рахунок № UA058201720313291001201001901 в банку ГУДКСУ в м. Києві код банку 820172

код ЗКПО: 05417331

для «ПОСТАЧАЛЬНИКА» — Інституту металофізики ім. Г. В. Курдюмова НАН України Свідоцтво платника податку № 36283185

ППН 054173326066

Код призначення платежу: 25010100

Призначення платежу: за збірник «Наносистеми, наноматеріали, нанотехнології» для РВВ
ІМФ НАНУ

ПІДСТАВА: передоплата 100%

в іноземній валюті (доларах США, євро) через відповідні банки-кореспонденти АТ «Державний експортно-імпортний банк України»:

«ОТРИМУВАЧУ»: Філія АТ «Державний експортно-імпортний банк України» в м. Києві (Україна, 04053 Київ, вул. Бульварно-Кудрявська, 11⁹)

на розрахунковий рахунок № UA603223130000025308000000067

МФО 322313

для «ПОСТАЧАЛЬНИКА» — Інституту металофізики ім. Г. В. Курдюмова НАН України

Призначення платежу: за збірник «Наносистеми, наноматеріали, нанотехнології» для РВВ
ІМФ НАНУ

ПІДСТАВА: передоплата 100%

За цього способу передплати необхідно сповістити редакцію збірника за поштовою адресою:

РВВ (№ 83) ІМФ НАНУ,
бульв. Акад. Вернадського, 36,
03142 Київ, Україна

e-mail: tatar@imp.kiev.ua; факс: +380 44 4242561; телефон: +380 44 4241221, +380 44 4249042

дату сплати, називу установи або найменування передплатника, адресу для поштової доставки, а за потреби — свої реквізити для податкової накладної.

Періодичність — том з 4 випусків у рік.

Із врахуванням поштової пересилки

для передплатників в Україну передплатна ціна: одного примірника випуску — 312 грн., тому — 1248 грн.;

для передплатників у країни СНД передплатна ціна: одного примірника випуску — 36 US\$, тому — 144 US\$;

для іноземних передплатників назовні СНД передплатна ціна: одного примірника випуску — 40 US\$ (36 EUR), тому — 160 US\$ (144 EUR).



Зразок для оплати річної передплати

Рахунок-фактура

«ПОСТАЧАЛЬНИК»: Інститут металофізики ім. Г. В. Курдюмова НАН України

«ОТРИМУВАЧ»: Філія АТ «Державний експортно-імпортний банк України» в м. Києві

(Україна, 04053 Київ, вул. Бульварно-Кудрявська, 11⁹)

на розрахунковий рахунок № UA60322313000002530800000067, МФО 322313

Призначення платежу: за збірник «Наносистеми, наноматеріали, нанотехнології» для ІМФ НАНУ

«ПЛАТНИК»:

ПІДСТАВА: передоплата 100%

№	Назва	Од. вим.	Кількість	Ціна	Сума
1	збірник «Наносистеми, наноматеріали, нанотехнології»	прим.	4	36 US\$ 144 US\$	
Сума до сплати					144 US\$

INFORMATION FOR SUBSCRIBERS

Editorial Board of Quarterly Collected Scientific Transactions

‘NANOSISTEMI, NANOMATERIALI, NANOTEHNOLOGII’

(*i.e.* ‘NANOSYSTEMS, NANOMATERIALS, NANOTECHNOLOGIES’)

(CODEN: NNNAAT; ISSN (Print): 1816-5230, ISSN (Online): 2617-3794)

advertises the subscription on an annual basis for this year. Orders should be placed through one of the methods described below.

Besides the subscription *via* the centralized service by JSC ‘Ukrposhta’ (22 Khreshchatyk Str., UA-01001 Kyiv, Ukraine; phone: 0 800 300 545; e-mail: ukrposhta@ukrposhta.ua) or *via* Internet:

<https://peredplata.ukrposhta.ua/index.php?route=product/search&search=94919&type=main>

the Editorial Board will take orders sent directly to the Editorial Board. To obtain our edition, the persons and institutions, interested in this title, should made the definite payment sent, according to the order, to the account of the Publisher—Institute for Metal Physics of the N.A.S. of Ukraine.

This edition frequency is 4 issues per year. The annual subscription rate for ‘Nanosistemi, Nanomateriali, Nanotekhnologii’ is 160 US\$ (or 144 EUR), including airmail postage, packing and handling charges. All other currency payments should be made using the current conversion rate set by the Publisher (subscribers should contact the Editorial Board).

Subscription is valid after obtaining by the Editorial Board of banker’s order. Banker’s order should be sent to the address:

G. V. Kurdyumov Institute for Metal Physics, N.A.S. of Ukraine,
currency account No. UA603223130000025308000000067, MFO 322313
in the Kyiv’s Branch of JSC ‘The State Export-Import Bank of Ukraine’
(Joint Stock Company ‘Ukreximbank’)
(11^b Bulvarno-Kudriavskaya Str., UA-04053 Kyiv, Ukraine)

simultaneously with written notice providing the Editorial Board with a copy of banker’s order for subscription and detailed address for mailing.

Address of the Editorial Board Office:

G. V. Kurdyumov Institute for Metal Physics, N.A.S. of Ukraine,
36 Academician Vernadsky Blvd.,
UA-03142 Kyiv, Ukraine.

E-mail: tatar@imp.kiev.ua (with subject beginning by word ‘nano’).
Fax: +380 44 4242561.

After receiving of banker’s order, the Editorial Board will send the guarantee letter to the subscriber’s address for mailing the collected scientific transactions for a corresponding term.

Editorial Board of this edition hopes for effective co-operation with its present and future readers and asks to promote the maximum information about its contents to persons, institutions and organizations concerned.

ІНФОРМАЦІЯ ДЛЯ АВТОРОВ

Сборник научных трудов «*Наносистеми, наноматеріали, нанотехнології*» (ННН) публикует ещё неопубликованные и не находящиеся на рассмотрении для опубликования в иных изданиях научные обзоры и оригинальные статьи, содержащие и характеризующие результаты экспериментальных и теоретических исследований в области физики, химии, биологии, техники, методов синтеза, обработки и диагностики наноразмерных систем и наномасштабных материалов: кластеров, наночастиц, нанотрубок, нанокристаллов иnanoструктур (апатитоподобных и др. биосистем, аморфных и коллоидных наноразмерных систем, nanoструктурных плёнок и покрытий, нанопорошков и т.д.).

Статьи публикуются на одном из двух языков: **англійськом** или **українськом**.

Статьи, в оформлении которых не соблюдаены следующие правила для публикации в ННН, возвращаются авторам без рассмотрения по существу. (Датой поступления считается день повторного представления статьи после соблюдения указанных ниже правил.)

1. Статья должна быть подписана всеми авторами (с указанием их адресов электронной почты); следует указать фамилию, имя и отчество автора, с которым редакция будет вести переписку, его почтовый адрес, номер телефона (факса), адрес электронной почты.

2. Изложение должно быть ясным, структурированным (разделами «1. Вступ», «2. Експериментальна/Теоретична методика», «3. Результати та їх обговорення», «4. Висновки», «Цитована література»), сжатым, без длинных введений, отступлений и повторов, дублирования в тексте данных таблиц, рисунков и подписей к ним. Аннотация и раздел «Висновки» должны не дублировать друг друга. Числовые данные следует приводить в общепринятых единицах.

3. Объём статьи должен быть не более 5000 слов (с учётом основного текста, таблиц, подписей к рисункам, списка литературы) и 10 рисунков. Вопросы, связанные с публикацией научных обзоров (не более 22000 слов и 60 рисунков), решаются редколлегией ННН на основании предварительно предоставленной авторами расширенной аннотации работы.

4. В редакцию предоставляется 1 экземпляр рукописи с иллюстративным материалом, напечатанный на бумаге формата А4 через двойной интервал в один столбец с одной стороны листа.

5. В редакцию обязательно предоставляется (по e-mail или на компакт-диске) файл рукописи статьи, набранный в текстовом редакторе Microsoft Word 2003, 2007 или 2010 с названием, состоящим из фамилии первого автора (латиницей), например, Smirnov.doc.

6. Печатный вариант рукописи и её электронная версия должны быть идентичными и содержать **5–7 індексов PACS** (последней редакции ‘‘Physics and Astronomy Classification Scheme 2010’’—<http://publishing.aip.org/publishing/pacs/pacs-2010-regular-edition>) и **аннотацию** (200–250 слов) статьи (вместе с **5–6 ключевыми словами**). Тексты украиноязычных статей должны также содержать заглавие статьи (вместе со списком авторов и адресами соответствующих учреждений), расширенную аннотацию (300–350 слов), ключевые слова, заголовки таблиц и подписи к рисункам на **англійському** языку. Кроме того, содержания аннотаций на украинском и английском языках должны быть идентичными по смыслу.

7. Рисунки (только черно-белые или полутоновые с градацией серого) предоставляются на отдельных листах с указанием номера рисунка и фамилии первого автора. Все рисунки должны быть дополнительно представлены в виде отдельных файлов (предпочтительно в **графических форматах TIFF, EPS** или **JPEG**) с названиями, состоящими из фамилии первого автора (латиницей) и номера рисунка, например, Smirnov_fig2a.tif. Качество **ілюстрацій** (в том числе полутоновых) должно обеспечивать их воспроизведение с разрешением 300–600 точек на дюйм. Дополнительно рисунки предоставляются в формате программы, в которой они создавались.

8. Надписи на рисунках (особенно на полутоновых) надо по возможности заменить буквенными обозначениями (набранными на контрастном фоне), а кривые обозначить цифрами или различного типа линиями/маркерами, разъясняемыми в подписях рисункам или в тексте. На графиках все линии/маркёры должны быть чёрного цвета и достаточных толщин/размеров для качественного воспроизведения в уменьшенном в 2–3 раза виде (рекомендуемая ширина рисунка — 12,7 см). Снимки должны быть чёткими и контрастными, а надписи и обозначения должны не закрывать существенные детали (для чего можно использовать стрелки). Вместо указания в подтекстовке увеличения при съёмке желательно проставить масштаб (на контрастном фоне) на одном из идентичных снимков. На графиках подписи к осям, выполненные на языке статьи, должны содержать обозначения (или наименования) откладываемых величин и через запятую их единицы измерения.

9. Формулы в текст необходимо вставлять с помощью редактора формул MathType, полностью совместимого с MS Office 2003, 2007, 2010.

10. Рисунки, а также таблицы и подстрочные примечания (сноски) должны иметь сплошную нумерацию по всей статье.

11. Ссылки на литературные источники следует давать в виде порядкового номера, напечатанного в строку в квадратных скобках. Список литературы составляется в порядке первого упоминания источника. Примеры оформления ссылок приведены ниже; просим обратить внимание на порядок следования инициалов и фамилий авторов, библиографических сведений и на разделительные знаки, а также на необходимость указания **всех** соавторов цитированной работы и (в конце каждой ссылки) её **цифрового ідентификатора DOI**, если таковой имеется у соответствующей публикации (и указан на её интернет-странице издательства):

ІНФОРМАЦІЯ ДЛЯ ПЕРЕДПЛАТНИКІВ І АВТОРІВ

1. T. M. Radchenko and V. A. Tatarenko, *Usp. Fiz. Met.*, **9**, No. 1: 1 (2008) (in Ukrainian);
<https://doi.org/10.15407/ufm.09.01.001>
2. T. M. Radchenko, A. A. Shylau, and I. V. Zozoulenko, *Phys. Rev. B*, **86**: 035418 (2012);
<https://doi.org/10.1103/PhysRevB.86.035418>
3. A. Meisel, G. Leonhardt, and R. Szargan, *Röntgenspektren und Chemische Bindung [X-Ray Spectra and Chemical Bond]* (Leipzig: Akademische Verlagsgesellschaft Geest & Portig K.G.: 1977) (in German).
4. J. M. Ziman, *Printsyipy Teorii Tvyordogo Tela* [Principles of the Theory of Solids] (Moscow: Mir: 1974) (Russian translation).
5. M. A. Stucke, D. M. Dimiduk, and D. M. Hazzledine, *High Temperature Ordered Intermetallic Alloys. V* (Eds. I. Baker and R. Darolia) (Pittsburgh, PA, USA: MRS: 1993), p. 471.
6. *Handbook of Mathematical Functions with Formulas, Graphs and Mathematical Tables* (Eds. M. Abramowitz and I. A. Stegun), Nat'l Bureau of Standards. Appl. Math. Ser. Vol. **55** (Washington, D.C.: U.S. Govt. Printing Office: 1964).
7. B. V. Karporvych and O. B. Borovkoff, *Proc. of Symp. 'Micromaterials Engineering'* (Dec. 25–31, 1999) (Kiev: RVV IMF: 2000), vol. 2, p. 113 (in Russian).
8. T. M. Radchenko, *Vplyu Uporiadkuvannya Defektnoyi Struktury na Transportni Vlastyvosti Zmishanykh Krystaliv* [Influence of Ordering of the Defect Structure on Transport Properties of the Mixed Crystals] (Thesis of Disser. for Dr. Phys.-Math. Sci.) (Kyiv: G. V. Kurdyumov Institute for Metal Physics, N.A.S.U.: 2015) (in Ukrainian).
9. E. M. Gololobov, V. B. Shipilo, N. I. Sedrenok, and A. I. Dudyak, *Sposob Polucheniya Karbonitridov Metallov* [Production Method of Metal Carbonitrides], Authors' Certificate 722341 SSSR (Published November 21, 1979) (in Russian).
10. V. G. Trubachev, K. V. Chuistov, V. N. Gorshkov, and A. E. Perekos, *Sposob Polucheniya Metallicheskikh Poroshkov* [The Technology of Metallic Powder Production]: Patent 1639892 SU. MKI, B22 F9/02, 9/14 (Otkrytiya i Izobreteniya, **34**, No. 13: 11) (1991) (in Russian).
11. Yu. M. Koval' and V. V. Nemoshkalenko, *O Prirode Martensitykh Prevrashchenij* [On the Nature of Martensitic Transformations] (Kyiv: 1998) (Prepr./N.A.S. of Ukraine. Inst. for Metal Physics. No. 1, 1998) (in Russian).

Следует применять общепринятые сокращения названий журналов и сборников трудов:
<http://www.cas.org/content/references/corejournals>; <http://rmp.aps.org/files/rmpguapb.pdf>;
http://images.webofknowledge.com/WOK46P9/help/WOS/A_abrvjt.html;
<http://www.ams.org/msnhtml/serials.pdf>.

Обязательным требованием является предоставление дополнительного списка цитированной литературы (**References**) в латинской транслитерации (система BGN/PCGN; рекомендуемые транслитераторы: <http://www.sloynyk.ua/services/translit.php>; <http://ru.translit.net/?account=bgn>). После транслитерированных названий книг, диссертаций, патентов и пр. надо приводить в квадратных скобках их англоязычный перевод. При транслитерации статей из НИН надо использовать написание Ф.И.О. авторов, приведённое **только** в англоязычном оглавлении соответствующего выпуска, и **официальное** транслитерированное название сборника (см. также сайт).

12. Корректура авторам может быть выслана электронной почтой в виде pdf-файла. На проверку корректуры авторам отводятся 5 рабочих дней, начиная со дня, следующего за датой отправки корректуры. По истечении указанного срока статья автоматически направляется в печать. Исправления следует отметить и прокомментировать в самом pdf-файле либо оформить в виде перечня исправлений и переслать (от имени уполномоченного представителя коллектива авторов) по электронной почте в адрес редакции.

Печатные версии рукописи направляются непосредственно в редакцию НИН по почтовому адресу: бульвар Акад. Вернадского, 36, каб. 210; 03142 Киев, Украина либо члену редакционной коллегии (состав редколлегии указан на 2-й странице обложки). Электронный вариант статьи направляется по e-mail: tatar@imp.kiev.ua (с темой, начинающейся словом 'напо').

В соответствии с договорённостью между редакцией НИН и учредителями сборника, редакция считает, что авторы, посыпая ей рукопись статьи, передают учредителям и редколлегии право опубликовать эту рукопись на **англійському (українському)** языке, и просит авторов сразу прикладывать к рукописи подписанное авторами «Соглашение о передаче авторского права»:

Угода про передачу авторського права

Ми, що нижче підписалися, автори рукопису «-----», передаємо засновникам і редколегії збірника наукових праць «*Наносистеми, наноматеріали, нанотехнології*» право опубліковувати цей рукопис англійською (українською) мовою. Ми підтверджуємо, що ця публікація не порушує авторського права інших осіб, установ або організацій.

Підписи авторів: ----- (ПРИЗВИЩЕ Ім'я, дата, адреса, № телефону, e-mail)

При этом за авторами сохраняются все остальные права как собственников этой рукописи. Авторы могут получить опубликованный выпуск со своей статьей в редакции сборника по вышеуказанному адресу (тел. №№: +380 44 4241221, +380 44 4249042), а также загрузить pdf-файл статьи с сайта сборника: <http://www.imp.kiev.ua/nanosys/ru/articles/index.html>.

INFORMATION FOR CONTRIBUTORS

Submission of Manuscripts: Papers should be sent to the Executive Managing Editor, Editorial Office, Institute for Metal Physics, N.A.S.U., 36 Academician Vernadsky Boulevard, UA-03142 Kyiv, Ukraine. Manuscripts may also be submitted to a member of the Editorial Advisory Board or to the appropriate Editorial Board Member who is familiar with the research presented.

Submission of a paper to '*Nanosistemi, Nanomateriali, Nanotehnologii*' (i.e., 'Nanosystems, Nanomaterials, Nanotechnologies') will be taken to imply that it represents original work not previously published, it is not being considered for publication elsewhere, and if accepted for publication, it will not be published in the same language without the consent of the Editors and Publisher. It is a condition of acceptance by the Editor of a typescript for publication that the Publishers acquire automatically the copyright in the typescript throughout the world.

Scope of the Collected Scientific Transactions: '*Nanosistemi, Nanomateriali, Nanotehnologii*' (i.e., 'Nanosystems, Nanomaterials, Nanotechnologies'—NNN) is the quarterly multidisciplinary peer-reviewed collected scientific transactions, which publish high-quality work on all aspects of nanoscience and nanotechnology. Currently, transactions stand alone in serving the 'nano' community in providing up-to-date information on all developments and progresses being made in nanoscience and nanotechnology and the future predictions for this extraordinary technology. The topics covered by the transactions relate to all 'nano' related areas of the latest research and recent development works including nanomaterials, characterization tools, fabrication methods, numerical simulation, and theory as well as discussions in the field of nanoscience and technology ranging from basic aspects of the science of nanoscale systems and materials to practical applications of such systems and materials ranging from civil engineering to advanced molecular electronics so promising to transform our everyday technology as well as basic economics. The subjects covered include the following: 1. physical sciences; 2. chemical sciences; 3. life sciences; 4. theoretical and computational science and engineering.

Language: The language of publication may be English or Ukrainian.

Abstract: Each paper requires an English abstract of 200–250 words summarizing the significant coverage and findings.

Keywords and PACS numbers: Up to six keywords and PACS numbers reflecting the content of the contribution should be supplied (see 'Physics and Astronomy Classification Scheme 2010' at <http://publishing.aip.org/publishing/pacs/pacs-2010-regular-edition>).

Manuscript Preparation: Papers should be typed (in duplicate) with double spacing and wide margins on good quality paper (A4 size). The length of original contributions should not in general exceed 5000 words and 10 figures, and subject review articles should not exceed 22000 words and 60 figures, including tables and diagrams. Authors are urged to arrange the subject matter clearly under headings such as: 1. Introduction, 2. Experimental/Theoretical Details, 3. Results, 4. Discussion, 5. Conclusion, References. Subsections should be identified with section and subsection numbers (such as 6.1. Second-Value Subheading).

References and Notes: Notes are indicated in the text by consecutive superior Arabic numbers (without parentheses). References should be numbered consecutively (in square brackets) throughout the text. The full list should be collected and typed at the end of the paper in numerical order. Listed references should be completed in all details including **DOI** (if available) but excluding article titles in journals. **All authors'** initials should precede their surnames. Examples of references preparation:

1. T. M. Radchenko and V. A. Tatarenko, *Usp. Fiz. Met.*, **9**, No. 1: 1 (2008) (in Ukrainian);
<https://doi.org/10.15407/ufm.09.01.001>
2. T. M. Radchenko, A. A. Shylau, and I. V. Zozoulenko, *Phys. Rev. B*, **86**: 035418 (2012);
<https://doi.org/10.1103/PhysRevB.86.035418>
3. A. Meisel, G. Leonhardt, and R. Szargan, *Röntgenspektren und Chemische Bindung* [X-Ray Spectra and Chemical Bond] (Leipzig: Akademische Verlagsgesellschaft Geest & Portig K.-G.: 1977) (in German).
4. J. M. Ziman, *Printsyipy Teorii Tvyordogo Tela* [Principles of the Theory of Solids] (Moscow: Mir: 1974) (Russian translation).
5. M. A. Stucke, D. M. Dimiduk, and D. M. Hazzledine, *High Temperature Ordered Intermetallic Alloys. V* (Eds. I. Baker and R. Darolia) (Pittsburgh, PA, USA: MRS: 1993), p. 471.
6. *Handbook of Mathematical Functions with Formulas, Graphs and Mathematical Tables* (Eds. M. Abramowitz and I. A. Stegun), Nat'l Bureau of Standards. Appl. Math. Ser. Vol. 55 (Washington, D.C.: U.S. Govt. Printing Office: 1964).
7. B. B. Karpovych and O. B. Borovkoff, *Proc. of Symp. 'Micromaterials Engineering'* (Dec. 25–31, 1999) (Kiev: RVV IMF: 2000), vol. 2, p. 113 (in Russian).
8. T. M. Radchenko, *Vplyv Uporyadkuvannya Defektnoi Struktury na Transportni Vlastyvosti*

ІНФОРМАЦІЯ ДЛЯ ПЕРЕДПЛАТНИКІВ І АВТОРІВ

Zmishanykh Krystaliv [Influence of Ordering of the Defect Structure on Transport Properties of the Mixed Crystals] (Thesis of Disser. for Dr. Phys.-Math. Sci.) (Kyiv: G. V. Kurdyumov Institute for Metal Physics, N.A.S.U.: 2015) (in Ukrainian).

9. E. M. Gololobov, V. B. Shipilo, N. I. Sedrenok, and A. I. Dudyak, *Sposob Polucheniya Karbonitridov Metallov* [Production Method of Metal Carbonitrides], Authors' Certificate 722341 SSSR (Published November 21, 1979) (in Russian).

10. V. G. Trubachev, K. V. Chuistov, V. N. Gorshkov, and A. E. Perekos, *Sposob Polucheniya Metallicheskikh Poroshkov* [The Technology of Metallic Powder Production]: Patent 1639892 SU. MKI, B22 F9/02, 9/14 (Otkrytiya i Izobreteniya, 34, No. 13: 11) (1991) (in Russian).

11. Yu. M. Koval' and V. V. Nemoshkalenko, *O Prirode Martensitnykh Prevrashchenij* [On the Nature of Martensitic Transformations] (Kyiv: 1998) (Prepr./N.A.S. of Ukraine. Inst. for Metal Physics. No. 1, 1998) (in Russian).

Journal title abbreviations should conform to generally accepted styles:

<http://www.cas.org/content/references/corejournals>; <http://rmp.aps.org/files/rmpguapb.pdf>;
http://images.webofknowledge.com/WOK46P9/help/WOS/A_abrvjt.html;
<http://www.ams.org/msnhtml/serials.pdf>.

Equations and Formulae: Formulas in the text should be inserted by MathType, which is fully compatible with MS Office 2003, 2007, 2010.

Tables: Number tables consecutively with arabic numerals and give a clear descriptive caption at the top.

Figures: All figures should be numbered with consecutive arabic numerals, have descriptive captions and be mentioned in the text. Keep figures separate at the end of the text and clearly label each figure with author's name and figure number. The labels at axis should contain the designation (or notation) of quantities and their units.

Preparation: Figures submitted (black-and-white or greyscale strongly recommended) must be of a high enough standard for reproduction with 300–600 dpi resolution (including half-tone illustrations). Redrawing or retouching of unusable figures will be charged to the authors.

Colour Plates: Whenever the use of colour is an integral part of the research, or where the work is generated in colour, the Transactions will publish the colour illustrations with charge to the author. Reprints in colour will carry a surcharge. Please write to the Publisher for details.

Submission of Electronic Text: Authors should also submit papers by e-mail or on a CD (in addition to hard copy with figures). The file should be saved in the native formats of the Microsoft Word 2003, 2007 or 2010 with a name consisting the name of the first author, for example, Smirnov.doc. The electronic form of figures (graphics files in **TIFF, EPS or JPEG** formats preferably and with name consisting the name of the first author also, for example, Smirnov_fig2a.tiff) should be planned so that they reduce to 12.7 cm column width (or less), and keep them separate from the text file. It is necessary to submit additionally all the **figures** within the format of the program, in which they were created.

Proofs: In a special emergency, contributors may receive page proofs for correction by e-mail as a PDF document. In that case, these must be returned to Kyiv office (tatar@imp.kiev.ua) with subject beginning by word 'nano' within 120 hours of receipt.

Page Charges: There are no page charges to individuals or institutions.

Reprints: Hard-copy reprints provided to the first-named author of each paper may be ordered by completing the appropriate form sent with proofs. Authors can de-archive a PDF version of their published article from Editorial Office site: <http://www.imp.kiev.ua/nanosys/ru/articles/index.html>.

Further Information: All questions arising after the acceptance of manuscripts, especially those relating to reprints, should be directed to Executive Managing Editor, Editorial Office, G. V. Kurdyumov Institute for Metal Physics, N.A.S.U., 36 Academician Vernadsky Blvd., UA-03142 Kyiv, Ukraine.

Fax: +380 44 4242561, e-mail: tatar@imp.kiev.ua (with subject beginning by word 'nano').

We ask the authors to apply with their manuscript

Copyright Transfer Agreement

We, the undersigned authors of the manuscript '_____, transfer to the founders and the Editorial Board of the collected scientific transactions 'Nanosistemi, Nanomateriali, Nanotekhnologii' the right to publish this manuscript in English language (or in the Ukrainian translation). We confirm that publication of this manuscript will not infringe a copyright of other persons, institutions or organizations.

Author(s):_____

(Last Name, First Name, Affiliation)

Correspondence Address: _____

Phone and e-mail: _____

(Signature) _____
(Date)

XIV

ISSN 1816-5230. Наносистеми, наноматеріали, нанотехнології. 2024

ІНФОРМАЦІЯ ДЛЯ ПЕРЕДПЛАТНИКІВ І АВТОРІВ

ВИДАВНИЧА ЕТИКА ТА ЗАПОБІГАННЯ НЕСУМЛІННІЙ ПРАКТИЦІ ПУБЛІКАЦІЙ

Редакційна колегія збірника наукових праць «Наносистеми, наноматеріали, нанотехнології» дотримується етичних норм, прийнятих міжнародним науковим співтовариством, і робить усе для запобігання будь-яким порушенням їх. У своїй діяльності редакція спирається на рекомендації Комітету з етики наукових публікацій (<http://publicationethics.org>).

Обов'язки редакції

- Всі представлені статті рецензуються експертами в даній області.
- Під час розгляду статті враховуються її відповідність предметній області, обґрунтованість, значимість, оригінальність, читабельність і мова (правопис).
- За результатами рецензування стаття може бути прийнята до опублікування без доробки, прийнята з доробкою або відхиlena.
- Відхилені статті повторно не рецензуються.
- Статті можуть бути відхилені без рецензії, якщо вони очевидним чином не підходять для публікації.
- Редакція ухвалює рішення щодо публікації, керуючись політикою збірника, з урахуванням діючого законодавства в області авторського права.
- Не допускається до публікації інформація, якщо є достатньо підстав уважати, що вона є плагіятом.

За наявності яких-небудь конфліктів інтересів (фінансових, академічних, особистих) всі учасники процесу рецензування повинні сповістити про це редколегії. Всі спірні питання розглядаються на засіданні редколегії.

Прийняті до опублікування статті розміщаються у відкритому доступі на сайті збірника; авторські права зберігаються за авторами.

Етичні принципи в діяльності рецензентів

- Рецензенти оцінюють статті за їхнім вмістом, безвідносно до національності, статі, сексуальної орієнтації, релігійних переконань, етнічної приналежності або політичних переконань авторів.
- Співробітники редакції не повинні повідомляти яку-небудь інформацію про статті, що надійшли, особам, які не є рецензентами, авторами, співробітниками редакції та видавництва.
- Рецензування повинне бути проведено об'єктивно. Персональна критика автора неприпустима. Рецензенти зобов'язані обґрунтувати свою точку зору чітко й об'єктивно.
- Рецензування допомагає видавцеві приймати рішення та за допомогою співробітництва з рецензентами й авторами поліпшити статтю.
- Матеріали, отримані для рецензії, є конфіденційними документами та рецензуються анонімно.
- Рецензент також зобов'язаний звертати увагу редактора на істотну або часткову подібність представленої статті з якою-небудь іншою роботою, з якою рецензент безпосередньо знайомий.

Принципи, якими повинні керуватися автори наукових публікацій

- Автори статей повинні надавати точний звіт про виконану роботу й об'єктивне обговорення її значимості.
- Автори статті повинні надавати достовірні результати проведеного огляду й аналізи досліджень. Свідомо помилкові або сфальсифіковані твердження неприйнятні.
- Стаття повинна містити достатню кількість інформації для перевірки та повторення експериментів або розрахунків іншими дослідниками. Шахрайські або свідомо неправдиві заяви прирівнюються до неетичного поводження і є неприйнятними.
- Автори можуть надавати оригінальні регулярні й оглядові роботи. За використання текстової або графічної інформації, отриманої з робіт інших осіб, обов'язково необхідні посилання на відповідні публікації або письмовий дозвіл їхніх авторів.
- Подача статті більш ніж в один журнал розцінюється як неетичне поводження і є неприйнятною.
- Авторство повинне бути обмежене тими, хто зробив значний внесок у концепцію, розробку, виконання або інтерпретацію заявленого дослідження.
- Джерела фінансової підтримки дослідження, що публікується, можуть бути зазначені.

ІНФОРМАЦІЯ ДЛЯ ПЕРЕДПЛАТНИКІВ І АВТОРІВ

PUBLICATION ETHICS

AND MALPRACTICE STATEMENT

The Editorial Board of the Collected Scientific Transactions ‘*Nanosistemi, Nanomateriali, Nanotehnologii*’ (i.e., ‘Nanosystems, Nanomaterials, Nanotechnologies’) follows ethics norms accepted by international scientific community and makes every endeavour to prevent any infringements of the norms. The Editorial Board follows the guidelines of the Committee on Publication Ethics (<http://publicationethics.org>).

Duties of Editors

- All submitted papers are subject to strict peer-review process by reviewers that are experts in the area of the particular paper.
- The factors, which are taken into account in reviewing process, are relevance, soundness, significance, originality, readability, and quality of language.
- The possible decisions include acceptance, acceptance with revisions, or rejection.
- If authors are encouraged to revise and resubmit a submission, there is no guarantee that the revised submission will be accepted.
- Rejected articles will not be re-reviewed.
- Articles may be rejected without review, if they are obviously not suitable for publication.
- The paper acceptance is constrained by such legal requirements as shall then be in force regarding libel, copyright infringement, and plagiarism.

When a conflict of interests arising, all the participants of reviewing process should inform the Editorial Board. All the contentious questions are considered in the Board meeting.

The accepted papers are allocated in open access on the journal site; copyrights reserved.

Duties of Reviewers

- The reviewers evaluate manuscripts for their intellectual content without regard to race, gender, sexual orientation, religious belief, ethnic origin, citizenship, or political philosophy of the authors.
- The staff must not disclose any information about a submitted manuscript to anyone other than the corresponding author, reviewers, other editorial advisers, and the Publisher, as appropriate.
- Reviews should be conducted objectively. Personal criticism of the author is inappropriate. Referees should express their views clearly with supporting arguments.
- Peer review assists the Publisher in making editorial decisions and through the editorial communications with the experts from the scientific board and the author may assist the author in improving the paper.
- Manuscripts received for review are treated as confidential documents and are reviewed by anonymous staff.
- A reviewer should also call to the Publisher's attention any substantial similarity or overlap between the manuscript under consideration and any other published paper of which they have personal knowledge.

Duties of Authors

- Authors of contributions and studies research should present an accurate account of the work performed as well as an objective discussion of its significance.
- A paper should contain sufficient details and references to permit others to replicate the work. Fraudulent or knowingly inaccurate statements constitute unethical behaviour and are unacceptable.
- The authors should ensure that they have written original regular or entirely review works, if the authors have used the work and/or words of others that this has been obligatory and appropriately cited or quoted.
- Submitting the same manuscript to more than one publication concurrently constitutes unethical publishing behaviour and is unacceptable.
- Authorship should be limited to those who have made a significant contribution to the conception, design, execution, or interpretation of the reported study.
- Sources of financial support for the reported results can be specified.

PACS numbers: 61.72.Cc, 61.72.Mm, 68.35.Ct, 68.37.Ps, 68.55.A-, 68.55.Jk, 81.15.Cd

Surface Morphology of Thin Films of $(Y_{0.06}Ga_{0.94})_2O_3$ Activated by Cr^{3+}

O. M. Bordun¹, B. O. Bordun¹, I. I. Medvid¹, M. V. Protsak¹,
I. Yo. Kukharskyy¹, K. L. Biliak¹, D. M. Maksymchuk¹, I. M. Kofliuk¹,
and D. S. Leonov²

¹Ivan Franko National University of Lviv,
50, Drahomanov Str.,
UA-79005 Lviv, Ukraine

²Technical Centre, N.A.S. of Ukraine,
13, Pokrovskaya Str.,
UA-04070 Kyiv, Ukraine

Thin films of $(Y_{0.06}Ga_{0.94})_2O_3:Cr$ are obtained by radio-frequency (RF) ion-plasma sputtering in an argon atmosphere on polycrystalline polycor and amorphous ν - SiO_2 substrates. The study of the surface morphology of thin films by atomic force microscopy (AFM) shows that the transition from ν - SiO_2 substrates to polycor increases the average diameter of crystallites, which form the film, from 123 nm to 372 nm for films annealed in an argon atmosphere. The heat treatment of films on ν - SiO_2 substrates in an argon atmosphere leads to an increase in the root-mean-square roughness of thin films, which is of 1.2 nm and 2.9 nm for the unannealed and annealed films in an argon atmosphere, respectively. The analysis of the distributions of crystallites by the value of the grain diameter is carried out, and, as found during the heat treatment of $(Y_{0.06}Ga_{0.94})_2O_3:Cr$ films on ν - SiO_2 substrates, the growth of crystallites perpendicular to the film surface is observed.

Методом високочастотного (ВЧ) іонно-плазмового розпорошення в атмосфері аргону на полікристалічних підкладинках полікору й аморфних підкладинках ν - SiO_2 одержано тонкі плівки $(Y_{0.06}Ga_{0.94})_2O_3:Cr$. Дослідження морфології поверхні тонких плівок методом атомно-силової мікрокопії (ACM) показали, що з переходом від підкладинок ν - SiO_2 до полікору зростає середній діаметр кристалітів, які формують плівку від 123 нм до 372 нм для плівок, відпалених у атмосфері аргону. Термооброблення плівок на підкладинках з ν - SiO_2 у атмосфері аргону приводить до збільшення середньоквадратичної шерсткості тонких плівок, що становлять для невідпаленої та відпаленої плівок у атмосфері аргону 1,2 нм і 2,9 нм відповідно. Проведено аналіз розподілів кристалітів за величиною діаметра зерен і встановлено, що за термооброблення плівок $(Y_{0.06}Ga_{0.94})_2O_3:Cr$ на підкладинках ν - SiO_2 спостерігається зростання кри-

сталітів перпендикулярно до поверхні плівки.

Key words: gallium oxide, chromium activator, thin films, crystallites, surface morphology, AFM.

Ключові слова: оксид Галію, хром-активатор, тонкі плівки, кристаліти, морфологія поверхні, АСМ.

(Received 21 December, 2023)

1. INTRODUCTION

In recent years, nanostructured oxide materials have been widely studied, among which Ga_2O_3 occupies an important place. Gallium oxide $\beta\text{-Ga}_2\text{O}_3$ belongs to the wide-bandgap semiconductors, with a bandgap width of 4.5 to 5.1 eV, depending on the preparation conditions. This material is widely used in solar cells, gas sensors, ultraviolet photodetectors, luminescent devices, high-power Schottky diodes, and transistors [1–10]. Due to its good chemical and thermal stability, this material is promising for use in luminescent devices. In this regard, pure gallium oxide thin films, activated by various impurities, obtained by various methods, are widely studied. The photoluminescence spectrum of gallium oxide at room temperature usually shows ultraviolet and blue radiation [11–15]. In general, the optical and electrical characteristics of thin films based on $\beta\text{-Ga}_2\text{O}_3$ are determined by the methods of their preparation, deposition modes, substrate type, and processing technology, as well as the introduction of impurities, which can purposefully change the spectral-luminescent and electrophysical properties of these films. To this end, thin films with the chemical composition $(\text{Y}_{0.06}\text{Ga}_{0.94})_2\text{O}_3:\text{Cr}$ were studied in this work, in which some Ga^{3+} ions were replaced by isovalent Y^{3+} ions, which did not require local compensation of the electric charge. This substitution is because Y_2O_3 films are also quite promising in terms of their use in modern optoelectronic and luminescent technology [16–19]. This also allows us to better study the luminescence centres in thin films based on $\beta\text{-Ga}_2\text{O}_3$ since the luminescence efficiency in these films is largely determined by the peculiarities of recombination processes, which luminescence centres of defective origin usually cause.

In general, the physical properties of thin films are complicated because films do not always have a perfect structure and can be polycrystalline, amorphous, and contain inclusions of other phases. Obtaining the required and stable reproducible properties of polycrystalline films is further complicated by the presence of intergranular boundaries (IGBs). The physical properties of polycrystalline thin films are largely determined not only by the material properties but also by the energy

levels arising from the presence of the IGBs. It is clear that such levels are also determined by the size of the crystallites that form the thin films. This led to the study of the surface morphology of thin films of $(Y_{0.06}Ga_{0.94})_2O_3:Cr$ using atomic force microscopy, which is presented in this paper. The films were obtained by the method of RF ion-plasma sputtering, which is optimal for obtaining homogeneous semiconductor and dielectric films [19].

2. EXPERIMENTAL TECHNIQUE

Thin films of $(Y_{0.06}Ga_{0.94})_2O_3:Cr$ with a thickness of 0.5–1.2 μm were obtained by RF ion-plasma sputtering on polycrystalline polycor ((99.8% α (alpha)- Al_2O_3) substrates and amorphous fused quartz v - SiO_2 substrates. The RF sputtering was carried out in an argon atmosphere in a system using the magnetic field of external solenoids for compression and additional ionization of the plasma column. The feedstock was a mixture of Y_2O_3 and Ga_2O_3 oxides of the stoichiometric composition of the ‘OCЧ’ grade (extra pure). The concentration of the Cr^{3+} activator was 0.5 mol.%. After the films were deposited on v - SiO_2 and polycor substrates, they were heat treated in argon at 1000–1100°C.

The structure and phase composition of the obtained films were studied by x-ray diffraction analysis (Shimadzu XDR-600). X-ray diffraction studies showed the presence of a polycrystalline structure with a predominant orientation in the (002), (111), (110), and (512) planes. The analysis of the obtained diffractograms shows that the structure of the films obtained corresponds to the monoclinic crystal structure of β - Ga_2O_3 . The diffractograms of $(Y_{0.06}Ga_{0.94})_2O_3:Cr$ thin films almost completely correspond to the diffractograms of unalloyed $(Y_{0.06}Ga_{0.94})_2O_3$ thin films, which were presented earlier in our work [20].

The surface morphology of the films was studied using an INTEGRA TS-150 atomic force microscope (AFM). The image of the surface of thin films was obtained in the semi-contact mode.

The x-ray photoelectron spectroscopy (XPS) method was used to analyse the elemental composition of the surface of the obtained thin films. The x-ray photoelectron spectroscopy (XPS, Phoibos 150, Specs) spectra were recorded using a monochromatic x-ray source $AlK\alpha$ (1486.6 eV). The binding energy was calibrated against the signal from C1s at 285.0 eV.

3. RESULTS AND DISCUSSION

Microphotographs of the surface of $(Y_{0.06}Ga_{0.94})_2O_3:Cr$ thin films obtained by RF ion plasma sputtering on v - SiO_2 substrates without

heat treatment and after heat treatment in an argon atmosphere and on polycor substrates after heat treatment in an argon atmosphere are shown in Fig. 1.

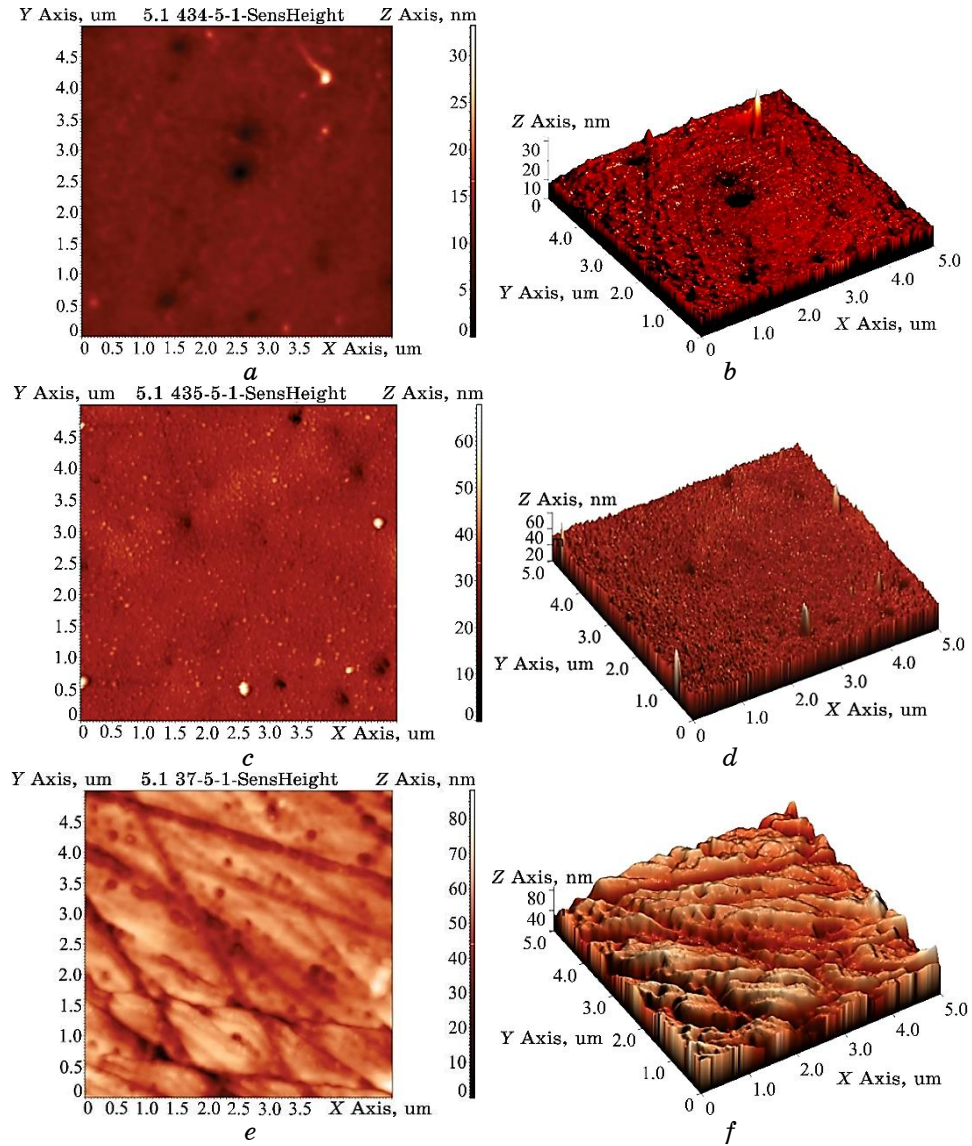


Fig. 1. Images of the surface morphology of $(Y_{0.06}Ga_{0.94})_2O_3:Cr$ thin films obtained by RF sputtering on $v\text{-SiO}_2$ substrates without heat treatment (*a*, *b*) and after heat treatment in an argon atmosphere (*c*, *d*) and on polycor substrates after heat treatment in an argon atmosphere (*e*, *f*). Images *a*, *c* and *e* are two-dimensional, *b*, *d* and *f* are three-dimensional.

TABLE. Parameters of crystal grains of thin films of $(Y_{0.06}Ga_{0.94})_2O_3:Cr$.

Parameter	Without heat treatment on $\nu\text{-SiO}_2$ substrate	Heat treatment in Ar on a $\nu\text{-SiO}_2$ substrate	Heat treatment in Ar on a polycor substrate
Average grain diameter, nm	181	123	372
RMS roughness, nm	1,2	2,9	9,5
Maximum grain height, nm	12	33	55
Average grain volume, nm^3	2960	6040	234000

The topography of the samples was quantitatively characterized by standard parameters: root-mean-square roughness, maximum grain height, average grain diameter, and average grain volume, which were calculated from AFM data using the Image Analysis 3.5 image-processing module for areas of the same size (5000×5000 nm).

The characteristic parameters of $(Y_{0.06}Ga_{0.94})_2O_3:Cr$ thin films deposited on $\nu\text{-SiO}_2$ substrates without heat treatment and for films deposited on $\nu\text{-SiO}_2$ and polycor substrates after heat treatment in an argon atmosphere are shown in Table.

As can be seen from the results obtained, different types of substrates and the presence of heat treatment have a significant effect on the size of crystal grains and surface roughness of the obtained samples.

The analysis of AFM images (Fig. 1) and parameters of crystal grains (Table) of the surface of $(Y_{0.06}Ga_{0.94})_2O_3:Cr$ films shows that the films deposited on the amorphous quartz substrate $\nu\text{-SiO}_2$ are formed from significantly smaller grains than when the films are deposited on a polycrystalline polycor substrate. The size of crystallites of thin films of $(Y_{0.06}Ga_{0.94})_2O_3:Cr$ deposited on a $\nu\text{-SiO}_2$ substrate after heat treatment in an argon atmosphere increases, although a decrease in the average size of the diameter of the grains, from which these films are formed is observed. At the same time, the value of the average volume of crystallites increases significantly. Such an increase in the size of crystalline grains and, in particular, an increase in the average grain volume and changes in the value of the root-mean-square roughness indicate a complication of the surface structure.

A comparison of the histograms of the distribution of grain heights (Fig. 2) shows that smaller grains are formed on fused quartz substrates, which form the surface of unannealed $(Y_{0.06}Ga_{0.94})_2O_3:Cr$ thin films, although their average diameters are

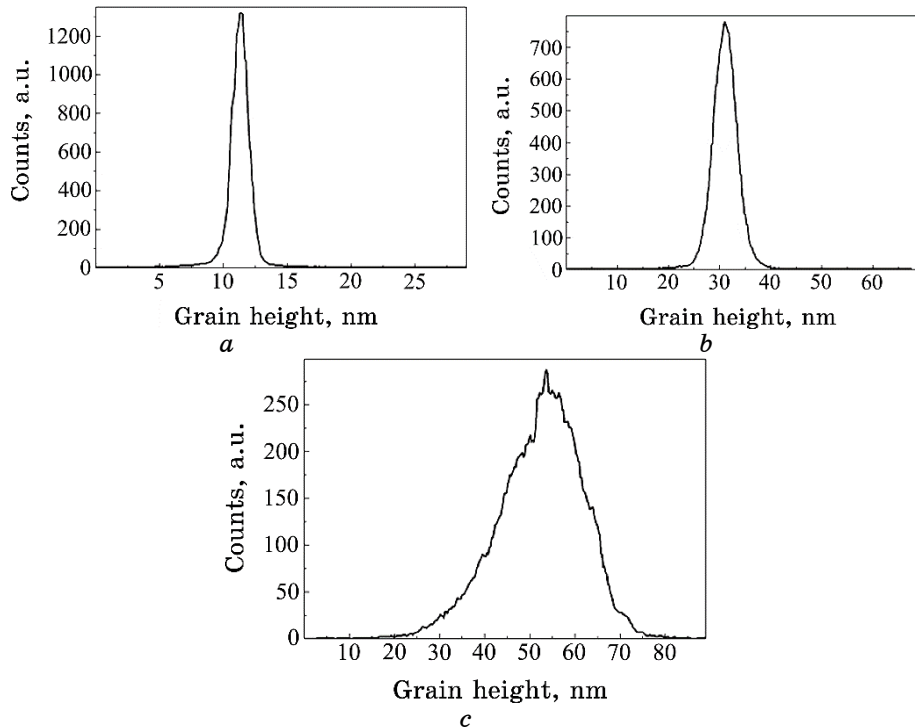


Fig. 2. Distribution of grain heights for AFM images of $(Y_{0.06}Ga_{0.94})_2O_3:Cr$ thin films obtained by RF sputtering on $v\text{-SiO}_2$ substrates without heat treatment (a), after heat treatment in an argon atmosphere (b), and on polycor substrates after heat treatment in an argon atmosphere (c).

larger than those of annealed films in an argon atmosphere are. Heat treatment of thin films of $(Y_{0.06}Ga_{0.94})_2O_3:Cr$ deposited on a quartz substrate in an argon atmosphere significantly affects the value of grain height compared to unannealed films (increases by about 2.4 times). If we compare the parameter RMS surface roughness of thin films, then, for films deposited on NaCl substrates, it is the highest value compared to unannealed films and films subjected to heat treatment in an argon atmosphere deposited on quartz substrates. For films annealed in an argon atmosphere and deposited on polycor substrates, the value of this parameter differs by about 3.3 times compared to thin films of $(Y_{0.06}Ga_{0.94})_2O_3:Cr$ deposited on a quartz substrate.

The increase in the size of crystalline grains in $(Y_{0.06}Ga_{0.94})_2O_3:Cr$ thin films after heat treatment (Table) indicates the possibility of the transition of the film surface to a more nanostructured state due to the crystallization of the surface layer.

The characteristic distributions of grain diameter sizes in thin films of $(Y_{0.06}Ga_{0.94})_2O_3:Cr$ depending on the type of substrate and the presence of heat treatment are shown in Fig. 3.

A thorough review [21] analysed the growth of crystal grains in thin films and the evolution of crystal structures and showed that polycrystalline thin films with thicknesses up to 1 μm , which is typical for our $(Y_{0.06}Ga_{0.94})_2O_3:Cr$ films, often have 2D-like structures. In such structures, most grain boundaries are perpendicular to the film surface. Most of the materials analysed in [21] form films of nonequilibrium grains with sizes smaller than the film thickness and form two-dimensional structures only after annealing. Based on numerical results, [21] also concluded that the formation of grains in thin films is difficult to describe accurately using modelling or comparison with experiments that described the study of foams or monolayers. In general, grain sizes in polycrystalline films are lognormally distributed in size.

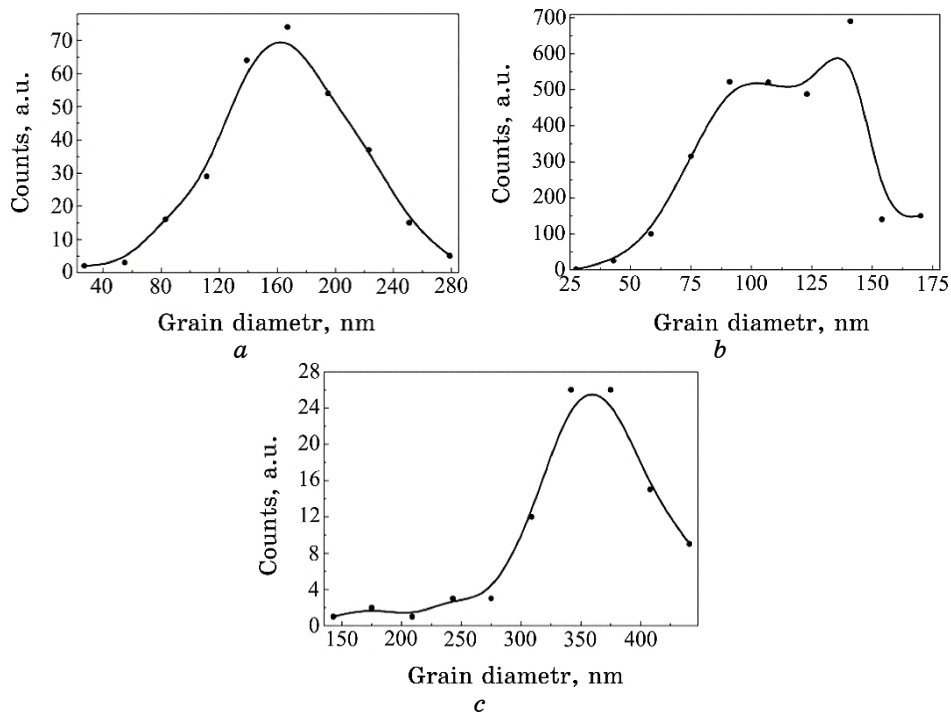


Fig. 3. The distribution of grain diameter sizes and the calculated approximate diameter distribution on AFM images of $(Y_{0.06}Ga_{0.94})_2O_3:Cr$ thin films obtained by RF sputtering on $v-SiO_2$ substrates without heat treatment (a), after heat treatment in an argon atmosphere (b), and on polycor substrates after heat treatment in an argon atmosphere (c).

In some cases, further grain growth is observed due to ‘anomalous’ growth or preferential growth of several grains, which usually have specific crystallographic orientation relations relative to the substrate surface plane. Our results show that such a situation is most likely characteristic of the $(Y_{0.06}Ga_{0.94})_2O_3:Cr$ films we obtained. When the number of growing grains leads to a ‘matrix’ of grains beyond the static boundaries, a bimodal grain size distribution develops, which is called secondary grain growth [22]. Grains that grow abnormally often have a limited or homogeneous texture. Secondary grain growth in thin films typically involves an evolution in the distribution of grain textures as well as an evolution in the grain size distribution.

Our results of the distribution of grain diameter sizes in thin films of $(Y_{0.06}Ga_{0.94})_2O_3:Cr$ (Fig. 3) indicate that when these films are deposited on polycor substrates after annealing in an argon atmosphere, an unimodal distribution of diameters with a maximum in the region of 365 nm is observed. A more complex shape of the diameter distribution is formed when the films are deposited on an amorphous $\nu\text{-SiO}_2$ substrate after annealing in an argon atmosphere. In particular, for freshly deposited films (Fig. 3, *a*), a unimodal distribution with a maximum in the 170 nm region is manifested. After heat treatment of such films in an argon atmosphere (Fig. 3, *b*), a bimodal distribution with maxima in the region of 100 and 135 nm is observed.

Analysing the situation described above, we can conclude that during the heat treatment process, grain growth occurs due to the processes of growth and sintering. It should be noted that a similar situation is observed during RF deposition on $\nu\text{-SiO}_2$ substrates and $\beta\text{-Ga}_2O_3$ thin films, where the growth of secondary and tertiary grains is observed [23]. The growth of secondary and even tertiary grains was observed in these films both during RF sputtering and during heat treatment.

For unannealed $(Y_{0.06}Ga_{0.94})_2O_3:Cr$ thin films deposited on $\nu\text{-SiO}_2$ substrates and annealed films in an argon atmosphere deposited on polycor substrates, the distribution of grains by diameter is well described by a normal logarithmic law. This situation is typical for the distribution of grains by diameter in polycrystalline films [24]. In particular, this situation is observed during the RF deposition of $Y_2O_3:\text{Eu}$ thin films [25].

To describe the obtained dependences (Fig. 3, *a*, *c*), we use the normal logarithmic law, which is used to distribute grains by diameter size in polycrystalline films [24]:

$$f(D) = \frac{1}{\sigma D \sqrt{2\pi}} \exp\left[-\frac{(\ln D - \mu)^2}{2\sigma^2}\right],$$

where $\int_0^{\infty} f(x)dx = 1$, D is the grain diameter divided by the film thickness; μ is the average value of $\ln D$; σ is the standard deviation (dispersion) of $\ln D - \mu$. When fitting the data, μ and σ are independent adjustable parameters.

Our analysis shows that during the RF deposition of thin films on a $v\text{-SiO}_2$ substrate, a unimodal distribution of grains in terms of diameter is observed (Fig. 3, a) with a maximum at 170 nm and a dispersion of 6.2 nm. The subsequent annealing of these films in an argon atmosphere results in a bimodal distribution of overlapping bands with maxima located in regions around 100 and 135 nm. Due to the significant overlap, the variances of these distributions are 25.1 and 13.3 nm, respectively. It is characteristic that grain growth during the annealing of thin films of $(Y_{0.06}Ga_{0.94})_2O_3:\text{Cr}$ occurs in the direction perpendicular to the film surface. During the annealing of $(Y_{0.06}Ga_{0.94})_2O_3:\text{Cr}$ films deposited on a polycor substrate, an unimodal lognormal distribution of grain diameter sizes with a maximum in the region of 365 nm and a dispersion of 2.7 nm is observed.

To verify the elemental composition of the obtained thin films, x-ray photoelectron spectroscopy (XPS) spectra were analysed. The characteristic XPS spectra for the unannealed $(Y_{0.06}Ga_{0.94})_2O_3:\text{Cr}$ thin films deposited on $v\text{-SiO}_2$ substrates and the annealed films in the argon atmosphere deposited on $v\text{-SiO}_2$ and polycor substrates are shown in Fig. 4.

The analysis showed that the recorded spectra contain peaks corresponding to O1s, C1s, Y3d, Ga3p, and Cr2p atoms. At the same

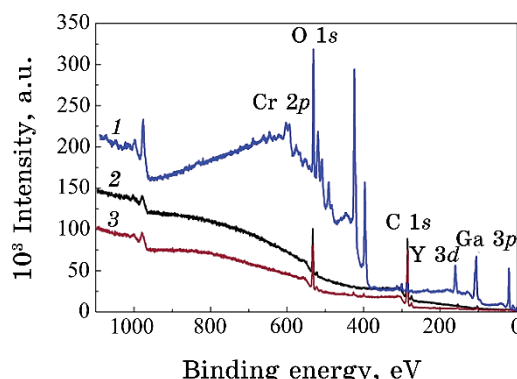


Fig. 4. XPS spectra of $(Y_{0.06}Ga_{0.94})_2O_3:\text{Cr}$ thin films obtained by RF sputtering on $v\text{-SiO}_2$ substrates without heat treatment (1), after heat treatment in an argon atmosphere (2), and on polycor substrates after heat treatment in an argon atmosphere (3).

time, the peak characteristic of the Cr $2p$ atom is expressed relatively weakly, since the chromium concentration in the obtained films is insignificant. It is characteristic that it is most intensively manifested in $(Y_{0.06}Ga_{0.94})_2O_3:Cr$ films deposited on polycor substrates.

4. CONCLUSIONS

It has been established that thin films of $(Y_{0.06}Ga_{0.94})_2O_3:Cr$ formed from nanometer grains are formed by RF ion-plasma sputtering on polycrystalline polycor and amorphous v-SiO_2 substrates. Based on the AFM images, it is shown that the average diameters of the crystallites of the films on polycor substrates after heat treatment in an argon atmosphere are of 372 nm, on v-SiO_2 substrates without heat treatment, are of 181 nm, and after heat treatment in an argon atmosphere, are of 123 nm. The heat treatment of films on v-SiO_2 substrates in an argon atmosphere leads to an increase in the root mean square roughness from 1.2 to 2.9 nm. It has been found that when thin films of $(Y_{0.06}Ga_{0.94})_2O_3:Cr$ are deposited on v-SiO_2 substrates, an unimodal lognormal distribution of grains in terms of diameter size with a maximum at 170 nm and a dispersion of 6.2 nm is observed. In the process of heat treatment of such films, a bimodal distribution appears with maxima at 100 and 135 nm and dispersions of 25.1 and 13 nm, respectively. During this heat treatment, grain growth perpendicular to the film surface is observed. During the heat treatment of films deposited on polycarbonate substrates, a unimodal distribution of grains by diameter with a maximum of 365 nm and a dispersion of 2.7 nm occurs.

REFERENCES

1. M. Higashiwaki, K. Sasaki, A. Kuramata, T. Masui and S. Yamakoshi, *phys. status solidi (a)*, **211**, No. 1: 21 (2014);
<https://doi.org/10.1002/pssa.201330197>
2. M. He, Q. Zeng, and L. Ye, *Crystals*, **13**, No. 10: 1434 (2023);
<https://doi.org/10.3390/cryst13101434>
3. X. Chen, K. W. Liu, Z. Z. Zhang, C. R. Wang, B. H. Li, H. F. Zhao, D. X. Zhao, and D. Z. Shen, *ACS Appl. Mater. Inter.*, **8**, No. 6: 4185 (2016);
<https://doi.org/10.1021/acsami.5b11956>
4. S. Kumar and R. Singh, *phys. status solidi (RRL)*, **7**, No. 10: 781 (2013);
<https://doi.org/10.1002/pssr.201307253>
5. D. Y. Guo, Z. P. Wu, Y. H. An, P. G. Li, P. C. Wang, X. L. Chu, X. C. Guo, Y. S. Zhi, M. Lei, L. H. Li, and W. H. Tang, *Appl. Phys. Lett.*, **106**, No. 6: 042105 (2015); <https://doi.org/10.1063/1.4907174>
6. S. Kumar, S. Dhara, R. Agarwal, and R. Singh, *J. Alloys Compounds*, **683**: 143 (2016); <https://doi.org/10.1016/j.jallcom.2016.05.079>

7. R. Suzuki, S. Nakagomi, Y. Kokubun, N. Arai, and S. Ohira, *Appl. Phys. Lett.*, **94**, No. 22: 222102 (2009); <https://doi.org/10.1063/1.3147197>
8. K. Sasaki, M. Higashiwaki, A. Kuramata, T. Masui, and S. Yamakoshi, *IEEE Electron. Device Lett.*, **34**, No. 4: 493 (2013); <https://doi.org/10.1109/LED.2013.2244057>
9. M. Higashiwaki, *AAPPS Bull.*, **32**: 3 (2022); <https://doi.org/10.1007/s43673-021-00033-0>
10. K. Sasaki, M. Higashiwaki, A. Kuramata, T. Masui, and S. Yamakoshi, *J. Cryst. Growth*, **378**: 591 (2013); <https://doi.org/10.1016/j.jcrysgro.2013.02.015>
11. O. M. Bordun, B. O. Bordun, I. Yo. Kukharskyy, and I. I. Medvid, *J. Appl. Spectrosc.*, **86**, No. 6: 1010 (2020); <https://doi.org/10.1007/s10812-020-00932-4>
12. A. K. Saikumar, Sh. D. Nehate, and K. B. Sundaram, *ECS J. of Solid State Science and Technol.*, **8**, No. 7: Q3064 (2019); <https://doi.org/10.1149/2.0141907jss>
13. Lingyi Kong, Jin Ma, Caina Luan, Wei Mi, and Yu Lv, *Thin Solid Films*, **520**, No. 13: 4270 (2012); <https://doi.org/10.1016/j.tsf.2012.02.027>
14. O. M. Bordun, B. O. Bordun, I. I. Medvid, and I. Yo. Kukharskyy, *Acta Physica Polonica A*, **133**, No. 4: 910 (2018); <https://doi.org/10.12693/APhysPolA.133.910>
15. K. H. Choi and H. C. Kang, *Materials Letters*, **123**: 160 (2014); <https://doi.org/10.1016/j.matlet.2014.03.038>
16. C. B. Willingham, J. M. Wahl, P. K. Hogan, L. C. Kupferberg, T. Y. Wong, and A. M. De, *Proc. SPIE*, **5078**: 179 (2003); <https://doi.org/10.1117/12.500986>
17. T. Igarashi, M. Ihara, T. Kusunoki, K. Ohno, T. Isobe, and M. Senna, *Appl. Phys. Lett.*, **76**, No. 12: 1549 (2000); <https://doi.org/10.1063/1.1260921>
18. O. M. Bordun, I. M. Bordun, and S. S. Novosad, *J. Appl. Spectr.*, **62**, No. 6: 1060 (1995); <https://doi.org/10.1007/BF02606760>
19. K. Wasa, M. Kitabatake, and H. Adachi, *Thin Film Materials Technology: — Sputtering of Compound Materials* (New York: Springer—William Andrew Inc Publishing: 2004).
20. O. M. Bordun, B. O. Bordun, I. J. Kukharskyy, I. I. Medvid, O. Ya. Mylyo, M. V. Partyka, and D. S. Leonov, *Nanosistemi, Nanomateriali, Nano-tehnologii*, **17**, Iss. 1: 123 (2019); <https://doi.org/10.15407/nnn.17.01.123>
21. C. V. Thompson, *Sol. State Phys.*, **55**: 269 (2001); [https://doi.org/10.1016/S0081-1947\(01\)80006-0](https://doi.org/10.1016/S0081-1947(01)80006-0)
22. C. V. Thompson, *J. Appl. Phys.*, **58**: 763 (1985); <https://doi.org/10.1063/1.336194>
23. O. M. Bordun, B. O. Bordun, I. Yo. Kukharskyy, I. I. Medvid, I. I. Polovynko, Zh. Ya. Tsapovska, and D. S. Leonov, *Nanosistemi, Nanomateriali, Nano-tehnologii*, **19**, Iss. 1: 159 (2021); <https://doi.org/10.15407/nnn.19.01.159>
24. J. E. Palmer, C. V. Thompson, and Henry L. Smith, *J. Appl. Phys.*, **62**, No. 6: 2492 (1987); <https://dx.doi.org/10.1063/1.339460>
25. O. M. Bordun, I. O. Bordun, I. M. Kofliuk, I. Yo. Kukharskyy, I. I. Medvid, Zh. Ya. Tsapovska, and D. S. Leonov, *Nanosistemi, Nanomateriali, Nano-tehnologii*, **20**, Iss. 1: 91 (2021); <https://doi.org/10.15407/nnn.20.01.091>

PACS numbers: 61.66.Fn, 64.75.Nx, 65.40.Ba, 81.30.Dz, 81.40.Cd, 82.33.Pt, 82.60.Lf

Predicting the Thermodynamic Stability of $(\text{Gd}_{1-x}\text{Ln}_x)_2\text{SiO}_5$ and $(\text{Lu}_{1-x}\text{Ln}_x)_2\text{SiO}_5$ Solid Solutions of the $P2_1/c$ Space Group

E. I. Get'man¹, O. Yu. Mariichak¹, L. I. Ardanova², and S. V. Radio¹

¹Vasyl' Stus Donetsk National University,
21, 600th Anniversary Str.,
UA-21027 Vinnytsia, Ukraine

²Department of Chemistry and Geology,
Minnesota State University,
56001 Mankato, Minnesota, USA

Within the framework of V. S. Urusov's crystal-energy theory of isomorphous substitutions, the mixing energies (interaction parameters) and critical decomposition (stability) temperatures are calculated for the $(\text{Gd}_{1-x}\text{Ln}_x)_2\text{SiO}_5$ systems, where Ln represents rare-earth elements (REEs) or yttrium. The values of the total mixing energies are determined mainly by contributions arising from the difference in sizes of the substituting structural units. The contributions due to differences in the degree of ionicity of the chemical bond between the components are significantly smaller and can be neglected in most cases. Diagrams of the thermodynamic stability of systems $(\text{Gd}_{1-x}\text{Ln}_x)_2\text{SiO}_5$ and decomposition domes of the $(\text{Gd}_{1-x}\text{Ln}_x)_2\text{SiO}_5$ and $(\text{Lu}_{1-x}\text{Ln}_x)_2\text{SiO}_5$ systems are presented, which allow for graphical prediction of decomposition temperatures of solid solutions within the specified substitution limits, equilibrium substitution limits at a given temperature, and ranges of thermodynamic stability for solid solutions. The predictions of thermodynamic stability are consistent with experimental data previously reported in the literature for solid solutions based on doped gadolinium oxyorthosilicate. The gadolinium oxyorthosilicate solid solutions, which exhibit luminescent, scintillation, and other practically important properties, due to their very low critical decomposition temperatures and a wide temperature range of thermodynamic stability compared to solid solutions of oxyorthosilicate of other REEs, can find practical applications as nanomaterials.

У рамках кристалоенергетичної теорії ізоморфних заміщень В. С. Урусова розраховано енергії змішання (параметри взаємодії) та критичні температури розпаду (стабільності) у системах $(\text{Gd}_{1-x}\text{Ln}_x)_2\text{SiO}_5$, де Ln — рідкісноземельні елементи (РЗЕ) й ітрій. Величини сумарної енергії

змішання визначаються в основному внесками, зумовленими ріжницею розмірів структурних одиниць, які заміщаються. Величини внесків за рахунок відмінностей у ступені іонності хемічного зв'язку компонентів істотно менші та здебільшого ними можна нехтувати. Представлено діяграму термодинамічної стабільності системи $(\text{Gd}_{1-x}\text{Ln}_x)_2\text{SiO}_5$ та бані розпаду систем $(\text{Gd}_{1-x}\text{Ln}_x)_2\text{SiO}_5$ і $(\text{Lu}_{1-x}\text{Ln}_x)_2\text{SiO}_5$, які уможливлюють графічно передбачати температури розпаду твердих розчинів за заданих границь заміщення, рівноважні границі заміщення за заданої температури й області термодинамічної стабільності твердих розчинів. Результати прогнозування термодинамічної стабільності не суперечать експериментальним даним, раніше наведеним у літературі для твердих розчинів на основі допованого Гадолінію оксиортосилікату. Тверді розчини Гадолінію оксиортосилікату, які мають люмінесцентні, сцинтиляційні й інші практично важливі властивості, внаслідок дуже низьких критичних температур розпаду та дуже широкого температурного інтервалу термодинамічної стабільності в порівнянні з твердими розчинами оксиортосилікатів інших РЗЕ можуть знайти практичне застосування в якості наноматеріалів.

Key words: solid solution, mixing energy, isomorphous substitutions, complex oxide systems, oxyorthosilicate, rare-earth elements, gadolinium, yttrium.

Ключові слова: твердий розчин, енергія змішання, ізоморфні заміщення, складнооксидні системи, оксиортосилікати, рідкісноземельні елементи, Гадоліній, Ітрій.

(Received 23 June, 2023)

1. INTRODUCTION

Gadolinium oxyorthosilicate (Gd_2SiO_5), doped with rare-earth elements (REEs), can be utilized as phosphors, gamma radiation detectors for high-energy physics in nuclear physics, single-crystal scintillators, and in the latest generation of scintillation detectors in positron emission tomography (PET). It is also employed for monitoring radiation levels in test sites and the operation of pulsed electron guns and electron beam technology, as well as in oil well logging [1–5]. This is due to the complex set of physicochemical and electrophysical properties possessed by Gd_2SiO_5 , including relatively high density, chemical and thermal stability, non-hygroscopicity, and radiation resistance [1]. It exhibits a high absorption coefficient, good uniformity of scintillation characteristics [2], sufficient radiation intensity, high potential as gamma radiation detectors [3], excellent energy resolution, rapid decay, and superior homogeneity of scintillation blinking [4]. Rare-earth elements Ce, Eu, Tb, Dy, and Yb are commonly used as dopants, while La, Gd, Lu, and Y serve as second components in the crystalline ma-

trices of mixed gadolinium oxyorthosilicates. Consequently, intensive research has been conducted in recent years to investigate the effects of isomorphous substitutions on various properties of solid solutions of REEs oxyorthosilicates based on Gd₂SiO₅, including mixed oxyorthosilicates, as described in works [6–18].

However, it is not always considered that solid solutions synthesized at high temperatures are prone to decomposition upon cooling within the region of thermodynamic instability, leading to changes in phase composition and properties [19–21]. This can result in material degradation and a lack of reproducibility of properties during practical application.

Therefore, it is desirable to evaluate the thermodynamic stability of solid solutions in the corresponding systems before their synthesis and properties investigation, considering the synthesis conditions, expected operating conditions, and even storage conditions. However, the physicochemical foundations for synthesizing of REEs oxyorthosilicates solid solutions, such as phase diagrams and their thermodynamic stability, have been scarcely studied to date.

The experimental determination of substitution limits by x-ray phase analysis (x-ray diffraction—XRD) using the ‘annealing and hardening’ method, and the subsequent evaluation of the stability regions of solid solutions, is complicated by the difficulty of reaching equilibrium at low temperatures due to slow diffusion rates in the solid phase and the possibility of partial decomposition upon cooling from high temperatures. Additionally, XRD may provide limited information when the components have nearly identical sizes of substituting structural units, or in the case of spinodal decomposition of the solid solution [19–21], or in the case of nanosized particles in the studied samples, which can lead to broadening and overlapping of x-ray reflections.

Insufficient information about the stability regions of solid solutions forces researchers to choose the composition of matrices and modifying additives (dopants) based either on analogous systems or through a ‘trial-and-error’ approach. This can result in excessive consumption of expensive reagents and prolonged research duration.

Therefore, it is rational to employ not only experimental but also computational methods that are free from the aforementioned limitations. As an example of such an approach, we can refer to studies [22, 23], where the synthesis conditions for samples of the Y_{1-x}Sc_xPO₄ system were determined based on computational results obtained for this system in [24].

Considering the above, the aim of this study was to predict the regions of thermodynamic stability for solid solutions of gadolinium oxyorthosilicates (Gd_{1-x}Ln_x)₂SiO₅ and lutetium oxyorthosilicates

$(\text{Lu}_{1-x}\text{Ln}_x)_2\text{SiO}_5$ with the space group $P2_1/c$.

The choice of gadolinium oxyorthosilicate as one of the components in the $(\text{Gd}_{1-x}\text{Ln}_x)_2\text{SiO}_5$ systems is justified by the fact that it does not have inherent absorption bands in the visible spectrum and is expected to form wide regions of solid solutions with oxyorthosilicates of most REEs at relatively low temperatures due to the similarity in ionic radii [25] and electronegativity values [26] between gadolinium and other REEs. According to [19], the prediction of substitution limits is based on 1 mole of substituting cation, and the anionic sublattice of oxyorthosilicates contains SiO_4^{4-} and O^{2-} anions not directly bonded to Si atoms [27]. Therefore, the composition of the oxyorthosilicate is presented as a pseudobinary compound $\text{Gd}[(\text{SiO}_4)_{0.5}\text{O}_{0.5}]$, and the corresponding solid solutions are denoted as $(\text{Gd}_{1-x}\text{Ln}_x)[(\text{SiO}_4)_{0.5}\text{O}_{0.5}]$, while the traditional formula notation of gadolinium oxyorthosilicate Gd_2SiO_5 is used in the article text.

2. CALCULATION METHODOLOGY AND INITIAL DATA

In the developed by V. S. Urusov crystal-energy theory of isomorphous substitutions [19–21], the main challenge in determining the limits of isomorphous substitutions and regions of thermodynamic stability is finding the mixing energy. Once the mixing energy is known, the substitution limit (x) can be calculated for a given decomposition (stability) temperature (T_d), or the decomposition temperature can be determined for a given substitution limit, allowing for the determination of regions of thermodynamic stability. The Becker equation in the regular solid solution approximation (Eq. (1)) can be used for these calculations [28]:

$$-\frac{1-2x}{\ln \frac{x}{1-x}} = R_g T_d / Q. \quad (1)$$

The critical decomposition temperatures (T_{cr}) in this case are calculated using Eq. (2) [19]:

$$T_{cr} = Q/(2kN), \quad (2)$$

where x is the substitution limit; R_g is the universal gas constant; Q is the mixing energy; k is the Boltzmann constant; N is Avogadro's number. In both cases, the value of Q is expressed in cal/mol [19].

The Becker equation can be used because the size parameter (Table 1) does not exceed 0.1 [19]. The size parameter was calculated based on the volumes of unit cells: $\delta = (V_{\text{Ln}_x\text{SiO}_5}^{1/3} - V_{\text{Gd}_2\text{SiO}_5}^{1/3})/V_{\min}^{1/3}$ [19], where V_{\min} is the volume of the smaller unit cell.

TABLE 1. Calculation of mixing energies of oxyorthosilicates (Gd_{1-x}Ln_x)₂SiO₅, Ln = La-Lu, Y, with the P2₁/c space group.

Ln	V^* , Å ³	δ	C	Q_R , kJ/mol	χ_{Ln}	ε	$\Delta\varepsilon$	Q_i , kJ/mol	Q , kJ/mol
La	465.2	0.03963	114.92	21.110	1.327	0.724	0.012	1.955	23.065
Ce	455.2	0.03212	114.08	13.770	1.348	0.720	0.008	0.869	14.639
Pr	445.1	0.02444	113.04	7.900	1.374	0.716	0.004	0.217	8.117
Nd	439.3	0.01996	112.72	5.254	1.382	0.714	0.002	0.054	5.308
Pm	431.9	0.01421	112.36	2.655	1.391	0.712	0	0	2.655
Sm	424.4	0.00830	111.16	0.900	1.410	0.708	0.004	0.217	1.117
Eu	417.9	0.003130	110.68	0.127	1.433	0.704	0.008	0.869	0.996
Gd	414.0		112.56		1.386	0.712			
Tb	409.2	0.003895	111.6	0.198	1.410	0.708	0.004	0.217	0.415
Dy	404.0	0.008183	110.96	0.869	1.426	0.706	0.006	0.489	1.358
Ho	397.5	0.013649	110.68	2.412	1.433	0.704	0.008	0.869	3.281
Er	395.6	0.0152695	110.48	3.014	1.438	0.703	0.009	1.100	4.114
Tm	389.7	0.020367	109.8	5.329	1.455	0.700	0.012	1.955	7.284
Yb	387.0	0.022735	108.84	6.582	1.479	0.695	0.017	3.925	10.507
Lu	384.0	0.0253914	110.76	8.355	1.431	0.705	0.007	0.665	9.010
Y	397.4	0.0137334	112.56	2.480	1.340	0.722	0.010	0.680	3.160

*Note: The unit cell volumes of cerium and promethium oxyorthosilicates are determined as the arithmetic means of the unit cell volumes of lanthanum and praseodymium oxyorthosilicates, as well as neodymium and samarium oxyorthosilicates, respectively.

The use of unit cell volumes for the calculation is justified by the lack of available literature providing interatomic distances for the low-temperature modification Ln_2SiO_5 , as seen in [29–31]. Furthermore, the authors in [29], who initially described the $P2_1/c$ space group for Ln_2SiO_5 , do not present cell parameters for Lu_2SiO_5 . Therefore, we determined the volume of the unit cell of the low-temperature modification Lu_2SiO_5 (approximately 384 \AA^3) through extrapolation of the unit cell volumes of Ln_2SiO_5 based on the ionic radii of REEs [32].

Since the components of the considered systems are isostructural [27, 29], the equation 3 for calculating the mixing energy (Q) consists of two contributions arising from the difference in sizes of substituting structural units (Q_δ) and the difference in the ionicity of the chemical bond between the components (Q_ϵ) [19].

$$Q = Q_\delta + Q_\epsilon = Cmnz_m z_x \delta^2 + \frac{1390mz_m z_x \alpha(\Delta\epsilon)^2}{2R} [\text{kJ/mol}]. \quad (3)$$

It should be noted that at temperatures above 1173–1373 K, the components of systems involving high-temperature modifications of oxyorthosilicates in the series of REEs from Dy to Lu and from La to Tb are not isostructural (the $P2_1/c$ space group is observed for oxyorthosilicates from La to Tb, while the $B2/b$ space group is observed for Dy to Lu oxyorthosilicates) [27]. Therefore, in this case, it is also necessary to consider a third contribution to the mixing energy due to the enthalpy of the polymorphic transition $P2_1/c \rightarrow B2/b$ [19], for which, according to our data, there is no information available in the literature.

In equation 3, the value of C is a constant calculated from the expression $C = 20(2\Delta\chi + 1)$ [21], where $\Delta\chi$ represents the electronegativity difference between the cations [26] and the anion [33] in the pseudobinary approximation of the structure (Table 1). The choice of the χ scale [26], unlike scales used by other authors, is based on the fact that χ values vary with periodicity, increasing in the series Ce^{3+} – Eu^{3+} from 1.348 to 1.433 and in the series Gd^{3+} – Yb^{3+} from 1.386 to 1.479, with a sharp decrease during the transitions Eu^{3+} – Gd^{3+} from 1.433 to 1.386 and Yb^{3+} – Lu^{3+} from 1.479 to 1.431. These variations are due to the peculiarities of the electronic shell filling of REEs. The lanthanum has a free $4f$ shell, europium and gadolinium have a half-filled $4f$ shell (7 electrons), and ytterbium and lutetium have a completely filled $4f$ shell (14 electrons). In the transition from Eu to Gd and from Y to Lu, as well as for La, the first electron appears on the $5d$ sublevel.

m is the number of formula units in the pseudobinary approximation of the structure $(\text{Gd}_{1-x}\text{Ln}_x)[(\text{SiO}_4)_{0.5}\text{O}_{0.5}]$ is calculated per 1 mole of substituting structural unit ($1 + 0.5 + 0.5 = 2$); n —the coordina-

tion number of the substituting structural unit in the pseudobinary approximation of the structure (in the first cation position, $n = 7:6\text{SiO}_4^{4-}$ tetrahedra and one O²⁻ ion; in the second position, $n = 6:3\text{SiO}_4^{4-}$ tetrahedra and three O²⁻ ions [27]), *i.e.*, on average, $n = 6.5$; z_m , z_x —the formal charges of the substituting and common structural units in the components: $z_m = 3$, $z_x = 4 \cdot 0.5 + 2 \cdot 0.5 = 3$; δ —the size parameter, calculated for each system based on the volumes of unit cells provided in [27, 29]; ϵ —the degree of ionicity of the chemical bond were determined based on the electronegativity difference χ between the REE cations and the anion, as provided in [26, 33]. The value of χ for the SiO₄⁴⁻ radical was adopted as χ of the oxide anion, following the recommendation [34], and it was taken as 3.7 [33].

α is the reduced Madelung constant, equal to 1.9, was calculated using the Hoppe formula [35]: $(\alpha/n)^2 + \alpha = 1.81$;

R is the average cation–anion interatomic distance in the pseudobinary approximation, was calculated for one of the previously studied structures of this structural type—Gd[(SiO₄)_{0.5}O_{0.5}] [27]. The distances between the cation and the tetrahedral anion were taken into account as the sum of the distances (Gd–O + Si–O) and the distance between the cation and oxygen (Gd–O) not bonded to a Si atom for both positions of gadolinium [27]. For the first position: the cation is surrounded by 6 tetrahedra + 1 oxygen, resulting in an average distance of $[6 \cdot (2.49 + 1.63) + 2.35]/7 = 3.86\text{\AA}$; for the second position: the cation is surrounded by 3 tetrahedra + 3 oxygen, resulting in an average distance of $[3 \cdot (2.39 + 1.63) + 3 \cdot 2.30]/6 = 3.15\text{\AA}$. The average distance, considering both cation positions, is $R = 3.5\text{\AA}$. The calculation error for T_{cr} was $\pm 100\text{ K}$ [19].

3. RESULTS OF THE CALCULATIONS AND DISCUSSION

3.1. Mixing Energies of Oxyorthosilicates (Gd_{1-x}Ln_x)₂SiO₅

Some initial data and results of the mixing energy calculations are summarized in Table 1 and Fig. 1. As can be seen from the provided data, with an increase in the atomic number of the REEs, the contributions to the total mixing energy due to differences in the sizes of substituting structural units Q_R (Fig. 1) smoothly vary in the series of systems from (Gd_{1-x}La_x)₂SiO₅ to (Gd_{1-x}Eu_x)₂SiO₅, decreasing significantly from 21.110 to 0.127, and then increasing from 0.198 to 8.355 kJ/mol in the series of solid solutions from (Gd_{1-x}Tb_x)₂SiO₅ to (Gd_{1-x}Lu_x)₂SiO₅.

Such variation in the Q_R mixing energy is caused by the fact that in the series of systems with La–Eu oxyorthosilicates, the differences between the crystal radii of the ions in the La–Eu range

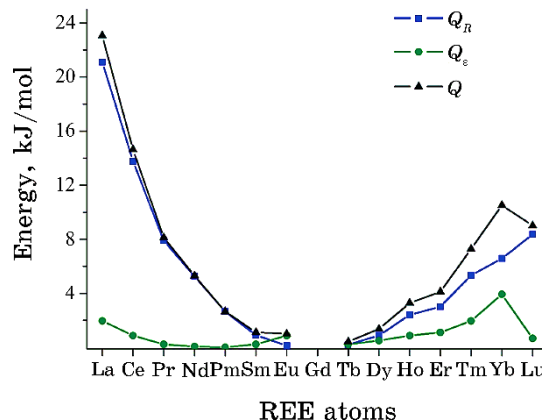


Fig. 1. Dependences of the calculated contributions to the mixing energies of solid solutions Q_R (■) and Q_e (●), as well as for Q (▲), in the systems $(\text{Gd}_{1-x}\text{Ln}_x)_2\text{SiO}_5$ for the La–Lu series.

(1.300–1.206 Å) and gadolinium (1.193 Å) decrease, while in the series of systems with Tb–Lu oxyorthosilicates (1.180–1.117 Å), on the contrary, they increase. This is because the crystal radius of gadolinium (1.193 Å) is very close to the radius of europium and terbium (1.206 and 1.180 Å). Here and further, the crystal ionic radii of cations are given according to R. Shannon [25] for a coordination number of 8.

The value of the total mixing energy Q is mostly determined by the contribution due to differences in the sizes of the substituting structural units Q_R , except for the systems $(\text{Gd}_{1-x}\text{Tm}_x)_2\text{SiO}_5$ and $(\text{Gd}_{1-x}\text{Yb}_x)_2\text{SiO}_5$, where the contribution Q_e is comparable to the corresponding values of Q_R . The minimal mixing energies of the systems in the series $(\text{Gd}_{1-x}\text{Sm}_x)_2\text{SiO}_5$ – $(\text{Gd}_{1-x}\text{Dy}_x)_2\text{SiO}_5$ are due to very close values of the crystal ionic radii and electronegativities of the respective REEs and gadolinium. The maxima in the contributions Q_e for $(\text{Gd}_{1-x}\text{La}_x)_2\text{SiO}_5$, $(\text{Gd}_{1-x}\text{Eu}_x)_2\text{SiO}_5$, and $(\text{Gd}_{1-x}\text{Yb}_x)_2\text{SiO}_5$ are due to the above-mentioned electronic shell structures of lanthanum, europium, and ytterbium.

3.2. Limits of Isomorphous Substitutions in Oxyorthosilicates $(\text{Gd}_{1-x}\text{Ln}_x)_2\text{SiO}_5$

The decomposition temperatures of limited series of solid solutions (Table 2) were calculated based on the given substitution limits at $x = 0.01$, 0.03, 0.09, and 0.20 using equation (1), while the critical decomposition (stability) temperatures were determined at $x = 0.50$ using Eq. (2).

TABLE 2. Decomposition temperatures of solid solutions of oxyorthosilicates (Gd_{1-x}Ln_x)₂SiO₅ for $x = 0.01$, 0.03, 0.09, and 0.20, and critical decomposition temperatures (T_{cr} [K] for $x = 0.50$).

Ln	Decomposition temperatures, K				
	$x = 0.01$	$x = 0.03$	$x = 0.09$	$x = 0.20$	$x = 0.50 (T_{cr})$
La	587	745	976	1178	1377
Ce	373	473	620	757	874
Pr	207	262	344	415	485
Nd	135	171	225	271	316
Pm	68	86	109	137	158
Sm	28	36	46	57	67
Eu	25	32	41	51	59
Tb	11	13	18	21	25
Dy	35	44	56	69	81
Ho	84	106	135	168	196
Er	105	133	174	210	246
Tm	186	235	308	377	435
Yb	268	339	445	543	628
Lu	229	291	381	466	538
Y	81	102	134	163	190

Based on the calculated values of the decomposition temperatures, their dependences on the REEs numbers were plotted (Fig. 2).

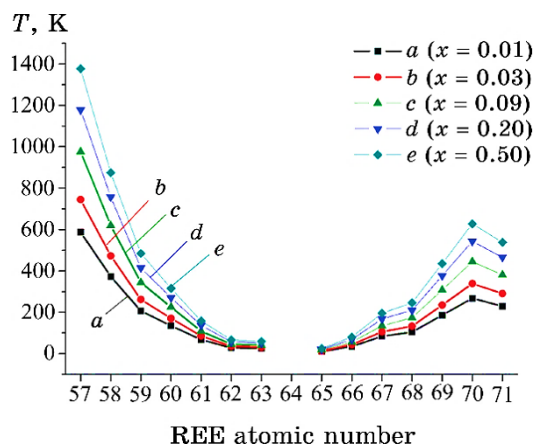


Fig. 2. Dependences of the calculated decomposition temperatures of solid solutions of oxyorthosilicates (Gd_{1-x}Ln_x)₂SiO₅ on the REEs atomic numbers for substitution limits $x = 0.01$ (a), $x = 0.03$ (b), $x = 0.09$ (c), $x = 0.20$ (d), and $x = 0.50$ (e).

These dependences allow for graphical determination of the equilibrium substitution limits (x) at specified decomposition temperatures (T_d), or the decomposition temperatures for given substitution limits for gadolinium oxyorthosilicate with REEs ranging from La to Lu [24]. The intersection points of an isotherm drawn from a given decomposition temperature and a vertical line drawn from the REE number allows for estimating the composition range within which the substitution limit is located, and interpolation along this vertical line segment between the two closest curves provides the actual substitution limit. To refine the substitution limit, the dependence of calculated decomposition temperatures on the specified composition (decomposition dome) can be plotted for a specific system. The critical decomposition temperatures for unlimited series of solid solutions (Fig. 2, e) vary with the REEs numbers in accordance with the changes in the total mixing energy, as predicted by the Becker equation.

3.3. Thermodynamic Stability Regions of $(\text{Gd}_{1-x}\text{Ln}_x)_2\text{SiO}_5$ Solid Solutions

Based on Figure 2, the thermodynamic stability regions of $(\text{Gd}_{1-x}\text{Ln}_x)_2\text{SiO}_5$ solid solutions can be assessed graphically. At temperatures above T_{cr} (curve e), the unlimited series of solid solutions are thermodynamically stable across the concentration range of $1.0 > x > 0$. In the region below curve e, at temperatures below T_{cr} , the unlimited solid solutions become unstable and can undergo decomposition into phases with limited solubility if the diffusion rate and time are enough for their formation [24]. Solid solutions with x values of 0.01, 0.03, 0.09, and 0.20 are thermodynamically stable in the regions above curves (a), (b), (c), and (d), respectively, while they become unstable below these curves.

It should be noted that solid solutions of $(\text{Gd}_{1-x}\text{Ln}_x)_2\text{SiO}_5$ systems have very low critical decomposition temperatures, with 8 out of 15 such systems even below room temperature. Therefore, the latter will exhibit thermodynamic stability over a wide temperature range, ranging from below room temperature to the melting temperatures, which for REEs oxyorthosilicates are in the range of 2170–2320 K [36]. This fact may indicate an advantage of Gd-based oxyorthosilicates solid solution materials in terms of stability of properties and their reproducibility compared to similar materials based on solid solutions of oxyorthosilicates of other REEs such as cerium [37].

For all $(\text{Gd}_{1-x}\text{Ln}_x)_2\text{SiO}_5$ systems, the decomposition temperatures were calculated within the composition range of $1.0 > x > 0$ with a step size of $x = 0.05$, and decomposition domes were plotted (Fig. 3). They allow for a more precise graphical determination of the ther-

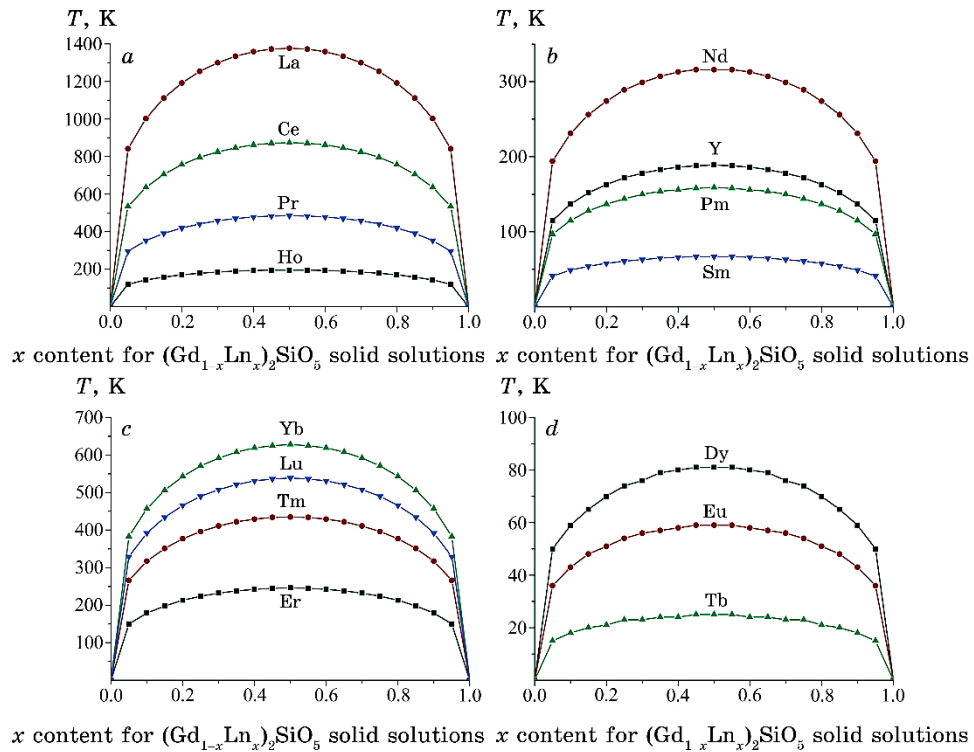


Fig. 3. Decomposition domes for solid solutions of $(\text{Gd}_{1-x}\text{Ln}_x)_2\text{SiO}_5$ oxyorthosilicates: (a) $\text{Ln} = \text{La}, \text{Ce}, \text{Pr}, \text{Ho}$; (b) $\text{Ln} = \text{Nd}, \text{Y}, \text{Pm}, \text{Sm}$; (c) $\text{Ln} = \text{Yb}, \text{Lu}, \text{Tm}, \text{Er}$; (d) $\text{Ln} = \text{Dy}, \text{Eu}, \text{Tb}$.

modynamic stability regions, the decomposition temperature for a given limiting composition of the solid solution, or its equilibrium composition at a given decomposition temperature.

4. COMPARISON OF CALCULATION RESULTS WITH LITERATURE DATA

In the literature, there is scarce data available on the thermodynamic stability, substitution limits, and critical decomposition temperatures of solid solution systems based on Gd_2SiO_5 . This, of course, hinders the assessment of the reliability of the conducted calculations. However, there are numerous studies on the synthesis temperatures of Gd_2SiO_5 doped with REEs, for example [11, 17, 40–42], and as far as we know, about 15 studies on the synthesis temperatures of mixed oxyorthosilicates [1–4, 6–10, 12–14, 16, 38, 39] (Table 3).

TABLE 3. Comparison of critical decomposition temperatures T_{cr} of solid solutions based on Gd_2SiO_5 oxyorthosilicate with literature data on synthesis temperatures.

Composition [Ref.]	x or %	Synthesis method	Synthesis temperature, K	T_{cr} , K
$\text{Y}_{1.92-x}\text{Gd}_x\text{SiO}_5:\text{Ce}_{0.08}$ [6]	0.00, 0.25, 0.50, 0.75 0.05, 0.1, 0.15, 0.20, 0.25, 0.30, 0.35, 0.40 0, 0.1, 0.3, 0.5, 0.7, 0.9, 1.0	solid phase MS&Sogel method + calcination Czochralski method Czochralski method, combined with annealing at 1373 K	1373 923 + 1473 Synthesis at 1673 + melting Synthesis at 1473 + melting	190 190 190 190 190
$(\text{Y}_{0.995-x}\text{Gd}_x\text{Ce}_{0.005})_2\text{SiO}_5$ [7]				
$(\text{Gd}_{1-x}\text{Y}_x)_2\text{SiO}_5:\text{Yb}5\%$ [8]				
$\text{Gd}_{1.99-x}\text{Y}_x\text{Ce}_{0.01}\text{SiO}_5$ [9]	0, 0.0995, 0.199			
$\text{Lu}_{2x}\text{Gd}_{2-2x}\text{SiO}_5:\text{Ce}0.33\%$ [10]	0, 0.2, 0.4, 0.6, 0.8, 1.0			
$\text{Gd}_2\text{SiO}_5:\text{Ce}^{3+}$ [11]	0.5, 1, 2, 5 mol.% 0.2, 1, 2, 5, 10 mol.-%	In Na_2CO_3 melt + annealing	Annealing at 1423	874
$\text{Gd}_2\text{SiO}_5:\text{Dy}^{3+}$ [11]		In Na_2CO_3 melt + annealing	Annealing at 1423	81
$\text{Gd}_2\text{SiO}_5:\text{Eu}^{3+}$ [11]	0.5, 1, 2, 5, 10 mol.-%	In Na_2CO_3 melt + annealing	Annealing at 1423	59
$\text{Gd}_2\text{SiO}_5:\text{Tb}^{3+}$ [11]	0.5, 1, 2, 5, 10 mol.-%	In Na_2CO_3 melt + annealing	Annealing at 1423	25
$(\text{Lu}_{1-x}\text{Gd}_x)_2\text{SiO}_5:\text{Ce}^{3+} 1.5\%$ [12]	0.2, 0.4, 0.5, 0.7	A single crystal film is formed from a melt- solution of $\text{PbO}:\text{B}_2\text{O}_3$	1273	538

Continuation of TABLE 3.

Composition [Ref.]	<i>x</i> or %	Synthesis method	Synthesis temperature, K	<i>T_{cr}</i> , K
LaGdSiO ₅ :Dy ³⁺ 1% [13] multiphase mixture	1 mol.%	by burning urea solution + laser evaporation coating	Annealing at 1273. Improvement of properties	1377
GdYSiO ₅ :Dy ³⁺ [14]	0.025, 0.05, 0.1, 0.25, 0.75, 1.0, 1.5, 2.0, 3.0, 5.0 mol.%	by burning urea solution + laser evaporation coating	Annealing at 1273. Improvement of properties	190
Gd ₂ SiO ₅ :Tb ³⁺ [15] La _{0.5} Gd _{1.5} SiO ₅ :Dy ³⁺ [16] two-phase films at all temperatures	2.33, 2.7 mol.%	solid phase	Substrate temperature 473 + 773, annealing at 1273. Improvement of properties	1773 1377 25
Gd ₂ SiO ₅ :Eu ³⁺ [17]	0.1, 0.2, 0.5, 1.0, 1.5, 2.0, 2.5 mol.%	solid phase	473 + 773, annealing at 1273. Improvement of properties	1473 1377
Gd _{1.9} Y _{0.1} SiO ₅ :0.5% Ce [18] La _{0.5} Gd _{1.5} SiO ₅ :Dy ³⁺ phases based on Gd ₂ SiO ₆ and La ₂ SiO ₅ with a shift of x- ray reflections [38]	0.5 mol.%	Czochralski method	1473 1377	190
La _{2-x} Gd _x SiO ₅ :Dy ³⁺ , Pr ³⁺ phases based on Gd ₂ SiO ₅ and La ₂ SiO ₅ with a shift of x-ray reflections can be observed in both powders and films, at <i>x</i> =0.5, 1.0, and 1.5 [39]		by burning urea solution + laser evaporation coating	Substrate temperature: 673, 773. Time: 15 minutes, 30 minutes, and 50 minutes	1473 1377
			Furnace temperature: 873. Synthesis by flame combus- tion	1377

Since the dopant content is usually in small quantity or several percent, solid solutions involving it can be thermodynamically stable over a wide temperature range [19]. On the other hand, the amount of the second REE in the mixed oxyorthosilicate matrix typically constitutes tens of percent, which can lead to the decomposition of the solid solution, accompanied by changes in phase composition and properties upon cooling after synthesis and during practical application. For example, mixed crystals of $\text{Lu}_{0.4}\text{Gd}_{1.6}\text{SiO}_5$ annealed after growth have shown improved scintillation emission, higher light output (2.0 times higher than that of Gd_2SiO_5), and good energy resolution [4], highlighting the need to ensure their thermodynamic stability during cooling and practical use.

Comparison of the calculation results with the experimental literature data on synthesis temperatures, as presented in Table 3, indicates that the synthesis of $(\text{Gd}_{1-x}\text{Ln}_x)_2\text{SiO}_5$ oxyorthosilicates solid solution in the majority of studies was conducted within the predicted ranges of thermodynamic stability. This is because the synthesis temperatures were higher than the calculated critical decomposition temperatures. Only in studies [13, 16] and possibly [38, 39], were the synthesis temperatures lower than the calculated critical decomposition temperatures. In other words, the authors carried out the synthesis of solid solution samples at temperatures below the decomposition dome temperatures of the $(\text{Gd}_{1-x}\text{La}_x)_2\text{SiO}_5$ solid solution (Table 3). This resulted in the formation of two-phase solid solutions samples in systems [13, 16, 38, 39], where the interplanar distances of each phase varied with the composition, which is also consistent with the prediction results. Below the decomposition dome, samples in an equilibrium state should not be single-phase.

5. DECOMPOSITION DOMES OF $(\text{Lu}_{1-x}\text{Ln}_x)_2\text{SiO}_5$ SYSTEMS

Previously [32], using the same methodology, we calculated the mixing energies and critical decomposition temperatures of $(\text{Lu}_{1-x}\text{Ln}_x)_2\text{SiO}_5$ systems. However, the decomposition domes were not presented. In addition to the work [32], the decomposition domes of $(\text{Lu}_{1-x}\text{Ln}_x)_2\text{SiO}_5$ systems are shown in Fig. 4.

6. CONCLUSIONS

1. The values of total mixing energies Q decrease in the case of substituting gadolinium with cerium subgroup REEs in the series from La to Eu, and they show a moderate increase when gadolinium is substituted with yttrium subgroup REEs. In both cases, these val-

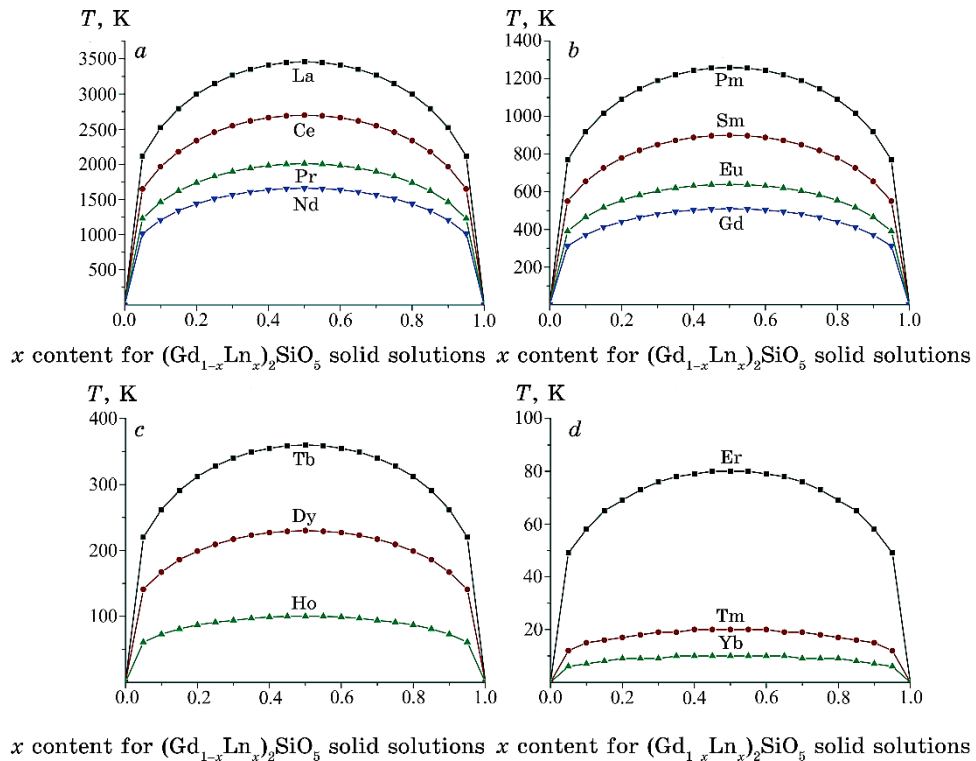


Fig. 4. Decomposition domes of oxyorthosilicates $(\text{Lu}_{1-x}\text{Ln}_x)_2\text{SiO}_5$ solid solutions: (a) $\text{Ln} = \text{La}, \text{Ce}, \text{Pr}, \text{Nd}$; (b) $\text{Ln} = \text{Pm}, \text{Sm}, \text{Eu}, \text{Gd}$; (c) $\text{Ln} = \text{Tb}, \text{Dy}, \text{Ho}$; (d) $\text{Ln} = \text{Er}, \text{Tm}, \text{Yb}$.

ues are mainly determined by contributions arising from the differences in sizes of the substituting structural units Q_R .

2. The contributions arising from the differences in the degree of ionicity of the chemical bond between the components are significantly smaller, and in most cases (except for $(\text{Gd}_{1-x}\text{Yb}_x)_2\text{SiO}_5$ and $(\text{Gd}_{1-x}\text{Tm}_x)_2\text{SiO}_5$ systems), they can be neglected. The insignificant maxima in the Q_e contributions for $(\text{Gd}_{1-x}\text{La}_x)_2\text{SiO}_5$, $(\text{Gd}_{1-x}\text{Eu}_x)_2\text{SiO}_5$, and $(\text{Gd}_{1-x}\text{Yb}_x)_2\text{SiO}_5$, are attributed to the peculiarities of the electronic shell structures of lanthanum, europium, and ytterbium.

3. The diagram of thermodynamic stability for the $(\text{Gd}_{1-x}\text{Ln}_x)_2\text{SiO}_5$ systems and the domes of decomposition for the $(\text{Gd}_{1-x}\text{Ln}_x)_2\text{SiO}_5$ and $(\text{Lu}_{1-x}\text{Ln}_x)_2\text{SiO}_5$ systems are presented, allowing for graphical prediction of solid solutions decomposition temperatures based on given substitution limits, equilibrium substitution limits for given temperature, and ranges of thermodynamic stability.

4. The calculation results are consistent with the experimental literature data in the sense that the synthesis of single-phase samples

of solid solutions $(\text{Gd}_{1-x}\text{Ln}_x)_2\text{SiO}_5$ in studies [6–12, 14, 15, 17, 18] was conducted within the predicted regions of thermodynamic stability, while the synthesis of multiphase samples [13, 16, 38, 39] was carried out within the predicted regions of solid solution decomposition.

5. The majority of solid solution systems (8 out of 15) have critical decomposition temperatures below room temperature. Therefore, they may hold promise in the production of nanomaterials, as their synthesis typically requires relatively low temperatures.

6. Due to the very wide temperature range of thermodynamic stability, materials based on gadolinium oxyorthosilicate solid solutions may exhibit superior properties and reproducibility compared to materials based on oxyorthosilicates solid solutions of other REEs.

ACKNOWLEDGMENTS

The work of R.S., M.O., and G.E. was partially supported by the Programme of Fundamental Research funded by the Ministry of Education and Science of Ukraine (grant ID 0122U000762). R.S. expresses gratitude to the ‘European Chemistry School for Ukrainians’ project for the support provided.

REFERENCES

1. O. Ts. Sidletsky and B. V. Grynyov, *Stsyntlyatsiyni Krystaly na Osnovi Tverdykh Rozchyniv Zamishchennya* [Scintillation Crystals Based on Solid Substitutional Solutions] (Kharkiv: ISMA: 2019) (in Ukrainian); http://functmaterials.org.ua/contents/book/Book_Sidletskiy.pdf
2. S. Shimizu, K. Kurashige, T. Usui, N. Shimura, K. Sumiya, N. Senguttuvan, A. Gunji, M. Kamada, and H. Ishibashi, *IEEE Transactions on Nuclear Science*, **53**, No. 1: 14 (2006); [doi:10.1109/TNS.2005.862975](https://doi.org/10.1109/TNS.2005.862975)
3. V. Jarý, E. Mihokova, J. A. Mareček, A. Bejtlerova, D. Kurtsev, O. Sidletskiy, and M. Nikl, *J. Phys. D: Appl. Phys.*, **47**, No. 34: 365304 (2014); [doi:10.1088/0022-3727/47/36/365304](https://doi.org/10.1088/0022-3727/47/36/365304)
4. T. Usui, S. Shimizu, N. Shimura, K. Kurashige, Y. Kurata, K. Sumiya, N. Senguttuvan, A. Gunji, M. Kamada, and H. Ishibashi, *IEEE Transactions on Nuclear Science*, **54**, No. 1: 19 (2007); [doi:10.1109/TNS.2006.886373](https://doi.org/10.1109/TNS.2006.886373)
5. A. I. Slesarev, V. Ju. Ivanov, A. V. Ishchenko, A. N. Cherepanov, B. V. Shulgin, A. V. Chepkasova, and M. Kobajashi, *Working Substance for Thermo-Exoelectronic Dosimetry* (Patent RU 2331086 C1, IPC G01T 1/20, G01T 3/06 (2006.01). Application: 2007113282/28, 09.04.2007. Date of publication: 10.08.2008 Bull. 22); <http://hdl.handle.net/10995/68666>
6. P. Thiagarajan, B. Tiwari, M. Kottaisamy, N. Rama, and M. S. Ramachandra Rao, *Appl. Phys. A*, **94**, No. 3: 607 (2009);

- <https://doi.org/10.1007/s00339-008-4861-z>
- 7. Q. Wu, X. Jing, and H. Jiao, *Opt. Mater.*, **31**, No. 8: 1123 (2009); <https://doi.org/10.1016/j.optmat.2008.12.004>
 - 8. L. H. Zheng, R. Lisiecki, Q. G. Wang, X. D. Xu, L. B. Su, W. Ryba-Romanowski, and J. Xu, *Lasers, Sources, and Related Photonic Devices* (OSA—Technical Digest (CD): Optica Publishing Group: 2012); <https://doi.org/10.1364/AIOM.2012.IW3D.4>
 - 9. M. Jie, G. Zhao, X. Zeng, L. Su, H. Pang, X. He, and J. Xu, *J. Cryst. Growth*, **277**, Nos. 1–4: 175 (2005); <https://doi.org/10.1016/j.jcrysgro.2004.12.160>
 - 10. D. Kurtsev, O. Sidletskiy, S. Neicheva, V. Bondar, O. Zelenskaya, V. Tarasov, M. Biatov, and A. Gektin, *Mater. Res. Bull.*, **52**: 25 (2014); <https://doi.org/10.1016/j.materresbull.2014.01.006>
 - 11. V. V. Shinde, A. Tiwari, and S. J. Dhoble, *J. Mol. Struct.*, **1217**: 128397 (2020); <https://doi.org/10.1016/j.molstruc.2020.128397>
 - 12. Yu. Zorenko, V. Gorbenko, V. Savchyn, T. Voznyak, B. Grinyov, O. Sidletskiy, D. Kurtsev, A. Fedorov, V. Baumer, M. Nikl, J. A. Mares, A. Beitlerova, P. Prusa, and M. Kucera, *J. Cryst. Growth*, **337**, No. 1: 72 (2011); <https://doi.org/10.1016/j.jcrysgro.2011.10.003>
 - 13. S. N. Ogugua, S. K. K. Shaat, H. C. Swart, and O. M. Ntwaeborwa, *J. Phys. Chem. Solids*, **83**: 109 (2015); <https://doi.org/10.1016/j.jpcs.2015.04.002>
 - 14. S. N. Ogugua, S. K. K. Shaat, H. C. Swart, and O. M. Ntwaeborwa, *J. Lumin.*, **179**: 154 (2016); <https://doi.org/10.1016/j.jlumin.2016.06.056>
 - 15. M. Gao, P. Zhang, L. Luo, R. Guo, and Yu. Wang, *Optik*, **225**: 165814 (2021); <https://doi.org/10.1016/j.ijleo.2020.165814>
 - 16. S. N. Ogugua, H. C. Swart, and O. M. Ntwaeborwa, *Physica B*, **535**: 143 (2018); <https://doi.org/10.1016/j.physb.2017.07.006>
 - 17. Ch. A. Rao and K. V. R. Murthy, *Int. J. Sci. Res. (IJSR)*, **10**, No. 1: 516 (2021); [doi:10.21275/SR21110114938](https://doi.org/10.21275/SR21110114938)
 - 18. H. Feng, J. Chen, Zh. Zhang, Y. Wang, Zh. Xu, J. Zhao, and R. Mao, *Radiat. Meas.*, **109**: 8 (2018); <https://doi.org/10.1016/j.radmeas.2017.12.001>
 - 19. V. S. Urusov, *Teoriya Izomorfnoi Smesimosti* [The Theory of Isomorphous Miscibility] (Moskva: Nauka: 1977) (in Russian).
 - 20. V. S. Urusov, *Fortschr. Mineral.*, **52**: 141 (1975).
 - 21. V. S. Urusov, V. L. Tauson, and V. V. Akimov, *Geokhimiya Tverdogo Tela* [Geochemistry of Solid State] (Moskva: GEOS: 1997) (in Russian).
 - 22. D. Spassky, A. Vasil'ev, V. Nagirnyi, I. Kudryavtseva, D. Deyneko, I. Nikiforov, I. Kondratyev, and B. Zadneprovski, *Materials*, **15**, No. 19: 6844 (2022); <https://doi.org/10.3390/ma15196844>
 - 23. V. S. Voznyak-Levushkina, A. A. Arapova, D. A. Spassky, I. V. Nikiforov, and B. I. Zadneprovski, *Phys. Solid State*, **64**, No. 11: 567 (2022); <https://doi.org/10.1134/S1063783422110130>
 - 24. E. I. Get'man, S. V. Radio, and L. I. Ardanova, *Inorg. Mater.*, **54**, No. 6: 596 (2018); <https://doi.org/10.1134/S0020168518060081>
 - 25. R. D. Shannon, *Acta Crystallogr., Sect. A*, **32**, No. 5: 751 (1976); <https://doi.org/10.1107/S0567739476001551>
 - 26. K. Li, and D. Xue, *J. Phys. Chem. A*, **110**, No. 39: 11332 (2006); <https://doi.org/10.1021/jp062886k>

27. J. Felsche, *The Crystal Chemistry of the Rare-Earth Silicates*. In: *Rare Earths. Structure and Bonding* (Berlin–Heidelberg: Springer: 1973), vol. 13; https://doi.org/10.1007/3-540-06125-8_3
28. R. Becker, *Z. Metallkd.*, **29**: 245 (1937) (in German).
29. J. Wang, Sh. Tian, G. Li, F. Liao, and X. Jing, *Mater. Res. Bull.*, **36**, No. 10: 1855 (2001); [https://doi.org/10.1016/S0025-5408\(01\)00664-X](https://doi.org/10.1016/S0025-5408(01)00664-X)
30. E. G. Yukihara, L. G. Jacobsohn, M. W. Blair, B. L. Bennett, S. C. Tornaga, R. E. Muenchhausen, *J. Lumin.*, **130**, No. 12: 2309 (2010); <https://doi.org/10.1016/j.jlumin.2010.07.010>
31. R. E. Muenchhausen, E. A. McKigney, L. G. Jacobsohn, M. W. Blair, B. L. Bennett, and D. W. Cooke, *IEEE Transactions on Nuclear Science*, **55**, No. 3: 1532 (2008); [doi:10.1109/TNS.2008.922844](https://doi.org/10.1109/TNS.2008.922844)
32. E. I. Get'man, Yu. A. Oleksii, S. V. Radio, and L. I. Ardanova, *Tonkie Khimicheskie Tekhnologii* [Fine Chemical Technologies], **15**, No. 5: 54 (2020); <https://doi.org/10.32362/2410-6593-2020-15-5-54-62>
33. S. S. Batsanov, *Strukturnaya Khimiya. Fakty i Zavisimosti* [Structural Chemistry. Facts and Dependences] (Moskva: Dialog-MGU: 2000) (in Russian).
34. S. S. Batsanov, *Russ. Chem. Rev.*, **37**, No. 5: 332 (1968); <https://doi.org/10.1070/RC1968v037n05ABEH001639>
35. R. Hoppe, *Adv. Fluor. Chem.*, **6**: 387 (1970).
36. B. Grynyov, V. Ryzhikov, J. K. Kim, and M. Jae, *Scintillator Crystals, Radiation Detectors & Instruments on Their Base* (Kharkiv: 2004); <http://functmaterials.org.ua/contents/book/Ryzhikov-2004.pdf>
37. E. I. Get'man and S. V. Radio, *Nanomaterials and Nanocomposites, Nanostructure Surfaces, and Their Applications. Springer Proceedings in Physics* (Eds. O. Fesenko and L. Yatsenko) (Springer: Cham.: 2021), vol. **246**; https://doi.org/10.1007/978-3-030-51905-6_39
38. S. N. Ogugua, R. L. Nyenge, P. T. Sechogela, H. C. Swart, and O. M. Ntwaeborwa, *J. Vac. Sci. Technol. A*, **34**, No. 19: 021520 (2016); <https://doi.org/10.1116/1.4942502>
39. S. N. Ogugua, S. K. K. Shaat, H. C. Swart, R. E. Kroon, and O. M. Ntwaeborwa, *J. Alloys Compd.*, **775**: 950 (2019); <https://doi.org/10.1016/j.jallcom.2018.10.090>
40. V. Y. Ivanov, V. A. Pustovarov, M. Kirm, E. S. Shlygin, and K. I. Shirinskii, *Phys. Solid State*, **47**, No. 8: 1492 (2005); <https://doi.org/10.1134/1.2014499>
41. K. Shakampally, P. M. Rao, and K. V. R. Murthy, *International Journal for Research in Applied Science & Engineering Technology (IJRASET)*, **5**, No. XI: 1735 (2017).
42. T. Utsu and S. Akiyama, *J. Cryst. Growth*, **109**, Nos. 1–4: 385 (1991); [https://doi.org/10.1016/0022-0248\(91\)90207-L](https://doi.org/10.1016/0022-0248(91)90207-L)

PACS numbers: 63.22.Rc, 65.40.Ba, 65.40.De, 65.80.Ck, 81.05.ue

Machine Learning of the Physicothermal Properties of Graphene

Mohammad Imran Aziz

*Shibli National College,
Physics Department,
Azamgarh, India*

Graphene is the emerging area of nanomaterials due to their prospect for coming generation electronic devices. Various studies of graphene have been carried out to investigate the phonon properties, elastic properties. However, the physicothermal properties such as heat capacity and Grüneisen parameter have been neglected. The Grüneisen parameter is the main physical parameter in thermal expansion mechanisms. These parameters are generally positive for some modes, but they are found to be negative for q values in high-symmetry directions. They are found negative for acoustic mode in case of graphene. The Debye model for the specific heat at low temperatures is also taken into account for acoustic branches. The heat capacity of the graphene is also computed. Physicothermal properties investigated by PYTHON program is agreed very close with the result of other researchers.

Графен є новою галуззю наноматеріалів через їхню перспективність для електронних пристройів майбутнього покоління. Були проведені різні дослідження графену для вивчення фононних властивостей, пружніх властивостей. Однак такими фізико-термічними властивостями, як тепломісткість і Грюнайзенів параметр, нехтували. Грюнайзенів параметр є основним фізичним параметром в механізмах теплового розширення. Ці параметри, як правило, позитивні для деяких мод, але вони виявляються негативними для значень q у напрямках високої симетрії. Вони виявляються негативними для акустичної моди у випадку графену. Дебаїв модель для питомої тепломісткості за низьких температур враховується і для акустичних гілок. Також обчислюється тепломісткість графену. Фізико-термічні властивості, досліджені за програмою PYTHON, дуже близькі до результатів інших дослідників.

Key words: Hamiltonian mechanics, harmonic oscillators, heat capacity, thermal properties of graphene.

Ключові слова: Гамільтонова механіка, гармонічні осцилятори, тепло-місткість, графенові теплові властивості.

(Received 6 May, 2023; in revised form, 20 February, 2024)

1. INTRODUCTION

For decades, scientists and researchers believed that two-dimensional (2D) crystals are thermodynamically unstable. Graphene was the first two-dimensional material that has successfully been exfoliated from bulk graphite in 2004. The graphene structure has interesting features, which is the good reason for studying its thermal properties. Graphene is a monolayer of hexagonally arranged carbon atoms, which has become practically available today [1–3].

The atoms in the 2D monolayer graphene are capable of executing oscillations about their equilibrium position (n, l) . In oscillating states, the instantaneous position of atoms (n, l) is denoted by $\mathbf{r}(n, l) = \mathbf{x}(n, l) + \mathbf{u}(n, l)$. Thus, the Hamiltonian of the graphene is

$$H = \sum_{nli} \frac{M_n}{2} \dot{u}_i^2(n, l) + \frac{1}{2} \sum_{nli} \sum_{mlj} \Phi_{ij} \binom{nm}{l, l'} u_i(n, l) u_j(m, l'), \quad (1)$$

where

$$\Phi_{ij} \binom{nm}{l, l'} = \left[\frac{\partial^2 U}{\partial u_i(n, l) \partial u_j(m, l')} \right]_0. \quad (2)$$

The force constants are defined as $\Phi_{ij} \binom{nm}{l, l'} = -\gamma e_i e_j$, where e_i and e_j are the unit-vector components; it is the force acting on the n^{th} atom in the l^{th} cell along i^{th} direction due to a unit displacement of the m^{th} atom in the l^{th} cell along j^{th} direction.

The equation of vibrating motion is given by

$$M_n \ddot{u}_i(n, l) = -\sum_{mlj} \binom{nm}{l, l'} u_j(m, l'). \quad (3)$$

The solution of above equation is modified by the periodicity of lattice with a wave-like solution of type

$$u_i(n, l) = M_n^{-1/2} u_{in} \exp[i\{\mathbf{q} \cdot \mathbf{r}(n, l) - \omega(\mathbf{q})t\}], \quad (4)$$

where u_{in} is the amplitude of vibration along i^{th} direction of the n^{th} atom, ω is the angular frequency, \mathbf{q} is wave vector, and the factor

$M_n^{-1/2}$ has been chosen for convenience in further calculations [4].

The equation of motion in matrix notation is

$$\omega^2(\theta)MU(\mathbf{q}) = D(\mathbf{q})U(\mathbf{q}) . \quad (5)$$

The condition for non-trivial solution

$$|D(\mathbf{q}) - \omega^2(\mathbf{q})MI| = 0 . \quad (6)$$

The elements of dynamical matrix are defined as

$$D_{ij} = \sum_{l,l'} \Phi_{ij} \binom{nm}{l,l'} \exp(i\mathbf{q} \cdot \mathbf{r}(nm, ll')) , \quad (7)$$

The above equation in matrix form is solved by MATLAB program. And the result is investigated along hexagonal Brillouin zone with symmetry points $\Gamma(0,0)$, $M\left(\frac{2\pi}{a\sqrt{3}}, 0\right)$ [13–15].

2. STUDY OF GRÜNEISEN PARAMETERS OF GRAPHENE

On the basis of oscillator model, Grüneisen predicted that the three important physical properties of a solid, the thermal expansion coefficient, the lattice specific heat, and the compressibility are linked together. To understand the physical importance of the relation, we examine that the frequency of a lattice vibration of specified wave vector changes with the lattice parameter of the solid; this leads to anharmonic effect. For simplicity, we assume that a given change in lattice parameter gives rise to the same relative change of frequency of every mode of vibration. The results of Kamlesh *et al.* were obtained by calculating individual values of the angular frequencies $\omega_{a,\mathbf{q},j}$ for different modes in high-symmetry direction [12, 14, 15]. The Grüneisen parameter for 2D nanostructure materials of IVth group of semiconductor is derived by Xu-Jin Ge *et al.* [21]:

$$\gamma(\mathbf{q}, j) = -\frac{a_0}{\omega_{a,\mathbf{q},j}} \left[\frac{\partial \omega_{a,\mathbf{q},j}}{\partial a} \right]_{a_0} . \quad (8)$$

It is now clear that, if $\omega_{a,\mathbf{q},j}$ is angular frequency of the solid, corresponding to wave vector \mathbf{q} , mode j , a_0 is the equilibrium lattice constant. $\gamma(\mathbf{q}, j)$ is independent of compressibility and, thus, it has the same value for every modes at low temperature. Thus, at low frequency modes, the variation is negligible for Grüneisen parameter. However, when Grüneisen parameter $\gamma(\mathbf{q}, j)$ is associated with acous-

TABLE 1. Calculated Grüneisen parameters of graphene for acoustic modes.

Wave vector, \mathbf{q}	Grüneisen parameter for acoustic mode
0.00	-0.0
0.05	-4.4801
0.10	-8.5944
0.15	-12.1295
0.20	-15.0468
0.25	-17.4116
0.30	-19.3231
0.35	-20.8768
0.40	-22.1518
0.45	-23.2099
0.50	-24.0980
0.55	-24.8514
0.60	-25.4972
0.65	-26.0559
0.70	-26.5433
0.75	-26.9719
0.80	-27.3515

tic modes, it is heavily weighted and tends to a decrease in $\gamma(\mathbf{q}, j)$. Grüneisen parameter $\gamma(\mathbf{q}, j)$ is the same for modes in the dispersive region of any given branch of acoustic modes and, here, the optic modes can be ignored. The $\gamma(\mathbf{q}, j)$ calculated in Table 1 comes from the PYTHON program.

In high-symmetry direction $M-\Gamma$, Grüneisen parameter of graphene is determined by acoustic modes:

$$\gamma(\mathbf{q}, j) = -a_0 \frac{\sqrt{3}}{4} q_y \left[\cot\left(\frac{\sqrt{3}}{4} q_y a_0\right) \right]. \quad (9)$$

The Grüneisen parameter plays greater role in finding the dependence of various thermal properties of nanomaterials on different temperature from phonon frequency to thermal conductivity of a nanomaterial [6, 7]. We have shown that the graphene *LA* and *TA* modes have negative Grüneisen parameters (Fig. 1). This negative value is because of the anomalous hardening of phonon modes upon expansion and *2D* buckled mode. However, the acoustic modes have Grüneisen parameters, which are varying from 0 to -27.35 for graphene corresponding to different wave vector \mathbf{q} . Such high values of Grüneisen parameters lead to high value of thermal conductivity. These acoustic modes generate highly negative Grüneisen parameters. The other modes such as *LA*, *LO*, *TA*, *TO* and the remaining transverse modes (*ZO*) has not dominant effect [12].

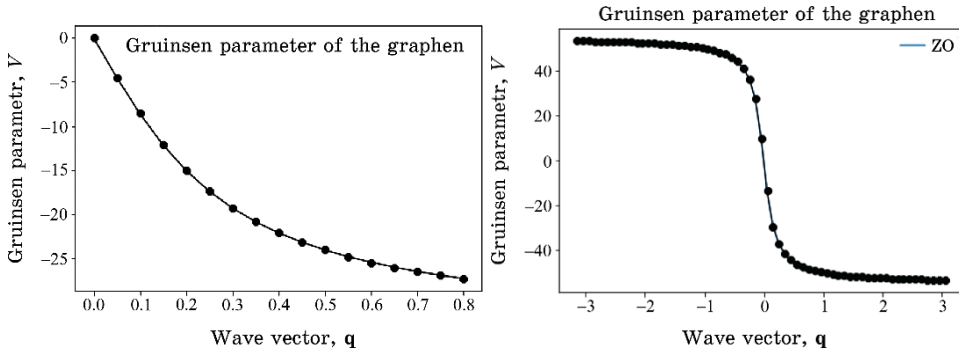


Fig. 1. Variation of Grüneisen parameter with wave vector \mathbf{q} in high-symmetry direction Γ - M .

3. DEBYE TEMPERATURE VARIATION OF GRAPHENE

The Debye theory agrees with both the classical and the Einstein quantum theories. The quantum considerations are of almost no significance at higher temperature range [5]. The theory gives a quite satisfactory account of the observed variation of the heat capacity in the low-temperature region. The Debye theory of specific heat also treats the atoms of the monolayer graphene as harmonic oscillators, however, incapable of vibrating independently of one another. It rather treats them to be strongly coupled together oscillating relative to their neighbours in the lattice. Therefore, we should consider the vibrational motion of the monolayer graphene as a whole rather than the vibrational motion of a single atom [16, 17].

The Debye formula for heat capacity of graphene as 2D material is derived as

$$C = 4R \left(\frac{T}{\theta} \right)^2 \int_0^{\theta/T} \frac{x^3 e^x}{(e^x - 1)^2} dx; \quad (10)$$

here, $x = \hbar\omega/(k_B T)$.

The value of $R = N_A k_B$ depends on the units involved, but it is usually stated with S.I. units as $R = 8.314 \text{ J}/(\text{mol}\cdot\text{K})$. The parameter θ entering into our present discussion is usually referred to as the Debye temperature. It plays the role of a characteristic temperature of a solid. With the Debye temperature at sufficiently low temperatures T , here, only acoustic modes are excited. In this case, $x \gg 1$ and the upper limit of the integration can be extended to infinity. The integral is then deduced in terms of Riemann-Zeta function ζ . The heat capacity of graphene is simulated with the PYTHON program.

The variation of the experimentally measured heat capacity is compared with that computed data (Table 2). This comparison is performed by plotting the heat capacity against the temperature. For determination of the exact variation of Debye temperatures, we have used PYTHON program. In this technique, the specific heat is expressed in terms of Riemann–Zeta function $\zeta(3)$. $\zeta(3)$ has a special value of the Riemann–Zeta function, which is equal to 1.202056903 [9]. From the calculated heat capacities at different temperatures, heat capacity of pure graphene is determined in terms of Riemann–Zeta function. We make a plot of this function by using the PYTHON program. It is seen from this plot that the heat capacity approaches the zero value as $T \rightarrow 0$ K. For higher temperature, heat capacity is not varying abruptly and almost constant $2Nk_B$. It is easily observed from the graph as shown in Fig. 2 that heat capacity for pure graphene reaches a 0.97 J/(g·K) near room temperature. The specific heat at constant volume behaviour of the graphene does not show any anomaly. Figure 2 illustrates the

TABLE 2. Variation of heat capacity with temperature of graphene.

Temperature, K	Heat capacity with Riemann–Zeta function, $\zeta(3)$	Heat capacity, J/(g·K)
0	0	0
40	0.0165000625919003·zeta(3)	0.0198
80	0.0660002503676014·zeta(3)	0.0793
120	0.148500563327103·zeta(3)	0.1785
160	0.264001001470406·zeta(3)	0.4958
200	0.412501564797509·zeta(3)	0.7140
240	0.594002253308412·zeta(3)	0.9718
280	0.808503067003117·zeta(3)	1.2693
320	1.05600400588162·zeta(3)	

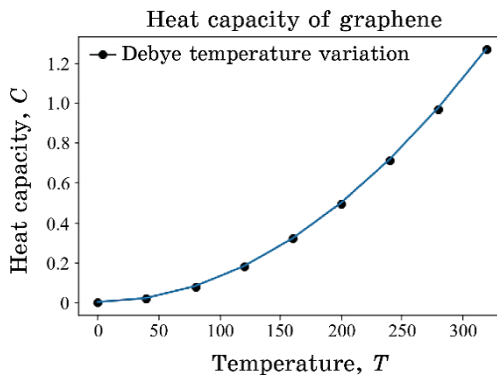


Fig. 2. Debye temperature variation at low temperatures.

higher order of agreement with other researchers [8–10].

4. CONCLUSIONS

Based on the discussion above, it is important to note that the physico-thermal properties, such as Grüneisen parameter, are strongly dependent on wave vector and Debye temperature, as well as on phonon polarizations [10, 11]. We evaluate it along high-symmetry directions for acoustic modes because this mode play main role in thermal expansion. We find that the Grüneisen parameter of graphene 2D materials is negative for low-frequency phonons near Γ . This is happening because the lower acoustic modes are excited at low temperatures. The computed Grüneisen parameters of the *LA* and *TA* branches are highest for graphene with similar results. The study of mono-layer graphene under quasi-harmonic approximation gives the negative values of Grüneisen parameters, which will be further used in determination of thermal expansion coefficients and thermal conductivity of nanomaterials. Figure 2 illustrates that the order of the agreement between the Debye curve and the experimental curve for graphene is remarkable [17]. This is, of course, what we should expect of the Debye approximation at sufficiently low temperatures. Long-wavelength acoustic modes are just the modes, which may be treated as in elastic continuum concept of Debye theory. Notwithstanding the great success of the Debye theory, precise measurements in the low-temperature region show certain deviations from the theoretical predictions. Debye model for the heat capacity of graphene has been remarkably successful in describing the simulations in the low-temperature range. This conclusion is supported by the work of Pop *et al.* [18].

ACKNOWLEDGEMENTS

The author is grateful to the computer centre, S.N.C., Azamgarh for computational assistance.

PROGRAM ORGANIZATION

Appendix A. PYTHON Program of the Grüneisen Parameter of Graphene

```
import matplotlib.pyplot as plt
import numpy as np
import math
# #vj = gamma
```

```

a = 2.47
vj = 8.98
points=np.arange(-np.pi, np.pi, 0.1)
def solve(fun):
    op = []
    for i in points:
        op.append(fun(i))

    return op
def v(qx):
    return (((-a)*math.sqrt(3))/2)*(math.sqrt(11*vj))*(np.arctan(math.sqrt(3)*qx*a))
v = solve(v)
plt.plot(points,v)
plt.ylabel("Grüneisen parameter V")
plt.xlabel("Wave vector (q)")
plt.plot(points, v, color= 'k', linewidth=1, marker='o')
plt.suptitle('Grüneisen Parameter of the Graphene', x=0.50, y=0.98)
plt.legend(['ZO'])
plt.show()

```

Appendix B. Python Program of the Heat Capacity of Graphene

```

import math
import numpy as np
import matplotlib.pyplot as plt
from __future__ import division
from sympy import *
x, T=symbols('x T')
integrate(((x*x*x)*exp(x))/((exp(x)-1)*(exp(x)-1)), (x, 0, oo))

C=[]
T=[0,40,80,120,160,200,240,280,320]

for i in T:
    calC=(2*zeta(3)*8.31*4*i*i)/(2539*2539)
    C.append(calC)
plt.ylabel("Heat Capacity(C)")
plt.xlabel("Temperature (T)")
plt.plot(T, C, color= 'k', linewidth=1, marker = 'o')
plt.suptitle('HEAT CAPACITY OF GRAPHENE', x=0.50, y=0.98)
plt.legend(['Debye temperature variation'])
plt.plot(T, C)
plt.show()

```

REFERENCES

1. J. W. Evans, P. A. Thiel, and M. C. Bartelt, *Surface Science Reports*, **61**, No. 1: 1 (2006); <https://doi.org/10.1016/j.surfrep.2005.08.004>
2. K. S. Novoselov, A. K. Geim, S. V. Morozov, D. Jiang, Y. Zhang, S. V. Dubonos, I. V. Grigorieva, and A. A. Firsov, *Science*, **306**, No. 5696: 666 (2004); <https://doi/10.1126/science.1102896>
3. A. K. Geim and K. S. Novoselov, *Nat. Mater.*, **6**: No. 5: 183 (2007); <https://doi.org/10.1038/nmat1849>
4. L. M. Woods and G. D. Mahan, *Physical Review B*, **61**: 10651 (2000); <https://doi.org/10.1103/PhysRevB.61.10651>
5. E. S. R. Gopal, *Specific Heats at Low Temperatures* (New York: Plenum Press: 1966); <https://doi.org/10.1007/978-1-4684-9081-7>
6. Seymur Cahangirov, Hasan Sahin, Guy Le Lay, and Angel Rubio, *Introduction to the Physics of Silicene and Other 2D Materials* (Springer: 2016); <https://doi.org/10.1007/978-3-319-46572-2>
7. Sumit Saxena, Raghvendra Pratap Chaudhary, and Shobha Shukla, *Scientific Reports*, **6**: 31073 (2016); <https://doi.org/10.1038/srep31073>
8. Gour P. Dasa, Parul R. Raghuvanshi, and Amrita Bhattacharya, *9th International Conference on Materials Structure and Micromechanics of Fracture Phonons and Lattice Thermal Conductivities of Graphene Family* (2019), vol. **23**, p. 334.
9. Olfa Boussaid, Ahlem Boussaid, and Mustapha Fnaiech, *Silicon*, **10**: 2307 (2018); <https://doi.org/10.1007/s12633-018-9765-8>
10. Bo Peng, Hao Zhang, Hezhu Shao, Yuanfeng Xu, Gang Ni, Rongjun Zhang, and Heyuan Zhu, *Phys. Rev. B*, **94**: 245420 (2016); <https://doi.org/10.1103/PhysRevB.94.245420>
11. Bo Peng, Hao Zhang, Hezhu Shao, Yuchen Xu, Xiangchao Zhang, and Heyuan Zhu, *Scientific Reports*, **6**: 20225 (2016); <https://doi.org/10.1038/srep20225>
12. Kamlesh Kumar and M. Imran Aziz, *American Journal of Nanosciences*, **8**, No. 1: 8 (2022); <https://doi.org/10.11648/j.ajn.20220801.12>
13. Xu-Jin Ge, Kai-Lun Yao, and Jing-Tao Lü, *Phys. Rev. B*, **94**: 165433 (2016); <https://doi.org/10.1103/PhysRevB.94.165433>
14. Kamlesh Kumar, M. Imran Aziz, and Nafis Ahmad, *IJSRST*, **9**, No. 2: 323 (2022); <https://doi.org/10.32628/IJSRST229259>
15. Kamlesh Kumar, Mohammad Imran Aziz, Khan Ahmad Anas, *American Journal of Nanosciences*, **8**, No. 2: 13 (2022); <https://doi.org/10.11648/j.ajn.20220802.11>
16. Kamlesh Kumar, Mohammad Imran Aziz, Khan Ahmad Anas, and Rahul Kumar Mishra, *American Journal of Nanosciences*, **8**, No. 3: 37 (2022); <https://doi.org/10.11648/j.ajn.20220803.12>
17. Sarita Mann, Ranjan Kumar, and V. K. Jindal, *RSC Adv.*, **7**: 22378 (2017); <https://doi.org/10.1039/C7RA01591G>
18. Eric Pop, Vikas Varshney, and Ajit K. Roy, *MRS Bull.*, **37**: 1273 (2012); <https://doi.org/10.1557/mrs.2012.203>

PACS numbers: 62.23.Pq, 68.37.Hk, 68.55.J-, 81.05.uj, 81.15.Pq, 81.16.Mk, 81.65.Kn

Laser-Assisted Electrodeposition of Composite Carbon-Containing Nickel Coatings

V. V. Tytarenko¹, V. A. Zabludovsky², and I. V. Tytarenko²

¹*Dnipro University of Technology,
19, Dmytra Yavornitskoho Ave.,
UA-49005 Dnipro, Ukraine*

²*Ukrainian State University of Science and Technologies,
2, Lazaryana Str.,
UA-49010 Dnipro, Ukraine*

The paper presents the study of the structure, protective and mechanical properties of nickel composite coatings modified with ultradispersed diamonds and electrodeposited under conditions of external stimulation by laser radiation. An analysis of the cathodic polarization curves shows that the presence of dispersed particles with a concentration of 2–15 g/l in the aqueous electrolyte solution leads to a shift in the cathodic potential to the electronegative region by 108–340 mV, respectively, that indicates an increase in charge-transfer resistance. Nickel composite coatings obtained by laser-assisted electrodeposition are characterized by a higher content of ultradispersed diamond particles in the coating (4.35–5.10 wt.%) as compared to the mode of deposition without laser irradiation (2.24–3.15 wt.%). In this case, the proportion of particles of smaller size ($\leq 0.25\text{--}1 \mu\text{m}$) increases in the coatings. The more intense penetration of dispersed-phase particles into the emerging coating during the laser stimulation of the electrodeposition process is due to the presence of a temperature gradient, which provides an additional supply of metal ions in the irradiation region. Increased concentration of the dispersed phase in nickel composite coatings promotes formation of a finer crystalline coating structure, enhanced hardness, corrosion resistance, and wear resistance of the coatings.

У даній роботі представлено дослідження структури, захисних і механічних властивостей нікlevих композиційних покрівель, модифікованих ультрадисперсними діамантами, електроосаджених в умовах зовнішнього впливу лазерним випроміненням. Аналіза катодних поляризаційних кривих показала, що наявність у водному розчині електроліту дисперсних частинок із концентрацією у 2–15 г/л приводить до зміщення катодного потенціялу в електронегативну область на 108–340 мВ відповідно, що вказує на збільшення опору передачі заряду. Нікль-

ві композитні покриття, одержані методом лазерного електроосадження, характеризуються вищим вмістом ультрадисперсних діамантових частинок у покритті (4,35–5,10 мас.%) порівняно зі способом осадження без лазерного опромінювання (2,24–3,15 мас.%). Водночас у покриттях збільшується частка частинок меншого розміру ($\geq 0,25\text{--}1 \mu\text{m}$). Більш інтенсивне проникнення частинок дисперсної фази у формівне покриття під час лазерної стимуляції процесу електроосадження зумовлено наявністю температурного градієнту, який забезпечує додаткове надходження іонів металу в область опромінювання. Підвищена концентрація дисперсної фази в нікlevих композиційних покриттях сприяє формуванню більш дрібнокристалічної структури покриття, підвищенню твердості, корозійної стійкості та зносостійкості покриттів.

Key words: ultradispersed diamond particles, composite nickel coatings, laser-assisted electrodeposition, structure, mechanical and protective properties.

Ключові слова: ультрадисперсні діамантові частинки, композиційні нікlevі покриття, лазерностимулюване електроосадження, структура, механічні та захисні властивості.

(Received 1 July, 2023)

1. INTRODUCTION

There are many ways to harden the surface of parts in order to increase the service life of mechanisms, parts and friction pairs, among them: thermochemical treatment or various methods of coating. One of the known ways to improve mechanical properties of the surface is its electrolytic modification by deposition of metal films with the required operational parameters, the most important of which are hardness and wear resistance. However, metal and alloy films, in terms of their physicochemical properties, often do not meet the increased requirements of modern technology. The solution to the surface hardening problem is the modification of the metal matrix with particles of the dispersed phase to obtain composite electrolytic coatings (CEC).

It is known that the introduction of solid dispersed particles (ultradispersed diamonds (UDD)) into electrolytic coatings increases their microhardness and wear resistance. The reasons for this are the reduction of crystallite sizes of the deposited metal and the presence of superhard particles in the coating [1–4]. The conducted literature analysis [5–10] showed that the methods of influencing the process of co-deposition of metal films with UDD include the use of ultrasonic or mechanical stirring of the electrolyte solution in the process of electrodeposition. Because of this activation of the electrodeposition process, solid dispersed particles incorporated into

the coating being formed, prevent the growth of the crystalline phase nuclei, which is the reason for the formation of a finer crystalline coating structure.

In this paper, we consider a laser-assisted method for the electrodeposition of composite nickel electrolytic coatings. The purpose of this work is to study the effect of laser radiation on the process of co-deposition of metal ions and ultradispersed diamond particles, structure, mechanical and protective properties of electrodeposited composite nickel coatings.

2. MATERIALS AND METHODS

Electrodeposition of composite coatings was carried out from sulphate nickel-plating electrolyte of the following composition: $\text{NiSO}_4 \cdot 7\text{H}_2\text{O}$ — 300 g/l, H_3BO_3 — 30 g/l, $\text{Na}_2\text{SO}_4 \cdot 10\text{H}_2\text{O}$ — 50 g/l at pH = 5. The concentration of UDD (C_{UDD}) in the aqueous electrolyte solution was varied in the range from 2 g/l up to 15 g/l.

Due to the developed surface and the presence of a large number of functional groups, individual nanodiamond particles with an average particle size of 4–5 nm form strong primary aggregates, which, as a rule, act as indestructible parts of nanodiamond powders. UDD particles are prone to spontaneous aggregation among themselves into extremely strong aggregates (40–100 nm) with the subsequent formation of less strong secondary aggregates (up to 1–5 μm) [1–4].

Electrodeposition was carried out under external exposure to radiation from a CO_2 gas-discharge laser generating in a continuous mode at a wavelength of 10.6 μm at a laser-radiation power of 25 W (Fig. 1). The temperature of the aqueous electrolyte solution in the near-

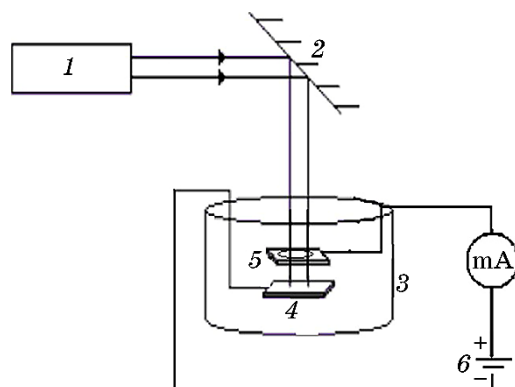


Fig. 1. Scheme of the test installation: 1—emitting source (CO_2 -laser); 2—rotary mirror; 3—electrolytic cell; 4—cathode; 5—anode; 6—power supply.

cathode irradiation region increased from 293 K to 351 K. For comparison, the coatings were also deposited using a direct current at a density of 100 A/m².

The microhardness of the coating was measured on a PMT-3 microhardness tester with an indenter load of 0.196 N. Wear tests of samples were conducted on the friction machine with reciprocating motion of samples with frequency of 0.5 s⁻¹ and amplitude of 0.15 m in conditions of dry friction against steel under load of 1.7 N. The friction path was parallel to the substrate. Wear resistance was evaluated by weight loss of the coating. X-ray microanalysis was performed using a JSM-64901LV scanning electron microscope (Japan). X-ray phase analysis of the films was conducted on a DRON-2.0 diffractometer using scintillation detection of x-rays. Shooting to determine the phase composition of nickel films was carried out in monochromatized CuK_α radiation.

The polarization dependences were recorded in the potentiodynamic mode on a P-5827M potentiostat at a potential sweep rate of 10 mV/s. The measurements were carried out in a three-electrode electrolytic cell. A copper plate was used as the working electrode (cathode). The reference electrode was a silver chloride electrode, and the auxiliary electrode was a platinum electrode.

The viscosity of the aqueous electrolyte solution was determined using a VPZh-4 capillary glass viscometer with an internal capillary diameter of 1.12 mm. A characteristic property of an aqueous nickel-plating electrolyte solution is low sedimentation resistance, leading to uneven distribution of nanodiamond particles in the metal matrix. In order to keep the UDD particles suspended in the electrolyte solution and to prevent settling of particles to the bottom of the electrolytic cell, the aqueous electrolyte solution was stirred with a magnetic stirrer before starting the electrodeposition process.

Accelerated corrosion tests consisted of immersing samples in a 3% sodium chloride solution. The corrosion rate was determined by the gravimetric method (by weight loss of the metal coating). External examination of the samples was carried out daily until the first signs of corrosion appeared and scored on a 10-point scale [11].

3. RESULTS AND DISCUSSION OF THEM

In order to determine the optimal modes of electrodeposition of composite coatings of increased hardness and wear resistance, we studied the effect of the concentration of UDD particles (C_{UDD} , g/L) in an aqueous electrolyte solution on the kinematic viscosity of the solution (ν , mm²/s) (Fig. 2).

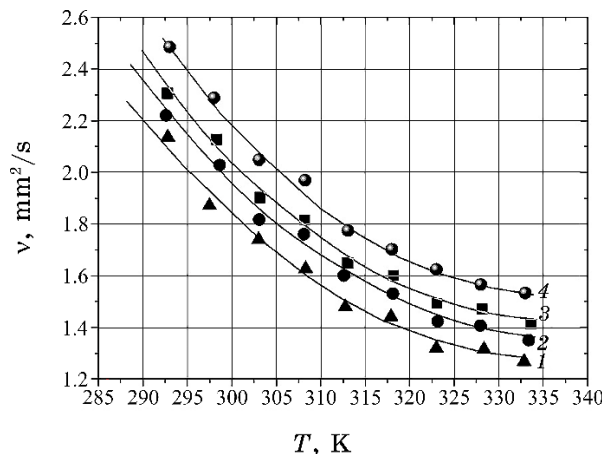


Fig. 2. Dependence of the kinematic viscosity of aqueous nickel-plating electrolyte solution on temperature and concentration of the dispersed phase in the electrolyte [g/l]: 1—0; 2—2; 3—10; 4—15.

From the analysis of the results obtained, it follows that with an increase in the temperature of the aqueous electrolyte solution, the viscosity of the solution decreases, because of which larger UDD particles settle in the lower layers of the electrolyte solution, and their number in the near-cathode region sharply decreases. The increase in concentration of the disperse phase particles of the finer fraction in the coating formed under the laser-assisted mode of electrodeposition is due to an increase in the flux density of metal ions adsorbed on the surfaces of UDD particles [12, 13], as a result of which the particles of the dispersed phase acquire a positive charge, which promotes electrophoretic co-deposition.

When using laser radiation sources, the main mechanism of laser stimulation of the electrodeposition process is the heating of the metal-electrolyte interface [14, 15]. In Refs. [16–18], the use of laser irradiation of the near-cathode region in the process of electrodeposition of composite coatings contributes to an increase in the cathode current density. Thus, it is of considerable interest to study the effect of laser radiation on the co-deposition of UDD particles and metal ions.

An analysis of the cathodic polarization curves (Fig. 3) showed that the presence of dispersed particles in the aqueous electrolyte solution leads to a shift in the cathodic potential to the electronegative region that indicates an increase in charge transfer resistance.

The increase in the cathodic overpotential during laser-assisted electrodeposition can be explained by the increased, in the direction of laser radiation, flux density of complexes formed because of ad-

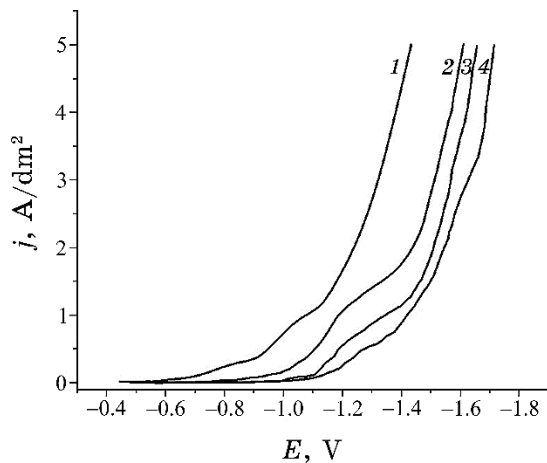


Fig. 3. Cathodic polarization dependences obtained in sulfuric acid nickel-plating electrolyte: 1—without UDD; 2—with UDD ($C_{UDD} = 2 \text{ g/l}$); 3—with UDD ($C_{UDD} = 15 \text{ g/l}$); 4—with UDD ($C_{UDD} = 15 \text{ g/l}$, laser-assisted mode).

sorption of metal ions on the surfaces of UDD particles. Electropositive charged complex aggregates formed because of the total charge, moving to the cathode surface, block it, thereby, leading to a decrease in the active surface area of the cathode.

Analysis of x-ray patterns of electrolytic nickel coatings (Fig. 4) shows that diffraction maxima corresponding to the diamond phase of carbon overlap with lines corresponding to the crystalline phase of electrolytic nickel that complicates determination of the nanodiamond/nickel ratio in the coating and determines the need for studies of the elemental composition of the coatings. In pure nickel coatings, the preferential orientation of crystallites in the [111] direction is observed (Fig. 4, *a*). The introduction of UDD did not lead to a change in the CEC phase composition, and the diffraction patterns do not show a significant redistribution of the line intensity (Fig. 4, *b*). In composite nickel coatings obtained in the laser-assisted electrodeposition mode, a redistribution of the intensity of the (111) and (220) lines is observed (Fig. 4, *c*), which indicates a change in the conditions of electrocrystallization.

Figure 5 shows the results of x-ray microanalysis of the elemental composition of the coating surface. From the results of x-ray microanalysis of the elemental composition of the coating surface, it follows that the fraction of UDD particles of certain sizes depends on the electrodeposition mode [19, 20]. The average diameter of UDD particles in CEC deposited without laser irradiation was 1.5–2 μm . Composite nickel coatings obtained by laser-assisted electrodeposition are characterized by a higher content of UDD parti-

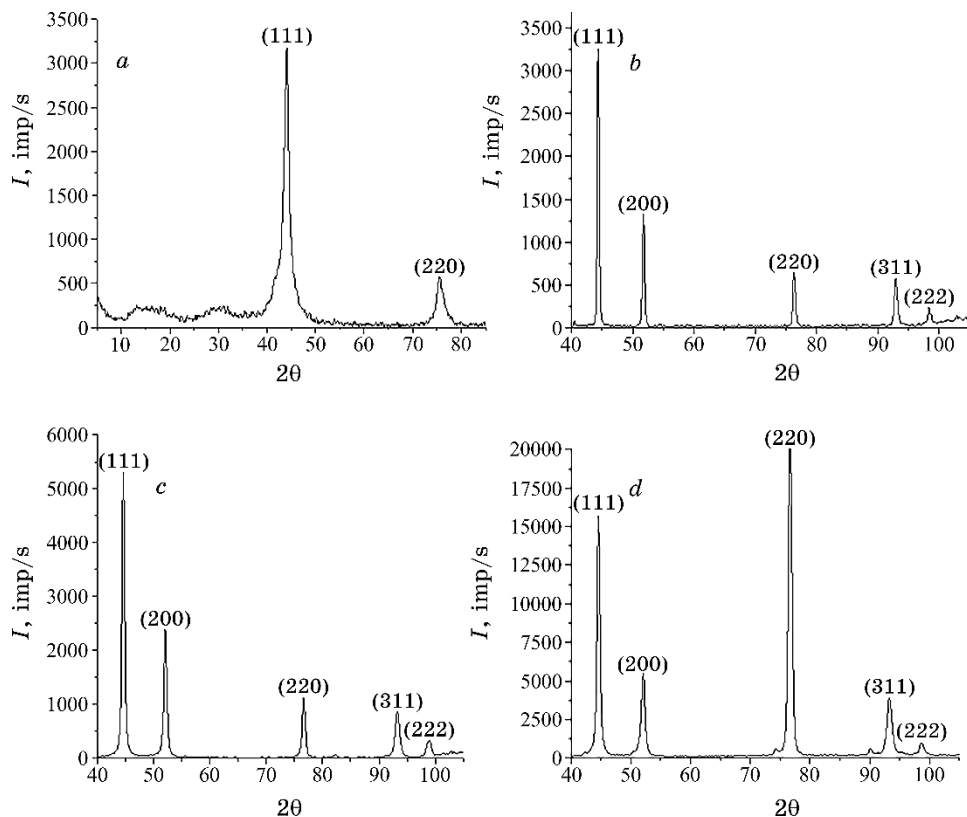


Fig. 4. Diffractograms: (a) UDD powder; (b) Ni (without laser irradiation); (c) Ni+UDD (without laser irradiation); (d) Ni+UDD (laser-assisted mode).

cles in the coating (4.35–5.10 wt.%) as compared to the mode of deposition without laser irradiation (2.24–3.15 wt.%). In this case, the proportion of particles of smaller size $\leq 0.25\text{--}1\ \mu\text{m}$ increases in the coatings.

According to the Nernst–Planck equation [21], the increase in disperse phase particle flux density in the aqueous electrolyte solution to the surface of the coating formed during laser-assisted electrodeposition is due to the potential gradient and rise in the diffusion coefficient [22].

The structure and mechanical properties of the resulting composite coating largely depend on the concentration and size of UDD particles in the coating. The results of studies of the fractional composition of UDD particles on the surface of composite electrolytic nickel coatings show that during DC electrodeposition UDD particles of larger size reach the cathode surface. Agglomerates of UDD particles with a size of $1.5\ \mu\text{m}$ are formed on the CEC surface

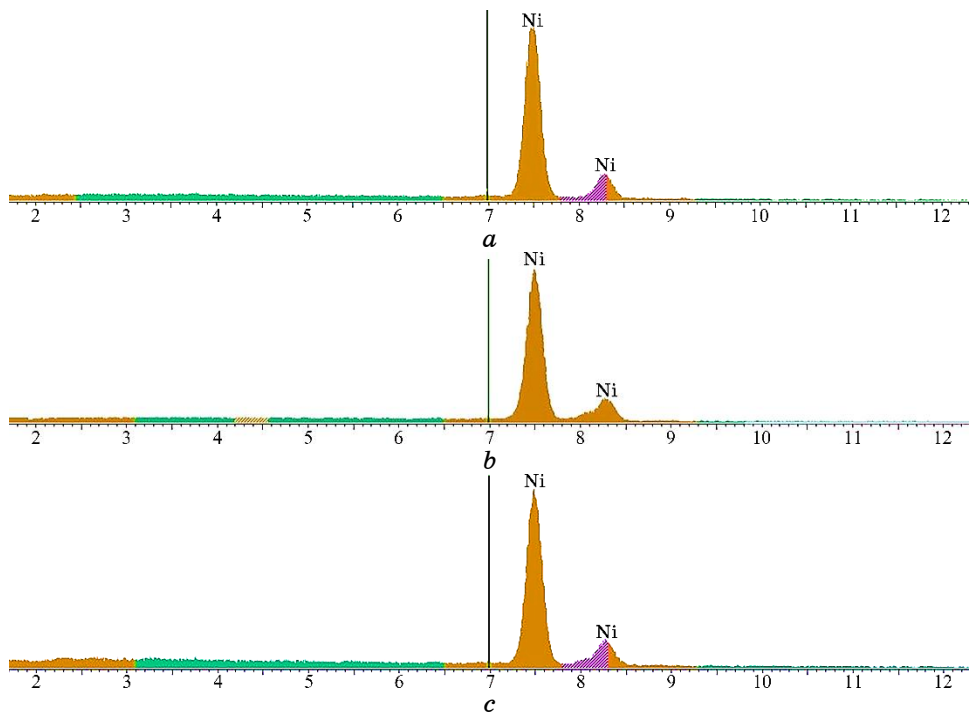


Fig. 5. X-ray microanalysis: (a) Ni (without laser irradiation); (b) Ni + UDD (without laser irradiation); (c) Ni + UDD (laser-assisted mode).

resulting in formation of coarser crystalline coatings (Fig. 6, *a*) with microhardness of 1800–1950 MPa.

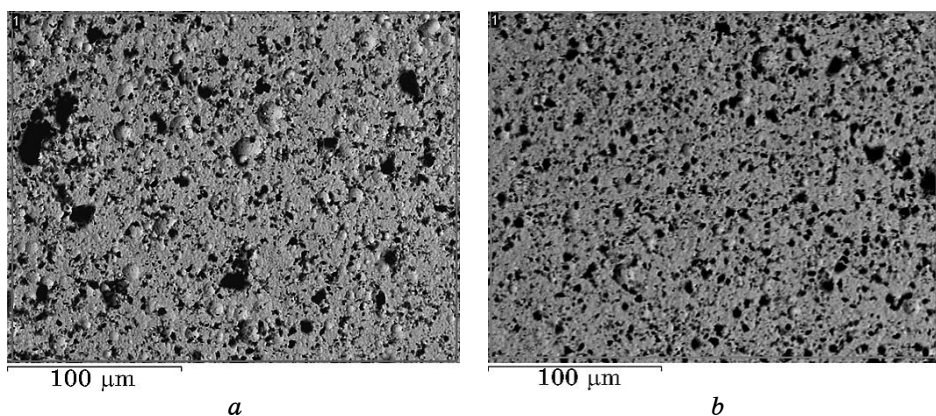


Fig. 6. Surface morphology of the electrolytic nickel composite coatings: (a) direct current without laser irradiation; (b) laser-assisted mode.

The inclusion of smaller UDD particles ($\approx 0.25\text{--}1\ \mu\text{m}$) in the coating composition in the laser irradiation region complicates the surface diffusion of metal adatoms and prevents the growth of nuclei of the crystalline phase that results in formation of a finer crystalline coating structure (Fig. 6, *b*).

Composite coatings are formed more fine-grained that determined microhardness increase from 2500 MPa outside the irradiation area to 3700 MPa in the irradiation area.

Figure 7 shows the results of the corrosion tests on nickel coatings. It should be noted that the corrosion rate of the samples tested was uniform. However, the change in mass of the carbon-containing nickel coatings over 144 hours is slower than in the pure nickel coatings. This is due to the increased extent of the interlayer boundaries that contain the UDD particles.

The results of the conducted studies make it possible to attribute nickel coatings deposited by means of direct current to the 'Resistant' group with a score of 4, and the intensification of the process of co-deposition of UDD particles under laser irradiation contributes to the production of composite nickel coatings that belong to the 'Extremely resistant' group with a score of 3. This is caused: firstly, by the fact that the UDD particles block the cathode surface thus reducing the area of the active cathode surface that changes the coating growth structure in the cross-section from columnar (Fig. 8, *a*) to microlayer (Fig. 8, *b*); secondly, by an increase in metal ion flux density adsorbed on the UDD particle surfaces, which contributes to a more intense incorporation of UDD particles into the deposited coating. Increased concentration of dispersed phase particles from 2.24 to 4.35 wt.% leads to the formation of fine-grained coatings with fewer pores, which prevents the formation of corrosion centres, in contrast to columnar growth, where the surface of coatings is more heterogeneous.

An increase in the UDD content of the nickel films enhances the wear resistance of the coatings. Nickel coatings electrodeposited from the aqueous electrolyte solution without UDD addition lose 10% of their weight after 5 hours of wear. When UDD with 2 g/l concentration were added to the aqueous electrolyte solution, the losses were of 6–8%, and for laser-assisted electrodeposition coatings, they were of 1–2%.

4. CONCLUSION

1. The increase in the concentration of smaller UDD particles ($\approx 0.25\text{--}1\ \mu\text{m}$) in the coating formed under laser-assisted deposition is due to the potential gradient and rise in the diffusion coefficient.
2. The increase in the flux density of complexes formed because of

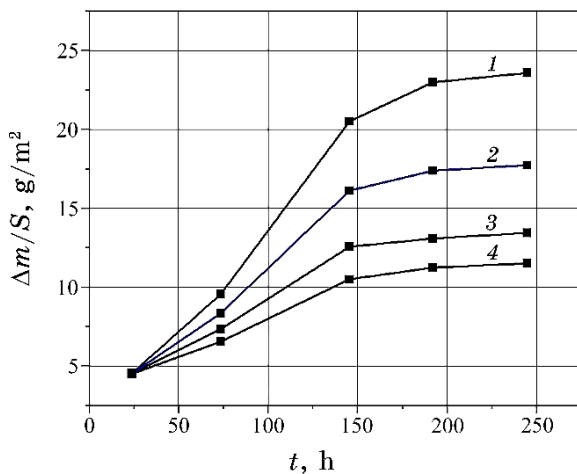


Fig. 7. Dependences of the mass change of electrolytic coatings: 1—Ni (without laser irradiation); 2—Ni + UDD ($C_{UDD} = 2 \text{ g/l}$, without laser irradiation); 3—Ni + UDD ($C_{UDD} = 15 \text{ g/l}$, without laser irradiation); 4—Ni + UDD ($C_{UDD} = 15 \text{ g/l}$, laser-assisted mode).

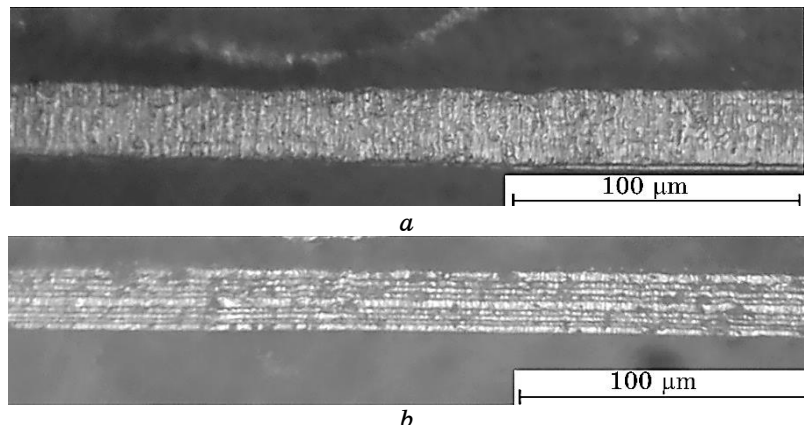


Fig. 8. Structure of electrolytic coatings in cross section: direct current: (a) Ni (without laser irradiation); (b) Ni + UDD (laser-assisted mode).

the adsorption of metal ions on the surfaces of UDD particles leads to an increase in oversaturation at the crystallization front. The formed coating is reached by smaller size UDD particles that block the growth of nuclei of the crystalline phase, which leads to the formation of a more densely packed coating and changes the cross-sectional growth structure from columnar to microlayer.

3. The formation of finer crystalline coatings and change of cross-

sectional growth structure from columnar to microlayer at laser-assisted deposition process resulted in improvement of mechanical and protective properties of carbon-containing nickel coatings (coating microhardness increased from 1800–1950 MPa to 2500–3700 MPa, corrosion resistance increased 2 times, and the wear of coatings decreased 3 times).

REFERENCES

1. G. K. Burkat and V. Yu. Dolmatov, *J. Phys. Chem. Solids*, **46**, No. 4: 685 (2004) (in Russian); <https://journals.ioffe.ru/articles/viewPDF/4203>
2. G. K. Burkat, V. Yu. Dolmatov, E. Osawa, and E. A. Orlova, *J. Superhard Mater.*, **2**: 43 (2010) (in Russian); <http://dspace.nbuv.gov.ua/bitstream/handle/123456789/63448/03-Burkat.pdf?sequence=1>
3. V. Yu. Dolmatov, *Russ. Chem. Rev.*, **70**: 607 (2001) (in Russian); <https://doi.org/10.1070/RC2001v070n07ABEH000665>
4. V. Yu. Dolmatov, *Russ. Chem. Rev.*, **77**, No. 3: 303 (2008) (in Russian); <https://doi.org/10.1070/RC2008v077n03ABEH003872>
5. Xiangzhu He, Yongxiu Wang, Xin Sun, and Liyong Huang, *Nanosci. Nanotechnol. Lett.*, **4**, No. 1: 48 (2012) <https://doi.org/10.1166/nnl.2012.1286>
6. G. A. Chiganova and L. E. Mordvinova, *Inorganic Materials*, **47**, No. 7: 717 (2011); <https://doi.org/10.1134/S0020168511070089>
7. Hiroshi Matsubara, Mikinori Kobayashi, Hiroshi Nishiyama, Nobuo Saito, Yasunobu Inoue, and Masao Mayuzumi, *Electrochemistry*, **72**, No. 6: 446 (2004); <https://doi.org/10.5796/electrochemistry.72.446>
8. Liping Wang, Yan Gao, Qunji Xue, Huiwen Liu, and Tao Xu, *Mater. Sci. Eng. A*, **390**, Nos. 1–2: 313 (2005); <https://doi.org/10.1016/j.msea.2004.08.033>
9. Xiangzhu He, Yongxiu Wang, Xin Sun, and Liyong Huang, *Nanosci. Nanotechnol. Lett.*, **4**, No. 1: 48 (2012); <https://doi.org/10.1166/nnl.2012.1286>
10. G. K. Burkat, T. Fujimura, V. Yu. Dolmatov, E. A. Orlova, and M. V. Veretennikova, *Diamond Relat. Mater.*, **14**, No. 8: 1761 (2005); <https://doi.org/10.1016/j.diamond.2005.08.004>
11. R. Winston Revie, *Uhlig's Corrosion Handbook* (Wiley: 2011); <https://www.wiley.com/en-us/9780470080320>
12. V. V. Tytarenko, E. Ph. Shtapenko, E. O. Voronkov, V. A. Zabludovsky, W. Kolodziejczyk, K. Kapusta, and V. N. Kuznetsov, *Journal of Surface Investigation: X-Ray, Synchrotron and Neutron Techniques*, **15**, No. 4: 866 (2021); [doi:10.1134/S102745102104039X](https://doi.org/10.1134/S102745102104039X)
13. V. V. Tytarenko, E. Ph. Shtapenko, E. O. Voronkov, Aruna Vangara, V. A. Zabludovsky, Wojciech Kolodziejczyk, K. Kapusta, and S. I. Okovytyy, *J. Chem. Technol.*, **29**, No. 1: 42 (2021); <https://doi.org/10.15421/082108>
14. V. A. Zabludovsky, V. V. Tytarenko, and E. Ph. Shtapenko, *Transactions of the IMF*, **95**, No. 6: 337 (2017); <https://doi.org/10.1080/00202967.2017.1355463>
15. V. A. Zabludovsky, V. V. Dudkina, and E. F. Shtapenko, *Lazerno-*

- Stimulirovannoje Elektroosazhdenie Metallov* [Laser-Stimulated Metal Electrodeposition] (Saarbrücken: Lambert Academic Publishing: 2014) (in Russian);
<https://eadnurt.diit.edu.ua/uk/bitstream/123456789/11210/1/Zabludovsky.pdf>
16. Yilin Yao, Jinqiu Zhang, Peixia Yang, and A. N. Maozhong, *Mater. Reports*, **36**, No. 3: 20080209-9 (2022); <https://doi.org/10.11896/cldb.20080209>
17. Xueren Dai, Kun Xu, Zhaoyang Zhang, Lingyue Zhang, Yucheng Wu, Hao Zhu, and Shuai Yang, *J. Electroanal. Chem.*, **904**, No. 1: 115855 (2021); [doi:10.1016/j.jelechem.2021.115855](https://doi.org/10.1016/j.jelechem.2021.115855)
18. Wenrong Shen, Kun Xu, Zhaoyang Zhang, Sheng Guo, Shuai Yang, Hao Zhu, Sishui Liu, and Yucheng Wu, *J. Electrochem. Soc.*, **169**, No. 8: 082507 (2022); [doi:10.1149/1945-7111/ac8646](https://doi.org/10.1149/1945-7111/ac8646)
19. V. A. Zabludovsky, V. V. Dudkina, and E. Ph. Shtapenko, *Science and Transport Progress. Bulletin of Dnipropetrovsk National University of Railway Transport Named after Academician V. Lazaryan*, **47**, No. 5: 70 (2013) (in Ukrainian); [doi:10.15802/stp2013/17968](https://doi.org/10.15802/stp2013/17968)
20. V. V. Tytarenko, V. A. Zabludovsky, E. Ph. Shtapenko, and I. V. Tytarenko, *Galvanotechnik*, **4**: 648 (2019);
[http://eadnurt.diit.edu.ua/bitstream/123456789/11211/1/Tytarenko.pdf](https://eadnurt.diit.edu.ua/bitstream/123456789/11211/1/Tytarenko.pdf)
21. A. V. Kovalenko and M. A. Urtenov, *Krayevyye Zadachi dlya Sistemy Uravneniy Ehlektrodiffuzii. Odnomernyye Zadachi* [Boundary Value Problems for a Set of Electrodiffusion Equations. One-Dimensional Problems] (Saarbrücken: Lambert Academic Publishing: 2011), part 1 (in Russian).
22. V. V. Tytarenko, V. A. Zabludovsky, E. Ph. Shtapenko, and I. V. Tytarenko, *Phys. Chem. Solid State*, **23**, No. 3: 461 (2022); [doi:10.15330/pcess.23.3.461-467](https://doi.org/10.15330/pcess.23.3.461-467)

PACS numbers: 61.43.Gt, 78.30.Na, 78.40.Ri, 81.05.Je, 81.05.Rm, 82.47.Wx, 82.80.Gk

Формування нанопор в анодно-окисненому алюмінії під впливом вуглецевих наночастинок

К. О. Куделко¹, О. Г. Дзязько², Л. М. Рождественська¹,
Л. Б. Харькова¹, В. М. Огенко¹

¹*Інститут загальної та неорганічної хімії ім. В. І. Вернадського НАН України,
просп. Акад. Палладіна, 32/34,
03141 Київ, Україна*

²*Київський національний університет імені Тараса Шевченка,
вулиця Володимирська, 64/13,
01601 Київ, Україна*

Досліджено умови синтезу та характеристики нанопористого анодно-окисненого алюмінію (АОА). Процес анодування проводили в розчині щавлевої кислоти, який містив вуглецеві наночастинки (ВНЧ). Згідно з даними сканувальної електронної мікроскопії, розмір пор оксидного шару становить 20–40 нм, товщина стінок пор — до 50 нм. У випадку анодування алюмінію за відсутності добавки вуглецевого матеріалу аналогічні параметри становлять 50–100 нм і 30 нм відповідно. Ефект впливу вуглецевого матеріалу на структуру поруватого шару пояснюється з точки зору адсорбції його на АОА під час процесу анодування. Вуглецеві наночастинки досліджено за допомогою UV–Vis-спектроскопії, динамічного лазерного розсіяння (в агрегованому стані), спектроскопії комбінаційного розсіяння та ІЧ-спектроскопії. Виявлено високу невпорядкованість структури вуглецевих наночастинок. Одержано ізотерму адсорбції, з якої встановлено, що сорбційна рівновага найбільш описується рівнянням Тьюмкіна. Запропоновано кристалізацію АОА в гідротермальних умовах за температури у 200°C.

The conditions and characteristics for nanoporous anodic oxidized aluminum (AOA) are presented. The anodizing process is carried out in a solution of oxalic acid containing carbon nanoparticles (CNPs). The carbon nanoparticles are studied by ultraviolet-visible spectroscopy, dynamic laser scattering (in the aggregated state), Raman spectroscopy, and infrared spectroscopy. Scanning electron microscopes are used to study the morphology of the AOA. The pore size of the porous layer is of 20–40 nm, and the pore-wall thickness is up to 50 nm. In the absence of the addition of carbon material, similar surface parameters are of 50–100 nm and 30

nm, respectively. The effect of the carbon material on the structuring of the pore layer is explained in terms of adsorption of it on the AOA during anodizing process. A high-disordered structure of carbon nanoparticles is revealed. The adsorption isotherm is obtained, and it is found that the Temkin model is the most suitable for describing the sorption equilibrium. The crystallization of AOA under hydrothermal conditions at 200°C is proposed. The addition of CNDs to the oxalic acid electrolyte reduces the pore size of obtained anodized aluminium. Carbon nanoparticles effect on the formation of the porous structure of AOA with adsorption. The advantage of CNDs over GO is the fabrication of AOA with smaller pores in mild conditions without aggressive reagents. The effect of CNDs on the porous structure of AOA can be explained, on the one hand, by its shielding by carbon nanoparticles, and on the other hand, by the ‘damping effect’ of CNDs on the faster thermal expansion of aluminium compared to Al₂O₃. It is possible to obtain samples of AOA with nanoscale pores by environmentally friendly synthesis using cheap and readily available chemicals. To obtain crystalline Al₂O₃, hydrothermal treatment can be implemented that has the advantage of a lower crystallization temperature over calcination.

Ключові слова: анодно-окиснений алюміній, вуглецеві наночастинки, нанопори, адсорбція, механізм анодування.

Key words: anodic oxidized aluminium, carbon nanoparticles, nanopores, adsorption, anodizing mechanism.

(*Отримано 21 червня 2023 р.*)

1. ВСТУП

Практичне застосування гідратованого оксиду Алюмінію (ГАО) охоплює велику кількість галузей [1]. У металургії та хемічній промисловості цей матеріал використовують для одержання чистого алюмінію, а також для одержання оксиду, сульфату, фториду алюмінію, синтетичних цеолітів тощо. Крім цього, гідратований оксид алюмінію застосовується у виробництві полімерів, каучуків, лакофарбових матеріалів. Застосовуючи ГАО у якості добавок можливо понизити горючість, займистість, виділення диму та токсичних газів під час пожежогасіння. У медицині ГАО використовується як обволікальний засіб та антацід-тривалої дії для нормалізації кислотно-лужного балансу шлунково-кишкового тракту людини, для лікування захворювань шлунка та дванадцятипалої кишки. У фармакології матеріал входить до складу вакцин і зубної пасті.

У водопідготовці ГАО виконує функцію адсорбенту, який адсорбує як катіони, так і аніони залежно від pH розчину [2]. Це відрізняє його від більшості неорганічних адсорбентів, таких як гід-

рофосфати багатовалентних металів, які мають лише катіонообмінну здатність [3–5]. ГАО використовують як добавку до гідратуваних оксидів Zr, Ti, Sn для посилення їхніх аніонообмінних властивостей [6–8]. ГАО також застосовують для модифікування полімерних мембрани баромембранного розділення з метою поліпшення їхніх затримувальної здатності, електропровідності та гідрофільних властивостей [9, 10]. Цей матеріал запропоновано для модифікування йонообмінних полімерів [11]. У згаданих випадках ГАО подібний до гідратованого діоксиду Цирконію, який використовується для тих же цілей [12–15]. Варто зазначити, що до ГАО можна віднести також аморфний анодно-окиснений алюміній (АОА) у вигляді готового продукту.

Процеси анодування широко використовуються для оброблення поверхні металів перед фарбуванням [16]. Іншими сферами застосування АOA є сенсори, каталіза, мембранне розділення [17]; його також використовують як матрицю для вирощування нанотрубок або нанострижнів [18].

У двох останніх випадках пориста структура АOA є особливо важливою. Однак під час анодування нанорозмірні пори утворюються в достатньо концентрованих розчинах агресивних реагентів (H_2SO_4 , H_3PO_4), навіть токсичних сполук, таких як H_2SeO_4 [17]. У середовищі екологічно чистої кислоти $H_2C_2O_4$ утворюються достатньо великі пори, розмір яких перевищує 100 нм. У той же час, часткове екранування поверхні АOA під час анодування може привести до збільшення густини струму на відкритих ділянках і, як наслідок, до зменшення розміру пор АOA. Іншою проблемою є заміна високочистого алюмінію, який зазвичай використовується для анодування, на більш дешевший матеріал з технічною чистотою [19].

Новітній вуглецевий наноматеріял, такий як оксид графену (ОГ), є гарним кандидатом в якості добавки до електроліту, оскільки він адсорбується на поверхні оксидів багатовалентних металів. Наприклад, це дає можливість одержати нанокомпозит TiO_2 –ОГ [20]. Раніше було виявлено, що додавання ОГ до розчину щавлевої кислоти забезпечує утворення менших пор порівняно з АOA, одержаними в чистому розчині цього електроліту [21].

В роботі досліджено вплив вуглецевих наночастинок (ВНЧ), яких можна легко одержати в гідротермальних умовах [22], на формування поруватого шару. Крім того, вирішується проблема термічного оброблення АOA. Зазвичай мембрани АOA наносять на алюмінійову підкладинку, щоб забезпечити хемічну та механічну стабільністі оксидного матеріялу; однак для більшої стабільності оксидного шару необхідне термічне оброблення за високою температурою. Однак температура топлення алюмінію становить 660°C. Тому запропоновано використання гідротермального

оброблення АOA, яке можна виконати за більш низької температури. Як правило, ця процедура викликає кристалізацію аморфного оксиду Алюмінію (іноді з утворенням корунду) [23].

2. ЕКСПЕРИМЕНТАЛЬНА ЧАСТИНА

Матеріали. В якості вихідних реагентів використовували: щавлеву кислоту $C_2H_2O_4$, хлорид Купруму $CuCl_2 \cdot 5H_2O$, Натрію гідроксід $NaOH$, соляну кислоту HCl , фосфорну кислоту H_3PO_4 , хромат Калію K_2CrO_4 , лимонну кислоту $C_6H_8O_7$, етилендіамін $C_2H_8N_2$ (всі реагенти марки х.ч.), дистильовану воду.

Синтезу ВНЧ здійснювали за методикою, описаною в роботі [22], яка ґрунтуються на підході [24]. Наважку 1,05 г лимонної кислоти розчиняли в дистильованій воді (10 см^3); далі додавали аліковоту 0,33 cm^3 етилендіаміну. Потім розчин виливали в герметичний реактор і нагрівали за 200°C впродовж 5 год. Згідно з даними ПЕМ-аналізи високої роздільчої здатності, за цих умов утворюються наночастинки (8–12 нм). Концентрацію ВНЧ у розчині визначали випаровуванням води з подальшим зважуванням на вагі. Приготований розчин використовували як добавку до щавлевого електроліту; частину розчину зберігали протягом 2 місяців.

Методи досліджень. Спектри комбінаційного розсіяння одержували за кімнатної температури в режимі зворотнього розсіяння на потрійному раманівському спектрометрі T-64000 Horiba Jobin-Yvon (Horiba scientific), оснащенному ПЗС-детектором з електричним охолодженням, з використанням методу лазерного динамічного розсіяння світла. Для збудження використовували лінію Ar-Kr-йонного лазера з довжиною хвилі у 488 нм. Збуджене випромінення фокусувалося на поверхні зразка за допомогою оптичних об'єктивів $\times 50$, що давало лазерну пляму діаметром близько 1 мкм. ІЧ-спектри реєстрували за допомогою ІЧ-спектрометра Spectrum BX (PerkinElmer Instruments, США).

Перед електрохемічним експериментом розчин активували ультразвуком із частотою у 30 кГц упродовж 10 хвилин за допомогою ультразвукової ванни (Bandelin, Угорщина).

Анодування. В експерименті використовували алюмінійову фолію товщиною у 0,1 мм і вмістом алюмінію у 99,97%. Крім цього, вихідний алюміній містив домішки Феруму, Силіцію та Купруму (по 0,1 ат.% кожного). Перед анодуванням фолію відпалювали за 500°C впродовж 2 годин, обробляли ультразвуком, промивали C_2H_5OH , а потім на одну сторону фолії наносили маску з фоторезисту. Плівковий фоторезист RISTON накладали на поверхню для одержання малюнка. Щільний захисний шар оксиду Алюмінію щавили за допомогою 5 М $NaOH$, далі промивали водою [21].

Вертикальну електрохемічну комірку було розділено на два відділення алюмінійовою фолією (анодною). Електроліт (0,3 М щавлева кислота), температуру якого підтримували на рівні 10°C, циркулював через відділення анодного щавлення. Платинову катоду було розташовано безпосередньо навпроти аноди. Анодування проводилося за напруги у 40 В; попередньо подавався імпульс у 100 В (для видалення неалюмінійових домішок).

З використанням однокомпонентного електроліту щавлевої кислоти окиснення алюмінію проводили в два етапи [17]. Після першого етапу анодного щавлення видаляли бар'єрний шар АOA 6% -розчином H_3PO_4 , що містив також H_2CrO_4 . Другу стадію анодування проводили в електроліті такого ж складу. У випадку використання в якості електроліту двокомпонентного розчину, що містить $H_2C_2O_4$ та ВНЧ, процес анодування включав лише одну стадію анодування. Для видалення залишкового алюмінію в отворах маски пластину АOA обробляли розчином $CuCl_2$ в концентрованій HCl . Розчин H_3PO_4 використовувався для видалення шару оксиду Алюмінію на дні пор для одержання наскрізних каналів.

Одержані зі змішаного електроліту АOA обробляли гідротермально за тиску у 2 бар і температури у 200°C. Для дослідження фазових перетворень проводили реєстрацію рентгенограми на дифрактометрі ДРОН-3М (ЛОМО, Росія) із зовнішніми стандартами SiO_2 (стандарт 20) і Al_2O_3 (стандарт інтенсивності). Дослідження проводили з Си-анодою із довжиною хвилі рентгенівського випромінення у 0,154178 нм з використанням Ni-фільтра.

Для дослідження морфології АOA використовували растрові електронні мікроскопи: SEO-SEM Inspect S50-B (Сумський завод «Електронна оптика») і Tescan Mira 3LMU (TESCAN, Чехія). Попередньо зразки АOA були покриті ультратонким шаром срібла.

Адсорбційні властивості АOA вивчали в стаціонарних умовах. Готовали розчин, що містив 0,0068 мг·см⁻³ ВНЧ, і розбавляли його для одержання зразків для UV-Vis-мірянь (калібрувальної кривої). Спектри записували на спектрофотометрі Shimadzu UV-VIS mini 1240 (Shimadzu, Японія) в діапазоні 200–600 нм; базова лінія відповідала дейонізованій воді. Калібрувальну лінію було побудовано на основі даних екстинкції для 350 нм. Далі зважені зразки АOA витримували в 50 см³ розчину ВНЧ впродовж 24 год. Після аналізи рідин розраховували адсорбційну місткість (A) за формулою

$$A = \frac{V_s(C_i - C)}{m},$$

де C_i і C — початкова та кінцева концентрації, V — об'єм розчину, m — маса адсорбенту.

Перед проведенням мірянь методом лазерного розсіяння для розбиття агрегованих частинок розчин ВНЧ піддавали впливу ультразвуку.

3. РЕЗУЛЬТАТИ ТА ЇХ ОБГОВОРЕННЯ

Як було встановлено раніше, розмір ВНЧ становить 8–12 нм [22]; водний колоїдний розчин має темно-жовтий колір. Люмінесценція спостерігається в темноті із УФ-випроміненням (рис. 1).

Під час старіння відбувається агрегування, і діаметер ВНЧ знаходиться у діапазоні 150–250 нм (рис. 2). У колоїдному розчині переважають агрегати, діаметер яких становить 200 нм.

На УФ-спектрах спостерігаються максимум поглинання для 200 нм, який пов'язаний з $\pi-\pi^*$ -переходом атомових С–С-зв'язків, і пік для 350 нм, зумовлений $n-\pi^*$ -переходами ароматичних С–С-зв'язків (рис. 3). Інтенсивність піків зменшується зі зменшенням концентрації розчину. Калібрувальну криву було побудовано для максимуму для 350 нм. Оскільки залежність є



Рис. 1. Люмінесценція ВНЧ у УФ-випроміненні.¹

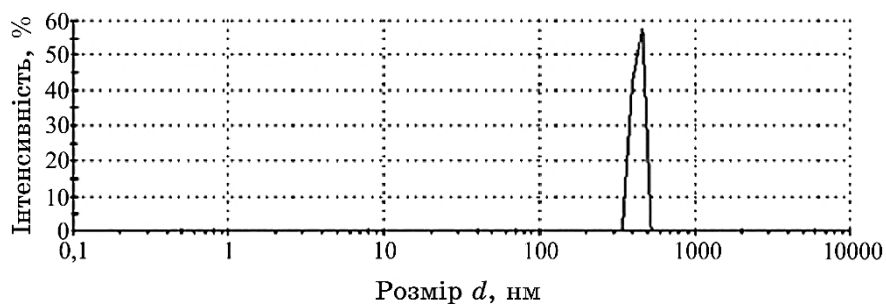


Рис. 2. Розподіл за розмірами агрегованих частинок ВНЧ.²

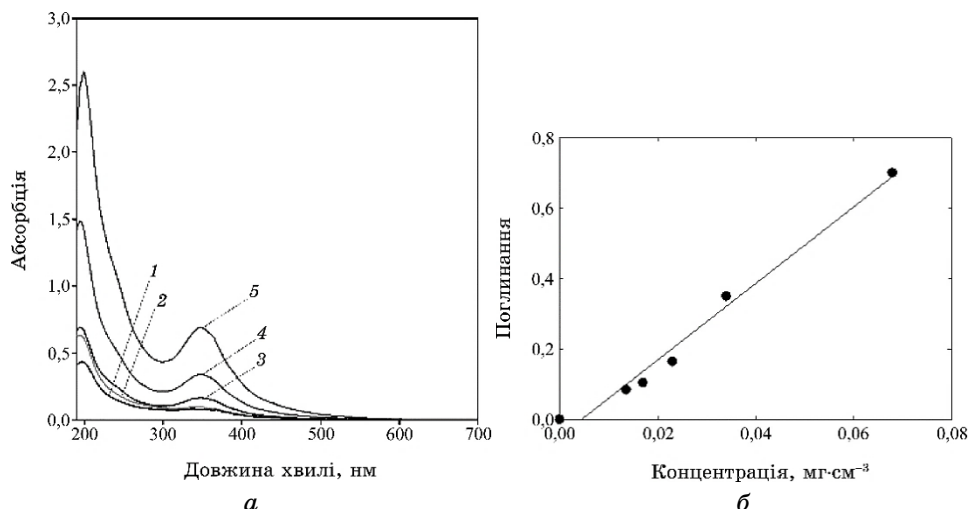


Рис. 3. Спектри розчинів ВНЧ, позначені цифрами, $\text{мг}\cdot\text{см}^{-3}$ (а): 1 — концентрація 0,0136; 2 — концентрація 0,017; 3 — концентрація 0,023; 4 — концентрація 0,034; 5 — концентрація 0,068; (б) калібрувальна крива.³

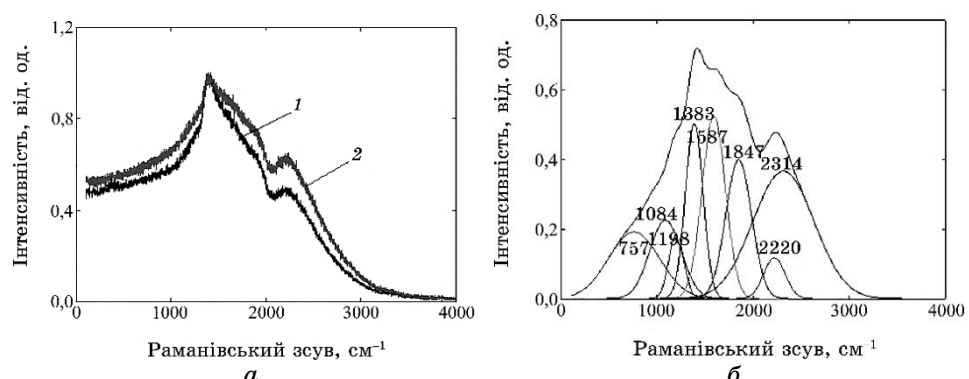


Рис. 4. Раманівські спектри ВНЧ (1) та АОА (2), одержані в електроліті, що містить ВНЧ (а); деконволюція спектру для останнього зразка (б).⁴

лінійною, можна визначити концентрацію ВНЧ.

Спектр комбінаційного розсіяння для АОА демонструє два асиметричних піки для 1383 і 2220 см^{-1} (рис. 4). Перший пік, вочевидь, пов'язаний зі структурою вуглецю. Оскільки метод синтезу передбачає формування легованої Нітрогеном структури графену [24], то другу смугу зумовлено коливаннями іонізованих аміногруп [25]. Вони можуть бути приєднані до площини графе-

ну через аліфатичні вуглеводневі ланцюги під час карбонізації. Асиметрія піків і видимих плечей уможливлює провести деконволюцію спектрів (рис. 4).

Після деконволюції спектр містить кілька піків. Найбільш інтенсивні смуги відносяться до смуг D (1383 см^{-1}) і G (1587 см^{-1}) [26]. D -смугу зумовлено режимами фононного дихання, спричиненими вуглецевими вакансіями. Смуга G є результатом вироджених E_{2g} -фононних мод вуглецевих sp^2 -зв'язків. Піки невпорядковані; відношення їхніх інтенсивностей становить 0,96, що свідчить про велику кількість дефектів, зумовлених легуванням Нітроген- і Оксигенвмісними функціональними групами. Смуги, які спостерігаються за менших значень зсуву комбінаційного розсіяння, зумовлено впливом підкладинки (SiO_2) та функціональних груп (карбокси-, епоксидних і фенольних). Піки, що знаходяться за більш високих значень зсуву, зумовлено валентними коливаннями аміногруп.

Широкий пік ІЧ-спектру в інтервалі $4000\text{--}3000 \text{ см}^{-1}$ зумовлений коливаннями H_2O , а також OH , CH і NH (NH_4^+ і пірольних) груп (рис. 5). CH_2 -групи відносяться до смуг для 2930 см^{-1} і 2858 см^{-1} (Оксиген- і Нітрогенвмісні групи можуть бути приєднані до площин графену саме через ці групи); коливання для 2367 см^{-1} , очевидно, пов'язане зі зв'язком Карбон–Нітроген [25]. Пік для 1722 см^{-1} зумовлений карбонілом карбоксильних груп; смуга для 1620 см^{-1} зумовлена вуглецевим каркасом, тобто С–С-коливаннями. Карбоксильні та фенольні групи відносяться до смуг для 1401 і 1257 см^{-1} ; епоксидні групи відповідають за пік для 1070 см^{-1} . Піридин дає максимум для 1200 см^{-1} ; смуга для 1560 см^{-1} належить піролу.

На рисунку 6 показано нижній бік АOA з бар'єрним шаром (з порожньої сторони електрохемічної комірки) до видалення неокисненого алюмінію. Видно нерівномірні опукlosti, які в першому наближенні є сферичними. Їхній розмір становить $75\text{--}100 \text{ нм}$. Трохи менші опукlosti спостерігаються для зразка, одержаного в присутності ВНЧ.

Додавання ВНЧ до щавлевого електроліту впливає на пори

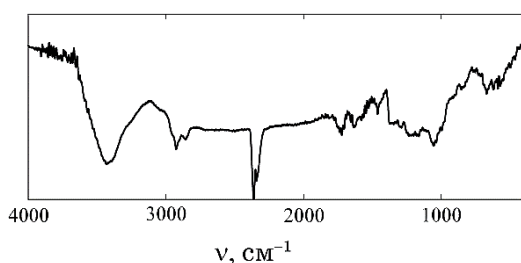


Рис. 5. Інфрачервоний спектр НЧ.⁵

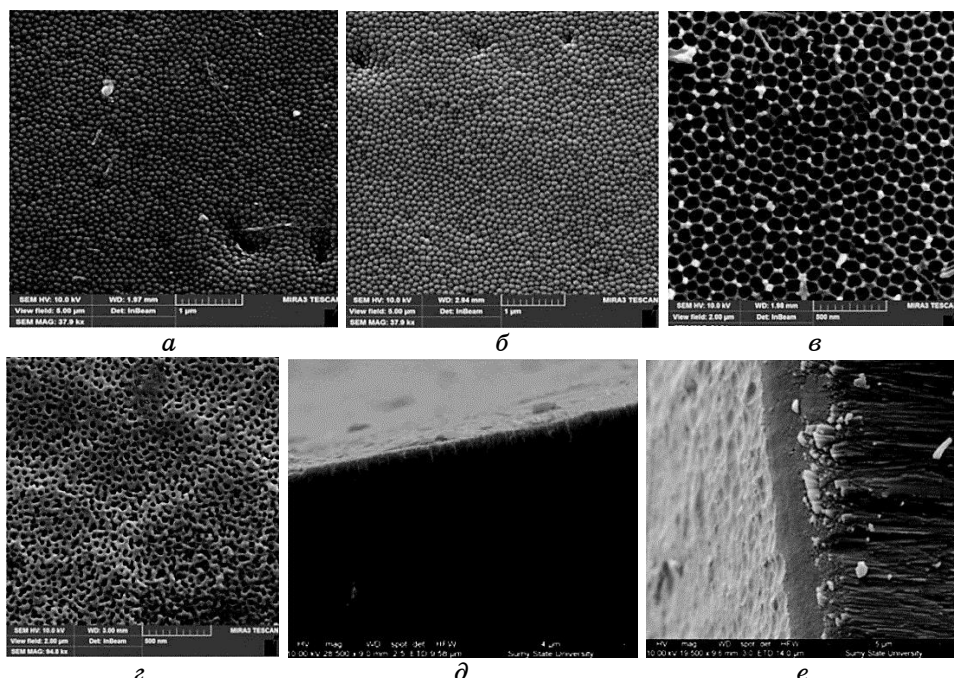


Рис. 6. Нижній бік до видалення залишкового алюмінію (*а, б*), верхній бік (*в, г*) та поперечний переріз (*д, е*) АОА, синтезованого з використанням чистого $\text{H}_2\text{C}_2\text{O}_4$ (*а, в, д*) і колоїдного розчину ВНЧ у $\text{H}_2\text{C}_2\text{O}_4$ (*б, г, е*).⁶

АОА. Для зразка, одержаного без ВНЧ, комірчасту пористу структуру видно з боку поверхні, що контактувала з електролітом. Форма пор є гексагональною; сторона гексагону має довжину у 23 нм. Діаметр пор — 50–100 нм; переважають пори найбільшого розміру. Стінки пор мають товщину близько 30 нм.

Під час синтезу зразків у змішаному електроліті видно менші пори більш неправильної форми. Розмір пор становить 20–40 нм, товщина стінок пор — до 50 нм. У поперечному перерізі видно стрижні, які розташовані близько один до одного. Порожнини між цими стрижнями відповідають наскрізним і прямим порам. У випадку зразків, одержаних у двокомпонентному електроліті, стрижні товщі. Це свідчить про товстіші стінки пор, оскільки пори цього АОА є меншими порівняно зі зразком, синтезованим в однокомпонентному електроліті.

Вплив ВНЧ можна пояснити, беручи до уваги механізми формування пористої структури АОА. Коли наночастинки адсорбуються на поверхні гідратованих оксидів, вони, ймовірно, здатні впливати на розмір пор (адсорбція підтверджується подібністю спектрів комбінаційного розсіяння ВНЧ і АОА; див. рис. 4, *a*).

Наприклад, теорія Богоявленського пропонує розглядати АOA як колоїдний об'єкт, а саме, як гель [17]. На аноді формуються активні центри, де зароджуються майбутні міцели. Вони збільшуються та перетворюються на полійони, які є волокнистими паличкоподібними міцелами. Ці міцели є основою скелету оксидного гелю. Міцели заряджаються негативно внаслідок адсорбції аніонів. Позитивний заряд аміногруп ВНЧ забезпечує адсорбцію наночастинок вуглецю на оксиді за рахунок електростатичної взаємодії. Це посилює екранування поверхні алюмінійових електродів. Дійсно, струм під час анодування зменшується з 40 до 35 mA (за відсутності ВНЧ в електроліті) і до 20 mA (за присутності ВНЧ).

Згідно з моделем пластичного потоку за Томпсоном, який згадується в [17], іони O^{2-} мігрують до межі поділу метал–розвчин під час анодування. Екранування частинок АOA за допомогою ВНЧ обмежує міграцію, тобто окиснення алюмінію.

Металевий алюміній, оксид Алюмінію та графен характеризуються різними значеннями теплопровідності [$\text{Вт}\cdot\text{м}^{-1}\cdot\text{К}^{-1}$]: 247 (Al), 35 (кристалічний Al_2O_3), 5000 (графен). Коефіцієнти теплового розширення становлять $2,3\cdot 10^{-5}$ і $8,4\cdot 10^{-6}\text{ K}^{-1}$ для Al і Al_2O_3 відповідно. Графену притаманне від'ємне теплове розширення ($-3,2\text{--}3,8\cdot 10^{-6}\text{ K}^{-1}$). Це означає, що адсорбовані наночастинки вуглецю є «демпферами», які запобігають розтріскуванню оксиду внаслідок інтенсивнішого нагрівання алюмінію під час анодування.

Крім спектрів комбінаційного розсіяння (рис. 4), поглинання ВНЧ поверхнею АOA підтверджується адсорбційними даними (рис. 7). Встановлено, що ізотерма поглинання описується рівнянням Тьюмкіна:

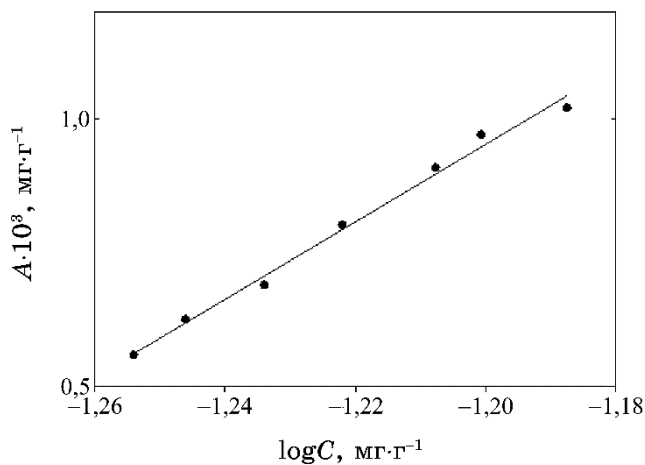


Рис. 7. Ізотерма адсорбції ВНЧ у Тьюмкінових координатах.⁷

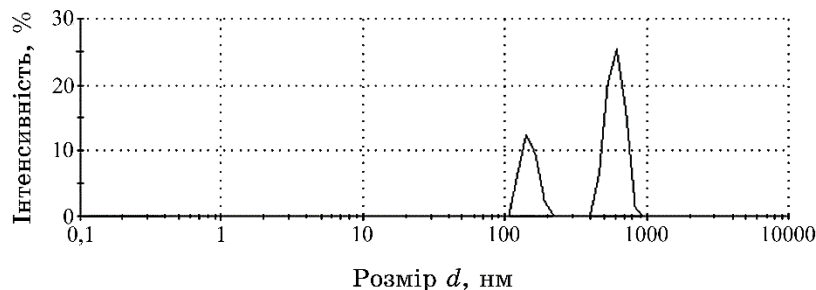


Рис. 8. Розподіл за розмірами агрегованих частинок ВНЧ у розчині, що містив дисперсний АОА.⁸

$$A = \frac{2,3a_{\max}}{f} \log bC,$$

де f — коефіцієнт поверхневої неоднорідності, b — константа, що відображає теплоту адсорбції, a_{\max} — максимальна місткість (на дату експерименту — $0,0011 \text{ мг}\cdot\text{г}^{-1}$).

Згідно з моделем Тьюмкіна, в першу чергу адсорбція відбувається на більш ненасичених центрах з максимальним виділенням тепла. Потім заповнюються центри зі слабшою адсорбційною здатністю. З переходом від більш до менш ненасичених центрів теплота адсорбції зменшується експоненційно. Як було знайдено, $f = 0,35$, $b = 20$. Це свідчить про достатньо високу гетерогенність поверхні АОА, яка включає як амфотерний оксид, так і оксалат-йони.

Агреговані наночастинки вуглецю також адсорбуються АОА, що підтверджено методом динамічного лазерного розсіяння (рис. 8). Частинки АОА, які були дисперговані за допомогою ультразвуку, мають розмір у 110–130 нм. Пік, який відповідає агрегатам, зміщується в область більших значень (від 150–250 до 200–800 нм). У розчині переважають частинки розміром у 300 нм.

4. ВИСНОВКИ

Додавання ВНЧ до щавлевого електроліту забезпечує зменшення розміру пор анодно-окисненого алюмінію. ВНЧ впливають на формування пористої структури АОА аналогічно до ОГ [21]. Переягою ВНЧ над ОГ є одержання АОА з меншими порами в м'яких умовах без агресивних реагентів. Вплив ВНЧ на пористу структуру АОА можна пояснити, з одного боку, її екрануванням наночастинками вуглецю, а з іншого — «амортизувальною дією» ВНЧ на більш швидке терморозширення алюмінію порівняно з Al_2O_3 .

Таким чином, можна одержати зразки АОА з нанорозмірними порами шляхом екологічно чистої синтези з використанням дешевих і доступних хемічних реагентів. Для одержання кристалічного Al_2O_3 може бути реалізовано гідротермальну синтезу, перевагою якої над прожарюванням є нижча температура кристалізації.

ЦИТОВАНА ЛІТЕРАТУРА—REFERENCES

1. K. A. Evans, *Properties and Uses of Aluminium Oxides and Aluminium Hydroxides* (Ed. A. J. Downs) (London—New York: Pergamon Press: 1993), p. 993.
2. H. K. Hami, R. F. Abbas, E. M. Eltayef, and N. I. Mahdi, *Samarra J. Pure Appl. Sci.*, **2**: 19 (2020); <https://doi.org/10.54153/sjpas.2020.v2i2.109>
3. M. Pica, *Molecules*, **26**: 2392 (2021); <https://doi.org/10.3390/molecules26082392>
4. Y. S. Dzyazko, L. M. Rozhdestvenska, and A. V. Palchik, *Sep. Pur. Techn.*, **45**: 141 (2005).
5. A. V. Pal'chik, Yu. S. Dzyaz'ko, and L. M. Rozhdestvenskaya, *Russ. J. Appl. Chem.*, **75**: 414 (2005).
6. T. V. Maltseva, E. O. Kudelko, and V. N. Belyakov, *Russ. J. Phys. Chem. A*, **83**: 2336 (2009).
7. T. V. Mal'tseva, T. V. Yatsenko, E. O. Kudelko, and V. N. Belyakov, *Russ J. Appl. Chem.*, **84**: 756 (2011).
8. T. V. Mal'tseva, A. V. Pal'chik, E. O. Kudelko, S. L. Vasiliuk, and K. A. Kazdobin, *J. Water Chem. Techn.*, **37**: 18 (2015); <https://doi.org/10.3103/S1063455X15010051>
9. X.-M. Wang, X.-Y. Li, and K. Shih, *J. Membr. Sci.*, **368**: 134 (2011); <https://doi.org/10.1016/j.memsci.2010.11.038>
10. T. A. Saleh and V. K. Gupta, *Sep. Purif. Tech.*, **89**: 245 (2012); [doi:10.1016/j.seppur.2012.01.039](https://doi.org/10.1016/j.seppur.2012.01.039)
11. M. Branchi, M. Sgambetterra, I. Pettiti, S. Panero, and M. A. Navarra, *Inter. J. Hydr. Ener.*, **40**: 14757 (2015); [doi:10.1016/j.ijhydene.2015.07.030](https://doi.org/10.1016/j.ijhydene.2015.07.030)
12. V. Myronchuk, Yu. Zmievskii, Yu. Dzyazko, L. Rozhdestvenska, and V. Zakharov, *Acta Periodica Techn.*, **49**: 103 (2018); <https://doi.org/10.2298/APT1849103M>
13. Yuliya Dzyazko, Liudmyla Rozhdestveskaya, Yurii Zmievskii, Yurii Volkovich, Valentin Sosenkin, Nadejda Nikolskaya, Sergey Vasiliuk, Valerii Myronchuk, and Vladimir Belyakov, *Mater. Today: Proceed.*, **2**: 3864 (2015); [doi:10.1016/j.matpr.2015.08.003](https://doi.org/10.1016/j.matpr.2015.08.003)
14. V. G. Myronchuk, Y. S. Dzyazko, Yu. G. Zmievskii, A. I. Ukrainets, A. V. Bildukevich, L. V. Kornienko, L. M. Rozhdestvenskaya, and A. V. Palchik, *Acta Periodica Techn.*, **47**: 153 (2016); <https://doi.org/10.2298/APT1647153M>
15. Y. S. Dzyazko, L. M. Rozhdestvenska, S. L. Vasiliuk, K. O. Kudelko, and V. N. Belyakov, *Nanoscale Res. Let.*, **12**: 1 (2017); [doi:10.1186/s11671-017-2208-4](https://doi.org/10.1186/s11671-017-2208-4)
16. S. Szabolcs, V. Fehér, D. Kurhan, A. Németh, M. Sysyn, and S. Fischer,

- Infrastructures*, **8**: 1 (2023);
<https://doi.org/10.3390/infrastructures8020027>
17. L. Rozhdestvenska, K. Kudelko, V. Ogenko, and M. Chang, *Ukr. Chem. J.*, **86**: 67 (2021); <https://doi.org/10.33609/2708-129X.86.12.2020.67-102>
18. R. Kavian, A. Vicenzo, and M. Bestetti, *J. Mater. Sci.*, **46**: 1487 (2011);
<doi:10.1007/s10853-010-4950-1>
19. L. Zaraska, E. Kurowska, G. D. Sulka, I. Senyk, and M. Jaskula, *J. Solid State Electrochem.*, **18**: 36 (2014); <https://doi.org/10.1007/s10008-013-2215-z>
20. G. Yongji, X. Mingyang, and Z. Jinlong, *Appl. Surf Sci.*, **319**: 8 (2014);
<doi:10.1016/j.apsusc.2014.04.182>
21. K. Kudelko, L. Rozhdestvenskaya, V. Ogenko, and V. Chmilenko, *Appl. Nanosci.*, **12**: 1967 (2022); <https://doi.org/10.1007/s13204-022-02457-y>
22. V. Ogenko, S. Orlysyk, L. Kharkova, O. Yanko, and D. Chen, *Ukr. Chem. J.*, **87**: 3 (2021); <https://doi.org/10.33609/2708-129X.87.09.2021.3-13>
23. A. Perrotta, *Mat. Res. Innovat.*, **2**: 33 (1998);
<https://doi.org/10.1007/s100190050058>
24. J. Schneider, C. J. Reckmeier, Y. Xiong, M. von Seckendorff, A. S. Susha, P. Kasák, and A. L. Rogac, *J. Phys. Chem. C*, **121**: 2014 (2017);
<doi:10.1021/ACS.JPCC.6B12519>
25. Kazuo Nakamoto, *Infrared and Raman Spectra of Inorganic and Coordination Compounds* (USA: John Wiley & Sons, Inc., Publication: 1997);
<https://download.e-bookshelf.de/download/0000/5722/69/L-G-0000572269-0002357953.pdf>
26. I. Childres, L. A. Jauregui, W. Park, H. Cao, and Y. P. Chen, *Raman Spectroscopy of Graphene and Related Materials*. In: *New Developments in Photon and Materials Research* (Ed. J. I. Jang) (Nova Science: 2013), pp. 1–20.

¹V. I. Vernadsky Institute of General and Inorganic Chemistry, N.A.S. of Ukraine,
 32/34, Acad. Palladin Ave.,
 UA-03141 Kyiv, Ukraine

²Taras Shevchenko National University of Kyiv,
 64/13, Volodymyrska Str.,
 UA-01601 Kyiv, Ukraine

¹ Fig. 1. Luminescence of CNPs under UV radiation.

² Fig. 2. Distribution according to the size of aggregated particles of CNPs.

³ Fig. 3. Spectra of CNPs' solutions marked with numbers [mg·cm⁻³] (a): 1—concentration 0.0136; 2—concentration 0.017; 3—concentration 0.023; 4—concentration 0.034; 5—concentration 0.068; (6) calibration curve.

⁴ Fig. 4. Raman spectra of CNPs (1) and AOA (2) obtained in an electrolyte containing CNPs (a); deconvolution of the spectrum for the last sample (6).

⁵ Fig. 5. Infrared spectrum of NPs.

⁶ Fig. 6. Lower side before removal of residual aluminium (a, 6), upper side (e, ε) and cross section (δ, e) of AOA synthesized using pure H₂C₂O₄ (a, e, δ) and colloidal solution of CNPs in H₂C₂O₄ (6, ε, e).

⁷ Fig. 7. Isotherm of adsorption of CNPs in Temkin's co-ordinates.

⁸ Fig. 8. Size distribution of aggregated particles of CNPs in a solution containing dispersed AOA.

PACS numbers: 61.80.Ba, 61.82.Rx, 77.84.Cg, 78.67.Rb, 81.16.Pr, 81.20.Fw, 82.50.Hp

Структурні та фотохемічні характеристики гібридних кatalізаторів $\text{TiO}_2/\text{SiO}_2$ /міковоластоніт, одержаних золь– гель-методом

О. В. Зінченко, В. Д. Єжова, О. Л. Толстов

Інститут хімії високомолекулярних сполук НАН України,
Харківське шосе, 48,
02155 Київ, Україна

Фотоактивні $\text{TiO}_2/\text{SiO}_2$ -композити одержано *in situ* золь–гель-методом шляхом осадження суміші $\text{TiO}_2 \cdot x\text{H}_2\text{O}$ та $\text{SiO}_2 \cdot y\text{H}_2\text{O}$ на поверхню мікронізованого природного CaSiO_3 (воластоніту) з їхньою подальшою конденсацією. Подальше температурне оброблення композитного шару сприяє сполученню ортоокислот і формуванню наноструктурованих матеріалів. Використання SiO_2 -вмісних сполук, зокрема органосиланів і Калій силікату, що відіграють роль сполучників і структурних модифікаторів фази TiO_2 , забезпечує формування гібридних дисперсних катализаторів, будову яких підтверджено даними ГЧ-Фур'є-спектроскопії. За даними рентгенофазової аналізу встановлено формування фази нанокристалічного TiO_2 анатазної кристалічної модифікації, вміст якої перевищує 70%. Дані порометрії свідчать, що наноструктуровані зразки є мікропористими матеріалами з питомою поверхнею у $60\text{--}225\text{ m}^2\cdot\text{g}^{-1}$ і об'ємом мікропор від 2 до $30\text{ mm}^3\cdot\text{g}^{-1}$. Оцінка ефективності одержаних композитних фотокatalізаторів у лабораторних умовах під опроміненням УФ-світлом у динамічних умовах та у реальних умовах у статичному режимі під опроміненням сонячним і розсіяним денним світлом продемонструвала їхню високу фотохемічну активність в реакції окиснення барвників метиленового блакитного (МБ) та нігрозину. Для фотокatalізаторів під опроміненням УФ-світлом характерно є висока швидкість деструкції (v_{cp}) барвника МБ, що сягає $7,2\text{ }\mu\text{моль}\cdot\text{г}^{-1}\cdot\text{год}^{-1}$. У випробуванні фотокatalітичної активності композитів у вигляді покріттів, нанесених на інертний субстрат, було показано, що одержані покріття під дією сонячного освітлення демонструють величину v_{cp} близько $0,115\text{ }\mu\text{моль}\cdot\text{см}^{-2}\cdot\text{добра}^{-1}$ (для МБ) і до $0,06\text{ }\mu\text{моль}\cdot\text{см}^{-2}\cdot\text{добра}^{-1}$ (для промислового барвника нігрозину). Одержані результати свідчать про можливість практичного використання одержаних фотокatalізаторів для виготовлення пристрійв для очищення стічних вод від органічних забруднювачів, а також для одержання покріттів, здатних до са-

моочищення для внутрішнього та зовнішнього застосування.

Photoactive $\text{TiO}_2/\text{SiO}_2$ composites are fabricated *via in situ* sol-gel approach by deposition of as-prepared mixture of orthotitanic ($\text{TiO}_2 \cdot x\text{H}_2\text{O}$) and orthosilicic ($\text{SiO}_2 \cdot y\text{H}_2\text{O}$) acids onto a surface of micronized natural mineral CaSiO_3 (wollastonite) followed by their condensation. Thermal treatment of the raw composite layer activates deep condensation of orthoacids and leads to the formation of nanostructured composite materials. Using SiO_2 precursors, namely, organosilicon compounds and potassium silicate playing the role of binders and structure modifiers of TiO_2 phase, provides the formation of hybrid-powdered catalysts. The hybrid structure of the composite catalysts is considered by FTIR spectroscopy. The results of WAXS demonstrate an appearance of nanocrystalline TiO_2 anatase phase with crystalline phase content of up to 70%. Porosity measurements of the composites show a formation of nanostructured materials with well-defined microporous structure, which is characterized by surface area in the range of $60\text{--}225 \text{ m}^2\cdot\text{g}^{-1}$ and micropore volume of $2\text{--}30 \text{ mm}^3\cdot\text{g}^{-1}$. Evaluation of efficacy of produced composite photocatalysts in laboratory conditions under the dynamic regime and irradiation by UV-light as well as in environmental conditions in the static regime and under irradiation by direct solar light or scattered daylight demonstrate high photochemical activity in the oxidation reaction of methylene blue (MB) and nigrosine dyes. The photocatalysts are characterized by a high degradation rate (v_{av}) of MB dye under UV-illumination that reaches $7.2 \text{ }\mu\text{mol}\cdot\text{g}^{-1}\cdot\text{hr}^{-1}$. Testing the photocatalytic coatings fabricated by spray-drying approach of powdered catalysts on inert substrate demonstrates appropriate activity as well. The degradation rate (v_{av}) value of the coatings under direct solar-light illumination reaches $0.115 \text{ nmol}\cdot\text{cm}^{-2}\cdot\text{day}^{-1}$ (for MB dye) and $0.06 \text{ nmol}\cdot\text{cm}^{-2}\cdot\text{day}^{-1}$ (for industrial nigrosine dye). Thus, the results evidence of perspectives of practical uses of produced photocatalysts for manufacturing of cartridges for purification and decontamination of wastewater as well as for producing self-cleaning coatings for internal and external uses.

Ключові слова: TiO_2 , воластоніт, композити, структура, властивості, фотокаталітичне очищення.

Key words: TiO_2 , wollastonite, composites, structure, properties, photocatalytic decontamination.

(*Отримано 15 червня 2023 р.*)

1. ВСТУП

Розробка нових високодисперсних фотохемічно активних матеріалів і покріттів на їхній основі є актуальним завданням впродовж багатьох років [1–3]. Незважаючи на тенденцію пошуку нових катализаторів на основі сполук Ti, Zn, Cd, Ce, Bi, W, Mo та

ін., найбільша увага незмінно надається фотокatalізаторам на основі TiO_2 , його комбінації з модифікаторами (Au, Ag, Pt, Pd, N, Si), іншими функціональними сполуками, а також гіbridним матеріялам на його основі [3–5].

Серед низки гібридних матеріалів на основі TiO_2 , композити $\text{TiO}_2/\text{SiO}_2$ мають найбільші перспективи застосування завдяки хемічній стабільноті, спрощеній технології одержання та високій фотохемічній активності. В процесі фотокаталітичної деструкції разом з мінералізацією також відбувається часткове окиснення та гідрофілізація органічних речовин, що поліпшує ефективність поверхонь, здатних до самоочищення. Водночас додавання до складу фотокаталізаторів SiO_2 зберігає достатній рівень гідрофільності поверхні каталізаторів внаслідок високої щільності $=\text{Si}-\text{OH}$ -груп [6, 7]. Гібридні покриття $\text{TiO}_2/\text{SiO}_2$, одержані золь-гель-методом, мають підвищено кислотність внаслідок наявності структурних фрагментів SiO_4 , що сприяє поліпшенню адсорбції радикалів OH^* та іонів OH^- і зростанню гідрофільності їхньої поверхні [8]. Як результат, активується процес сорбції молекул H_2O та десорбції продуктів руйнування органічних сполук-забруднювачів. Підвищити гідрофільність фотокаталізаторів також можна, збільшуючи густину поверхневих OH -груп під час модифікування TiO_2 сполуками Al та Zn .

Додатковою функцією SiO_2 в процесі утворення TiO_2 -вмісних композитів є контроль реакції конденсації й росту наночастинок TiO_2 . В результаті взаємодії між $=\text{Ti}-\text{OH}-$ і $=\text{Si}-\text{OH}$ наночастинок гідратованих олігомерних форм відповідних ортокислот відбувається утворення гібридних зв'язків $=\text{Ti}-\text{O}-\text{Si}=$, що в подальшому підвищує фотоактивність нанокристалів TiO_2 . Крім того, олігомери ортокремнійової кислоти виконують функцію сполучного, що з'єднує нанокристали TiO_2 , а їхні аморфна структура та полідисперсність підвищують пористість і поліпшують доступність каталітичних центрів таких композитів у фотокatalітичних процесах [9]. Цей процес позитивно впливає на питому поверхню та кількість каталітичних центрів $\text{TiO}_2/\text{SiO}_2$ -композитів. Такий підхід до створення фотокatalізаторів з кристалічною фазою TiO_2 , що мають невпорядковану будову як результат сполучення складових різної природи та функціональності [10], є відомим і широко використовується для підвищення фотохемічної активності композитних каталізаторів.

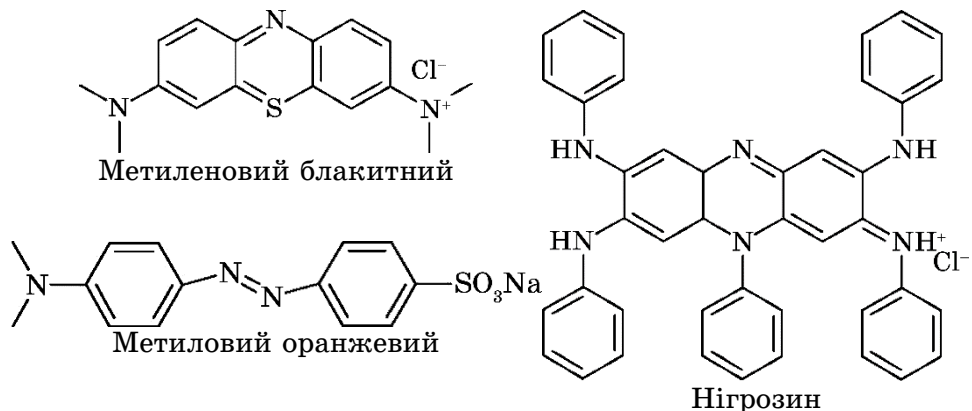
Перспективність використання SiO_2 для створення фотокatalізаторів відображену у великій кількості досліджень з цієї проблематики [3, 5, 11–14]. Активного розвитку воднораз набув новий підхід із заміною широко застосованих нестабільних органічних похідних Силіцію [15] на стабільні неорганічні модифікати [16], штучні SiO_2 -вмісні матеріали (пірогенний SiO_2 , силіка́гелі

лі, аерогелі, скло) [7, 17, 18] та природні силікатні мінерали — глини, бентоніти, шпати, цеоліти, кварц [19–22]. Важливими перевагами субстратів природнього походження є можливість ефективного використання TiO_2 за його осадження на субстрат у вигляді тонкого шару та, за потреби, модифікування поверхні субстрату. Зокрема, введення $\text{TiO}_2/\text{SiO}_2$ композиту в цементну суміш надає їй помітні фотокatalітичні властивості, а сполучення кількох компонентів з різними функціями (конструкційними, в'язальними, каталітичними, захисними тощо) поліпшує стабільність фотокatalітичних поверхонь до впливу кліматичних чинників [19]. Дисперсні композити $\text{TiO}_2/\text{SiO}_2$, одержані піролізою з біогенного SiO_2 , демонструють задовільну ефективність деструкції органічних забруднювачів [20]. Контрольоване осадження шару TiO_2 на природні алюмосилікати уможливлює одержати шаруваті каталізатори для очищення кислотних стічних вод [21]. Автори багатьох робіт відзначають, що мінеральні субстрати не погіршують фотохемічні характеристики каталізаторів, натомість дають змогу застосувати відомі способи модифікування TiO_2 для підвищення активності фотокatalізаторів, в тому числі у видимій області спектру [22]. Але слід зазначити відомий факт, що деякі неорганічні сполуки та йони, наприклад Na^+ , що присутні в більшості природніх мінералів, здатні погіршувати фотохемічні властивості TiO_2 -вмісних каталізаторів [23, 24]. Одним з природніх субстратів з високим потенціалом застосування для одержання фотокatalізаторів є мінерал воластоніт — природній CaSiO_3 , що не містить іонів Na^+ , натомість може містити слідові кількості інших елементів (Fe , Mg , Mn), що можуть бути потенційними модифікаторами кінцевих fotoактивних систем. Формування зовнішнього шару на поверхні інертних природніх носіїв має й економічне підґрунтя, оскільки уможливлює спростити метод одержання та зменшити витрату компонентів, призначених для створення каталізаторів, із збереженням їхньої ефективності.

В більшості досліджень для визначення фотохемічної активності каталізаторів використовують стандартні (модельні) органічні забруднювачі — водорозчинні барвники: метиленовий блакитний (МБ), метиловий оранжевий, родамін тощо, що уможливлює спростити вивчення процесів фотохемічного окиснення під дією фотокatalізаторів. Але ці барвники не є еталонними сполуками-забруднювачами, оскільки, по-перше, не завжди зустрічаються у відходах промисловості та, по-друге, завдяки особливостям хемічної будови, зокрема здатності до окиснення у достатньо м'яких умовах, повноцінно не відтворюють потенційні можливості каталізаторів. На відміну від «еталонних» барвників, є потенційно небезпечні органічні сполуки, що активно використовуються в промислових процесах і появя яких у природному середовищі

нese потенційну шкоду довкіллю. Однією з таких органічних сполук є барвник нігроzin, що є продуктом окиснення аніліну. Завдяки особливій хемічній структурі нігроzin важко піддається глибокій деструкції, особливо в природніх умовах, що є головним критерієм його небезпеки для навколошнього середовища.

Спираючись на сучасні досягнення в області фотоактивних композитів TiO_2/SiO_2 , спрямування матеріалознавства на ресурсозбереження й економічну доцільність промислової синтези композитних каталізаторів, в даній роботі запропоновано спосіб одержання нових гібридних фотокatalізаторів TiO_2/SiO_2 з використанням перспективного природного субстрату — мінералу воластаніту та гідрофільних SiO_2 -вмісних структурних модифікаторів і сполучних, досліджено структурні, сорбційні та фотохемічні характеристики дисперсних композитів, а також перевірено кінетичні параметри фотохемічної активності одержаних каталітично активних наноструктурованих покрійтів у природніх умовах, для чого було застосовано метод УФ-вид-спектроскопії на відбивання.



2. ЕКСПЕРИМЕНТАЛЬНА ЧАСТИНА

Для одержання фотоактивних композитів використали Титан(IV) хлорид $TiCl_4$ (95%) та водний розчин NH_3 (28%). Як вихідні компоненти для одержання гідратованої форми ортоокремнійової кислоти, структурного модифікатора та неорганічного сполучного, було обрано частково гідролізований $(C_2H_5O)_4Si$ (продукт ЕС-40; вміст SiO_2 — 40%) і водний розчин Калій силікату K_2SiO_3 (36%; $K_2O/SiO_2 = 3,05$). Як органічні сполуки-забруднювачі, використовували барвник метиленовий блакитний (МБ) і промисловий барвник, що використовують у шкіряному виробництві, — нігроzin чорний. Як мінеральний субстрат використовували мікронізований природній мінерал воластаніт (B^{MB} ; марка Миволл

15–96; вміст SiO_2 — 49,2% мас.; середній лінійний розмір частинок або діаметер волокон — 12 ± 7 мкм). Як субстрат для покриття фотокatalізатором, використовували очищено цементно-бетонну поверхню — основний тип поверхні промислових і житлових приміщень, придатний для нанесення декоративних і функціональних покріттів.

Дисперсні композитні фотокatalізатори одержано конденсацією гідратованих форм ортотитанової (H_4TiO_4) та ортокремнійової (H_4SiO_4) кислот з подальшим осадженням конденсованого гібридного гідрозолю на поверхню мікронізованого воластоніту. Згідно з методикою, до водного розчину TiCl_4 за інтенсивного перемішування додавали певну кількість розчину амоніаку для часткової нейтралізації суміші; далі вводили воластоніт та ЕС-40 як модифікатор (SiO_2^{EC}), додавали залишкову кількість NH_3 для повної нейтралізації суміші та витримували за 90°C протягом 2 год для завершення процесів конденсації й осадження. За використання модифікатора K_2SiO_3 ($\text{SiO}_2^{\text{K}_2\text{SiO}_3}$) амоніак не використовували внаслідок високої лужності розчину Калій силікату, а інші стадії процесу були аналогічними. Одержані дисперсні композити відділяли центрифугуванням, промивали дистильованою водою для видалення іонів Cl^- , сушили за температури у 90°C та кальцинували за 400°C впродовж 1 год.

Для одержання покріттів до 10% мас. водної дисперсії композитів додавали 5% мас. ЕС-40 і за допомогою методу напорошення наносили потрібний шар покриття на цементно-бетонну поверхню, чергуючи процес нанесення з сушкою (spray drying) за кімнатної температури. За обраних умов одержаний шар покриття мав товщину у 100 ± 20 мкм.

Хемічну будову вихідних складових і композитів вивчали методом ІЧ-спектроскопії на приладі Bruker TENSOR 37 в діапазоні ν від 4000 до 400 cm^{-1} . Рентгенофазову (РФА) структуру композитів досліджено методом ширококутньої рентгенографії з використанням рентгенівської камери IPM-1 і CuK_α -випромінення, монохроматизованого Ni -фільтром, та визначено ступінь кристалічності (X_{kp}) і середній розмір нанокристалів TiO_2 композитів (D_{kp}). Питому поверхню ($S_{\text{піт}}$) й об'єм мікропор ($V_{\text{мікро}}$) зразків композитів оцінювали за методом ВЕТ на аналізаторі KELVIN 1042. Сорбційні характеристики композитів у водному середовищі по відношенню до органічних молекул визначали методом фотометрії шляхом темнової адсорбції 50 мкМ-розчину барвника МБ упродовж 3 год. Адсорбційна місткість дисперсних матеріалів (χ_{MB} [ммоль·г⁻¹]) є важливою характеристикою активності поверхонь фотокatalізаторів.

Фотохемічну активність каталізаторів перевіreno на органічних забруднювачах — барвниках МБ та нігрозині з використан-

ням методу УФ-вид-спектрометрії у режимах поглинання та відбивання. Модельні дослідження фотокatalітичної дії композитів проводили методом фотометрії для $\lambda = 670$ нм за зменшенням концентрації МБ (ΔC_{MB} [нмоль·г⁻¹]) за час опромінення. За методикою наважку композиту масою у 0,05 г диспергували у 40 мл 0,05 мМ водного розчину МБ та піддавали УФ-опроміненню (джерело — комплекс ламп Philips TLK 40W105 загальною потужністю у 300 Вт, $I = 1,26 \text{ мВт}\cdot\text{см}^{-2}$, $\lambda_{\text{макс}} = 365$ нм). За результатами досліджень визначали швидкість фотодеструкції ($v_{\text{ср}}$ [нмоль·г⁻¹·год⁻¹]) барвників. За відсутності каталізатора фотодеградація МБ в даних умовах не відбувалася.

Дослідження фотожемчінних характеристик покриттів проводили за наступною методикою. На покриття наносили розчин барвника (еквівалент 3 нмоль), сушили за кімнатної температури та піддавали опроміненню за двох режимів. *Фотокаталітичний режим 1* — пряме сонячне світло 3 год. ($E_{\text{ср}} = 0,145 \text{ мВт}\cdot\text{см}^{-2}$), розсіяне денне світло 9 год. ($E_{\text{ср}} = 0,024 \text{ мВт}\cdot\text{см}^{-2}$). *Фотокаталітичний режим 2* — розсіяне денне світло 12 год. ($E_{\text{ср}} = 0,024 \text{ мВт}\cdot\text{см}^{-2}$). Енергетичні параметри опромінення, розраховані як середній показник 5 місянь упродовж кожного періоду освітлення (пряме сонячне освітлення, розсіяне денне освітлення) за допомогою радіометра АТТ-1515 у спектральному діапазоні 320–390 нм, що є основним діапазоном поглинання для фотокatalізаторів на основі TiO₂ (фотожемчіною активністю більшості TiO₂-вмісних каталізаторів для $\lambda > 400$ нм можна нехтувати). Тривалість фотокаталітичних випробувань для МБ складала 14 діб, для нігроzinу — 21 добу. За результатами досліджень визначено середню та максимальну швидкість фотодеструкції барвників ($v_{\text{ср}}$ та $v_{\text{макс}}$ відповідно [нмоль·см⁻²·добра⁻¹]), а також питомий показник фотодеструкції барвників на 1 см² поверхні покриття (ΔC).

3. РЕЗУЛЬТАТИ ТА ЇХ ОБГОВОРЕННЯ

Одержання гібридних фотокatalізаторів на основі TiO₂ за обраним методом є сукупністю процесів гідролізу TiCl₄ з перетворенням у дисперсну гідратовану форму ортотитанової кислоти (TiO₂·xH₂O) та її конденсації з частинками гідратованої ортокремнійової кислоти SiO₂·yH₂O з утворенням гібридного гідрозолю, який внаслідок взаємодії з поверхнею воластоніту, що має поверхневу Si-OH- і Ca-OH-функціональність [25], осаджуються у вигляді композитного шару на поверхню субстрату. Температурне оброблення сприяє дегідратації гідрозолю та конденсації складових з утворенням гібридних дисперсних фотокatalізаторів. Склад та основні характеристики одержаних композитів у високодисперсному стані наведено в табл. 1.

ТАБЛИЦЯ 1. Характеристики зразків дисперсних фотокatalізаторів.¹

Зразок	Монодисперсний (MoI)	ПФА			Порометрія	$V_{\text{мікро}}, \text{мм}^3 \cdot \text{л}^{-1}$	$S_{\text{пінт}}, \text{м}^2 \cdot \text{л}^{-1}$	$D_{\text{кп}}, \text{нм}$	$X_{\text{кр}}, \%$	Адсорбція (темохра) χ_{MB} , $\text{ммоль} \cdot \text{l}^{-1}$	Ефективність фотоядечтвлення $(3,5 \text{ год})$, $\text{ммоль} \cdot \text{l}^{-1}$	$\Delta_{\text{cp}}, \text{ ммоуб} \cdot \text{l}^{-1} \cdot \text{тоА}^{-1}$	Інтенсивність фотоядечтвлення MB ,
		ПФА	Порометрія	ПФА									
B _{MB}	—	0:100:0	84	20,0	—	—	—	—	< 0,01	—	—	—	—
TiB _{MB} -1	—	50:50:0	—	—	—	—	—	—	0,44	20,3	—	5,8	—
TiB _{MB} -2	—	66,7:33,3:0	72	21,8	59,3	2,2	0,40	11,8	—	—	3,4	—	—
TiB _{MB} -3	—	25:75:0	—	—	—	—	—	—	2,12	8,1	2,3	—	—
TiB _{MB} Si-4	SiO ₂ ^{EC}	40:20:40	68	19,0	224,5	16,7	5,32	25,0	—	—	7,2	—	—
TiB _{MB} Si-4 ²⁾	SiO ₂ ^{EC}	40:20:40	—	—	—	—	3,64	< 1	—	—	—	—	—
TiB _{MB} Si-5	SiO ₂ ^{EC}	20:40:40	—	—	—	—	0,12	2,3	—	—	0,7	—	—
TiB _{MB} Si-6	SiO ₂ K ₂ SiO ₃	20:40:40	74	19,5	181,7	30,1	6,12	—	—	—	4,2	—	—
TiB _{MB} Si-7	SiO ₂ ² K ₂ SiO ₃	60:20:20	71	18,9	87,7	3,0	1,24	20,4	—	—	5,8	—	—
TiB _{MB} Si-8	SiO ₂ ²	25:50:25	—	—	164,6	10,5	5,08	16,2	—	—	4,6	—	—

При *min ka*: ¹⁾ вміст воластоніту та модифікатора вказано в перерахунку на SiO₂; ²⁾гібридний композит без температурного оброблення (400°C).

Особливості хемічної будови композитних фотокаталізаторів вивчені за допомогою ІЧ-Фур'є-спектроскопії (рис. 1, а) [26, 27]. Якщо розглянути спектр субстрату (CaSiO_3 ; зразок 5), можна відзначити низький вміст поверхневих OH-груп ($\nu_{\text{OHmax}} = 3458 \text{ см}^{-1}$) як результат щільної кристалічної будови мінералу та низький вміст адсорбованої води ($\nu_{\text{H}_2\text{Omax}} = 1635 \text{ см}^{-1}$), що є типовим для непористої структури воластоніту. Також можна спостерігати наявність CO_3^{2-} -йонів ($\nu_{\text{CO}_3\text{max}} = 1428 \text{ см}^{-1}$), що зазвичай є у складі природних мінералів. Також для мікрочастинок субстрату спостерігається низка смуг поглинання, що підтверджують структурні особливості силікатних матеріалів, а саме, наявність зв'язків O-Si-O з максимумами для 1081 см^{-1} (валентні місткові, $\nu_{\text{OSiO,bridge}}$) і 966 см^{-1} (валентні немісткові, $\nu_{\text{OSiO,non-bridge}}$), 921 і 900 см^{-1} (асиметричні та симетричні деформаційні, $\delta_{\text{OSiO,as}}$ та $\delta_{\text{OSiO,s}}$ відповідно). Додатково ідентифіковано зв'язки Si-O-Si, смуги коливань яких мають максимуми для 1060 і 1016 см^{-1} ($\delta_{\text{SiOSi,as}}$ і $\delta_{\text{SiOSi,s}}$), 681 і 644 см^{-1} ($\delta_{\text{SiOSi,as}}$ і $\delta_{\text{SiOSi,s}}$ відповідно), та смугу, типову для кристалічних силікатних структур для 472 см^{-1} . Крім того, ідентифіковано смуги деформаційних коливань силанольних Si-OH-груп з максимумами для 566 і 509 см^{-1} та ν_{CaOSi} для 451 см^{-1} .

На ІЧ-спектрах композитів внаслідок формування розвиненої поверхні та пористої структури спостерігається підвищення вмісту поверхневих OH-груп ($\nu_{\text{OH}} = 3450 \text{ см}^{-1}$) і адсорбованої води ($\nu_{\text{H}_2\text{O}} = 1635 \text{ см}^{-1}$). Наявність широкої комплексної смуги Si-O-Si в діапазоні 1250 – 1160 см^{-1} і нової смуги δ_{OSiO} з максимумом для

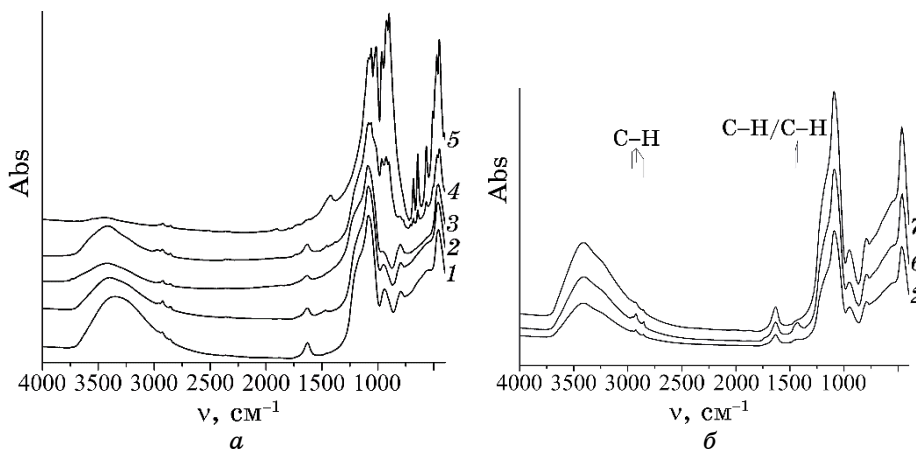


Рис. 1. ІЧ-Фур'є-спектри воластоніту та композитних фотокаталізаторів (а) і композиту $\text{TiB}^{\text{MB}}\text{Si-4}$ до та після опромінення за наявності МБ (б): $\text{TiB}^{\text{MB}}\text{Si-4a}$ (1), $\text{TiB}^{\text{MB}}\text{Si-4}$ (2), $\text{TiB}^{\text{MB}}\text{Si-7}$ (3), $\text{TiB}^{\text{MB}}\text{Si-6}$ (4), воластоніт (5), $\text{TiB}^{\text{MB}}\text{Si-4}$ з адсорбованим МБ (6), $\text{TiB}^{\text{MB}}\text{Si-4}$ після фотодеструкції МБ (7).²

793 см⁻¹ вказує на появу в складі композитів аморфного SiO₂, що утворюється в результаті конденсаційних процесів за участю гідратованої форми ортокремнійової кислоти під час одержання TiO₂/SiO₂-композитів. Крім того, на спектрах зразків у діапазоні $\nu > 800$ см⁻¹ ідентифіковано широку комплексну смугу коливань, що утворилася внаслідок суперпозиції смуг коливань зв'язків Si—O—Si воластоніту зі смугами Ti—O—Si з максимумом для 937 см⁻¹ і Ti—O—Ti для 797 см⁻¹ [28]. За температурного оброблення (кальцинування) композитів (зразки 2–4) відбувається видалення гідратної та сорбованої воді часткова конденсація вільних Si—OH-груп [29] у поверхневому шарі композиту, що спричиняє помітне пониження інтегральної інтенсивності смуги ν_{OH} . Водночас природа кремнійвмісного модифікатора помітно не впливає на структурні характеристики гібридних систем.

На прикладі гібридного композиту TiB^{MB}Si-4 та барвника МВ (рис. 1, б і рис. 2, а) було досліджено послідовність стадій процесу фотокatalітичної деструкції органічних сполук каталізаторами даного типу. За диспергування дисперсного каталізатора в розчині барвника за відсутності освітлення спостерігається активна фаза адсорбції органічних молекул поверхнею частинок композиту, що можна спостерігати появі у ІЧ-спектрі композиту відповідних смуг коливань (C—H і C—H/C—N; рис. 1, б, спектр 6). Варто вказати, що наявність смуг з дуже низькою інтенсивністю в області зазначених смуг C—H і C—H/C—N як на спектрах вихідного воластоніту, так і в ІЧ-спектрі композиту TiB^{MB}Si-4 після опромінення пов'язана з наслідками пробопідготовки.

Аналіза УФ-вид-спектрів поглинання розчинів МВ до та після адсорбції свідчить про значну ріжницю в концентрації барвника — майже зникають характерні для МВ основні смуги поглинання в УФ-діапазоні (246 і 291 нм) та у видимій області спектру (612 і 664 нм) (рис. 2, а, спектри 1 і 2 відповідно). Також під впливом УФ-опромінення в ІЧ-спектрі каталізатора з адсорбованим МВ зникають смуги коливань, притаманні барвнику, що свідчить про перебіг реакцій його окиснення на поверхні каталізатора та десорбції продуктів деструкції в об'єм розчину (рис. 1, б, спектр 7).

Аналіза спектру модельного розчину МВ після фотодеструкції свідчить про повне зникнення смуг поглинання МВ, але повної мінералізації молекул МВ за 1 год. УФ-опромінення не відбувається, оскільки окрім продукти деструкції залишаються в реакційному середовищі, що видно по наявності остаточного поглинання розчину в діапазоні $\lambda < 280$ нм (рис. 2, а, спектр 3). Слід відзначити, що відсутність смуги з $\lambda_{\text{max}} = 246$ нм свідчить про руйнування ароматичного фенотіазольного ядра МВ [30] як одного з хемічно стабільних фрагментів молекули, що важко піддається руйнуванню в природніх умовах.

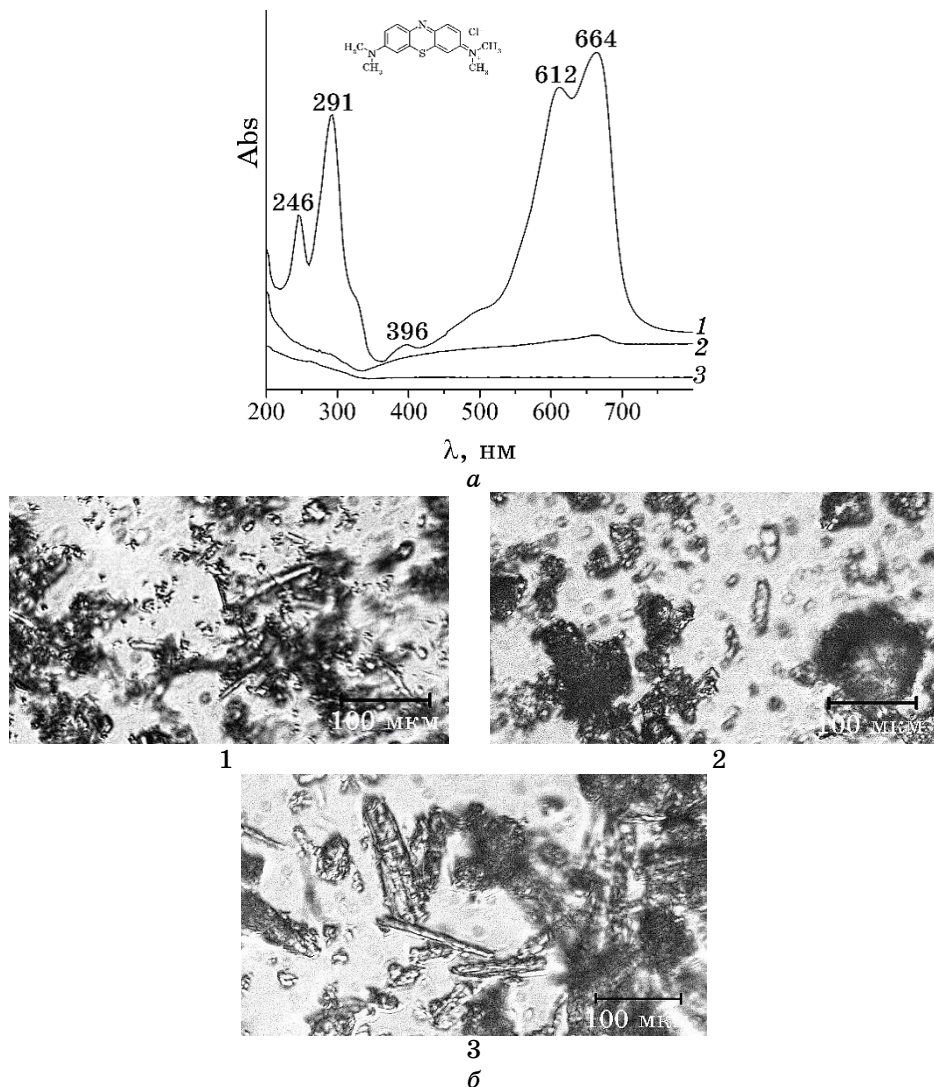


Рис. 2. УФ-вид-спектри поглинання (а) розчинів МБ: вихідний $5 \cdot 10^{-5}$ М (1), після темнової адсорбції на $\text{TiB}^{\text{MB}}\text{Si}-4$ (2), після фотодеструкції на $\text{TiB}^{\text{MB}}\text{Si}-4$ (3); оптичні мікрофотографії (б) зразків: B^{MB} (1), $\text{TiB}^{\text{MB}}\text{-}2$ (2), $\text{TiB}^{\text{MB}}\text{Si-}6$ (3).³

Аналіза мікрофотографій дисперсних композитів (рис. 2, б) демонструє збільшення лінійних розмірів частинок воластоніту від 7–10 мкм до 15–29 мкм ($\text{TiB}^{\text{MB}}\text{-}2$) і 19–37 мкм ($\text{TiB}^{\text{MB}}\text{Si-}6$) за осадження на їхню поверхню гібридного шару $\text{TiO}_2/\text{SiO}_2$. За цими даними приблизна товщина пористого каталітично активного шару на поверхні частинок складає 4–12 мкм і залежить від

співвідношення компонентів. Але тенденція до агрегації поверхнево-модифікованих мікрочастинок воластоніту на стадії сушки та кальцинування зразків композитів погіршує точність мірянь.

Розглядаючи взаємозв'язок між адсорбційною та фотохемічною активностями, а також рентгенофазовою та пористою будовами гіbridних композитів, можна визначити певні ознаки перспективних композитних фотокatalізаторів (табл. 1). Для таких матеріалів, одержаних за запропонованим методом, характерне зменшення середнього розміру нанокристалів (< 20 нм) та ступеня кристалічності ($< 75\%$). Крім того, кристалічна фаза TiO_2 композитних каталізаторів складається переважно з анатазної модифікації (рефлекс для $2\Theta = 25,4^\circ$; рис. 3, a), а відносний вміст модифікації рутилу точно визначити неможливо внаслідок його малого вмісту. Необхідно зазначити, що однією з ключових особливостей, що визначають ефективність каталізаторів, є їхня пориста будова. Результати порометрії свідчать, що використання SiO_2 -вмісних сполучників забезпечують високі значення питомої поверхні та задовільний об'єм мікропор ($10\text{--}30 \text{ mm}^3/\text{г}$) у порівнянні з композитом $\text{TiB}^{\text{MB}}\text{-}2$, одержаним осадженням TiO_2 на поверхню воластоніту за відсутності структурних модифікаторів. Збільшення вмісту TiO_2 по відношенню до модифікатора також приводить до компактування складових композиту в процесі конденсації ($\text{TiB}^{\text{MB}}\text{Si-7}$) та погіршення його пористості. Отже, для низки дисперсних $\text{TiO}_2/\text{SiO}_2$ -композитів, зокрема $\text{TiB}^{\text{MB}}\text{Si-4}$ та $\text{TiB}^{\text{MB}}\text{Si-6}$, характерними є високий рівень темнової адсорбції барвника, що сягає $5\text{--}6 \text{ моль}\cdot\text{г}^{-1}$, спричинений пористою будовою матеріалу, одержаного золь-гель-методом за підвищеною вмісту сполучного (SiO_2 -вмісного модифікатора), а також підвищені швидкість і ефективність фотодеструкції барвника, що сягають $7 \text{ моль}\cdot\text{г}^{-1}\cdot\text{год}^{-1}$ і $25 \text{ моль}\cdot\text{г}^{-1}$ відповідно. Натомість окремі зразки каталізаторів, як от $\text{TiB}^{\text{MB}}\text{-1}$, $\text{TiB}^{\text{MB}}\text{-2}$ та $\text{TiB}^{\text{MB}}\text{Si-7}$, характеризуються низьким рівнем адсорбції барвника із задовільними параметрами фотохемічної активності, що можна пов'язати з підвищеним вмістом TiO_2 , велика кількість якого в процесі одержання композитів сприяє компактуванню в процесі конденсації ортокислот і, відповідно, послаблює пороутворення зі збереженням високої кількості каталітичних центрів у поверхневому шарі композиту. За відсутності температурного оброблення композит з аморфним поверхневим шаром $\text{TiO}_2/\text{SiO}_2$ ($\text{TiB}^{\text{MB}}\text{Si-4a}$) характеризується високим рівнем функціоналізації поверхні (підвищений вміст Ti-OH -та Si-OH -груп), завдяки чому має поліпшені сорбційні властивості до полярних органічних молекул, але за відсутності кристалічної фази TiO_2 фотохемічна активність майже не проявляється.

Узагальнюючи експериментальні дані з фотохемічних властивостей дисперсних композитів в модельних умовах, можна ствер-

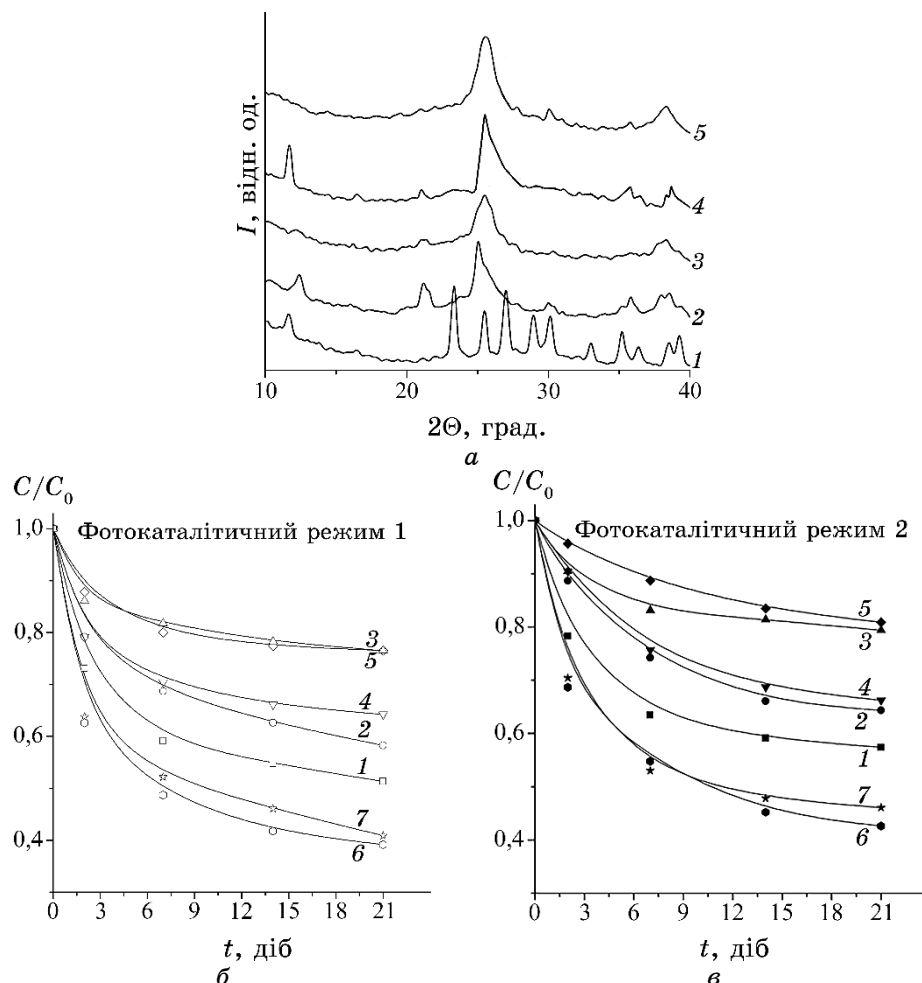


Рис. 3. Дифрактограми ширококутнього розсіяння Рентгено-вих променів (а) воластоніту та його композитів: B^{MB} (1), $\text{TiB}^{\text{MB}}\text{-}2$ (2), $\text{TiB}^{\text{MB}}\text{Si}\text{-}4$ (3), $\text{TiB}^{\text{MB}}\text{Si}\text{-}6$ (4), $\text{TiB}^{\text{MB}}\text{Si}\text{-}7$ (5); кінетичні криві фотодеградації ($C/C_0(t)$) нігроzinу на поверхні покриттів за різних умов опромінення (б) і (в): $\text{TiB}^{\text{MB}}\text{-}1$ (1), $\text{TiB}^{\text{MB}}\text{-}2$ (2), $\text{TiB}^{\text{MB}}\text{-}3$ (3), $\text{TiB}^{\text{MB}}\text{Si}\text{-}4$ (4), $\text{TiB}^{\text{MB}}\text{Si}\text{-}5$ (5), $\text{TiB}^{\text{MB}}\text{Si}\text{-}6$ (6), $\text{TiB}^{\text{MB}}\text{Si}\text{-}7$ (7).⁴

джувати, що гібридні системи мають задовільну активність.

Та найцікавішим було визначити, чи зберігають фотохемічні характеристики композитні кatalізатори в умовах, наблизених до реальних — у вигляді покриттів. Для цього було застосовано метод УФ-вид-спектроскопії в режимі відбивання для вивчення кінетики фотохемічного окиснення барвників на поверхні каталітично активних композитних покриттів. Дані міряння фотохемічної активності покриттів гібридних композитів наведено в табл. 2.

Результати свідчать, що, незважаючи на низькі енергетичні характеристики опромінення в обох режимах дослідження композитних покріттів ($0,145 \text{ мВт}\cdot\text{см}^{-2}$ і $0,024 \text{ мВт}\cdot\text{см}^{-2}$ за різних умов експерименту), загальні тенденції, одержані в модельних умовах для дисперсних кatalізаторів, зберігаються. Для покріттів на основі високоактивних композитів показники загального рівня фотодеструкції барвників мають значення $1,2\text{--}1,6 \text{ нмоль}\cdot\text{см}^{-2}$ із $v_{cp} = 0,09\text{--}0,12 \text{ нмоль}\cdot\text{см}^{-2}\cdot\text{дoba}^{-1}$ (для МБ) і $1,0\text{--}1,2 \text{ нмоль}\cdot\text{см}^{-2}$ із v_{cp} близько $0,05\text{--}0,06 \text{ нмоль}\cdot\text{см}^{-2}\cdot\text{дoba}^{-1}$ (для нігрозину) під час *фотокаталітичного режиму 1*. Невелику ріжницю у показниках ΔC барвників можна пояснити різною тривалістю проведення мірянь (МБ — 14 діб, нігрозин — 21 доба). Теоретичне значення тривалості окиснення барвників за визначеними показниками v_{cp} , розраховане за даними швидкості фотодеструкції, становить $17,5\text{--}23$ доби (для МБ) і $34,5\text{--}43,5$ доби (для нігрозину). За відсутності прямого сонячного світла (*фотокаталітичний режим 2*) показники ΔC і v_{cp} понижуються до $0,9\text{--}1,2 \text{ нмоль}\cdot\text{см}^{-2}$ і $0,07\text{--}0,09 \text{ нмоль}\cdot\text{см}^{-2}\cdot\text{дoba}^{-1}$ (для МБ) та до $0,8\text{--}1,1 \text{ нмоль}\cdot\text{см}^{-2}$ і $0,04\text{--}0,05 \text{ нмоль}\cdot\text{см}^{-2}\cdot\text{дoba}^{-1}$ (для нігрозину). Теоретичний час розкладання барвників за даних умов зростає на 5–15 діб і 2–6 діб для МБ і нігрозину відповідно.

Незважаючи на відносно низькі показники v_{cp} , слід відмітити істотну відмінність в умовах проведення випробувань у порівнянні з модельним експериментом. В модельному дослідженні міряння фотокаталітичної активності проводили за високої потужності опромінення та в динамічних дифузійно-сприятливих умовах, що передбачає участь більшості каталітичних центрів на поверхні частинок композитів, а також поліпшенні умови процесів сорбції/десорбції барвників і продуктів їхніх перетворень. Натомість під час міряння активності покріттів у фотокаталітичному процесі бере участь певна частка поверхні частинок композиту, а процес деструкції органічних сполук відбувається у статичних умовах, що не забезпечує дифузійний обмін барвника та продуктів його перетворення із зовнішнім середовищем до досягнення мінералізації органічних молекул. Сукупність негативних чинників впливу на процес фотокаталітичної деструкції органічних сполук значно понижує активність покріттів, одержаних з високоактивних композитних кatalізаторів.

Детальна аналіза кінетичних кривих фотодеструкції нігрозину на покріттях (рис. 3, б, в) свідчить, що за проведення мірянь активності в енергодефіцитному *фотокаталітичному режимі 2* для більшості композитів (або для малоактивних зразків $TiB^{MB}\text{-}3$ та $TiB^{MB}Si\text{-}5$ з низьким вмістом TiO_2 за *фотокаталітичного режиму 1*) спостерігається «отруєння кatalізатора» — падіння v_{cp} через 14–17 діб від початку експерименту.

ТАБЛИЦЯ 2. Кінетичні параметри фотокаталітичної деструкції барвників на покриттях гібридних композитів.⁵

Зразок	Фотокаталітичний режим 1			Фотокаталітичний режим 2		
	$V_{\text{ср}}^2$, нмоль·см ⁻² ·дoba ⁻¹	$V_{\text{макс}}^2$, нмоль·см ⁻² ·дoba ⁻¹	ΔC , нмоль·см ⁻²	$V_{\text{ср}}^2$, нмоль·см ⁻² ·дoba ⁻¹	$V_{\text{макс}}^2$, нмоль·см ⁻² ·дoba ⁻¹	ΔC , нмоль·см ⁻²
Метиленовий блакитний						
TiB ^{MB} -1	0,088	0,55	1,24	0,067	0,40	0,93
TiB ^{MB} -2	0,057	0,19	0,79	0,044	0,09	0,62
TiB ^{MB} -3	0,064	0,28	0,90	0,039	0,07	0,55
TiB ^{MB} Si-4	0,118	0,36	1,62	0,089	0,28	1,24
TiB ^{MM} Si-5	0,025	0,04	0,34	0,017	0,04	0,24
TiB ^{MB} Si-6	0,054	0,17	0,76	0,039	0,12	0,55
TiB ^{MM} Si-7	0,096	0,34	1,34	0,079	0,31	1,10
Нігроzin						
TiB ^{MB} -1	0,056	0,36	1,18	0,051	0,30	1,08
TiB ^{MB} -2	0,058	0,37	1,22	0,055	0,31	1,14
TiB ^{MB} -3	0,022	0,12	0,47	0,018	0,04	0,38
TiB ^{MB} Si-4	0,034	0,21	0,72	0,032	0,10	0,67
TiB ^{MM} Si-5	0,022	0,14	0,47	0,020	0,10	0,41
TiB ^{MB} Si-6	0,040	0,21	0,83	0,034	0,11	0,71
TiB ^{MM} Si-7	0,046	0,27	0,97	0,041	0,22	0,85

Зазначене пов'язане з «екрануванням» поверхні композитів із низькою концентрацією каталітичних центрів від УФ-опромінення продуктами неповного окиснення барвника (поліцикличними молекулами з високим ступенем ароматичності та карбонізованими продуктами). Даний ефект було помічено під час дослідження фотодеструкції обох барвників, але найбільш істотним він виявився саме для нігрозину завдяки більшій оксидативній стійкості його молекул. Дійсно, якщо розглянути хемічну будову нігрозину, видно, що для його молекул характерний високий ступінь ароматичності та схильність до конденсації за глибокого окиснення з утворенням поліциклических структур, яким притаманна здатність поглинати УФ- і видиме світло у широкому спектральному діапазоні. Для високоактивних композитів у динамічних режимах досліджень і за використання менш оксидативно стійких сполук (як МБ) ефект «отруєння каталізатора» помічено не було.

4. ВИСНОВКИ

В результаті проведеної роботи одержано композитні фотокatalізатори шляхом осадження гідрозолів з конденсованих гідратованих форм орто-титанової та ортокремнійової кислот на поверхню природного Кальцій силікату — воластоніту. Обрані умови одержання композитів уможливлюють одержати матеріали з гібридною будовою, в якій SiO_2 виконує роль сполучного та структурного модифікатора, що сприяє утворенню пористих композитних матеріалів з поліпшеними здатністю до адсорбції молекул органічних речовин і фотохемічною активністю. Результати дослідження продемонстрували важливість стадії сорбції–десорбції в процесі фотокatalітичного окиснення органічних сполук, що дає змогу досягти швидкість фотодеструкції метиленового блакитного в модельних умовах УФ-опромінення до $4,2\text{--}7,2 \text{ нмоль}\cdot\text{г}^{-1}\cdot\text{год}^{-1}$. Під час проведення мірянь фотокatalітичної активності покриттів в умовах, наблизених до реальних (пряме сонячне або розсіяне денне освітлення), для чого для кількісної оцінки каталітичної активності TiO_2 -вмісних каталізаторів було використано метод УФ-вид-спектроскопії на відбивання, середня швидкість фотодеструкції органічних сполук помітно понижується і сягає $0,12 \text{ нмоль}\cdot\text{см}^{-2}\cdot\text{добра}^{-1}$ для МБ та $0,06 \text{ нмоль}\cdot\text{см}^{-2}\cdot\text{добра}^{-1}$ для промислового забруднювача нігрозину за часткового опромінення сонячним світлом. В енергодефіцитних умовах за відсутності прямого сонячного опромінення ці показники складають $0,09$ і $0,05 \text{ нмоль}\cdot\text{см}^{-2}\cdot\text{добра}^{-1}$ для МБ і нігрозину відповідно. Загальна ефективність фотокatalітичної деструкції органічних забруднювачів у зазначених умовах теж понижується й дорівнює $1,24\text{--}1,62$ та

0,97–1,22 нмоль·см⁻² для МБ і нігроzinу відповідно, що пов'язане з ріжницею в інтенсивності джерел опромінення, відсутністю дифузійного обміну органічних молекул і продуктів деструкції їх, участю у фотохемічних процесах обмеженої частки каталітично активних центрів поверхні композиту тощо. Але, незважаючи на зазначені відмінності, створені гібридні композити та покриття на їхній основі продемонстрували ефективність як фотокatalітично активні поверхні, здатні до самоочищення, та можливість використання їх для видалення небезпечних забруднювачів у промисловості та побуті за різних режимів освітлення.

ЦИТОВАНА ЛІТЕРАТУРА—REFERENCES

1. X. Chen and S. S. Mao, *Chem. Rev.*, **107**: 2891 (2007);
<https://doi.org/10.1021/cr0500535>
2. K. P. Gopinath, N. V. Madhav, A. Krishnan, R. Malolan, and G. Rangarajan, *J. Environ. Manag.*, **270**: 110906 (2020);
<https://doi.org/10.1016/j.jenvman.2020.110906>
3. O. L. Stroyuk and S. Ya. Kuchmy, *Theoret. Experim. Chem.*, **56**, No. 3: 143 (2020); <https://doi.org/10.1007/s11237-020-09648-0>
4. C. Liu, Y. Li, and Q. Duan, *Appl. Surf. Sci.*, **503**: 144111 (2020);
<https://doi.org/10.1016/j.apsusc.2019.144111>
5. N. I. Romanovska, P. A. Manoryk, N. I. Ermokhina, P. S. Yaremov, and V. M. Grebennikov, *Theoret. Experim. Chem.*, **55**, No. 5: 345 (2019);
<https://doi.org/10.1007/s11237-019-09627-0>
6. V. F. Matyushov, A. L. Tolstov, P. S. Yaremov, and V. G. Ilyin, *Theoret. Expim. Chem.*, **49**, No. 5: 333 (2013); <https://doi.org/10.1007/s11237-013-9334-6>
7. M. Zhang, E. Lei, R. Zhang, and Z. Liu, *Surface Interfaces*, **16**: 194 (2019);
<https://doi.org/10.1016/j.surfin.2018.10.005>
8. K. Guan, *Surface Coat Technol.*, **191**: 155 (2005);
<https://doi.org/10.1016/j.surfcoat.2004.02.022>
9. K. Balachandaran, *Int. J. Eng. Sci. Technol.*, **2**, No. 8: 3695 (2010);
<http://www.ijest.info/docs/IJEST10-02-08-66.pdf>
10. Z. Bielan, A. Sulowska, S. Dudziak, K. Siuzdak, J. Ryl, and A. Zielinska-Jurek, *Catalysts*, **10**: 672 (2020); <https://doi.org/10.3390/catal10060672>
11. S. Varnagiris, M. Urbonavicius, S. Sakalauskaitė, R. Daugelavicius, and D. Milcius, *Sci. Total Environ.*, **720**: 137600 (2020);
<https://doi.org/10.1016/j.scitotenv.2020.137600>
12. E. Loccufier, K. Deventer, D. Manhaeghe, S. W. H. Van Hulle, and K. De Clerck, *Chem. Eng. J.*, **387**: 124143 (2020);
<https://doi.org/10.1016/j.cej.2020.124143>
13. Q. Li and F.-T. Li, *Adv. Colloid Interface Sci.*, **284**: 102275 (2020);
<https://doi.org/10.1016/j.cis.2020.102275>
14. E. I. Cedillo-González, J. M. Hernández-López, J. J. Ruiz-Valdés, V. Barbieri, and C. Siligardi, *Construct. Build. Mater.*, **237**: 117692 (2020);
<https://doi.org/10.1016/j.conbuildmat.2019.117692>
15. A. Matsuda, T. Matoda, and T. Kogure, *Chem. Mater.*, **17**: 749 (2005);
<https://doi.org/10.1021/cm048135h>

16. N. Negishi, M. Sugasawa, Y. Miyazaki, Y. Hirami, and S. Koura, *Water Res.*, **150**: 40 (2019); <https://doi.org/10.1016/j.watres.2018.11.047>
17. E. P. Ferreira-Neto, M. A. Worsley, and U. P. Rodrigues-Filho, *J. Environ. Chem. Eng.*, **7**, No. 5: 103425 (2019); <https://doi.org/10.1016/j.jece.2019.103425>
18. G. J. Rincyn and E. J. La Motta, *Heliyon*, **5**, No. 6: e01966 (2019); <https://doi.org/10.1016/j.heliyon.2019.e01966>
19. D. Wang, P. Hou, D. Stephan, S. Huang, and X. Cheng, *Construct. Build Mater.*, **241**: 118124 (2020); <https://doi.org/10.1016/j.conbuildmat.2020.118124>
20. I. Fatimah, N. I. Prakoso, I. Sahroni, M. M. Musawwa, and O. Muraza, *Heliyon*, **5**, No. 11: e02766 (2019); <https://doi.org/10.1016/j.heliyon.2019.e02766>
21. A. S. Yusuff, I. I. Olateju, and O. A. Adesina, *Materialia*, **8**: 100484 (2019); <https://doi.org/10.1016/j.mtla.2019.100484>
22. V. Wongso, C. J. Chen, A. Razzaq, N. A. Kamal, and N. S. Sambudi, *Appl. Clay Sci.*, **180**: 105158 (2019); <https://doi.org/10.1016/j.clay.2019.105158>
23. H. Xie, N. Li, B. Liu, J. Yang, and X. Zhao, *J. Phys. Chem. C*, **120**, No. 19: 10390 (2016); <https://doi.org/10.1021/acs.jpcc.6b01730>
24. M. E. Kurtoglu, T. Longenbach, and Yu. Gogotsi, *Int. J. Appl. Glass Sci.*, **2**, No. 2: 108 (2011); <https://doi.org/10.1111/j.2041-1294.2011.00040.x>
25. S. Sanna, W. G. Schmidt, and P. Thissen, *J. Phys. Chem. C*, **118**: 8007 (2014); <https://doi.org/10.1021/jp500170t>
26. C. Palusziewicz, M. Blazewicz, J. Podporska, and T. Gumula, *Vibrat. Spectr.*, **48**: 263 (2008); <https://doi.org/10.1016/j.vibspec.2008.02.020>
27. A. M. Hofmeister and J. E. Bowey, *Mon. Not. R. Astron. Soc.*, **367**: 577 (2006); <https://doi.org/10.1111/j.1365-2966.2006.09894.x>
28. V. A. Zeitler and C. A. Brown, *J. Phys. Chem.*, **61**, No. 9: 1174 (1957); <https://doi.org/10.1021/ac60132a615>
29. A. Burneau, O. Barres, J. P. Gallas, and J. C. Lavalle, *Langmuir*, **6**, No. 8: 1364 (1990); <https://doi.org/10.1021/la00098a008>
30. B. Brem, E. Gal, L. Găină, L. Silaghi-Dumitrescu, E. Fischer-Fodor, C. I. Tomuleasa, A. Grozav, V. Zaharia, L. Filip, and C. Cristea, *Int. J. Mol. Sci.*, **18**: 1365 (2017); <https://doi.org/10.3390/ijms18071365>

*Institute of Macromolecular Chemistry, N.A.S. of Ukraine,
48, Kharkiv'ske Shose,
UA-02155 Kyiv, Ukraine*

¹ TABLE 1. Basic characteristics of powdered photocatalysts.

² Fig. 1. FTIR spectra of wollastonite, composite photocatalysts (*a*), and TiB^{MB}Si-4 composite before and after irradiation in the presence of MB dye (*b*): TiB^{MB}Si-4a (1), TiB^{MB}Si-4 (2), TiB^{MB}Si-7 (3), TiB^{MB}Si-6 (4), wollastonite (5), TiB^{MB}Si-4 with adsorbed MB dye (6), TiB^{MB}Si-4 after photodecomposition of MB (7).

³ Fig. 2. UV-vis absorbance spectra of MB solutions (*a*): initial 5·10⁻⁵ M (1), after dark sorption process on TiB^{MB}Si-4 surface (2), after photodegradation on TiB^{MB}Si-4 surface (3); optical microphotographs (*b*) of the composites: B^{MB} (1); TiB^{MB}-2 (2); TiB^{MB}Si-6 (3).

⁴ Fig. 3. (*a*) WAXS scattering plots for wollastonite and the composites: B^{MB} (1), TiB^{MB}-2 (2), TiB^{MB}Si-4 (3), TiB^{MB}Si-6 (4), TiB^{MB}Si-7 (5); (*b*) and (*c*) kinetic curves of nigrosine dye photodegradation ($C/C_0(t)$) at different irradiation conditions on a surface of the photocatalytic coatings: TiB^{MB}-1 (1), TiB^{MB}-2 (2), TiB^{MB}-3 (3), TiB^{MB}Si-4 (4), TiB^{MB}Si-5 (5), TiB^{MB}Si-6 (6), TiB^{MB}Si-7 (7).

⁵ TABLE 2. Kinetic parameters of photocatalytic degradation of the dyes on hybrid composite-based coatings.

PACS numbers: 68.37.Lp, 68.65.Hb, 73.21.La, 78.67.Hc, 81.07.Ta, 84.30.Vn, 85.35.Be

SBR Capped ZnS Quantum Dots as Nanoelectronic Filter

Abhigyan Ganguly¹, Saradindu Panda², Siddhartha Sankar Nath³,
and Gautam Gope⁴

¹*Parul Institute of Technology, Parul University,
491760 Vadodara, India*

²*Dr. Sudhir Chandra Sur Institute of Technology and Sports Complex,
700074 Kolkata, India*

³*Assam University,
788001 Silchar, Assam, India*

⁴*University of North Bengal,
734013 Siliguri, India*

The quantum dots (QD) based filtering circuits work on the principle of capacitive admittance, due to which they have less power dissipation, small dimension, and almost zero noise. In the present study, we report synthesis, characterization, and application of the styrene butadiene rubber (SBR) capped ZnS quantum dots as nanodimensional tuned filter. The ZnS quantum dots are characterized by standard characterization techniques such as absorption spectroscopy, XRD study, and high-resolution TEM microscopy; the admittance variation with frequency is tested for the same. The SBR capped ZnS quantum dots are found to work as a tuned band pass filter with pass band in the range of 20–32 MHz with a critical frequency of 20 MHz.

Схеми фільтрації на основі квантових цяток працюють за принципом ємнісної пропускної здатності, завдяки чому вони мають меншу розсіювану потужність, малі розміри та майже нульовий шум. У цьому дослідженні ми повідомляємо про синтезу, характеристизацію та застосування квантових цяток ZnS, покритих стирол-бутадіеновим каучуком (СБК), як нанорозмірного налаштованого фільтра. Квантові цятки ZnS характеризуються стандартними методами визначення характеристик, такими як спектроскопія поглинання, дослідження рентгенівської дифракції та просвітна електронна мікроскопія з високою роздільчою здатністю; зміна пропускної здатності з частотою перевіряється на те саме. Встановлено, що квантові цятки ZnS, покриті СБК, працюють як налаштований смуговий фільтер із смugoю пропускання в діапазоні 20–32 МГц із критичною частотою у 20 МГц.

Key words: ZnS, quantum dots, SBR latex, nanofilter, nanotechnology.

Ключові слова: ZnS, квантові цятки, СБК латекс, нанофільтр, нанотехнології.

(Received 18 May, 2023)

1. INTRODUCTION

Electronic filter is the component that allows a specific range of frequencies to pass through it and rejects the other. Depending upon the frequency range, electronic filters are classified as low pass filter (0 Hz to several kHz or MHz), high pass filter (several kHz to several MHz), band pass that allows a band of frequency, band reject filter that rejects a band of frequency. In case of quantum dots, admittance changes with operating frequency. This is the primary characteristic of tuned device and filter. The variation in quantum dot admittance with frequency occurs because quantum dots are associated with capacitance and quantum dot admittance (or impedance) is basically due to capacitance present in the specimen. The capacitance (hence, capacitive admittance) is a function of quantum dot size, shape and material [1].

There are several advantages of using QD based filtering circuits compared to traditional filtering circuits. It works on the principle of QD admittance which is basically capacitive in nature while in general the tuned circuits are made using R and L elements. In QD based filters, power dissipation is very less and producing no considerable noise. Also, as the dimension is very small, simple circuitry, may be used for detecting any signal in a very sophisticated receiver section. The resonance frequency of QD (assembly) is a function of size, shape and material used. Hence, these parameters are fixed for specific QD (assembly) [2].

For disk and spherical shaped quantum dots of radius r , the capacitance is given as follow:

$$C = 8\epsilon_0(\epsilon/\epsilon_0)r \text{ for disk,} \quad (1)$$

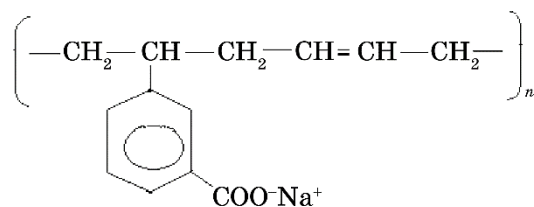
$$C = 4\pi\epsilon_0(\epsilon/\epsilon_0)r \text{ for sphere,} \quad (2)$$

where ϵ/ϵ_0 is the dimensionless dielectric constant of the semiconducting material, which forms the dot, and $\epsilon_0 = 8.8542 \cdot 10^{-12}$ F/m is the dielectric constant of free space. Our quantum dots are of spherical shape, hence, the admittance of our quantum dot variation with size/shape follows the relation (2).

The capping material used for the synthesis is styrene butadiene rubber (SBR) latex, which controls the growth of QD size. The

TABLE 1. Physical properties of styrene butadiene rubber (SBR) latex.

Physical properties of SBR	
Melting point, °C	273
Specific gravity	0.93
Specific heat, J/(gm·K)	1.89
Thermal conductivity, W/(m·K)	1.34
Refractive index	1.53
Dielectric constant	3.1

**Fig. 1.** Structure of styrene butadiene rubber (SBR) latex.

physical properties of SBR and the chemical structure is shown in Table 1 and Fig. 1, respectively [3].

2. EXPERIMENTAL

One coat of SBR latex is drawn over glass substrate and then dried slowly to avoid spilling. The coated glass substrate is dipped into ZnCl_2 solution mixed with few drops of HNO_3 for one hour and then taken out followed by ammonia passivation for half an hour. Finally, the glass substrate is dipped into freshly prepared 2 wt.% $\text{Na}_2\text{S D/D}$ water solution, until it appears fully yellow. The milky white thin film contains the semiconductor ZnS quantum dots embedded in SBR latex [4].

The synthesized samples have been tested by UV/VIS spectrophotometer, x-ray diffraction spectrometer, and high-resolution transmission microscope (HRTEM). UV-vis light absorption spectra were obtained using Perkin Elmer Perkin Elmer Lambda 35 ultraviolet visible (UV-vis) spectrophotometer. X-ray diffraction (XRD) patterns were obtained (Bruker AXS, X-ray source: CuK_α) as well as high-resolution transmission electron microscopy (JEM 1000 C XII).

To study the admittance of our synthesized quantum dot samples (assembly of quantum dots), two ends of 99% pure fine gold wire of 0.01 mm diameter are made fixed very close to each other within micron range over the glass substrate. By means of a syringe, a

single tiny drop of quantum dot liquid sample is gently put over the two free ends of gold wires to make the microcontact. The specimen is dried partially by natural process to avoid spilling and then in oven to stick it properly upon the substrate. After that, the free ends of probing wires are connected to admittance (impedance) analyser (Solartron SI 1260). The sample is ready for admittance analysis. Though the quantum dots are embedded in nonconducting matrix (SBR), the electrons (current) can pass through the sample (assembly of quantum dots) by means of tunnelling of electrons from one quantum dot to the another as the quantum dots are isolated from each other by very thin insulating wall of matrix, which is obvious from TEM images of the samples.

3. RESULTS AND DISCUSSION

The absorption spectra of the synthesized ZnS quantum dots are shown in Fig. 2. It can be observed from the figure that a strong absorbance edge occurs at 225 nm for undoped ZnS, determined by drawing a tangent on point, from which there is sudden increase in the absorption (as observed in Fig. 2) to meet the x -axis. From the absorption edge, the nanoband gap of the quantum dot (E_{gn}) is determined from the formula $E_{gn} = hc/\lambda$, where $hc = 1.12$ eV, and λ is the value of absorption edge [5].

In the case of doped samples the absorption spectra are a little ‘blue shifted’. The reason for this ‘blue-shift’ towards lower wavelength is due to increased nucleation rate in the quantum dot crystal on introducing dopant ions into it [6]. This slight blue shift in spectra is also considered an indication of the successful doping of quantum dots. From the absorbance edge, particle size has been estimated by hyperbolic band model [6].

$$R = \sqrt{\frac{2\pi^2 h^2 E_{gb}}{m^*(E_{gn}^2 - E_{gb}^2)}} . \quad (3)$$

Here, R is the quantum dot radius to be calculated; whereas, m^* (effective mass of the specimen), h (Planck’s constant), E_{gb} (bulk band-gap) are constant for each material. Thus, the size of quantum dots varies with the increase in E_{gn} (the quantum dot band gap), which is determined from the absorption edge in the UV-vis spectrum. The other values used in the present estimation are as follows: bulk band-gap (E_{gb}) for ZnS is of 3.65 eV, electron effective mass of ZnS at room temperature is of $3.64 \cdot 10^{-31}$ Kg [7], and the Plank’s constant is of $6.626 \cdot 10^{-34}$ J.s. The estimated size of ZnS quantum dots from the ‘hyperbolic band model’ is of 10.5 nm.

The XRD characteristics of synthesized ZnS quantum dot samples

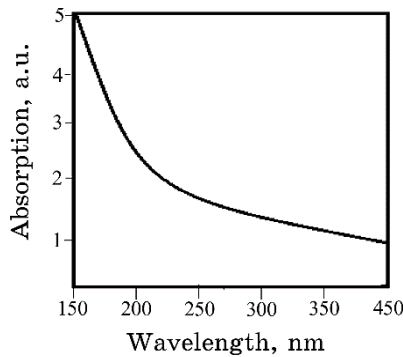


Fig. 2. UV-vis absorption spectra of ZnS quantum dots.

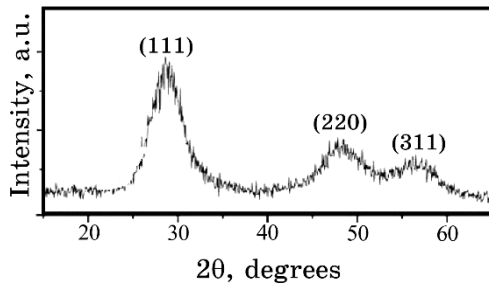


Fig. 3. XRD of ZnS quantum dots.

are shown in Fig. 3. The approximate (average) size of the particle is calculated by using the Debye–Scherrer formula [8]:

$$D = \frac{0.9\lambda}{W \cos \theta}, \quad (2)$$

where λ and θ are the wavelength of x-rays (0.1541 nm) and the glancing angle, respectively. The W and D are full width at half maxima ($FWHM$) and particle diameter (crystallite size), respectively. The crystalline planes corresponding to the first, second, and third XRD peaks are (111), (220), and (311), respectively [9]. The average particle size of the synthesized quantum dots has been estimated to be in the range of 9.61 nm to 11.2 nm from the XRD spectra from the x-ray diffractogram peaks. Further, by comparing the obtained XRD spectra peaks with the International Center Diffraction Data (ICDD) card number JCPDS-00.001.0792, it has been revealed that obtained peaks match that of standard ZnS data. Thus, quantum dots are also having a Wurtzite crystalline structure [10].

Quantum dots' formation and sizes are confirmed by taking high-

resolution transmission electron microscope (HRTEM) images of the prepared samples. It can be observed in Fig. 4 that the size of synthesized ZnS quantum dots is around 10 nm, which is in close agreement with that of the estimated sizes obtained from absorption spectroscopy and XRD.

The admittance *versus* frequency plot for the synthesized SBR capped ZnS quantum dots are shown in Fig. 5. Admittance analysis of ZnS quantum dots capped with SBR is shown in Table 2 to study the changes of admittance with frequency.

It is observed that admittance increases slowly with increase in frequency up to a certain frequency range 2 and after that, at a particular critical frequency, admittance rises in a relatively steeper fashion. This critical frequency of ZnS is of 20 MHz. The admittance remains almost constant in higher frequencies, 32 MHz in present investigation, for ZnS sample in SBR latex.

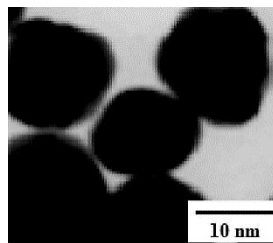


Fig. 4. HRTEM image of ZnS quantum dots.

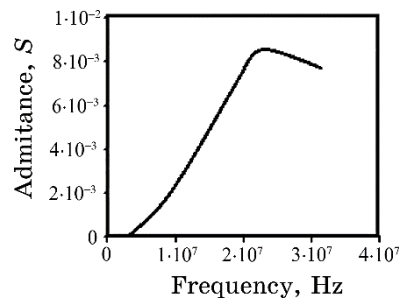


Fig. 5. Filtering behaviour ZnS quantum dots on SBR latex.

TABLE 2. Nanofilter characteristic data for SBR capped ZnS quantum dots.

Sample	Matrix used	Stop band, MHz	Pass band, MHz	Critical frequency (f_c), MHz
ZnS SBR QD	SBR	0 to 20	20 to 32	20

4. CONCLUSIONS

ZnS quantum dots are synthesized on SBR latex matrix using simple, low cost chemical synthesis method. The optical and structural properties of the synthesized quantum dots are studied using standard characterization techniques, from which it was found that the quantum dots have an absorption edge of 225 nm and have a wurtzite structure. The size of the quantum dots are found to be in and around 10 nm that matches with the estimation from the absorption and XRD spectra analysis. To check the nanofilter application of ZnS quantum dots, admittance characteristics of quantum dots are studied and the variation is plotted against changing frequencies. It was noted that SBR capped ZnS quantum dots can successfully act as band pass filter with stop band and pass band frequencies in the range 0–20 MHz and 20–32 MHz, respectively. The critical frequency for the ZnS nanofilter is observed to be around 20 MHz.

REFERENCES

1. Z. Fan, P. Chang, and J. G. Lu, *Appl. Phys. Lett.*, **85**, No. 25: 6128 (2004); <https://doi.org/10.1063/1.1841453>
2. S. S. Nath, D. Chakdar, and G. Gope, *J. Mat. Online*, <https://doi.org/10.2240/azojono0128>
3. R. Das, M. Choudhury, S. S. Nath, D. Chakdar, and G. Gope, *Assam University Journal of Science & Technology*, **6**: 46 (2010).
4. D. Mohanta, N. C. Mishra, and A. Choudhury, *Mat. Lett.*, **58**, No. 29: 3694 (2004); <https://doi.org/10.1016/j.matlet.2004.06.061>
5. B. Debnath, G. Halder, and S. Bhattacharya, *Sci. Adv. Mat.*, **6**, No. 6: 1160 (2014); <https://doi.org/10.1166/sam.2014.1881>
6. S. S. Nath, A. Ganguly, G. Gope, and M. R. Kanjilal, *Nanosys.: Phys. Chem. Math.*, **8**, No. 5: 661 (2017); <https://doi.org/10.17586/2220-8054-2017-8-5-661-664>
7. Soumee Chakraborty, S. Dhara, T. R. Ravindran et al., *AIP Advances*, **1**: 032135 (2011); <https://doi.org/10.1063/1.3628347>
8. P. K. Santra and P. V. Kamat, *J. Am. Chem. Soc.*, **134**: 2508 (2012); <https://doi.org/10.1021/ja211224s>
9. A. Ganguly, S. S. Nath, and V. M. Srivastava, *Chalcogenide Lett.*, **17**, No. 10: 487 (2020).
10. Houcine Labiad and Slah Hidouri, *J. King Saud. Univ.-Sci.*, **29**, No. 4: 444 (2017); <https://doi.org/10.1016/j.jksus.2016.12.001>

PACS numbers: 61.43.Er, 65.60.+a, 68.35.bm, 73.50.Pz, 78.40.Me, 82.35.Np, 83.60.-a

Features of Relationship Between Rheological and Photogeneration Characteristics of PEPC-C₆₀ Composites

M. A. Zabolotnyy¹, L. I. Aslamova¹, V. P. Vashchyn¹, D. O. Grynko²,
A. A. Kolesnichenko², D. S. Leonov², D. O. Krasnovyd⁴, V. V. Vovk⁴,
M. M. Petryshyn⁴, R. V. Lytvyn^{2,3}, S. O. Rudenkyi⁴,
and M. Yu. Barabash^{2,4,5}

¹*Taras Shevchenko National University of Kyiv,
60, Volodymyrska Str.,
UA-01033 Kyiv, Ukraine*

²*Technical Centre, N.A.S. of Ukraine,
13, Pokrovs'ka Str.,
UA-04070 Kyiv, Ukraine*

³*I.M. Frantsevych Institute for Problems of Materials Sciences, N.A.S. of Ukraine,
3, Omeljan Pritsak Str.,
UA-03142 Kyiv Ukraine*

⁴*National Technical University of Ukraine
'Igor Sikorsky Kyiv Polytechnic Institute',
37, Beresteiskyi Ave.,
UA-03056 Kyiv, Ukraine*

⁵*Gas Institute, N.A.S. of Ukraine,
39, Degtyarivska Str.,
UA-03113 Kyiv, Ukraine*

The process of photogeneration of charges and the temperature of the transition to the viscous-flow state (T_v) in thin films of polyepoxypropyl-carbazole PEPC-C₆₀ composites fabricated by means of toluene-solution casting in strong external electric fields are investigated. Consistent and correlated changes in the temperature of the transition of the sample material to viscous-flow state (T_v) and in the effective temperature of the quantum yield of photogeneration (T_0) are found out. As shown, the difference between T_v and T_0 for the PEPC-C₆₀ composites does not exceed 10% of these values, when the concentration of C₆₀ fullerene changes. This indicates changes in the molecular structure and, consequently, dielectric constant in the vicinity of the centre of photogeneration of electric-charge carriers.

Досліджено процес фотогенерації зарядів і температуру переходу до в'язкоплинного стану (T_v) у тонких плівках поліепоксипропілкарбазольних ПЕПК–С₆₀-композитів, одержаних літтям з толуольного розчину в сильних зовнішніх електричних полях. Виявлено послідовні та корелювані зміни температури переходу матеріалу зразка у в'язкоплинний стан (T_v) та ефективної температури квантового виходу фотогенерації (T_0). Показано, що ріжниця між T_v і T_0 композитів ПЕПК–С₆₀ не перевищує 10% цих значень із зміною концентрації фуллерену С₆₀. Це вказує на зміни молекулярної структури і, як наслідок, діелектричної проникності в околі центру фотогенерації носіїв електричного заряду.

Key words: amorphous molecular semiconductor, fullerene, photogeneration, electric charge, current density.

Ключові слова: аморфний молекулярний напівпровідник, фуллерен, фотогенерація, електричний заряд, густина струму.

(Received 27 December, 2023; in revised form, 12 January, 2024)

1. INTRODUCTION

The magnitude of the quantum yield (η) of photogeneration of electric charge carriers in light-sensitive amorphous molecular semiconductors (AMSSs) is one of the basic parameters that determine the fields and possibilities of their use. For the development of photosensitive media, the determining parameter is the amplification of signals using selective plasmon resonance electromagnetic fields. These effects appear in the development of AMSSs for solar batteries, reversible layers for the registration and analysis of their 2- and 3-dimensional amplitude–phase optical information, and optical sensors [1–4].

According to the literature [5–7], the quantum yield of photogeneration depends significantly on the molecular composition and structure of the material. In the AMSSs, the photogeneration process [2, 5–7] is determined by the features of the structure of the photosensitive medium directly in the centre of charge photogeneration. The mobilities of charge carriers of different signs differ significantly. In particular, PEPC and polyvinylcarbazole (PVC) sensitized by electron-acceptor impurities have linear dimensions of the zone, beyond which the movement of twin charge carriers ceases to be correlated, and the charges become independent of each other and are determined by the Onsager radius.

At the same time, there is no satisfactory explanation of the linear dependence of the logarithm of photocurrent (J_{PhC}) on the inverse thermodynamic temperature (T^{-1}) of the medium [8]. This phenomenon is observed under strong (pre-breakdown) electric

fields. There is no explanation of the nature of the characteristic temperature (T_0) [8, 9]. By means of the analysis of the quantum yield of photogeneration of charge carriers and their mobility, the temperature is renormalized, *i.e.*, T^{-1} is replaced by $T_{\text{eff}}^{-1} = T^{-1} - T_0^{-1}$. According to Ref. [8], the occurrence of T_0 is determined by the relative probabilities, when overcoming the Coulomb barrier of the charged centre of localization of a mobile charge due to the activation and tunnelling transitions. In Refs. [2, 3, 10], the temperature T_0 was registered; however, the physical factors that caused this phenomenon were not discussed. Therefore, it is necessary to find out which characteristics (local or integral) of a sensitized AMS determine the process of photogeneration of charge carriers and to investigate the dependence of the effective temperature on the structure and parameters of the material.

The aim of the work was to study the dependence of the effective temperature (T_0) in the layers of PEPC doped with C₆₀ fullerenes on the concentration of dopants, and to determine the correlation between T_0 and the temperature of the transition of the material into the viscous-flow state.

2. EXPERIMENTAL TECHNIQUES

Samples of PEPC films doped with C₆₀ fullerene were investigated, which were produced by the techniques of toluene solution casting and deposition by thermal evaporation in vacuum. It was taken into account that the properties of nanocomposites are determined by the characteristics of their constituents and the method of their production [8]. The photoluminescence spectra of the PEPC + C₆₀ composite also indicate significant differences in the production of the samples. Therefore, the use of a certain technology for obtaining samples provides a specific nature of their properties and the interaction of existing structures in the PEPC + C₆₀ composite.

With aim to prepare cast samples, a fixed amount of C₆₀ was previously dissolved in toluene heated up to 50°C. After the fullerene powder had been completely dissolved, the solution was weighed, which made it possible to determine its weight and volume concentration. PEPC powder was used for the preparation of composite samples. The PEPC powder was dissolved in toluene without heating. The prepared solutions were mixed with each other in such a way that the concentration of the composite was equal 0; 0.5; 0.7; 2.5 and 3 wt.%. Then, these solutions were cast onto a rigid base with a thickness of $d = 0.9\text{--}1.2 \mu\text{m}$ to produce thick films. After casting, the samples were dried in a thermal cabinet at 80°C for 4 hours. Rigid rectangular 1 cm×2 cm quartz plates were used as substrates. A translucent conductive SnO₂ (ITO) layer with a resistance

of 30 Ohm per square centimetre was applied to the surface of the substrate. The surface AMS layer was applied on the plate from the SnO_2 side. A conductive silver contact was deposited onto the free surface of the AMS layer. The optical absorption spectra were obtained at a Specord M-40 spectrophotometer. The photocurrent density of the samples was measured when they were irradiated with monochromatic light of the visible range. An incandescent lamp with a set of light filters was used to irradiate the samples. The light intensity was varied using neutral light filters and was in the range of 0.2–5 W/m^2 . The electric field strength between the silver contacts and SnO_2 was measured in the range of $(1\text{--}20)\cdot10^7 \text{ V/m}$. The kinetics of the current during irradiation and after turning off the light was recorded using a memory oscilloscope.

The melting point was measured by the well-known optical method of determining the rheological characteristics of thin films [10]. The block-diagram of the device is shown in Fig. 1.

According to the method of [11], the layer of AMS material was electrically charged to the pre-breakdown potential difference. During heating, the thin film reaches the temperature of the transition to the viscous-flow state. Therefore, it becomes possible to form a phase diffraction grating on the free surface of the sample due to the ponderomotive forces caused by the electrocapillary effect.

The melting point of the sample was measured using optical method [3]. The method consists in measuring the logarithmic decrements (w) of the change in the amplitudes of the harmonic relief

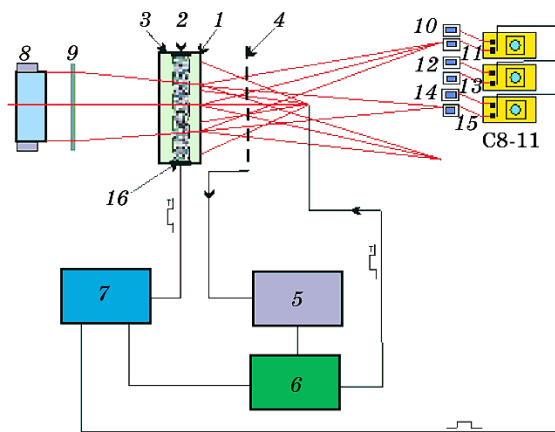


Fig. 1. Block diagram of device for measuring melting point: 1—thin film; 2— SnO_2 ; 3—glass; 4—measuring probe; 5—unit for measuring the potential of thin film; 6—high-voltage generator; 7—block for isothermal heating of thin film; 8—LG-38 laser; 9—Fourier lens; 10–15—photoreceivers; 16—electric contacts.

(h) formed on the free surface of the thin AMS film deposited on a planar substrate and heated above the glass transition temperature. The values of w depend on both the rheological characteristics of the material and the spatial frequency (k) of the relief on the free surface of the layer [3]. The dynamics of h changes over time according to the law

$$h(k, t) = h_0 \exp(w(k)t) \sin(ky), \quad (1)$$

where h_0 is the amplitude at the moment $t = 0$.

The logarithmic decrement of the change in the deformation amplitude of an electrically neutral layer of deformed material is determined by the forces of surface tension and viscosity and can be written as [4, 8]:

$$w(k) = -\frac{\Delta}{2\eta d} \left[\frac{0.5 \operatorname{sh}(2kd) - kd}{\operatorname{ch}^2(kd) + (kd)^2} \right], \quad (2)$$

where Δ is the coefficient of surface tension of the sample, η is the dynamic viscosity of the sample, and d is the sample thickness.

A harmonic relief formed on the surface of the sample; the dynamics of the amplitude of this relief was studied by measuring the first-order intensity of light diffracted on the grating. The intensity of the diffracted light, which is proportional to the square root of the relief amplitude, was taken into account. The rheological parameters of the sample were determined by analysis of the dynamics of the diffraction pattern and using relations (1) and (2). Using the Newton model of the dynamics of heated sample, the kinetics of the logarithm of the ratio of the intensity of diffracted light $I(t)$ to the intensity of light I_0 at the initial moment of time is described by the relationship

$$\ln \left(\frac{I(t)}{I_0} \right) \propto -\frac{\Delta}{\eta} t, \quad (3)$$

At the temperature T_v , the linear dependence (3) begins to break that indicates the transition of the sample from a viscous to a highly-elastic state [12]. The accuracy of T_v measurements is determined by the minimum value of the registered residual relief. The error of this method does not exceed 1.5–2%.

With aim to select the wavelength of the excitation light, optical absorption spectra (A) of composite PEPC + C₆₀ film samples were measured at room temperature. The results of the measurements are shown in Fig. 2.

A comparison of curves 1 and 2 (Fig. 2), which correspond to the spectra of PEPC without dopants and PEPC with 0.5 wt.% C₆₀,

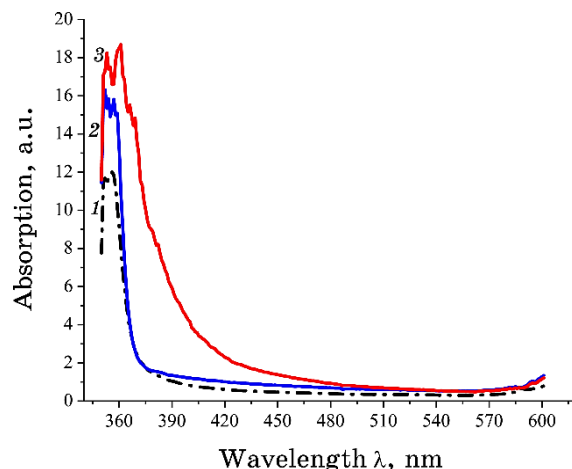


Fig. 2. Absorption spectra of cast samples; radiation source is a hydrogen lamp, $T = 300$ K, quartz substrate: 1—PEPC; 2—PEPC with 0.5 wt.% C₆₀; 3—PEPC with 3 wt.% C₆₀.

shows that the dopant at small concentrations increases the intensity of absorption in the short-wavelength region of the spectrum ($\lambda < 375$ nm) and does not affect the absorption in the long-wavelength region ($\lambda > 375$ nm). This may indicate the additive nature of absorption of the components of the composite. When the concentration of the dopant increases (at least up to 1 wt.%), the absorption spectra change significantly: a wide diffuse band appears in the region $\lambda > 375$ nm. This effect can occur due to the formation of new absorption centres in the region $\lambda > 375$ nm with dimers involved [13].

The occurrence of bands in the spectra of PEPC nanocomposite with fullerenes, which are not observed for pure PEPC and pure C₆₀, is explained by the formation of charge-transfer complexes (CTCs) in the PEPC + C₆₀ system. The formation of these CTCs should lead to the formation of new energy levels, which form zones of jump transport of charge carriers [13].

The characteristics of the quantum yield of the photogeneration of charge carriers were determined by studying the photocurrent. For a reasonable use of this technique, the following factors should be fulfilled: the approximation of small charge drift (the field of volume charge carriers is much lower than the external electric field E), the blocking nature of the electrical contacts of the samples, an insignificant contribution of the processes of thermally activated generation of charges and recombination to the density of current through the sample.

The analysis of weak absorption of light passing through the

sample layer is implemented in the case of $\alpha d \ll 1$, where α is the absorption coefficient of the sample material. When the irradiation is uniform and the approximation of small charge drift is fulfilled, the stationary distributions of concentrations of holes $p(y)$ and electrons $n(y)$ inside the sample layer are determined by the equations (4) and (5). These equations are valid, when the electric field E is directed along the OY axis:

$$G + G_{dark} - \gamma n(y)p(y) + \mu_n E \frac{dn(y)}{dy} = 0, \quad (4)$$

$$G + G_{dark} - \gamma n(y)p(y) - \mu_p E \frac{dp(y)}{dy} = 0. \quad (5)$$

The boundary conditions should take into account the possibility of injection (or exit) of charge carriers and the volume of AMS; so, they have the following form:

$$p(y = 0) = p_0, \quad (6)$$

$$n(y = d) = n_0. \quad (7)$$

Here, G is the efficiency of photogeneration of electrons (holes) per unit time, G_{dark} is the efficiency of thermofield photogeneration of charge carriers, $n_0(p_0)$ is the concentration of electrons (holes) in the near-contact region near the injecting contacts, which determine the injection current, $\mu_n(\mu_p)$ is the mobility of electrons (holes), γ is the constant of geminate recombination of charge carriers, which determines the intensity of recombination processes and governs the nonlinear character of transport processes.

The current density passing through the sample without its illumination (j_{dark}) under a weak effect of recombination processes is described by the equation

$$j_{dark} = e\mu_p Ep_0 + e\mu_n En_0 + eG_{dark}d, \quad (8)$$

where e is the elementary electric charge.

When the sample is irradiated, the current density j_{light} is determined by the expression:

$$j_{light} = \frac{e}{d} \int_0^d [\mu_p Ep(y) + \mu_n En(y)] dy. \quad (9)$$

The solution to the problem (4)–(7) has a rather complex form, which is significantly simplified by taking into account only expressions, which depend on no more than the first order of γ . In this

case, the following relation holds:

$$j_{light} = eGd + j_{dark} - e\gamma \left[dn_0 p_0 + \frac{d^2 G j_{dark}}{2\mu_n \mu_p e E^2} + \frac{d^3 G^2 j_{dark}}{6\mu_n \mu_p E^2} \right], \quad (10)$$

For a given j_{dark} , the maximum possible value $n_0 p_0 = \frac{(j_{dark})^2}{\mu_n \mu_p e^2 E^2}$.

Thus, when the following condition is met:

$$eGd + j_{dark} >> \frac{e\gamma}{\mu_n \mu_p E^2} \left[d \frac{(j_{dark})^2}{e^2} + \frac{d^2 G j_{dark}}{2e} + \frac{d^3 G^2}{6} \right], \quad (11)$$

we have

$$j_{light} \approx eGd + j_{dark}, \quad j \equiv j_{light} - j_{dark}. \quad (12)$$

According to this expression, the current through the irradiated AMS sample is the sum of the injection current and the currents caused by the processes of thermofield generation and photogeneration of electric charge carriers. To fulfil condition (11), a small recombination coefficient, small sample layer thicknesses, and a strong external electric field are needed. The condition (11) is a criterion for the validity of using the results of the investigation of stationary photocurrents in flat layers of low-conductive materials with non-blocking contacts to study the quantum yield of photogeneration of electric charge carriers.

3. DISCUSSION

Current density measurements were carried out in PEPC samples doped with C₆₀ without irradiation. The results of j_{dark} measurements at room temperature for various d are shown in Figs. 3, a, b.

The values of current density j_{dark} between the deposited contacts in the general case were determined by the thermofield generation of charge carriers and the processes of injection from the metal into the AMS layer. As can be seen, the current density is weakly dependent on the electric field at $E > 7 \cdot 10^7$ V/m. This indicates the dominant role of the thermofield generation of charge carriers, and the field dependence of the injection currents should be described by an exponential relationship of the Richardson–Schottky type [4, 8]. A comparison of the plots in Figs. 3, a, b shows that j_{dark} increases with the concentration of C₆₀. This is explained by the clustering of fullerene molecules in the process of forming solid compo-

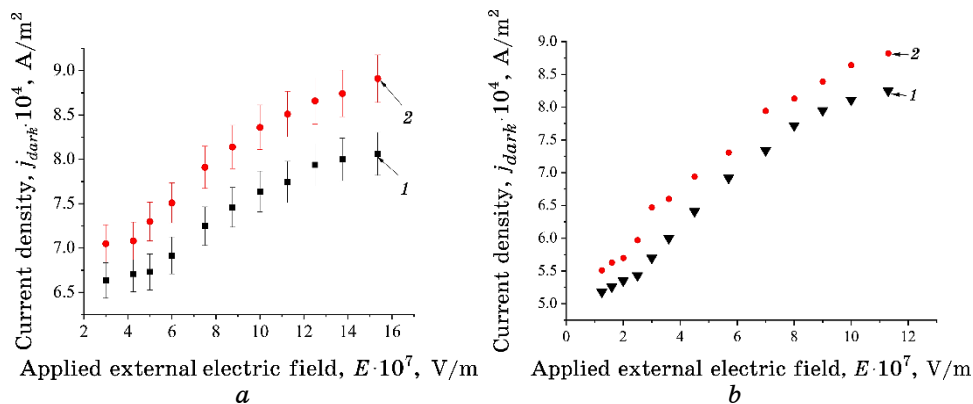


Fig. 3. Dependence of current density j_{dark} on magnitude of applied external electric field at room temperature for samples: *a*—PEPC + 0.7 wt.% C₆₀: 1— $d = 0.9$ μm , 2— $d = 1.2$ μm ; *b*—PEPC + 2.5 wt.% C₆₀: 1— $d = 0.95$ μm , 2— $d = 1.17$ μm .

sites based on the AMS matrix.

The studies of the dependence of the photocurrent density j on the intensity of the excitation light (Fig. 4) showed a proportional relationship between them, taking into account the relationship (12).

It is shown that the dependence (1) in Fig. 4 was obtained at field strength $E = 1.25 \cdot 10^7$ V/m, and the dependence (2), at $E = 1.67 \cdot 10^7$ V/m. A comparison of the currents in Figs. 3, 4 shows that the relationship $j_{dark} \ll j_{light}$ holds. This provides an opportunity to use the

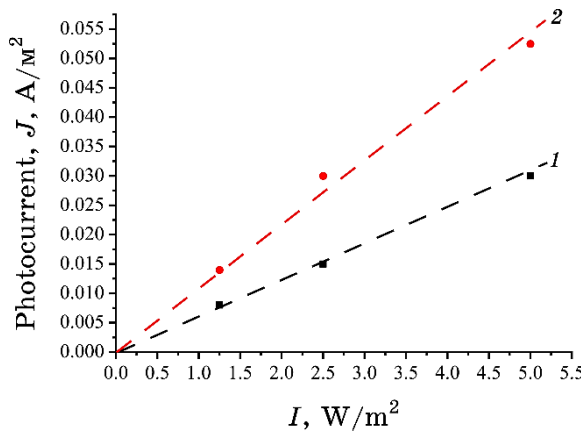


Fig. 4. Dependence of photocurrent for PEPC + 2 wt.% C₆₀ sample on power density of excitation light for different values of field strength.

measurements of steady-state photocurrents and to investigate the quantum yield properties of the photogeneration of charge carriers.

Further analysis shows that the dependence of the photocurrent density (as well as the efficiency of the photogeneration quantum yield) on the intensity of the applied field is well described by the following relationship [4, 7, 8]:

$$j(E) = j_0 \exp\left[\frac{\beta_{PF}\sqrt{E}}{k_B}\left(\frac{1}{T} - \frac{1}{T_0}\right)\right], \quad (13)$$

where j_0 is a value weakly dependent on E , $\beta_{PF} = \sqrt{q^3/\pi\epsilon\epsilon_0}$ is the Poole–Frenkel constant, T is the sample temperature, T_0 is the effective temperature, $\epsilon\epsilon_0$ is the dielectric constant of the material, and k_B is the Boltzmann constant. This dependence well describes the features of the behaviour of the photocurrent density of previously studied samples of fullerene-containing polymers with various sensitizers. The following expression was used for the analysis of the experimental data (13):

$$\ln j(E) \propto \sqrt{E} \frac{\beta_{PF}}{k_B} \left(\frac{1}{T} - \frac{1}{T_0}\right). \quad (14)$$

As can be seen, the value of the Poole–Frenkel constant depends on the dielectric constant of material. For thin-film PEPC + C₆₀ composites produced by toluene solution casting, this parameter is not precisely determined. Therefore, the value of the Poole–Frenkel constant was calculated for several values of the dielectric constant: $\epsilon = 3, 3.5$ and 4 .

Based on these calculations, the dependence of the product of the Poole–Frenkel constant on the difference between the inverse tem-

perature and the inverse effective temperature $\delta = \frac{\beta_{PF}}{k_B} \left(\frac{1}{T} - \frac{1}{T_0}\right)$ on

the value of the effective temperature (this value determines the inclination angle of the dependence $\ln j(E)$) was determined. The results are shown in Fig. 5.

As seen from Fig. 5, the angle of inclination of the dependence $\ln j(E)$ depends significantly both on the dielectric constant of material and on T_0 . Using the dielectric constant 3, which is close to the value for pure PEPC [4], the theoretical dependence $\ln j(E)$ for PEPC samples with various concentrations of fullerenes was calculated.

The calculated and experimental dependences, $\ln j(E)$, were compared. The angle of inclination of the theoretical dependence changed due to the change in T_0 . The T_0 value was chosen in such a way that the root-mean-square difference between the theoretical

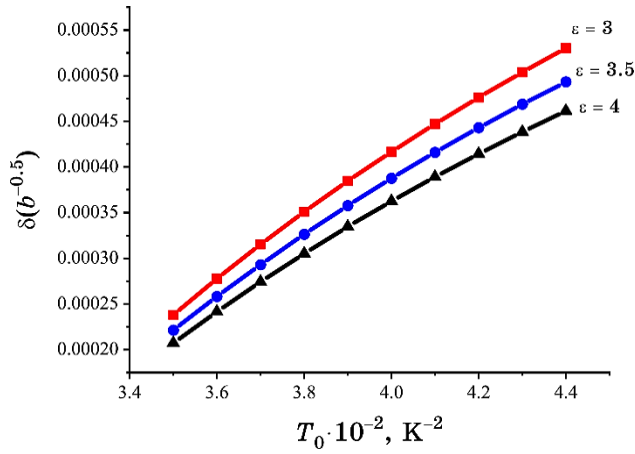


Fig. 5. Dependence of parameter δ on value of effective temperature for various values of dielectric constant: 3, 3.5 and 4.

and experimental curves was minimal. The results of this comparison for the PEPC + C₆₀ nanocomposites with different fullerene content are shown in Figs. 6, *a*, *b*. Using the experimental and theoretical results, the effective temperature of the samples was determined.

As can be seen from the above data, the effective temperature for PEPC samples with different concentrations of fullerenes increases with C₆₀ content, which may indicate decreasing role of tunnelling processes in the electron–hole pair separation [2, 8].

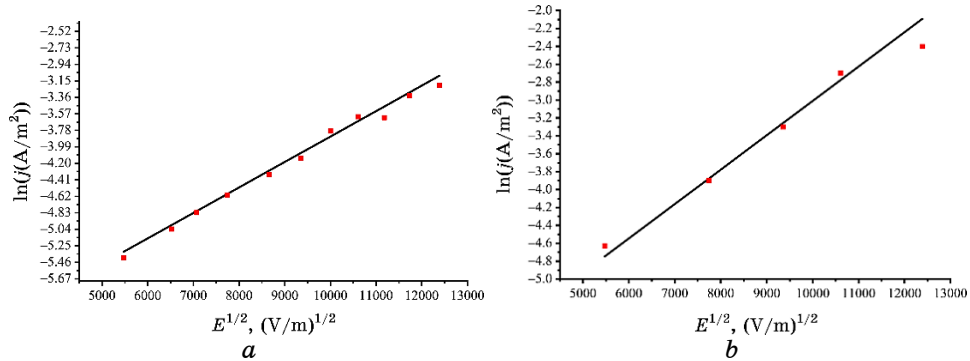


Fig. 6. Dependence of theoretical (solid line) and experimental (red squares) of photocurrent density j logarithm on applied field for samples: *a*—PEPC + 0.7 wt. % C₆₀, for dielectric constant $\epsilon = 3$, temperature 300 K, effective temperature 360 K; *b*—PEPC + 2.5 wt. % C₆₀ for dielectric constant $\epsilon = 3$, temperature 300 K, effective temperature 380 K.

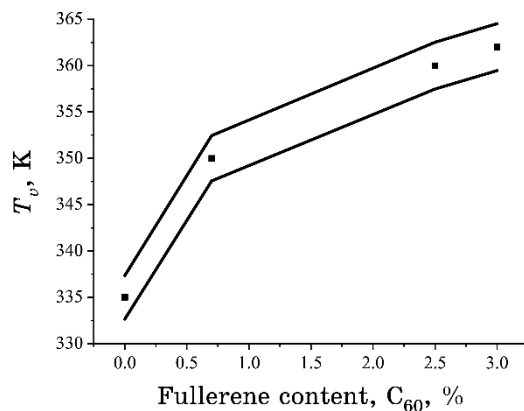


Fig. 7. Dependence of temperature of transition into viscous-flow state on fullerene content in composites.

The temperatures of the transition to the viscous-flow state T_v of PEPC samples with 0, 0.7, 2.5, and 3 wt.% C₆₀ were determined; the results are shown in Fig. 7.

Figure 7 shows that the temperature T_v increases with C₆₀ content. This indicates either an increase in the intensity of intermolecular interaction, or the formation of undeformed hard nanostructures that contain C₆₀; the size of these nanostructures depends on fullerene content. It is worthwhile to note that the T_v values coincide with the values of the effective temperature with an accuracy of 10% ($T_0 \approx T_v$). This effect may indicate that the effective temperature, as well as the melting point, are determined by the forces of intermolecular interaction in the nanocomposite, or both these parameters are determined by the processes of C₆₀ coagulation in the polymer matrix.

4. SUMMARY

At low concentrations of fullerenes in the PEPC matrix (less than 0.5 wt.%), the absorption spectrum in the visible region is formed by independent optical transitions in PEPC and C₆₀. When the concentration of C₆₀ dopant increases (above 1 wt.%), new bands appear in PEPC composites with fullerenes. This non-linear nature of the effect of C₆₀ concentration may indicate the dominant role of the interaction of PEPC molecules with C₆₀ dimers. The dependence of the density of photocurrent generated in volume of PEPC + C₆₀ films on the electric field is consistent with the modified Poole–Frenkel law, which indicates a jump mechanism of the transport of charge carriers during their photogeneration. The modified Poole–Frenkel

constant depends on the C₆₀ concentration that indicates a change in the local dielectric constant in the vicinity of the photogeneration centre when the C₆₀ concentration changes.

The temperature of the transition to the viscous-flow state in the PEPC + C₆₀ composite samples depends on the C₆₀ concentration; it increases with concentration, which indicates increasing intensity of intermolecular interaction, or the formation of undeformed hard nanostructures containing C₆₀. The characteristic temperature coincides with an accuracy of 10% with the value of the melting point of the PEPC + C₆₀ composite that indicates that the photogeneration of charge carriers and melting depend on the same processes.

REFERENCES

1. G. Dennler, N. S. Sariciftci, and C. J. Brabec, *Conjugated Polymer-Based Organic Solar Cells, Semiconducting Polymers: Chemistry, Physics and Engineering* (Eds. G. Hadzioannou and G. G. Hunsray) (Weinheim: Wiley: 2006), vol. 1, p. 455–519.
2. M. A. Zabolotnyi, L. I. Aslamova, E. M. Boboshko, A. A. Kolesnichenko, D. S. Leonov, R. V. Lytvyn, A. Yu. Sezonenko, M. M. Yamshinskij, and M. Yu. Barabash, *Nanosistemi, Nanomateriali, Nanotekhnologii*, **21**, Iss. 2: 261 (2023); <https://doi.org/10.15407/nnn.21.02.261>
3. V. Anand, T. Tahara, and W. M. Lee, *Advanced Optical Holographic Imaging Technologies. Appl. Phys. B*, **128**: 198 (2022); <https://doi.org/10.1007/s00340-022-07921-9>
4. H. H. Vlaikov, M. Yu. Barabash, M. A. Zabolotnyi, D. O. Hryntko, Yu. M. Barabash, and L. Yu. Kunytska, *Formuvannya Nanostruktur Templantnym Syntezom* [Formation of Nanostructures by Template Synthesis] (Kyiv: G. V. Kurdumov Inst. For Metal Physics, N.A.S. of Ukraine: 2010) (in Ukraine).
5. Piotr Grygiel, Karol Falkowski, Daniel Pelczarski, and Waldemar Stampor, *Organic Electronics*, **39**: 328 (2016); <https://doi.org/10.1016/j.orgel.2016.10.023>
6. G. Pfister and D. J. Williams, *J. Chem. Phys.*, **61**: 2416 (1974); <https://doi.org/10.1063/1.1682344>
7. V. Gulbinas, *Lithuanian Journal of Physics*, **60**, No. 1: 1 (2020); <https://doi.org/10.3952/physics.v60i1.4160>
8. N. H. Kuvshynskyi, N. A. Davydenko, and B. M. Komko, *Physics of Amorphous Molecular Semiconductors* (Kyiv: Lybed': 1994) (in Russian).
9. Kye-Si Kwon, Md Khalilur Rahman, Thanh Huy Phung, Stephen D Hoath, Sunho Jeong, Jang Sub Kim, *Flex. Print. Electron.*, **5**: 043003 (2020); <https://doi.org/10.1088/2058-8585/abc8ca>
10. N. P. Kulish, Yu. M. Barabash, M. A. Zabolotny, D. A. Grinko, O. P. Dmitrenko, and E. S. Kobus, *Physics of the Solid State*, **50**: 1374 (2008); <https://doi.org/10.1134/S1063783408070305>
11. Shantharama and Sreeram K Kalpathy, *Electrocapillary Effect in Liquid Films with an Electrically Charged Interface, Materials Today: Proceedings*, **44**, part 2: 3006 (2021); <https://doi.org/10.1016/j.matpr.2021.02.406>

12. Seher Ozkan and Roger L. McMullen, *Rheological Characterization of N-Vinyl Pyrrolidone and N-Vinyl Caprolactam-Based Polymers* (Wiley Online Library: 2021); <https://doi.org/10.1002/9781119468769.hpcbm019>
13. M. A. Zabolotnyj, E. S. Kobus, O. P. Dmitrenko, N. P. Kulish, N. M. Belyj, E. V. Stasjuk, Yu. M. Barabash, G. I. Dovbeshko, E. M. Fesenko, Yu. P. Pirjatinskij, and D. A. Grin'ko, *Fizika Tverdogo Tela*, **52**, Iss. 4: 826 (2010) (in Russian); <https://journals.ioffe.ru/articles/viewPDF/1807>

PACS numbers: 68.37.Hk, 68.55.J-, 81.07.Pr, 81.70.Fy, 82.35.Np

Synthesis, Characterization and Application of PVA–CMC/SiO₂–Cr₂O₃ Nanostructures

Rehab Shather Abdul Hamza and Majeed Ali Habeeb

*College of Education for Pure Sciences,
Department of Physics,
University of Babylon,
Hilla, Iraq*

This study investigates the synthesis of new nanocomposites (NCs) comprising polyvinyl alcohol (PVA) and carboxymethyl cellulose (CMC) with silicon dioxide (SiO₂) and chromium trioxide (Cr₂O₃) for the use in gamma-rays'-shielding applications. The nanocomposites exhibit desirable properties such as low weight, elasticity, high attenuation coefficients, and cost-effectiveness for gamma-rays' shielding. The structural properties of PVA–CMC–SiO₂–Cr₂O₃ nanocomposites are studied. The scanning electron microscopy reveals that the top surface of the PVA–CMC/SiO₂–Cr₂O₃ NCs films exhibits uniform and cohesive aggregates or fragments distributed randomly, when the weight percentage reaches 8%. The uniform distribution of nanoparticles (NPs) in the blend is evidenced by the optical microscope images and leads to a continuous network within the polymer matrix. The study results regarding the utilization of gamma-rays' shielding demonstrate that the nanocomposites composed of PVA–CMC/SiO₂–Cr₂O₃ display significant attenuation coefficients for gamma rays.

У цьому дослідженні досліджується синтез нових нанокомпозитів (НК), що складаються з полівінілового спирту (ПВА) та карбоксиметилцелюлози (КМЦ) з діоксидом Силіцію (SiO₂) та триоксидом Хрому (Cr₂O₃) для використання в екрануванні гамма-променів. Нанокомпозити демонструють такі бажані властивості, як мала вага, пружність, високі коефіцієнти загасання й економічність для екранування гамма-променів. Досліджено структурні властивості нанокомпозитів ПВА–КМЦ–SiO₂–Cr₂O₃. Сканувальна електронна мікроскопія показує, що верхня поверхня плівок ПВА–КМЦ/SiO₂–Cr₂O₃ НК демонструє однорідні та зв'язані агрегати або фрагменти, розподілені випадковим чином, коли ваговий відсоток досягає 8%. Рівномірний розподіл наночастинок (НЧ) у суміші підтверджується зображеннями в оптичному мікроскопі та приводить до безперервної мережі всередині полімерної матриці. Результати дослідження щодо використання екранування гамма-променів

демонструють, що нанокомпозити, які складаються з ПВА–КМЦ/SiO₂–Cr₂O₃, демонструють значні коефіцієнти загасання гамма-променів.

Key words: nanocomposites, SiO₂–Cr₂O₃ nanoparticles, polyvinyl alcohol, carboxymethyl cellulose, structural properties, gamma-rays' shielding.

Ключові слова: нанокомпозити, наночастинки SiO₂–Cr₂O₃, полівінілової спирт, карбоксиметилцелюлоза, структурні властивості, екранування гамма-променів.

(Received 30 June, 2023)

1. INTRODUCTION

Nanotechnology is a nascent scientific discipline that emerged from the observation that materials exhibit markedly distinct characteristics at the nanoscale in contrast to their properties at larger particle sizes [1]. Nanotechnologies are considered crucial technologies of the current century, and significant research endeavours are being undertaken in this domain. There is a possibility that additional applications will be accessible shortly. Nanotechnology exhibits significant potential across multiple domains due to the distinctive physical, chemical, and biological properties of structural features at the nanoscale compared to their macroscopic counterparts [2, 3]. The field of nanomaterials research adopts a materials science-oriented methodology in the realm of nanotechnology. One nanometer (nm) is one billionth of a meter. Nanomaterials are materials with a characteristic unit size ranging from 1 to 100 nanometers. The distinctive characteristics of these materials are frequently attributed to their dimensions, morphology, and chemical constitution [4]. Two primary factors contribute to nanomaterials' distinct properties compared to other materials. The augmentation of the relative surface area and the manifestation of quantum effects are being considered [5]. Nanocomposites are composite materials containing at least one nanometric scale component (10^{-9} m) [6].

Nanocomposites (NCs) are composed of polymers, both natural and synthetic and nanomaterials. The term 'nanomaterials' refers to materials, which possess topography at the nanoscale or are constructed of nanosize building components. Nanocomposites' fundamental concept involves establishing a substantial interface between the polymer matrix and the nanosize constituent units. Nanocomposites' mechanical, electrical, thermal, optical, electrochemical, and catalytic properties are expected to exhibit significant differences from those of their constituent materials [7, 8]. Polyvinyl alcohol (PVA) is a water-soluble synthetic polymer. Its low toxicity and exceptional properties characterize it as a wound dressing and biore-

actor material. PVA is characterized by its semi-crystalline nature, attributed to the coexistence of amorphous and crystalline regions. This unique feature results in interfacial effects that enhance the materials' physical properties [9, 10].

Polyvinyl alcohol exhibits distinctive characteristics, including biodegradability, environmental sustainability, good chemical stability, elongation, tensile strength, elevated abrasion resistance, good charge storage capacity, flexibility, facile film process ability, thermal stability, and economical manufacturing expenses [11, 12]. The substance undergoes rapid decomposition when exposed to elevated temperatures. Various additives, including polymers, salts, nanocomposites, and ions, are commonly incorporated into polyvinyl alcohol (PVA) to enhance and alter its characteristics [13]. PVA exhibits inadequate electrical insulation properties, but can acquire conductivity upon doping with certain inorganic fillers [14].

Carboxymethyl cellulose (CMC) is a significant polymer in various industrial sectors such as drag reduction, detergents, drugs, paper, and oil well drilling operations, textiles, and foods. The diverse characteristics of carboxymethyl cellulose are contingent upon three key factors: the distribution of carboxyl substituents along the polymer chains, the average carboxyl content per hydro glucose unit, and the molecular weight of the polymer [15]. The anionic polymer CMC is derived from natural cellulose through chemical modification and is characterized by its biodegradability, biocompatibility, and natural origin [16]. The particles of silicon dioxide (SiO₂) exhibit solid plasticizing properties that have the potential to improve both chemical and mechanical characteristics [17].

Silicon dioxide (SiO₂) is an amorphous, nontoxic material with many potential applications. Nanofillers composed of fumed silicon dioxide (SiO₂) are utilized in electronics and thermoplastic polymers [18]. SiO₂ nanoparticles are utilized as additives in electronic packaging and thermoplastic polymers [19]. Chromium oxide (Cr₂O₃) is classified as a *p*-type metal oxide semiconductor with a hexagonal crystal structure. It possesses remarkable properties, including exceptional decay resistance, the ability to conduct electricity, and a high melting point. These valuable properties have enabled its application in various practical biomedical contexts. The utilization of Cr₂O₃ nanoparticles as a highly effective catalyst in chemical reactions has been observed [20]. The radiation phenomenon is characterized by the transfer of energy from a source through space, which can penetrate various materials [21]. Synthetic polymers have the potential to be utilized in the production of innovative materials that can serve as radiation shielding. Moreover, the supplementary benefits of low industrial cost, durability, and high chemical and thermal stability are among the favoured characteristics and qual-

ties of enhanced shielding [22]. The present study endeavours to fabricate a nanosystem comprising PVA, CMC, SiO_2 , and Cr_2O_3 for radiation attenuation.

2. EXPERIMENTAL PART

Silicon dioxide (SiO_2)–chromium trioxide (Cr_2O_3) nanoparticles (NPs) were used in various weight percentages in the films of nanocomposites (0, 2, 4, 6, and 8 wt.%), which were created using the casting process.

The process involved dissolving pure PVA and CMC (68/32) in 40 ml of distilled water for 40 minutes while stirring with a magnetic stirrer at 70°C to achieve a more homogeneous solution; this resulted in the creation of PVA–CMC– SiO_2 – Cr_2O_3 nanocomposite films. The fluid was confined within a Petri dish. The resultant solution was subjected to a four-day drying period at ambient temperature after synthesizing polymer mixture nanocomposites.

To measure, NCs were removed from the petri dish and used. The surface morphology of the PVA–CMC– SiO_2 – Cr_2O_3 nanocomposites was observed using a scanning electron microscope (Model/Mira-3; Details/1.2 nm at 30 kV; 2.3 nm at 3 kV; Manufacturing and Country/Tescan, France) and an Olympus type Nikon-73346 optical microscope with a magnifying power of $\times 10$ and a camera for microscopic photography was utilized.

The present study investigates the gamma ray attenuation properties of SiO_2 – Cr_2O_3 nanoparticles with varying volume fractions, utilizing nanocomposites for gamma ray shielding. Samples were positioned before a collimated beam from gamma-ray sources ($\text{Cs}-137.5$ mci). The separation between the gamma ray and the detector is 2 cm. The present study involved the determination of linear attenuation coefficients through the utilization of Geiger counter measurements. The measurements were conducted on transmitted gamma ray fluxes that passed through nanocomposites composed of PVA–CMC– SiO_2 – Cr_2O_3 NCs.

The equation presented below can be utilized to calculate the linear attenuation coefficients (μ) based on the material thicknesses [23]:

$$N = N_0 e^{-\mu x}, \quad (1)$$

where the number of radiation particles, denoted as N_0 , detected over a specified time interval in the absence of an absorber, and the attenuation coefficient of gamma radiation, represented by μ . Additionally, the study examines the number of particles, denoted as N , detected over the same time interval when a sample of thickness x is introduced.

3. RESULTS AND DISCUSSIONS

3.1. Scanning Electron Microscope (SEM) Measurements of PVA-CMC/SiO₂-Cr₂O₃ NCs

Scanning electron microscopy (SEM) images give a good impression of the size and morphology of PVA-CMC/SiO₂-Cr₂O₃ nanocomposites in Fig. 1. The findings indicate that the polymer image (*a*) exhibits soft-

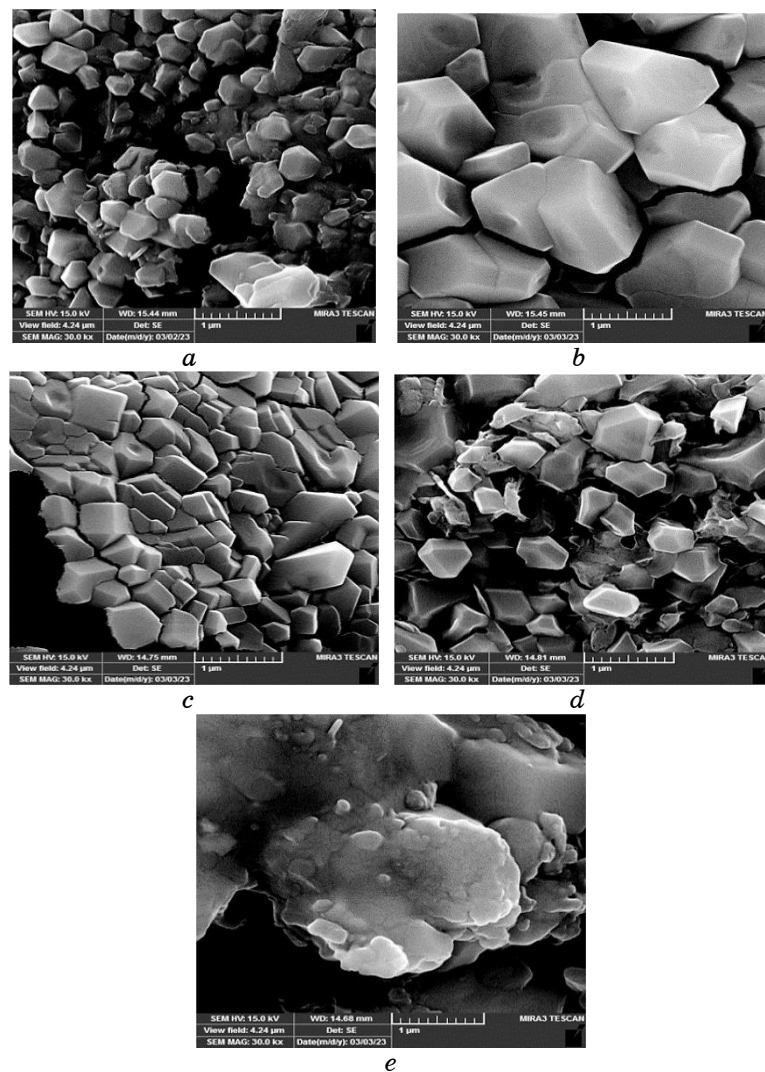


Fig. 1. SEM images of PVA-CMC/SiO₂-Cr₂O₃ NCs: (a) PVA-CMC; (b) 2 wt.% SiO₂-Cr₂O₃; (c) 4 wt.% SiO₂-Cr₂O₃; (d) 6 wt.% SiO₂-Cr₂O₃; (e) 8 wt.% SiO₂-Cr₂O₃.

ness, uniformity, and coherence [21]. The alterations in the surface morphology of PVA–CMC/SiO₂–Cr₂O₃ nanocomposites are observed to be correlated with the incorporation of SiO₂ and Cr₂O₃ nanoparticles, as depicted in Figs. 1, *b*, *c*, *d* and *e*. The photographic evidence indicates that the size of granule particles is increasing with the augmentation of the SiO₂ and Cr₂O₃ nanoparticles' content.

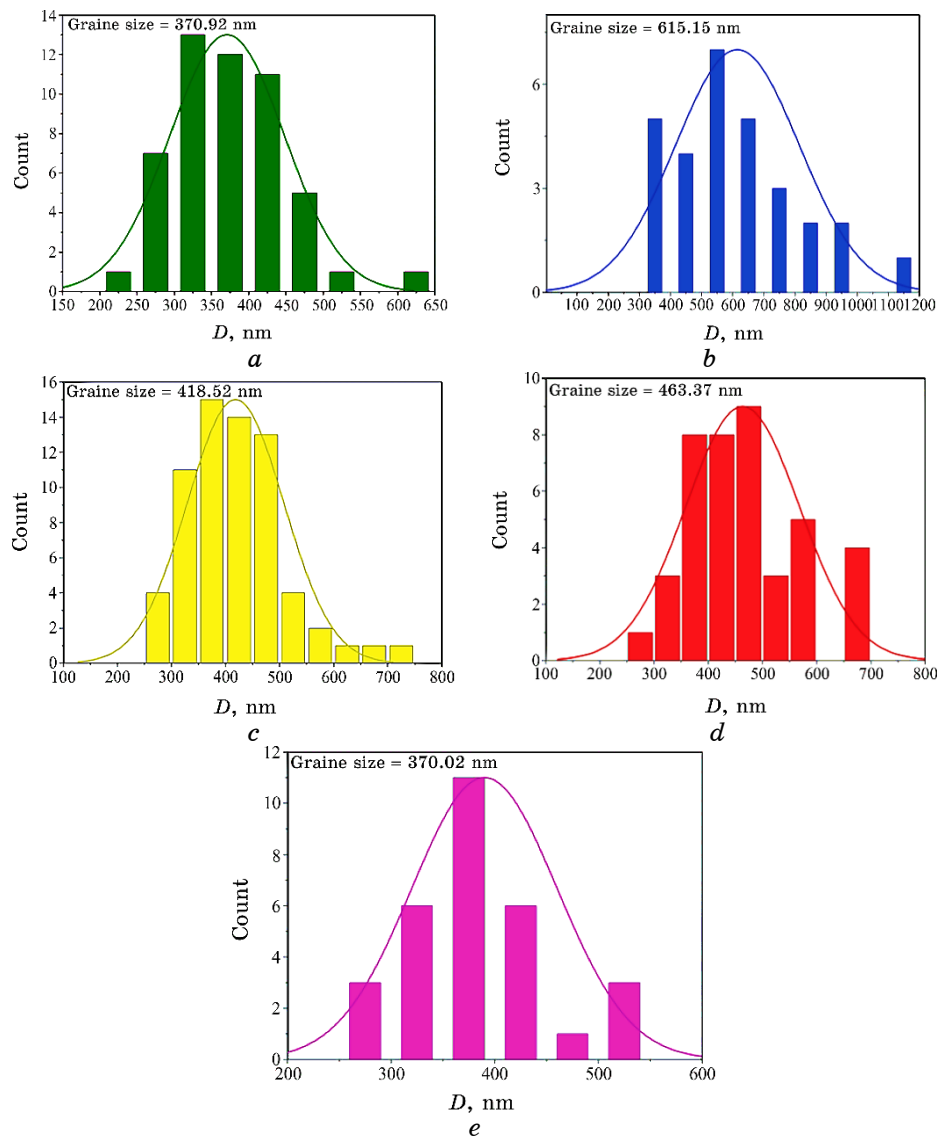


Fig. 2. Grain size for PVA–CMC/SiO₂–Cr₂O₃ NCs: (*a*) PVA–CMC; (*b*) 2 wt.% SiO₂–Cr₂O₃; (*c*) 4 wt.% SiO₂–Cr₂O₃; (*d*) 6 wt.% SiO₂–Cr₂O₃; (*e*) 8 wt.% SiO₂–Cr₂O₃.

The surface morphology of the nanocomposites composed of PVA, CMC, SiO₂, and Cr₂O₃ displays numerous dispersed lumps or pieces on the top surface. The image depicts how the amount of silicon dioxide (SiO₂) and chromium trioxide (Cr₂O₃) nanoparticles on the surface increases as their concentration rises [24–27]. Figure 2 shows the grain size for PVA-CMC/SiO₂-Cr₂O₃ nanocomposites calculate from SEM images.

3.2. Optical Microscope for PVA-CMC-SiO₂-Cr₂O₃ NCs

Figure 3 displays magnified images of PVA-CMC-SiO₂-Cr₂O₃

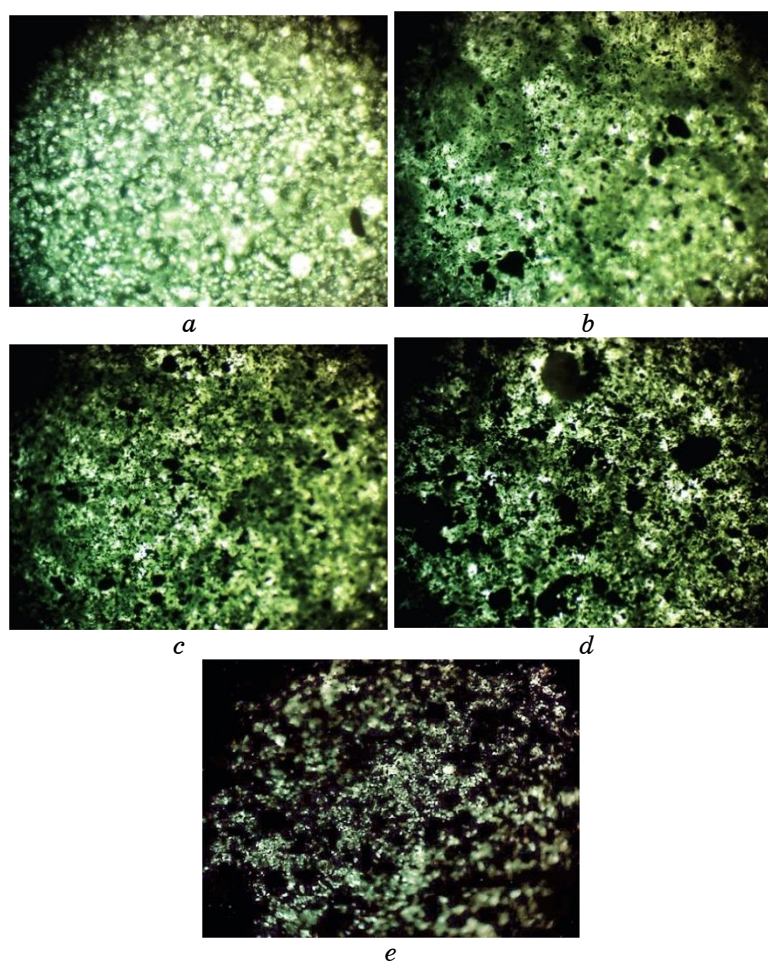


Fig. 3. Optical microscope images of PVA-CMC/SiO₂-Cr₂O₃ NCs at a magnification ($\times 10$): (a) PVA-CMC; (b) 2 wt.% SiO₂-Cr₂O₃; (c) 4 wt.% SiO₂-Cr₂O₃; (d) 6 wt.% SiO₂-Cr₂O₃; (e) 8 wt.% SiO₂-Cr₂O₃.

nanocomposite films at different concentrations. The nanocomposites exhibited distinguishable characteristics between the $\text{SiO}_2\text{-Cr}_2\text{O}_3$ nanoparticles and the PVA/CMC blend. Upon incorporating $\text{SiO}_2\text{-Cr}_2\text{O}_3$ nanoparticles into the polymeric blend, they exhibit a uniform dispersion throughout the blend and a high degree of proximity. Upon reaching a concentration of 8 wt.%, the $\text{SiO}_2\text{-Cr}_2\text{O}_3$ particles transition to form a cohesive network. Nanoparticles are linked within polymers, specifically in polyvinyl alcohol (PVA) and carboxymethyl cellulose (CMC), in the context of films. The network depicted in Figs. 3, *a*, *b*, *c*, *d*, and *e* facilitates the movement of charge carriers, resulting in a modification of the material characteristics [28–30].

3.3. Application of PVA–CMC/ $\text{SiO}_2\text{-Cr}_2\text{O}_3$ NCs for Gamma-Rays' Shielding

Figure 4 illustrates the oscillations of (N/N_0) in PVA–CMC composites with different concentrations of $\text{SiO}_2\text{-Cr}_2\text{O}_3$ nanoparticles. The attenuation of radiation increases due to the rise in concentrations of $\text{SiO}_2\text{-Cr}_2\text{O}_3$ nanoparticles, leading to a decrease in transmission radiation [31–33]. Figure 5 shows increasing $\ln(N/N_0)$ of PVA/CMC mixture with increases of $\text{SiO}_2\text{-Cr}_2\text{O}_3$ NPs concentrations [34].

The graphical representation in Fig. 6 depicts the fluctuation in attenuation coefficients of gamma radiation concerning the concentrations of $\text{SiO}_2\text{-Cr}_2\text{O}_3$ nanoparticles in a PVA–CMC blend. The escalation observed in attenuation coefficients with increasing nanopar-

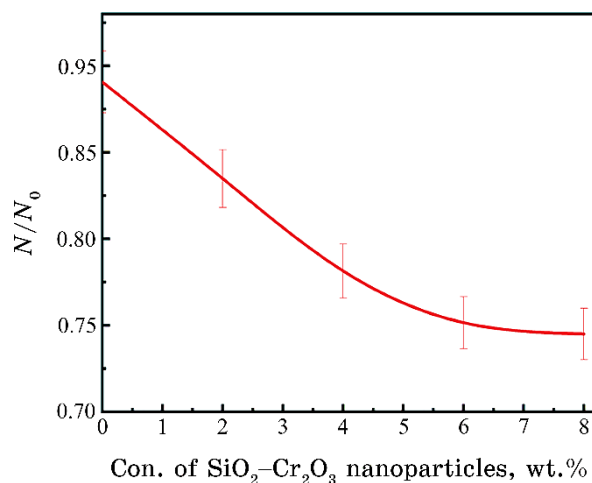


Fig. 4. Variance of (N/N_0) for PVA/CMC mixture with different concentrations of $\text{SiO}_2\text{-Cr}_2\text{O}_3$ NPs.

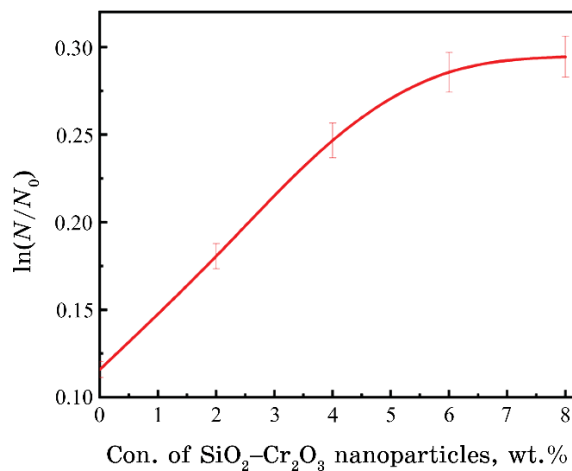


Fig. 5. Change of $\ln(N/N_0)$ for PVA/CMC blend with different concentrations of $\text{SiO}_2/\text{Cr}_2\text{O}_3$ nanoparticles

ticle concentrations can be attributed to the absorption or reflection of gamma radiation by the nanocomposite shielding materials, as documented in Refs. [35–39].

Upon comparison, the outcomes of polymer nanocomposites and concrete, as depicted in figure below, exhibited a high degree of similarity. The composite polymer exhibited superior properties to concrete owing to its enhanced mobility, absence of electrical con-

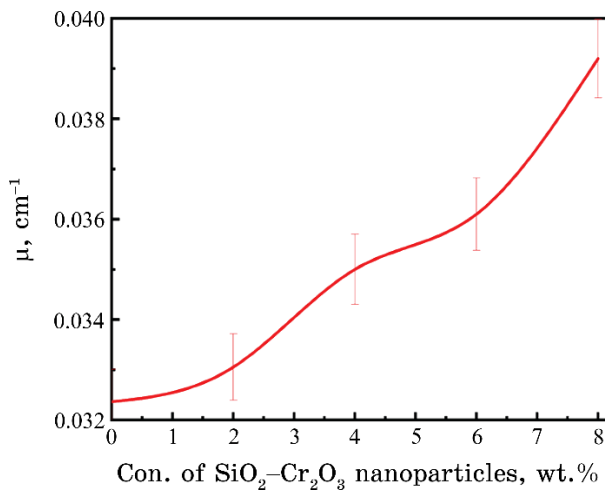


Fig. 6. Variance of attenuation coefficients of gamma radiation for PVA/CMC blends with different concentrations of $\text{SiO}_2/\text{Cr}_2\text{O}_3$ nanoparticles.

ductivity, and potential to impede the escape of neutrons [40–43].

4. CONCLUSIONS

The present study involved the production of plastic nanocomposite films utilizing the casting solution fabrication method. The films were comprised of silicon dioxide (SiO_2), chromium trioxide (Cr_2O_3) nanoparticles, polyvinyl alcohol (PVA), and carboxymethyl cellulose (CMC). The top surface of the PVA–CMC/ SiO_2 – Cr_2O_3 NCs films was analysed using SEM to depict its surface morphology. The results revealed the presence of diverse fragments or aggregates that were randomly dispersed across the surface. When silicon dioxide (SiO_2) and chromium trioxide (Cr_2O_3) nanoparticles are formed in a polymer mixture at a concentration of eight percent by weight, images taken using an optical microscope (OM) reveal that they form a continuous network. Finally, as concentration NPs increases, the attenuation coefficient rises for gamma radiation with an increase in the concentration of SiO_2 – Cr_2O_3 nanoparticles.

REFERENCES

1. A. J. Hassan, *Journal of Modern Physics*, **5**, No. 18: 2184 (2014); <https://doi.org/10.4236/jmp.2014.518212>
2. M. A. Habeeb, *European Journal of Scientific Research*, **57**, No. 3: 478 (2011).
3. A. Khan, *Journal of Nanomaterials*, **2012**: 66 (2012).
4. M. A. Habeeb and Z. S. Jaber, *East European Journal of Physics*, **4**: 176 (2022); doi:[10.26565/2312-4334-2022-4-18](https://doi.org/10.26565/2312-4334-2022-4-18)
5. A. H. Hadi and M. A. Habeeb, *Journal of Mechanical Engineering Research and Developments*, **44**, No. 3: 265 (2021); <https://jmerd.net/03-2021-265-274>
6. Q.M. Jebur, A. Hashim, and M. A. Habeeb, *Egyptian Journal of Chemistry*, **63**: 719 (2020); <https://dx.doi.org/10.21608/ejchem.2019.14847.1900>
7. N. Othman, N. A. Azahari, and H. Ismail, *Malaysian Polymer Journal*, **6**, No. 6: 147 (2011).
8. S. M. Mahdi and M. A. Habeeb, *Optical and Quantum Electronics*, **54**, Iss. 12: 854 (2022); <https://doi.org/10.1007/s11082-022-04267-6>
9. N. Hayder, M. A. Habeeb, and A. Hashim, *Egyptian Journal of Chemistry*, **63**: 577 (2020); doi:[10.21608/ejchem.2019.14646.1887](https://dx.doi.org/10.21608/ejchem.2019.14646.1887)
10. J. Selvi, S. Mahalakshmi, and V. Parthasarathy, *Journal of Inorganic and Organometallic Polymers and Materials*, **27**: 1918 (2017); <https://doi.org/10.1007/s10904-017-0662-1>
11. M. A. Habeeb, A. Hashim, and N. Hayder, *Egyptian Journal of Chemistry*, **63**: 709 (2020); <https://dx.doi.org/10.21608/ejchem.2019.13333.1832>
12. A. Hashim, M. A. Habeeb, and Q. M. Jebur, *Egyptian Journal of Chemistry*, **63**: 735 (2020); <https://dx.doi.org/10.21608/ejchem.2019.14849.1901>

13. S. M. Mahdi and M. A. Habeeb, *Physics and Chemistry of Solid State*, **23**, No. 4: 785 (2022); [doi:10.15330/pcss.23.4.785-792](https://doi.org/10.15330/pcss.23.4.785-792)
14. F. Liu, S. Wang, M. Zhang, M. Ma, C. Wang, and J. Li, *Applied Surface Science*, **280**: 686 (2013); <https://doi.org/10.1016/j.apsusc.2013.05.043>
15. M. A. Habeeb and W. S. Mahdi, *International Journal of Emerging Trends in Engineering Research*, **7**, No. 9: 247 (2019); [doi:10.30534/ijeter/2019/06792019](https://doi.org/10.30534/ijeter/2019/06792019)
16. M. A. Habeeb and R. S. Abdul Hamza, *Journal of Bionanoscience*, **12**, No. 3: 328 (2018); <https://doi.org/10.1166/jbns.2018.1535>
17. M. Barakat, R. Bahareth, E. Mahrous, S. Aldawood, and S. Nouh, *The European Physical Journal Applied Physics*, **97**: 35 (2022); <https://doi.org/10.1051/epjap/2022210268>
18. M. A. Habeeb, A. Hashim, and N. Hayder, *Egyptian Journal of Chemistry*, **63**: 697 (2020); <https://dx.doi.org/10.21608/ejchem.2019.12439.1774>
19. M. A. Habeeb and W. K. Kadhim, *Journal of Engineering and Applied Sciences*, **9**, No. 4: 109 (2014); [doi:10.36478/jeasci.2014.109.113](https://doi.org/10.36478/jeasci.2014.109.113)
20. K. Rajesh, V. Crasta, K. N. B. Rithin, G. Shetty, and P. D. Rekha, *J. Polym. Res.*, **26**, No. 4: 1 (2019); <https://doi.org/10.1007/s10965-019-1762-0>
21. M. A. Habeeb, *Journal of Engineering and Applied Sciences*, **9**, No. 4: 102 (2014); [doi:10.36478/jeasci.2014.102.108](https://doi.org/10.36478/jeasci.2014.102.108)
22. J. B. Ramesh and K. K. Vijaya, *Chemtech.*, **7**: 171 (2014).
23. S. M. Mahdi and M. A. Habeeb, *Digest Journal of Nanomaterials and Biostructures*, **17**, No. 3: 941 (2022); <https://doi.org/10.15251/DJNB.2022.173.941>
24. S. Ju, M. Chen, H. Zhang, and Z. Zhang, *Journal of express Polymer Letters*, **8**, No. 9: 682 (2014); <https://doi.org/10.3144/expresspolymlett.2014.71>
25. A. H. Hadi and M. A. Habeeb, *Journal of Physics: Conference Series*, **1973**, No. 1: 012063 (2021); [doi:10.1088/1742-6596/1973/1/012063](https://doi.org/10.1088/1742-6596/1973/1/012063)
26. Q. M. Jebur, A. Hashim, and M. A. Habeeb, *Egyptian Journal of Chemistry*, **63**, No. 2: 611 (2020); <https://dx.doi.org/10.21608/ejchem.2019.10197.1669>
27. G. Aras, E. L. Orhan, I. F. Selçuk, S. B. Ocak, and M. Ertuğrul, *Procedia-Social and Behavioral Sciences*, **95**: 1740 (2015); <https://doi.org/10.1016/j.sbspro.2015.06.295>
28. M. Roy, J. AK Bajpai, and R. G Mahloniya, *Advanced Materials Letters*, **3**, No. 5: 426 (2012); <https://doi.org/10.5185/amlett.2012.6373>
29. M. H. Dwech, M. A. Habeeb, and A. H. Mohammed, *Ukr. J. Phys.*, **67**, No. 10: 757 (2022); <https://doi.org/10.15407/uje67.10.757>
30. S. M. Mahdi and M. A. Habeeb, *Polymer Bulletin*, 2023; <https://doi.org/10.1007/s00289-023-04676-x>
31. M. Martin, N. Prasad, M. M Siva lingam, D. Sastikumar, and B. Karthikeyan, *Journal of Material Science: Material in Electronics*, **29**: 365 (2018); <https://doi.org/10.1007/s10854-017-7925-z>
32. M. A. Habeeb and W. H. Rahdi, *Optical and Quantum Electronics*, **55**, Iss. 4: 334 (2023); <https://doi.org/10.1007/s11082-023-04639-6>
33. A. A. Mohammed and M. A. Habeeb, *Silicon*, **15**: 5163 (2023); <https://doi.org/10.1007/s12633-023-02426-2>

34. R. Dalven and R. Gill, *J. Appl. Phys.*, **38**, No. 2: 753 (1967);
[doi:10.1063/1.1709406](https://doi.org/10.1063/1.1709406)
35. N. K. Al-Sharifi and M. A. Habeeb, *Silicon*, **15**: 4979 (2023);
<https://doi.org/10.1007/s12633-023-02418-2>
36. R. N. Bhagat and V. S. Sangawar, *Int. J. Sci. Res. (IJSR)*, **6**: 361 (2017).
37. R. S. Abdul Hamza and M. A. Habeeb, *Optical and Quantum Electronics*, **55**, Iss. 8: 705 (2023); <https://doi.org/10.1007/s11082-023-04995-3>
38. A. Goswami, A. K. Bajpai, and B. K. Sinha, *Polym. Bull.*, **75**, No. 2: 781 (2018); <https://doi.org/10.1007/s00289-017-2067-2>
39. S. M. Mahdi and M. A. Habeeb, *AIMS Materials Science*, **10**, No. 2: 288 (2023); [doi:10.3934/matersci.2023015](https://doi.org/10.3934/matersci.2023015)
40. O. E. Gouda, S. F. Mahmoud, A. A. El-Gendy, and A. S. Haiba, *Indonesian Journal of Electrical Engineering*, **12**, No. 12: 7987 (2014);
<https://doi.org/10.11591/telkomnika.v12i12.6675>
41. M. A. Habeeb and R. S. A. Hamza, *Indonesian Journal of Electrical Engineering and Informatics*, **6**, No. 4: 428 (2018); [doi:10.11591/ijeei.v6i1.511](https://doi.org/10.11591/ijeei.v6i1.511)
42. A. R. Farhadizadeh and H. Ghomi, *Materials Research Express*, **7**, No. 3: 36502 (2020); <https://doi.org/10.1088/2053-1591/ab79d2>
43. P. Vasudevan, S. Thomas, K. Arunkumar, S. Karthika, and N. Unnikrishnan, *Journal of Materials Science and Engineering*, **73**: 1 (2015); [doi:10.1088/1757-899X/73/1/012015](https://doi.org/10.1088/1757-899X/73/1/012015)

PACS numbers: 07.07.Df, 78.67.Pt, 81.05.Xj, 81.20.Ym, 84.40.Ba

Metamaterial Sensors in Liquid Detection: An Illustrious Review

N. V. Krishna Prasad¹ and N. Madhavi²

¹*Department of Physics, G.S.S.,
GITAM University,
Bengaluru, India*

²*Govt. College (Autonomous),
Department of Statistics,
Rajhamundry, India*

Liquid detection has been one of the buzzwords that refer to sensing of various liquids, which include water, chemicals, oils, *etc.* This detection gains more significance with the advent of metamaterials. Metamaterials are proved well suited in antenna designing, cloaking devices, solar cells, and sensors. Many papers reported metamaterial sensors, which can detect liquid chemicals, oils, *etc.* through shift in resonance frequency. Very few papers reported the applications of metamaterial sensors in water treatment. Water purification is one of the prime essentials for the existence of healthy humankind. It can be used to remove unwanted chemicals, contaminants and gases from water. The process of water purification can be done with various methods such as thermal, adsorption, distillation, desalination, reverse osmosis, *etc.* The main aim is to produce water required for specific purpose. In this context, role of metamaterials in water purification is of prime significance. Keeping this in view, an attempt is made to review the importance of metamaterial sensors in liquid detection along with water purification and its importance in comparison with earlier techniques already available.

Виявлення рідини було одним із модних слів, які стосуються зондування різних рідин, до яких належать вода, хемікати, олії тощо. Це виявлення набуває більшого значення з появою метаматеріялів. Доведено, що метаматеріяли добре підходять для розробки антен, маскувальних пристройів, сонячних батарей і давачів. У багатьох роботах повідомлялося про давачі з метаматеріялів, які можуть виявляти рідкі хемікати, масла тощо через зсув резонансної частоти. Дуже мало статей повідомляли про застосування давачів з метаматеріялів у обробленні води. Очищення води є однією із найважливіших умов існування здорового людства. Його можна використовувати для видалення з води

небажаних хемічних речовин, забруднень і газів. Процес очищення води може здійснюватися різними методами, такими як термічні, адсорбційні, дистиляційні, опріснювальні, зворотня осмоза тощо. Основною метою є одержання води, необхідної для певних цілей. У цьому контексті роль метаматеріалів у очищенні води має першорядне значення. Зважаючи на це, зроблено спробу переглянути важливість давачів з метаматеріалів у виявленні рідин разом із очищенням води та важливість їх у порівнянні з попередніми, вже доступними методами.

Key words: metamaterial (MTM) sensors, liquid detection, water purification, sludge volume index, finite integration technique (FIT).

Ключові слова: датчики з метаматеріалів, виявлення рідини, очищення води, індекс об'єму мулу, метод скінченної інтеграції.

(Received 7 June, 2023)

1. INTRODUCTION

It is not possible to think of any application related to metamaterial without Russian physicist Veselago (1968) who demonstrated negative refraction with tailored materials [1]. He indicated that negative permittivity and permeability values lead to negative refraction in a material. Such material was developed by Pendry after thirty years [2]. Materials tailored for electromagnetic properties beyond their inherent nature are called metamaterials (MTM).

MTM's find various applications in design of antennas, cloaking devices, sensors *etc.* to name the few. Antennas designed metamaterials exhibit lightweight, high gain, high bandwidth and maximum channel efficiency [3]. Cloaking makes objects to be invisible. This technique became prominent with the advent of metamaterials. Cloaking techniques involve acoustic or EM waves with current focus on extension of bandwidth for invisibility of specific objects. Cloaking is achieved by using metamaterials by deflecting certain frequencies [4–19].

Solar cells designed with metamaterials are of prime importance. They can reduce reflected light and increase incident light. At the same time, solar cells designed with MTM's have limited absorption for majority of the solar spectrum. Keeping this in view, various absorbers that utilize solar energy in effective ways were innovated with metamaterials. Semi-circular solar cells with 77% absorption of solar and 84% of visible regions were reported with Ni and SiN materials [20]. Solar cells designed with silicon and metamaterial reflectors are reported to have high efficiency [21]. Apart from these applications MTM's play vital role, when used as sensing devices.

2. METAMATERIAL SENSORS

Sensors have become part of our daily life. They can be designed with different materials; however, sensors developed from metamaterials find various advantages as compared to ordinary materials. In spite of some limitations on usage of metamaterials as sensors [22, 23], they are preferred. Broadband materials can be replaced with sensors as they can operate at single frequency. In addition, MTM sensors possess high sensitivity and resolution [24] making metamaterials significant in enhancing the sensors performance. Even though MTM sensors are widely developed for various applications in measuring humidity, temperature, *etc.*, designing and fabrication of MTM sensors in liquid detection plays a vital role. Liquid detection can be related to chemicals, acids as well as water, oil, *etc.*

3. METAMATERIAL SENSORS IN LIQUID DETECTION

Detection of chemicals having similar dielectric properties is a major task as the principle of detection depends on the change in dielectric parameters of the samples under investigation. In this context, an MTM-based sensor capable of detecting liquid chemicals between 8 GHz to 12 GHz was designed and fabricated. This was achieved by testing different designs using CST microwave studio in which a genetic algorithm was embedded and optimizing the required resonator dimensions.

Any MTM sensor generally consists of a resonator of designated shape and dimensions. Depending on the type of application, the structure of resonator is changed. The main principle behind the design of resonator depends on the frequency shift between simulated and experimental values or a comparison between similar samples in a particular band. Many resonators of different shape and dimensions were reported depending on the sensing application.

Figure 1 shows the MTM based sensor that operates in X-band with proposed dimensions ($22.86 \times 10.16 \text{ mm}^2$) that can detect liquid chemicals. As shown in this figure, it consists of three layers. The top layer is a G-shaped copper resonator deposited on either side of middle layer, which is FR-4 (Flame Retardant) substrate. The bottom layer is of 10 mm thickness, which can be used to keep the test sample. Figure 1, *a* represent a unit cell compatible with X-band waveguide, which correlates with experimental study.

Figure 2 shows the design of MTM sensor with two ports added on either side with necessary boundary conditions as per the simulation output. During simulation, various boundary conditions are applied in order to measure the *S*-parameters as per the measure-

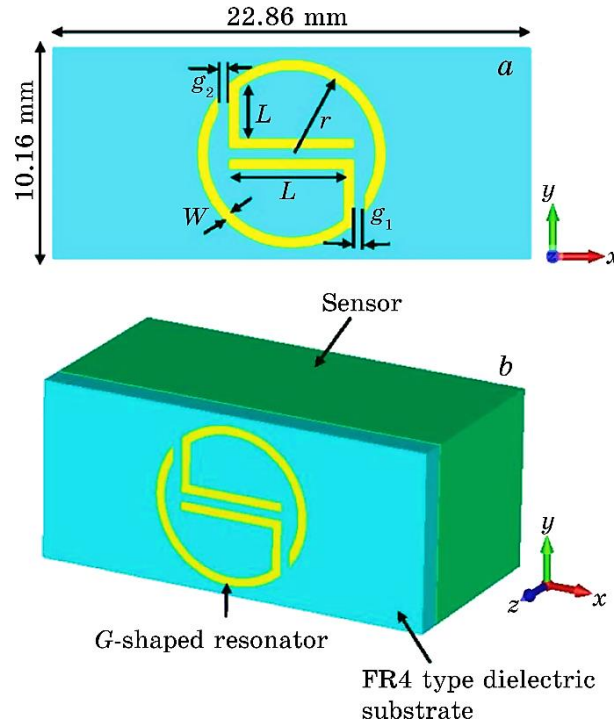


Fig. 1. MTM based sensor for liquid detection (reproduced with permission from [25]).

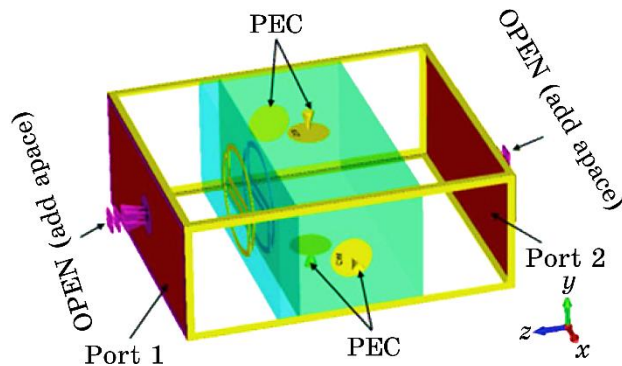


Fig. 2. MTM sensor with simulated boundary conditions (reproduced with permission from [25]).

ments of wave-guide WR-90 as well to assign x - y directions to boundary conditions of perfect electrical conductor (PEC) with z -axis for the direction of propagation.

Figure 3 shows the complete experimental setup with developed MTM-based sensor, waveguide configuration and sample holder with sample under study.

The above-mentioned experimental setup was used to measure transmission coefficient (S_{21}) with liquid sample. Initially the sample was injected into holder and (S_{21}) was measured between 8–12 GHz. This was repeated every sample. In addition, (S_{21}) was calculated numerically by taking the dielectric properties of each sample. Both simulated and experimental results confirmed the ability of the designed sensor in detecting various liquids through resonance frequency shift of 250 MHz (transformer oil and diesel oil), 200 MHz (corn, cotton, olive oil, 150 MHz (ethyl alcohol substituted with aniline) and 50 MHz (carbon tetrachloride with benzene). This was achieved by developing a resonator in X-band. It was reported that this sensor could differentiate clean and waste transformer oils, branded and unbranded diesel oils by a resonant shift of 250 MHz even though their dielectric constants are very close of about (2.84 and 2.73) and (2.71 and 2.48). Similar measurements have confirmed 200 MHz shift for cotton, corn and olive oils with 3.2, 3.08 and 2.55 dielectric values. The experimental and simulated results are highly correlated confirming the ability of designed sensor in chemical detection. At the same time, it is of low cost, durable

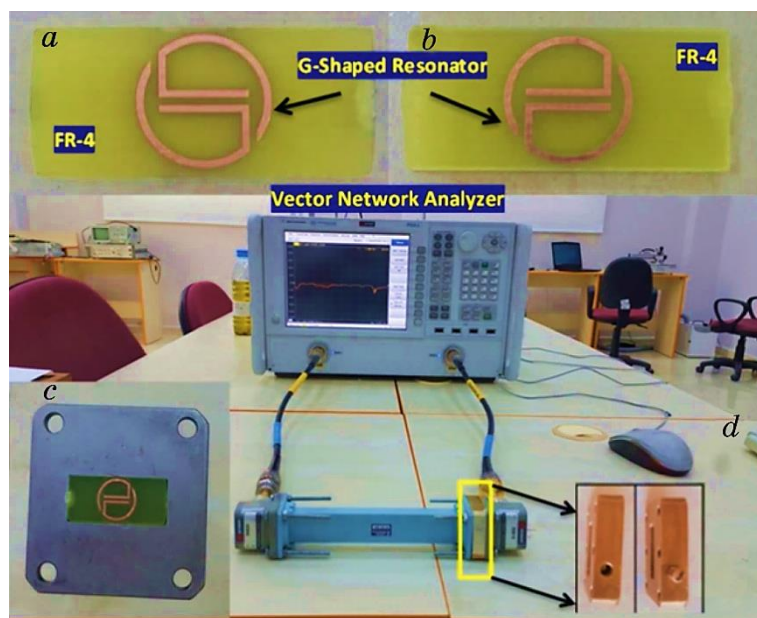


Fig. 3. Experimental setup of MTM sensor (reproduced with permission from [25]).

and highly accurate. This MTM sensor is of high importance in liquid chemical detection [25].

An MTM-based optical sensor for sucrose detection has been reported. The sensor was optimized by developing a metamaterial surface of broad wavelength using E-beam lithography. The detection accuracy of the sensor was very high as compared to an ordinary thin film sensor. The central wavelength of MTM sensor (967 nm) was much higher than the gold film sensor (933 nm). A big shift in wavelength (148.7 nm) between gold film and MTM sensors was reported. This large shift in wavelength is assigned to high resonance intensity experienced by metamaterial surface attributed to low particle size. These outputs confirmed better sensitivity with metamaterials [26]. In continuation, various MTM sensors are designed that include temperature sensors based on semiconductor metamaterials [27], sensors for sensing permittivity of alcohol, *etc.* [28] were reported.

In a similar way, a MTM absorber based on resonator of swastika shape resonator was designed. The sensing ability of this sensor at X-band frequency was demonstrated both theoretically and experimentally. This structure consists of a resonator of swastika shape on top of dielectric layer having gap to fill liquids under test.

Figure 4 shows an MTM-based sensor that can determine liquid chemicals and the ratios in water. It has a swastika shaped copper resonator of width 1mm placed on FR4 substrate with 1.6 mm thickness and 4.2 dielectric constant and 0.02 tangent losses. A reservoir of 3.5 mm thickness between copper plate and resonator was set up to place the chemical liquids for detection.

As every liquid chemical has its own electrical and permittivity values, shift in resonance frequency takes place by bringing a change in absorption value of MTM absorber. This is correlated with systems impedance matching. The swastika resonator is designed as per the numerical results, which have unique properties as compared to other resonators. It is also reported that compatibility between unit cell dimensions and X-band waveguide has been established.

Figure 5, *a* shows the fabricated MTM sensor with dimensions as per simulation output. The sample under study (Fig. 5, *b*) has been placed into the X-band waveguide. Figure 5, *c* shows the reservoir for liquid chemical. X-band waveguide is fed by VNA between 8 and 12 GHz for each sample separately. Simulation was done using finite integrate technique to find MTM structures absorption of liquid chemical depending on its electrical property. With the help of Vector Network Analyser, loss tangents and dielectric constants for acetone, ethanol, water, methanol, *etc.* are measured in specified frequency range. It was reported that absorption ratios significantly

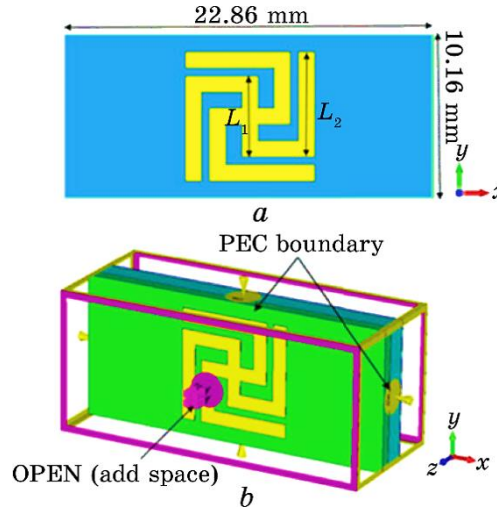


Fig. 4. Swastika-shaped MTM resonator (reproduced with permission from [29]).

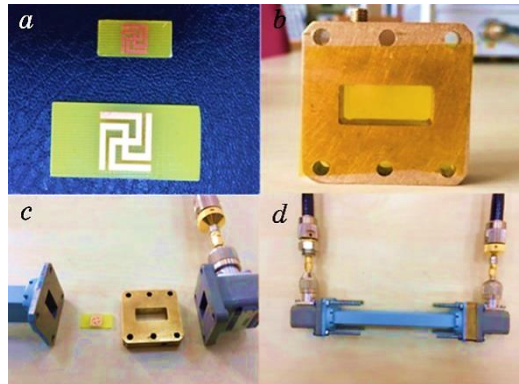


Fig. 5. (a)—Fabricated MTM sensor with simulated dimensions; (b)—X-band waveguide; (c)—reservoir (reproduced with permission from [29]).

differ between the investigating samples. In addition, the shift in resonance frequency estimates their density rate accurately. It is also demonstrated that absorption properties of the MTM sensor varies with resonator dimensions. Both observed and simulated results inferred the linear relation between resonance frequency and permittivity of swastika shaped MTM sensor for the samples under study. Since they are highly correlated, this sensor might be considered for detecting different liquid chemicals [29].

3. METAMATERIAL SENSORS IN WATER TREATMENT

Huge amount of wastewater was being processed throughout the world [30]. In this sewage water is one which was the wastewater released after consumption for household purposes like washing, flushing, *etc.* This water is generally made to accumulate in a sewer facility, which is black (due to bathing, dishwashing) and grey (toilet water) in colour. It is a combination of paper wrappers, sanitary items, soap residue and chemical composition of waste material with foul smell. This results in sewage pollution creating threat to environment and human health apart from affecting agriculture, aquatic and biodiversity. Hence, this water needs to be treated that is known as sewage treatment. Sewage treatment involve various processes [31] that include pre-treatment, primary, secondary, tertiary and sludge treatments. Pre-treatment is the first step, in which large materials such as bottles are scanned and reduced to smaller particles. These particles are removed and the water is ready for primary treatment. During primary treatment, heavy particles settle down the surface while biological content will be removed during secondary treatment. Even though secondary treatment removes most of the virus and bacteria, components like nitrogen, phosphorus, *etc.* may be present in the wastewater. This can be removed through tertiary treatment. This water can be reused as industrial water. Further treatment may help to use this water for cleaning. Beyond all these treatments, wastewater can be treated using sludge treatment. In this process, disintegration of organic matter and hydrolysis of macromolecular components leads to usage of solid deposits of sludge as fertilizers and for production of energy, *etc.* [32].

Sludge disintegration technique may be thermal, mechanical, chemical or microwave radiation based. It is reported that release-ment of organic matter depends on final temperature [33], which affect dielectric properties of materials. Dielectric properties play important role in determining its EM-field distribution in a given material. The electrical properties of Waste activated sludge (WAS) which prevalent in sewage treatment plant has been reported by [34] with the help of open-ended coaxial probe technique. In this context, MTM sensor that sense variation in complex permittivity with resonance frequency shift is of importance. Metamaterials are tailored to control and manipulate electromagnetic waves [35]. Since the year 2000 when negative permittivity and permeability are demonstrated by metamaterials [36], various applications like antenna designing, cloaking devices have been stimulated [37]. Similarly, metamaterial absorbers are being used in various fields [38, 39]. Energy harvesting applications with microwave metamaterial

absorbers have been developed [40, 41]. In continuation, metamaterial sensors that sense temperature, pressure, liquid chemicals, *etc.* are being reported [42–45]. Majority of MTM sensors are designed to study the change in complex permittivity through shift in resonance frequency based on capacitive effects [46]. For a given material, dipoles behave as per the complex dielectric constant that depends on its physical and chemical properties [47–55]. The impact of environmental parameters on complex permittivity using open-ended coaxial probe was reported [56].

Sludge volume index (SVI) is one of the *parameters in process control, which describes the sludge settled in an aeration tank of an activated sludge*. It is measured dividing amount of sludge settled in thirty minutes for one litre sample by concentration of suspended solids. Its value should range between 50–150 mL/g beyond which measures need to be taken to control the sludge levels. Various techniques to measure SVI has been earlier reported [57, 58], but for the first time a MTM sensor was reported for prediction of SVI and validate in microwave range. This technique demonstrated better visibility than the regular method of using a coaxial probe in which complex permittivity values are being measured. Later, an MTM sensor was designed as per the frequency of operation through simulation using FIT. Such MTM sensor was simulated and developed with the help of CNC (computerized numerical control) controlled PCB machine. Its ability was tested with vector network analyser (VNA) whose results demonstrated high sensitivity and effectiveness of designed sensor for water treatment. The designed sensor structure has two square copper resonators front and back along with another resonator with meander lines from left top to the right bottom of substrate made with Isola material of low dielectric loss. A sensor layer of thickness 10 mm was placed behind the backside resonator whose dimensions are compatible for X-band. The front and rear sides of waveguide sample holders are covered with kapton film of 25- μm thickness that was considered in simulation to correlate with experiment similar to lab setup.

Using this sensor, SVI index was measured in three stages of wastewater treatment given by water entry point, aeration and exit stages. Measurements of dielectric constant and MTM sensor are considered. Three samples tested between 8 GHz and 12 GHz for entrance, aeration and exit stages are reported to vary from 67 to 32.54, 39.64 and 56. Secondly, the measured dielectric constants of wastewater samples were simulated by assigning these values to a microwave simulator. The resonant frequencies of entrance, aeration and exit stages of water are found to be 10.208 GHz, 10.024 GHz and 10.232 GHz with about 230 MHz bandwidth indicating the ability of sensor in distinguishing different stages of water sam-

ples. These results are compared with experimental values obtained from network analyser, which are highly correlated with small differences in resonance frequency. Hence, this technique suits determination of liquid type [59].

4. CONCLUSIONS

This paper mainly reviewed the role of MTM sensors in liquid detection with prime focus on designed resonators and their successful implementation. It is observed that MTM sensors used in detection of liquids replace the traditional coaxial tube technique in X-band range of frequency. Mainly we observed that replacement of coaxial tube technique along with simulation is being carried out simultaneously. These sensors could differentiate between clean and waste transformer oils by a frequency shift of 250 MHz even their dielectric constants are very close by a difference of 0.11. Similarly, a frequency shift of 200 MHz was observed for olive, corn and cotton oils with dielectric constants 2.55, 3.08 and 3.2. Similar is the case with branded and unbranded diesels. This sensor proved to be successful in terms of speed, economical and accuracy. Apart from liquid detection, MTM sensors are proved very useful in water treatment centres. In this review, we observed an excellent MTM sensor that can detect sludge volume Index (SVI) efficiently. For the first time in the journey of MTM sensors this was reported, which may lead to many applications in detecting water quality in future. To design this sensor, complex permittivity values of water samples are being measured. The simulated and experimental results proved the efficiency of this sensor with high sensitivity and its effectiveness for usage in water treatment. For a given water treatment centre, five experimental values for same sample were reported to have about 0.5% standard deviation at resonance frequency. The simulation values are highly correlated with experimental values for entrance, aeration and exit of the water treatment centre with a shift of 72 MHz, 16 MHz and 88 MHz, respectively. A minimum of 230 MHz frequency shift exist between different samples under study, which can determine water quality. This journey of MTM sensors in water treatment may lead to new inventions in detecting and purifying water quality with low cost and high speed masking the existing conventional techniques.

REFERENCES

1. V. G. Veselago, *Sov. Phys. Usp.*, **10**, No. 4: 509 (1968).
2. R. A. Shelby, D. R. Smith, and S. Schultz, *Science*, **292**, No. 5514: 77

- (2001).
3. Wojciech Jan Krzysztofik and Thanh Nghia Cao, *Metamaterials in Application to Improve Antenna Parameters* (Ed. Josep Canet-Ferrer) (IntechOpen: 2018);
[doi:10.5772/intechopen.80636](https://doi.org/10.5772/intechopen.80636)<https://www.intechopen.com/books/metamaterials-and-metasurfaces/metamaterials-in-application-to-improve-antenna-parameters/>
 4. Pekka Alitalo and Sergei Tretyakov, *Materials Today*, **12**, No. 3: 22 (2009);
[https://doi.org/10.1016/S1369-7021\(09\)70072-0](https://doi.org/10.1016/S1369-7021(09)70072-0)
 5. Mário G. Silveirinha, Andrea Alù, and Nader Engheta, *Phys. Rev. E*, **75**, No. 3: 036603 (2007); <https://doi.org/10.1103/PhysRevE.75.036603>
 6. Ulf Leonhardt, *Science*, **312**, No. 5781: 1777 (2006);
<http://doir.org.10.1126/science.1126493>
 7. J. B. Pendry, D. Schurig, and D. R. Smith, *Science*, **312**, No. 5781: 1780 (2006); <http://doi.org.10.1126/science.1125907>
 8. Baile Zhang, Bae-Ian Wu, Hongsheng Chen, and Jin Au Kong, *Phys. Rev. Lett.*, **101**: 063902 (2008);
<https://doi.org/10.1103/PhysRevLett.101.063902>
 9. Min Yan, Zhichao Ruan, and Min Qiu, *Phys. Rev. Lett.*, **99**: 233901 (2007);
<https://doi.org/10.1103/PhysRevLett.99.233901>
 10. Pekka Alitalo, Olli Luukkonen, Liisi Jylha, Jukka Venermo, and Sergei A. Tretyakov, *IEEE Transactions on Antennas and Propagation*, **56**, No. 2: 416 (2008); <doi:10.1109/TAP.2007.915469>
 11. P. Ufimtsev, *IEEE Antennas Propag. Mag.*, **56**, No. 12: 3883 (2008);
<doi:10.1109/TAP.2008.2007397>
 12. J. B. Pendry, D. Schurig, and D. R. Smith, *Science*, **312**, No. 5781: 1780 (2006); <doi:10.1126/science.1125907>
 13. D. Schurig, J. J. Mock, B. J. Justice, S. A. Cummer, J. B. Pendry, A. F. Starr, and D. R. Smith, *Science*, **314**, No. 5801: 977 (2006);
<doi:10.1126/science.1133628>
 14. Guan Xia Yu, Tie Jun Cui, and Weixiang Jiang, *J. Infrared Millim. Terahertz Waves* **30**, No. 6: 633 (2009); <doi:10.1007/s10762-009-9484-8>
 15. Marco Rahm, David Schurig, Daniel A. Roberts, Steven A. Cummer, David R. Smith, and John B. Pendry, *Photonics Nanostructures*, **6**: 87 (2008);
<doi:10.1016/j.photonics.2007.07.013>
 16. Yun Lai, Jack Ng, HuanYang Chen, DeZhuan Han, JunJun Xiao, Zhao-Qing Zhang, and C. T. Chan, *Phys. Rev. Lett.*, **102**, Iss. 25: 253902 (2009);
<doi:10.1103/PhysRevLett.102.253902>
 17. Yun Lai, Jack Ng, HuanYang Chen, DeZhuan Han, JunJun Xiao, Zhao-Qing Zhang, and C. T. Chan, *Phys. Rev. Lett.*, **102**, Iss. 9: 093901 (2009);
<doi:10.1103/PhysRevLett.102.253902>
 18. Siming Yang, Peng Liu, Mingda Yang, Qiugu Wang, Jiming Song and Liang Dong, *Scientific Reports*, **6**, No. 1: 21921 (2016); <doi:10.1038/srep21921>
 19. Guozhi Zhao, Shihua Bi, Mowen Niu, and Yancheng Cui, *Materials Today Communications*, **21**: 100603 (2019);
<https://doi.org/10.1016/j.mtcomm.2019.100603>
 20. Yang Liu, Yitung Chen, Jichun Li, Tzu-chem Hung, Jianping Li. *Solar Energy*, **86**, No. 5: 1586 (2012); <doi:10.1016/j.solener.2012.02.021>
 21. A. Dhar, M. Choudhuri, A. B. Roy, P. Banerjee, A. Kundu, *Materials Today*

- Proceedings*, **5**, No. 11: 23203 (2018);
<https://doi.org/10.1016/j.matpr.2018.11.051>
22. Philippe Horvath and Rodolphe Barrangou, *Science*, **327**, No. 5962: 167 (2010); [doi:10.1126/science.1179555](https://doi.org/10.1126/science.1179555)
23. Zoran Jakšić, Olga Jakšić, Zoran Djurić, and Christoph Kment, *J. Opt. A: Pure Appl.*, **9**, No. 9: 377 (2007); [doi:10.1088/1464-4258/9/9/S16](https://doi.org/10.1088/1464-4258/9/9/S16)
24. J. B. Pendry, *Phys. Rev. Lett.*, **85**, No. 18: 3966 (2000);
<https://doi.org/10.1103/PhysRevLett.85.3966>
25. I. Yadgar, A. L. Deng, H. Luo, S. Huang, M. Karaaslan, O. Altintas, M. Bakır, F. F. Muhammadsharif, H. N. Awl, C. Sabah, K. S. L. Al-badri, *Journal of Materials Research and Technology*, **9**, No. 5: 10291 (2020);
<https://doi.org/10.1016/j.jmrt.2020.07.034>
26. Sajal Agarwal and Y. K. Prajapati, *Optik — International Journal for Light and Electron Optic*, **205**: 164276 (2020);
<https://doi.org/10.1016/j.ijleo.2020.164276>
27. Mehdi Aslinezhad, *Optics Communications*, **463**: 125411 (2020);
<https://doi.org/10.1016/j.optcom.2020.125411>
28. Mustafa Suphi Gulsu, Fulya Bagci, Sultan Can, Asim Egemen Yilmaz, and Baris Akaoglu, *Sensors and Actuators A: Physical*, **312**: 112139 (2020);
<https://doi.org/10.1016/j.sna.2020.112139>
29. Y. I. Abdulkarim, L. Deng, O. Altintas, E. Unal, and M. Karaaslan, *Physica E: Low-Dimensional Systems and Nanostructures*, **114**: 113593 (2019);
<https://doi.org/10.1016/j.physe.2019.113593>
30. R. J. LeBlanc, P. Matthews, and R. P. Richard, *Global Atlas of Excreta, Wastewater Sludge, and Biosolids Management. Moving Forward the Sustainable and Welcome Uses of a Global Resource* (Nairobi: United Nations Human Settlements Programme (UN-HABITAT): 2008).
31. S. M. Khopkar, *Environmental Pollution Monitoring And Control* (New Delhi: New Age International: 2004); p. 299.
32. P. V. Kovacs, B. Lemmer, G. K-Szabo, C. Hodur, and S. Beszedes, *Water Science and Technology*, **77**, No. 9: 2284 (2018);
<https://doi.org/10.2166/wst.2018.144>
33. C. Eskicioglu, N. Terzian, J. Kennedy, R. Droste, and M. Hamoda, *Water Research*, **41**, No. 11: 2457 (2007);
<https://doi.org/10.1016/j.watres.2007.03.008>
34. J. S. Bobowski, T. Johnson, and C. Eskicioglu, *Progress in Electromagnetics Research Letters*, **29**: 139 (2012); <https://doi.org/10.2528/pierl11120304>
35. R. Bogue, *Sensor Review*, **37**, No. 3: 305 (2017);
<https://doi.org/10.1108/SR-12-2016-0281>
36. D. R. Smith, W. J. Padilla, D. Vier, S. C. Nemat-Nasser, and S. Schultz, *Physical Review Letters*, **84**, No. 18: 4184 (2000);
<https://doi.org/10.1103/PhysRevLett.84.4184>
37. J. J. Yang, M. Huang, C. F. Yang, and J. Yu, *European Physical Journal D*, **61**, No. 3: 731 (2011); [doi:10.1140/epjd/e2010-10507-2](https://doi.org/10.1140/epjd/e2010-10507-2)
38. David Shrekenhamer, Wen-Chen Chen, and Willie J. Padilla, *Phys. Rev. Lett.*, **110**, No. 17: 177403 (2013); [doi:10.1103/PhysRevLett.110.177403](https://doi.org/10.1103/PhysRevLett.110.177403)
39. Ankit Vora, Jephias Gwamuri, Nezih Pala, Anand Kulkarni, Joshua M. Pearce, and Durdu Ö. Güney, *Scientific Reports*, **4**: 4901 (2014);
[doi:10.1038/srep04901](https://doi.org/10.1038/srep04901)

40. Thamer S. Almoneef and Omar M. Ramahi, *Progress In Electromagnetics Research*, **146**: 109 (2014); [doi:10.2528/PIER14031603](https://doi.org/10.2528/PIER14031603)
41. M. Bakır, M. Karaaslan, F. Dincer, K. Delihacioglu, and C. Sabah, *Journal of Materials Science: Materials in Electronics*, **27**: 12091 (2016); [doi:10.1007/s10854-016-5359-7](https://doi.org/10.1007/s10854-016-5359-7)
42. M. T. Islam, M. M. Islam, Md. Samsuzzaman, M. R. Faruque, I. Faruque, and N. Misran, *Sensors*, **15**, No. 5: 11601 (2015); [doi:10.3390/s150511601](https://doi.org/10.3390/s150511601)
43. Mehmet Bakır, Muharrem Karaaslan, Furkan Dincer, Oguzhan Akgol, and Cumali Sabah, *International Journal of Modern Physics B*, **30**, No. 20: 1650133 (2016); [doi:10.1142/S0217979216501332](https://doi.org/10.1142/S0217979216501332)
44. V. F. Krapivin, C. A. Varotsos, and S. V. Marechek, *Water, Air, & Soil Pollution*, **229**, No. 4: 110 (2018); [doi:10.1007/s11270-018-3773-6](https://doi.org/10.1007/s11270-018-3773-6)
45. Asha Srinivasan, Moutoshi Saha, Kit Caufield, Otman Abida, Ping Huang Liao, and Kwang Victor Lo, *Water, Air, & Soil Pollution*, **229**, No. 7: 227 (2018); [doi:10.1007/s11270-018-3894-y](https://doi.org/10.1007/s11270-018-3894-y)
46. Y. I. Abdulkarim, L. Deng, M. Karaaslan, and E. Unal, *Chemical Physics Letters*, **732**, No. 5801: 136655 (2019); [doi:10.1016/j.cplett.2019.136655](https://doi.org/10.1016/j.cplett.2019.136655)
47. Kandammathe Valiyaveedu Sreekanth, Yunus Alapan, Mohamed ElKabbash, Efe Ilker, Michael Hinczewski, Umut A. Gurkan, Antonio De Luca, and Giuseppe Strangi, *Nature Materials*, **15**, No. 6: 621 (2016); [doi:10.1038/NMAT4609](https://doi.org/10.1038/NMAT4609)
48. Jiong Wu, Peng Wang, Xiaojun Huang, Fang Raoa, Xiaoyu Chena, Zhaoyang Shena, and Helin Yang, *Sensors and Actuators A: Physical*, **280**: 222 (2018); <https://doi.org/10.1016/j.sna.2018.07.037>
49. Mehmet Esen, İlhami İlhan, Muharrem Karaaslan, and Ramazan Esen, *Applied Nanoscience*, **1** (2019); <https://doi.org/10.1007/s13204-019-01122-1>
50. Olcay Altintaş, Murat Aksoy, Emin Ünal, Oğuzhan Akgöl, and Muharrem Karaaslan, *Measurement*, **145**: 678 (2019); [doi:10.1016/j.measurement.2019.05.087](https://doi.org/10.1016/j.measurement.2019.05.087)
51. Mehmet Bakır, Muharrem Karaaslan, Furkan Dincer, and Cumali Sabah, *International Journal of Numerical Modelling: Electronic Networks, Devices and Fields*, **30**, No. 5: 2188 (2016); [doi:10.1002/jnm.2188](https://doi.org/10.1002/jnm.2188)
52. Mehmet Bakır, Şekip Dalgaç, Muharrem Karaaslan, Faruk Karadağ, Oğuzhan Akgöl, Emin Ünal, Tolga Depçi, and Cumali Sabah, *Journal of the Electrochemical Society*, **166**, No. 12: 1044 (2019); [doi:10.1149/2.1491912jes](https://doi.org/10.1149/2.1491912jes)
53. Mehmet Bakır, Muharrem Karaaslan, Faruk Karadag, Şekip Dalgaç, Emin Ünal, and Oğuzhan Akgöl, *The Applied Computational Electromagnetics Society Journal (ACES)*, **34**, No. 5: 799 (2019); <https://journals.riverpublishers.com/index.php/ACES/article/view/8499/7027>
54. Oğuz Derin, Muharrem Karaaslan, Emin Ünal, Faruk Karadağ, Olcay Altintaş, and Oğuzhan Akgöl, *Bulletin of Materials Science*, **42**, No. 4: 191 (2019); [doi:10.1007/s12034-019-1882-5](https://doi.org/10.1007/s12034-019-1882-5)
55. Emin Ünal, Mehmet Bağmancı, Muharrem Karaaslan, Oğuzhan Akgöl, and Cumali Sabah, *International Journal of Modern Physics B*, **32**: 18502752 (2018); [doi:10.1142/S0217979218502752](https://doi.org/10.1142/S0217979218502752)
56. J. S. Bobowski, T. Johnson, and C. Eskicioglu, *Progress in Electromagnetics Research Letters*, **29**: 139 (2012); <https://doi.org/10.2528/pierl11120304>
57. Daniela P. Mesquita, A. Luís Amaral, and Eugénio C. Ferreira, *Analytica*

- Chemica Acta*, **802**: 14 (2013); <https://doi.org/10.1016/j.aca.2013.09.016>
58. Halime Boztoprak, Yüksel Özbay, Dünyamin Güçlü, and Murat Küçükhemek, *Desalination and Water Treatment*, **57**, No. 37: 1 (2015);
[doi:10.1080/19443994.2015.1085909](https://doi.org/10.1080/19443994.2015.1085909)
59. Mehmet Bakir, Şekip Dalgaç, Emin Ünal, Faruk Karadağ, Mustafa Demirci, Ahmet Sertol Köksal, Oğuzhan Akgöl, and Muharrem Karaaslan, *Water Air Soil Pollut.*, **230**: 304 (2019); <https://doi.org/10.1007/s11270-019-4355-y>

PACS numbers: 62.23.Pq, 77.84.Lf, 81.05.Je, 81.05.U-, 82.45.Yz, 82.45.Uv, 84.60.Ve

MXenes-Based Supercapacitors: A Review on Energy Storage Devices

N. V. Krishna Prasad¹ and N. Madhavi²

¹*Department of Physics, G.S.S.,
GITAM University,
Bengaluru, India*
²*Govt. College (Autonomous),
Department of Statistics,
Rajhamundry, India*

Energy storage and energy-storage devices have been a buzzword for long time as it is one of the essential needs in human life. These devices include mechanical systems, thermal systems, and batteries. These systems embedded with software can monitor the charging and discharging phenomena of energy. In this context, the role of rechargeable batteries needs to be reviewed. Even though novel types of rechargeable batteries are being continuously developed for storage of electricity, more attention and research towards supercapacitors is on the way. Huge number of researchers around the globe is involved in developing supercapacitors with improved performance making them more and more useful. The main aim is to improve their efficiency, energy density, operating voltage, miniaturization, optimization, economy, and environmental acceptance. For the last few years, lightweight and carbon-based novel wearable supercapacitors are developed. High durability, eco-friendliness, being non-volatile and electrostatic mechanism of supercapacitors make them advantageous than conventional batteries. In this regard, advances in microelectronics demand microsupercapacitors (MSCs). The selection of electrode in microsupercapacitor plays significant role in the fabrication. In this selection, MXenes as a family of 2D material play a vital role. Very high conductivity and high capacity of charge storage makes MXenes as one of the potential materials for electrodes in microsupercapacitors. This prompts us to review the role of MXenes in microsupercapacitors. This article reviews the recent advances of MXenes-based MSCs with emphasis on their fabrication techniques.

Накопичувачі енергії та пристрой накопичення енергії вже давно стали модним словом, оскільки це одна з найважливіших потреб у житті людини. До таких пристройів належать механічні системи, теплові системи

й акумулятори. Ці системи, вбудовані в програмне забезпечення, можуть контролювати явища заряджання та розряджання енергії. У цьому контексті необхідно переглянути роль акумуляторних батарей. Неважаючи на те, що для зберігання електроенергії постійно розробляються нові типи акумуляторних батарей, все більше уваги та досліджень у галузі суперконденсаторів вже на підході. Величезна кількість дослідників по всьому світу бере участь у розробці суперконденсаторів з поліпшеною продуктивністю, що робить їх все більш корисними. Основною метою є підвищення їхньої ефективності, густини енергії, робочої напруги, мініяторизації, оптимізації, економічності й екологічного сприйняття. За останні кілька років були розроблені легкі та карбонові нові придатні для носіння суперконденсатори. Висока довговічність, екологічність, енергонезалежність і електростатичний механізм суперконденсаторів роблять їх вигіднішими перед звичайними акумуляторами. У зв'язку з цим досягнення мікроелектроніки вимагають мікросуперконденсаторів (МСК). Вибір електроди в мікросуперконденсаторі відіграє значну роль у виготовленні. У цій добірці максени як сімейство 2D-матеріалів відіграє життєво важливу роль. Дуже висока провідність і висока ємність накопичувача заряду робить максени одним з потенційних матеріалів для електроду у мікросуперконденсаторах. Це спонукає нас розглянути роль максенів у мікросуперконденсаторах. У цій статті розглядаються останні досягнення МСК на основі максенів з акцентом на технологіях виготовлення їх.

Key words: 2D MXenes, microsupercapacitors, energy storage, E-textiles, health monitoring.

Ключові слова: 2D-максени, мікросуперконденсатори, накопичувачі енергії, електронний текстиль, моніторинг здоров'я.

(Received 19 May, 2023)

1. INTRODUCTION

High capacitance value is being one of the top priorities since few decades in electrochemical systems. This could not be achieved earlier, but researchers have proved that supercapacitors could show a new direction in developing electrical energy storage systems [1]. Novel materials, technologies, huge surfaces and minute interelectrode distances are being developed in recent times. Many materials exhibit high pseudo-capacitance achieving large capacitance values as compared to normal capacitors and are called supercapacitors or ultra-capacitors) [2]. Figure 1 shows the image of a supercapacitor.

Supercapacitors play a significant role in new generation electronic devices and systems. Carbon and its allotropes play a vital role in supercapacitors in view of their thermal stability, chemical stability, mechanical strength, good conductivity, high electron mobility, wide range of temperatures, large surface area and morphology.

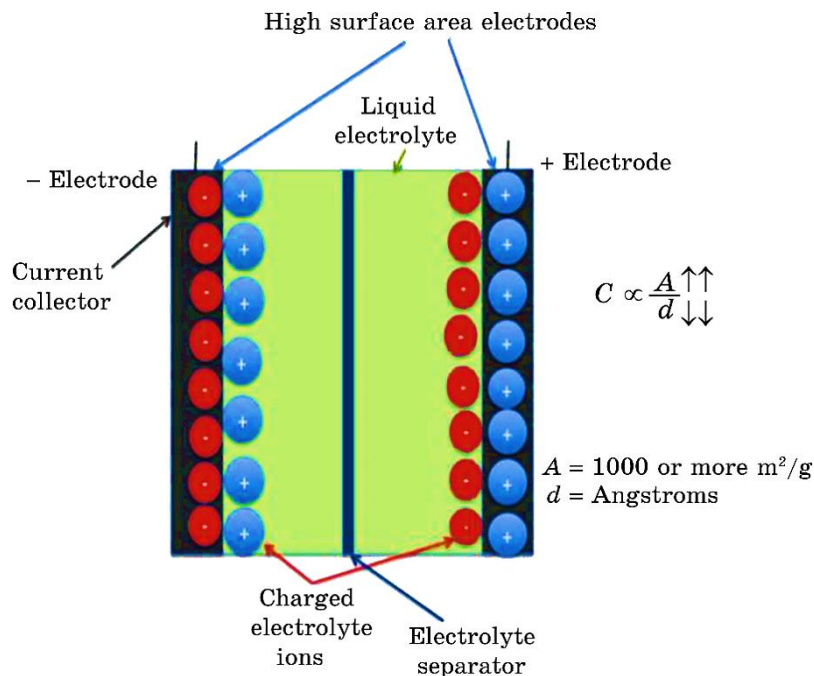


Fig. 1. Supercapacitor (courtesy [3]).

Figure 2 shows the classification of supercapacitors.

Depending on the mechanism involved in energy storage, supercapacitors are of two types: pseudo-capacitors where charge storage is fast due to redox reactions, double-layered capacitors where charge storage depends on electrostatic principles [3, 4]. If an electrode material exhibit either one or both mechanisms mentioned above, hybrid capacitors can be formed with them. Figure 3 shows different types of supercapacitors.

High-power rapid charging and discharging make supercapacitors significant in energy harvesting from renewable energy sources, power, industrial control, transport, consumer electronics, defence, medical, communications, electric and hybrid vehicles [6–9].

2. MATERIALS FOR SUPERCAPACITORS

Supercapacitors are widely used for energy storage mainly due to their environment friendly nature, huge number of charge, discharge cycles and durability with less maintenance [10]. However, as compared to battery they have low energy density. This drawback force researchers towards new materials and technologies. In this context, 2D nanomaterials such as graphene, fullerene, and carbon

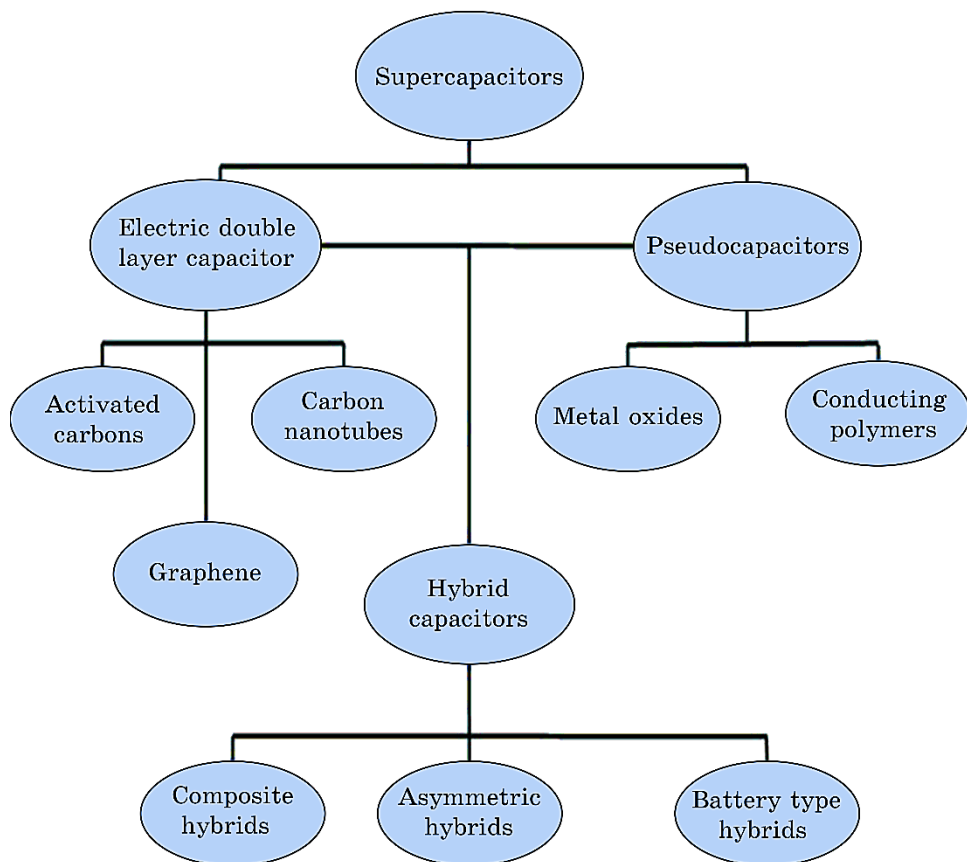


Fig. 2. Classification of supercapacitors (courtesy [3]).

nanotubes are used as appropriate electrolytes [11]. In this journey, usage of copper minerals, chalcosine [12] and coveline [13] was taken up. In addition, perovskite oxides based on lanthanum, strontium, and cerium, *etc.* are being researched [14]. In order to improve further the efficiency of supercapacitors, MXenes were used.

Increased demand for flexible and smart wearable energy micro-devices force researchers towards design and development of micro-energy storage devices. Since microbatteries have limited life and power density, best alternative to them are microsupercapacitors (MSCs) despite lower energy density. Still stability and fast charge/discharge cycles MSCs are preferred [15]. MSCs may be of regular sandwich type or plane interdigital pattern type, in which the second one offers better performance [16, 17]. Various 2D materials such as graphene, MXenes with excellent electronic, optical, mechanical, physical and chemical properties make them significant

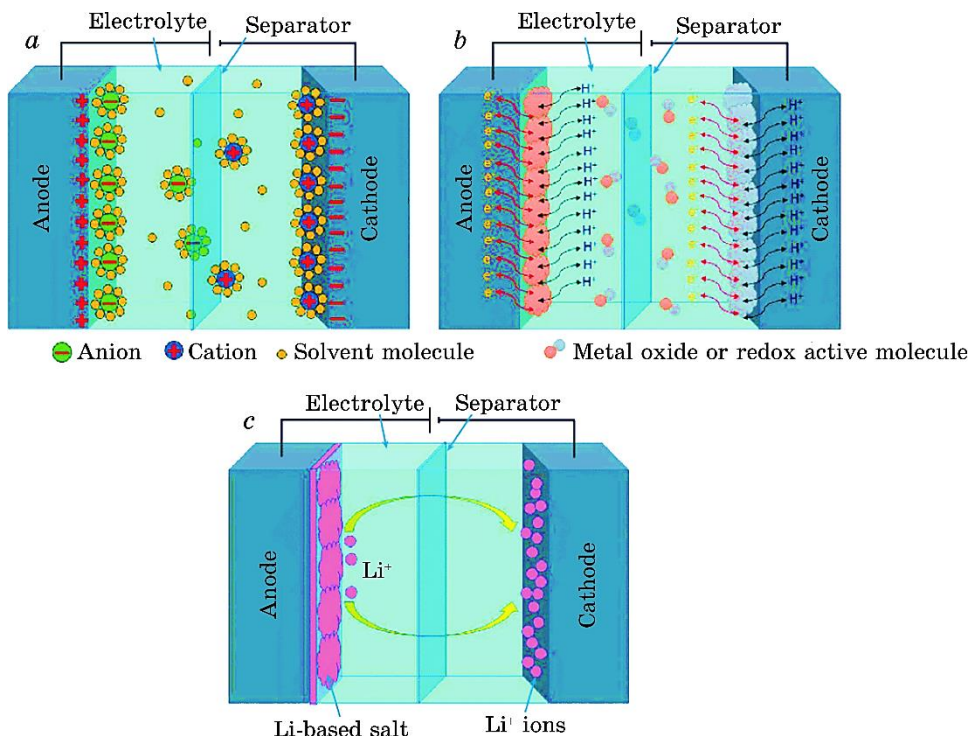


Fig. 3. (a) Electrical double layer capacitor (EDLC); (b) pseudo-capacitor (PC); (c) hybrid supercapacitor (HSC) (courtesy [5]).

in energy storage applications [18]. Even with large conductivity and surface area, carbon based materials lack high energy density [19–24]. Likewise, pseudo-capacitive materials, which have low conductivity [25–28], are used in MSCs. Since the discovery of MXenes in 2011, they have gathered the attention of scientific community for usage in MSCs [29].

2. MXenes: SYNTHESIS AND PROPERTIES

MXenes are synthesized either by selective etching or through chemical vapour deposition. First reports on synthesis of MXene indicated elimination of Al layer from Ti_3AlC_2 (MAX) by using hydrogen fluoride [28]. Exfoliated two-dimensional $Ti_3C_2T_x$ possess morphology similar to 2D sheets resembling graphene sheets [30]. Various methods were used to avoid highly acidic HF acid.

Figure 4 below demonstrates the development of MXenes from MAX phases through HF treatment and their compositions in periodic table.

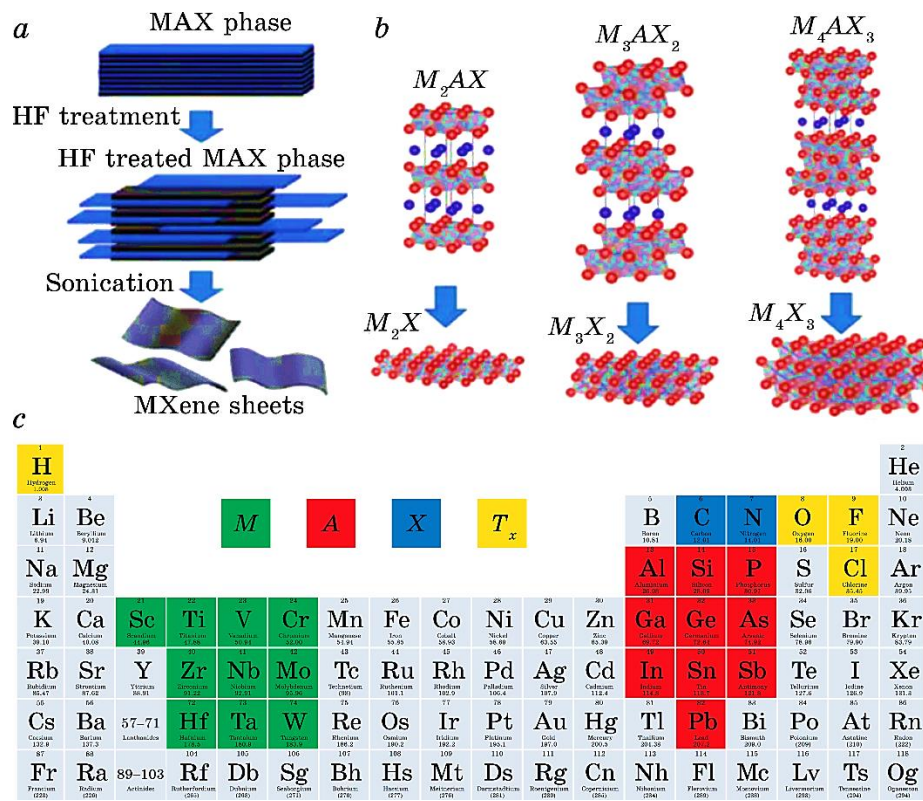


Fig. 4. (a) Schematic showing the synthesis of MXene from MAX by HF treatment; (b) synthesis mechanism of different order of MXenes by MAX phases; (c) compositions of MXene elements in periodic table (courtesy [31]).

Based on the method of synthesis, the characteristics of MXene are altered. It is reported that more than twenty types of MXenes have been synthesized experimentally [32].

MXenes act as significant platforms for supercapacitors in view of their electrical, mechanical properties and their surface morphology. They are classified into metallic, semi-metallic and semi-conducting materials [33]. Usually uncovered, they exhibit high conductivity and their electronic properties strongly depend on morphology and stacking of MXene sheets. It is reported that delaminated MXenes exhibit ultrahigh conductivity of up to 9880 S/cm [34]. Also depending on the synthesis method, a conductivity of 1 000 S/cm with HF etching was reported by MXene. This can be tuned to an extent of 4600 S/cm to 6500 S/cm in case of thick films with delaminated MXene by altering sonication and etching [35].

Mechanical properties of MXenes depend on their specific physical

and chemical properties. Many studies on mechanical, electronic and thermal properties of various MXenes have been reported [36–40]. Young's modulus of $\text{Ti}_3\text{C}_2\text{O}_2$ and Ti_3CO_2 were reported as 466 and 983 GPA [41], which correlate with values predicted by simulation [42]. In this context, a study reported a paper film with $\text{Ti}_3\text{C}_2\text{T}_x/\text{PVA}$ composite of thickness of 5 μm that can withstand approximately 15 000 times of its weight [43] indicating its strong wear. However, surface properties can be modified through surface terminations.

3. MXenes AND THEIR HYBRIDS FOR MICROSUPERCAPACITORS

High metallic conductivity and unique morphology of MXenes make them highly significant in microsupercapacitors. Low cost MXene MSC with 128 S/cm electrical conductivity and 25 mF/cm² capacitance in PVA–H₂SO₄ gel electrolyte was reported [44]. They also demonstrated that capacitance increases with thickness of the material. Similarly, MXene based MSC with wafer scale approach using photolithography with more capacitance was reported. This device was capable of converting the output peak voltage from 0.6 V to –0.56 V as compared to a commercial capacitor with 4mF [45]. A $\text{Ti}_3\text{C}_2\text{T}_x$ spray coated glass substrate with inter digital pattern with an areal capacitance of 20 mF/cm² at 20 mV/s and ultrahigh volumetric capacitance of 357F/cm³ at 0.2 mA/cm² was fabricated. This was superior to other carbon materials already reported. However, usage of platinum collectors was reported to increase an areal capacitance to 27.3 mF/cm² [46]. Recently a semi-transparent MXene film was used with micropatterns of various transparency levels. With increase of 50% transparency, an areal capacitance increased by almost fifteen times from 19 $\mu\text{F}/\text{cm}^2$ to 283 $\mu\text{F}/\text{cm}^2$. At the same time, increase in resistance from 0.8 k Ω to 2 k Ω with increase in coating cycle has been observed [47]. Double-sided MSCs with MXene ink of 7.2 V potential were fabricated. Sharp rise in capacitance was observed with decrease of inter spacing between MXene electrodes. Such device with an inter electrode gap of 10 μm offered huge volumetric capacitance of 308 F/cm³ at 5 mV/s and 96.4% efficiency above 10 000 cycles too [48]. Series connected MSCs achieved a high potential of up to 2.4 V [49]. Fabrication of MSCs with MXene as negative and MXene–MoO₂ film as positive electrode was reported. This technique included vacuum filtration of films followed by laser cutting of interdigital patterns as shown in Fig. 5 [50].

By using the technique of vacuum filtration, thick sheets of MXene were used to develop films with conductivity up to $1.25 \cdot 10^5$ S/m for flexible microsupercapacitor. Likewise, MSCs with interdigital pattern having 340 mF/cm² areal capacitance and 183 F/cm³ volumetric capacitance with energy density of 12.4 mWh/cm³ and

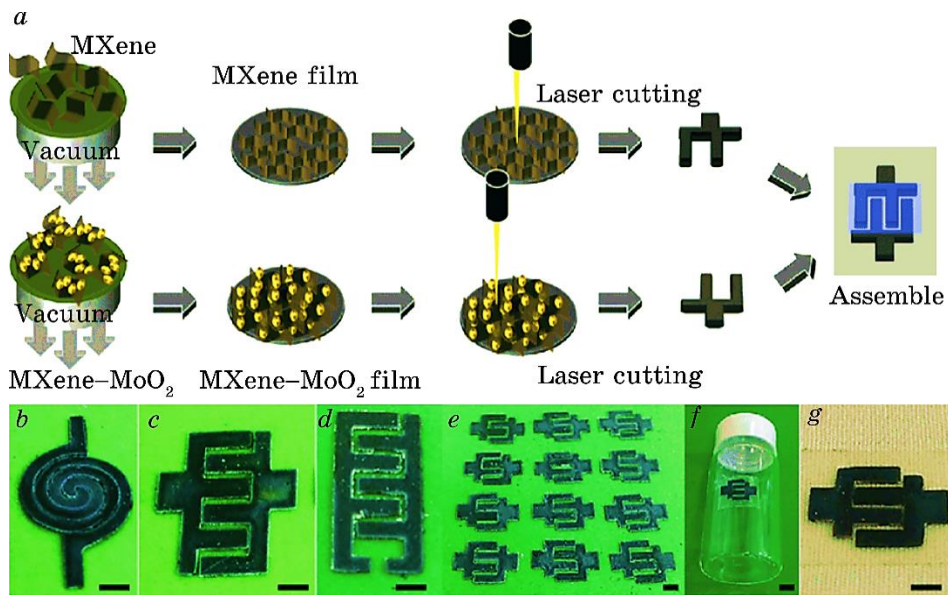


Fig. 5. (a) Fabrication process of MXene//MXene–MoO₂–MSCs with different shapes such as spiral (b), parallel inter digital fingers (c, d), twelve parallel inter digital MSCs integrated on one paper (e), and MSCs transferred onto glass substrate (f) and cloth substrate (g) (courtesy [50]).

power density of 218 mW/cm³ are fabricated [51]. In addition, paper based MXene electrodes with high conductivity and areal capacitance of 23.4 mF/cm² at 0.05 mA/cm² was fabricated. In continuation, fabrication of electrodes in series as well as parallel was taken up to achieve required capacitance [52].

MSCs based on MXenes and CNT with fast ion diffusion and high conductivity were reported. They achieved this by fixing a gap of 500 nm between interdigital fingers and obtained areal capacitance of 317.3 mF/cm² at 50 mV/s. Decrease in gap increased an areal capacitance and energy density attributed to improved rate of ionic transfer [53, 54]. Fabrication of a three dimensional MXene/rGO aerogel MSC was reported. Figure 6 show the fabrication process, in which the device was embedded with polyurethane for adhering to external damage. This device exhibits an areal capacitance of 34.6 mF/cm² at 1 mV/s with excellent recovery of electronic and mechanical properties even after full breakdown [55, 56].

A high performance asymmetric flexible MSC with rGO as positive and MXene as negative electrodes achieved a working potential of 1 V with number of bending cycles and 2.4 mF/cm² areal capacitance at 2 mV/s indicating MXenes potential for negative electrodes in asymmetric devices with high stability and strong performance [56].

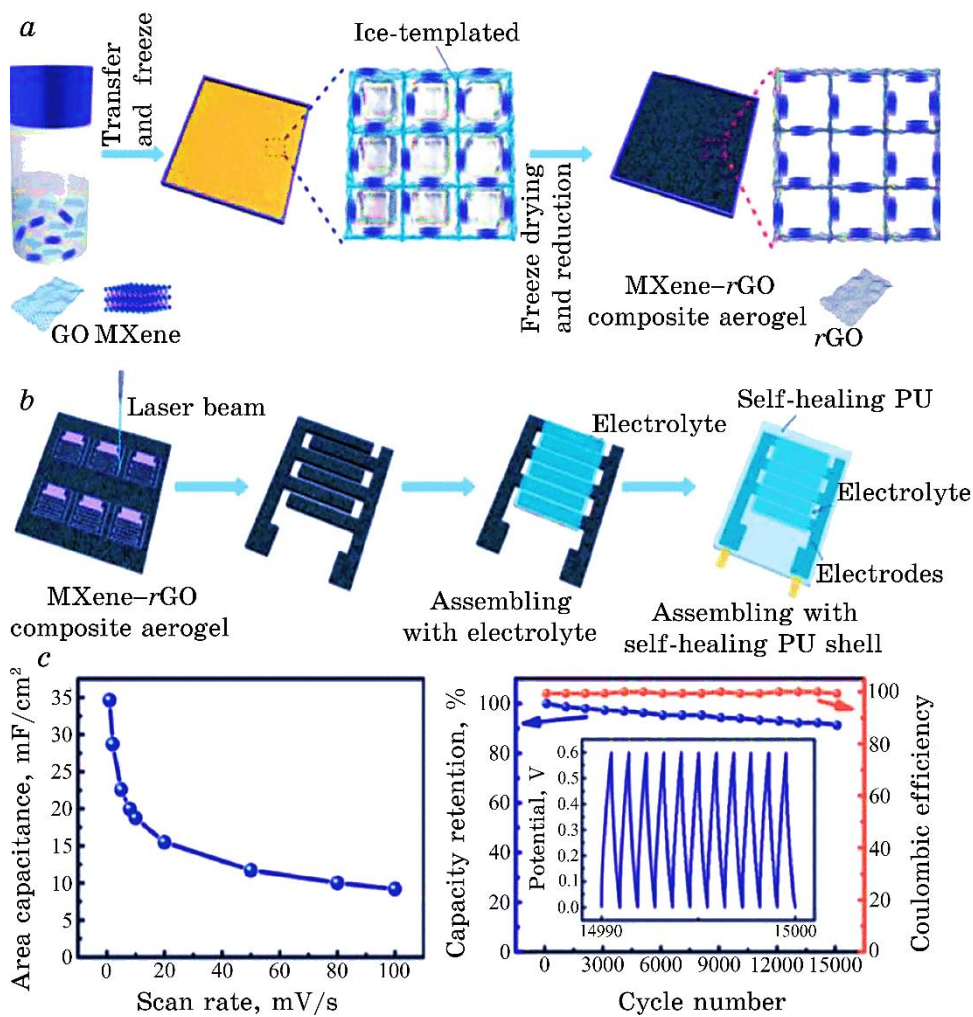


Fig. 6. (a) Fabrication of MXene-rGO composite aerogels; (b) laser cutting of interdigital pattern on MXene-rGO composite followed by assembling with self-healing PU; (c) plot showing the areal capacitance *vs* scan rate MXene-rGO composite; (d) cycling stability of MXene-rGO composite aerogel MSC at $2 \text{ mA}\cdot\text{cm}^{-2}$.

MXenes are also capable of producing textile based energy storage devices with high stability and tunability. Helical shaped MXene/CNT with scaffold hybrid structure reported 19.1 F/cm^3 volumetric capacitance at 1 A/cm^3 in aqueous LiCl electrolyte. Its energy density was of about 2.55 to 1.15 mWh/cm^3 at power density of 0.046 W/cm^3 to 1.82 W/cm^3 , which is almost equal to the best performing capacitor [57].

Similarly, fabricated MXene/*r*GO hybrid fibre supercapacitors using wet spinning exhibit high volumetric capacitance of 586.4 F/cm^3 at 10 mV/s . These fibres report high conductivity of $3 \cdot 10^4\text{ S/cm}$ whose flexibility can be enhanced by changing the grapheme content [58]. Similarly, fabrication of MSCs by introducing the MoS₂ into MXenes enhanced the electrochemical performance by 60% in comparison to pristine MXene [59]. Self-restacking of MXene layers was taken up by adding RuO₂ nanoparticles in order to improve ion exchange rate. Integration of conductive Ag nanowires into MXene decreases electrodes surface resistance. These strategies achieved MSC with volumetric capacitance of $864.2\text{ F}\cdot\text{cm}^{-2}$ at 1 mV/s with 90% of capacitance retention even after 10 000 cycles [60].

PANI/MXene-based film electrodes with an exceptionally high volumetric capacitance of $1167\text{ F}\cdot\text{cm}^{-3}$ were reported for the first time [61]. Stretchable MSCs based on MXene/bacterial cellulose composite with high Young's modulus of $15\text{--}35\text{ GPa}$ and tensile strength of up to $200\text{--}300\text{ GPa}$ were fabricated. Here, bacterial cellulose acts as a gap between MXene sheets preventing re-stacking of MXene flakes [62]. MXene–polymer composite nanofibers as flexible yarn electrodes were synthesized. This was achieved by electro spinning of active material on PET sheets. This device displays high areal capacitance of up to 18.39 mF/cm^2 at scan rate of 50 mV/s , which is better than many other carbon based yarn fibre supercapacitors [63]. In continuation, another group reported similar MSCs such as MXene/PEDOT-PSS-based yarn supercapacitors (YSCs) with 95% capacitive retention after 10 000 cycles, which is found significant in portable electronics [64]. In the same way, fabrication of dual-core yarn supercapacitor (YSC) with *r*GO and MXene hybrid fibres encapsulated with PVA–H₂SO₄ was reported. Its mean diameter was of approximately $500\text{ }\mu\text{m}$ with excellent linear capacitance of 43.6 mF/cm at 20 mV/s [65].

5. CONCLUSIONS

Right from the discovery of MXenes, they have become one of the unique choices for microelectrodes in MSCs for electronics applications. Their excellent properties such as large conductivity, volumetric capacitance makes them well suited for MSCs. However, fabrication of MXene-based MSCs is in the development stage, which needs to be further optimized in terms of material used for electrode, substrates and electrolytes. As per the existing literature, main focus of MXene based MSCs is towards the increase in areal capacitance and power density. Already, it is observed that self-discharging in open circuit condition needs to be attended on immediate basis. As per the earlier reports, this drawback can be rectified through integrating MSCs with solar power cells to enhance long-term charge storage property instead

of self-discharging. In order to increase the electrochemical performance, electrolyte selection plays a vital role. Usually, polymer gel electrolyte was used for ion exchange in MXene-based electrodes for microdevices, whose output voltage is low. Hence, alternative is required in order to increase the voltage and stability. Hence, different electrolytes and polymers need to be envisaged, which enhance performance of MSCs. However, ionogel may be one option with high stability in terms of mechanical and thermal than regular gel electrolytes. Expansion of potential may be possible with asymmetric devices for real time applications. Apart from the $Ti_3C_2Ti_x$ (MXene) based MSCs, many MXene materials might be synthesised for better understanding of charge storage mechanism that lead to future MSCs devices.

REFERENCES

1. B. E. Conway, *Electrochemical Supercapacitors* (Kluwer Academic/Plenum Publishers: 1999); <https://doi.org/10.1007/978-1-4757-3058-6>
2. Z. Stevic, I. Radovanovic, M. Rajcic-Vujasinovic, S. Bugarinovic, and V. Grekulovic, *ChemInform*, **45**, No. 27: 234 (2014); <https://doi.org/10.1002/chin.201427234>
3. Thibeorchews Prasankumar, Jemini Jose, Sujin Jose, and Sreeja P. Balakrishnan, *Pseudocapacitors* (IntechOpen: 2021); <doi:10.5772/intechopen.98600>
4. Shanshan Xiong, Shuyao Jiang, Juan Wang, Hongjun Lin, Mengxian Lin, Shuting Weng, Shuai Liu, Yang Jiao, Yanchao Xu, and Jianrong Chen, *Electrochimica Acta*, **340**: 135956 (2020); <https://doi.org/10.1016/j.electacta.2020.135956>
5. Xuli Chen, Rajib Paul, and Liming Dai, *National Science Review*, **4**: 453 (2017); <doi:10.1093/nsr/nwx009>
6. K. Adib, S. Esmail, M. Ghalkhani, and H. R. Naderi, *Ceramics International*, **47**, No. 10: 14075 (2021); <http://doi.10.1016/j.ceramint.2021.01.277>
7. J. Park, J. Lee, S. Kim, and J. Hwang, *Materials*, **14**, No. 10: 2597 (2021); <https://doi.org/10.3390/ma14102597>
8. D. Tie, S. Huang, J. Wang, Y. Zhao, J. Ma, and J. Zhang, *Energy Storage Materials*, **21**: 22 (2019); <https://doi.org/10.1016/j.ensm.2018.12.018>
9. W. Zuo, R. Li, C. Zhou, Y. Li, J. Xia, and J. Liu, *Advanced Science*, **4**, No. 7: 1600539 (2017); <https://doi.org/10.1002/advs.201600539>
10. H. Shifei, X. Zhu, S. Sarkar, and Y. Zhao, *APL Materials*, **7**: 100901 (2019); <https://doi.org/10.1063/1.5116146>
11. R. Banavath, S. S. Nemala, S.-H. Kim, S. Bohm, M. Z. Ansari, and D. Mohapatra, *Flat. Chem.*, **33**: 100373 (2022); <http://doi.org/10.1016/j.flatc.2022.100373>
12. A. G. Olabi, M. A. Abdelkareem, T. Wilberforce, and E. T. Sayed, *Renewable and Sustainable Energy Reviews*, **135**: 110026 (2021); <http://doi.org/10.1016/j.rser.2020.110026>
13. Z. Stević and M. Rajčić-Vujasinović, *Journal of Power Sources*, **160**: 1511 (2006); <http://doi.org/10.1016/j.jpowsour.2006>
14. M. Rajcic Vujasinovic, Z. Stevic, and S. Bugarinovic, *Open Journal of Metal.*, **2**,

- No. 3: 60 (2012); <http://doi.org/10.4236/ojmetal.2012.23009>
15. C. Yang, J. Liang, L. Xue, L. Yue, Q. Liu, and S. Lu, *Chemical Communication*, **57**: 2343 (2021); <https://doi.org/10.1039/D0CC07970G>
16. J. Wang, F. Li, F. Zhu, and O. G. Schmidt, *Small Methods*, **3**, No. 8: 1800367 (2019); <https://doi.org/10.1002/smtd.201800367>
17. F. Bu, W. Zhou, Y. Xu, Y. Du, C. Guan, and W. Huang, *Npj Flex Electron.*, **4**, No. 31: 1 (2020); <https://doi.org/10.1038/s41528-020-00093-6>
18. Qiu Jiang, Yongjiu Lei, Hanfeng Liang, Kai Xi, Chuan Xia, and Husam N. Alshareef, *Energy Storage Mater.*, **27**: 78 (2020); <https://doi.org/10.1016/j.ensm.2020.01.018>
19. Panpan Zhang, Faxing Wang, Minghao Yu, Xiaodong Zhuang, and Xinliang Feng, *Chem. Soc. Rev.*, **47**, No. 19: 7426 (2018); <https://doi.org/10.1039/C8CS00561C>
20. David Pech, Magali Brunet, Pierre-Louis Taberna, Patrice Simon, Norbert Fabre, Fabien Mesnilgrente, Véronique Conédéra, and Hugo Durou, *J. Power Sources*, **195**, No. 4: 1266 (2010); <http://dx.doi.org/10.1016/j.jpowsour.2009.08.085>
21. John Chmiola, Celine Largeot, Pierre-Louis Taberna, Patrice Simon, and Yury Gogotsi, *Science*, **328**, No. 5977: 480 (2010); <doi:10.1126/science.1184126>
22. David Pech, Magali Brunet, Hugo Durou, Peihua Huang, Vadym Mochalin, Yury Gogotsi, Pierre-Louis Taberna, and Patrice Simon, *Nat. Nanotechnol.*, **5**, No. 9: 651 (2010); <doi:10.1038/NNANO.2010.162>
23. Jiaxing Liang, Anjon Kumar Mondal, Da-Wei Wang, and Francesca Iacop, *Adv. Mater. Technol.*, **4**, No. 1: 1800200 (2019); <https://doi.org/10.1002/admt.201800200>
24. Jian Lin, Chenguang Zhang, Zheng Yan, Yu Zhu, Zhiwei Peng, Robert H. Hauge, Douglas Natelson, and James M. Tour, *Nano Lett.*, **13**, No. 1: 72 (2013); <https://doi.org/10.1021/nl3034976>
25. Narendra Kurra, Qiu Jiang, Pranati Nayak, and Husam N. Alshareef, *Nano Today*, **24**: 81 (2019); <https://doi.org/10.1016/j.nantod.2018.12.003>
26. Wenping Si, Chenglin Yan, Yao Chen, Steffen Oswald, Luyang Han, and Oliver G. Schmidt, *Energy Environ. Sci.*, **6**, No. 11: 3218 (2013); <https://doi.org/10.1039/C3EE41286E>
27. Torsten Brezesinski, John Wang, Sarah H. Tolbert, and Bruce Dunn, *Nat. Mater.*, **9**, No. 2: 146 (2010); <https://doi.org/10.1038/nmat2612>
28. Jinhong Du and Hui-Ming Cheng, *Macromol. Chem. Phys.*, **213**: 1060 (2012); <https://doi.org/10.1002/macp.201200029>
29. Narendra Kurra, Chuan Xia, M. N. Hedhili, and H. N. Alshareef, *Chem. Commun.*, **51**, No. 52: 10494 (2015); <https://doi.org/10.1039/C5CC03220B>
30. Michael Naguib, Murat Kurtoglu, Volker Presser, Jun Lu, Junjie Niu, Min Heon, Lars Hultman, Yury Gogotsi, and Michel W. Barsoum, *Adv. Mater.*, **23**, No. 37: 4248 (2011); <https://doi.org/10.1002/adma.201102306>
31. Aditya Sharma and Chandra Sekhar Rout, *Two-Dimensional MXene Based Materials for Micro-Supercapacitors* (IntechOpen: 2021); <doi:10.5772/intechopen.97650>
32. Johnson Michael, Zhang Qifeng, and Wang Danling, *Nanomaterials Nanotechnology*, **9**: 1 (2019); <https://doi.org/10.1177/1847980418824470>
33. Michael Naguib, Vadym N. Mochalin, Michel W. Barsoum, and Yury Gogotsi, *Adv. Mater.*, **26**, No. 7: 992 (2014); <https://doi.org/10.1002/adma.201304138>
34. Michael Naguib, Olha Mashtalar, Joshua Carle, Volker Presser, Jun Lu, Lars

- Hultman, Yury Gogotsi, and Michel W. Barsoum, *ACS Nano*, **6**, No. 2: 1322 (2012); <https://doi.org/10.1021/nn204153h>
35. Chuanfang (John) Zhang, Babak Anasori, Andrés Seral-Ascaso, Sang-Hoon Park, Niall McEvoy, Aleksey Shmeliov, Georg S. Duesberg, Jonathan N. Coleman, Yury Gogotsi, and Valeria Nicolosi, *Adv. Mater.*, **29**, No. 36: 1702678 (2017); <https://doi.org/10.1002/adma.201702678>
36. Faisal Shahzad, Mohamed Alhabeb, Christine B. Hatter, Babak Anasori, Soon Man Hong, Chong Min Koo, and Yury Gogotsi, *Science*, **353**, No. 6304: 1137 (2016); [doi:10.1126/science.aag2421](https://doi.org/10.1126/science.aag2421)
37. Mohammad Khazaei, Masao Arai, Taizo Sasaki, Chan-Yeup Chung, Natarajan S. Venkataraman, Mehdi Estili, Yoshio Sakka, and Yoshiyuki Kawazoe, *Adv. Funct. Mater.*, **23**, No. 17: 2185 (2013); <https://doi.org/10.1002/adfm.201202502>
38. Mohammad Khazaei, Masao Arai, Taizo Sasaki, Mehdi Estilic, and Yoshio Sakka, *Phys. Chem. Chem. Phys.*, **16**, No. 17: 7841 (2014); <https://doi.org/10.1039/C4CP00467A>
39. I. R. Shein and A. L. Ivanovskii, *Comput. Mater. Sci.*, **65**: 104 (2012); <https://doi.org/10.1016/j.commatsci.2012.07.011>
40. Guoying Gao, Guangqian Ding, Jie Li, Kailun Yao, Menghao Wu, and Meichun Qian, *Nanoscale*, **8**, No. 16: 8986 (2016); <https://doi.org/10.1039/C6NR01333C>
41. Mohammad Khazaei, Ahmad Ranjbar, Mahdi Ghorbani-Asl, Masao Arai, Taizo Sasaki, Yunye Liang, and Seiji Yunoki, *Phys. Rev. B*, **93**, No. 20: 205125 (2016); <https://doi.org/10.1103/PhysRevB.93.205125>
42. Youngbin Lee, Sung Beom Cho, and Yong-Chae Chung, *ACS Appl. Mater. Interfaces*, **6**, No. 16: 14724 (2014); <https://doi.org/10.1021/am504233d>
43. Gabriel Plummer, Babak Anasori, Yury Gogotsi, and Garritt J. Tucker, *Comput. Mater. Sci.*, **157**: 168 (2019); <https://doi.org/10.1016/j.commatsci.2018.10.033>
44. Vadym N. Borysiuk, Vadym N. Mochalin, and Yury Gogotsi, *Nanotechnology*, **26**, No. 26: 265705 (2015); <https://doi.org/10.1088/0957-4484/26/26/265705>
45. Zheng Ling, Chang E. Ren, Meng-Qiang Zhao, Jian Yang, James M. Giamarco, Jieshan Qiuc, Michel W. Barsouma, and Yury Gogotsi, *Proc. Natl. Acad. Sci.*, **111**, No. 47: 16676 (2014); <https://doi.org/10.1073/pnas.1414215111>
46. Narendra Kurra, Bilal Ahmed, Yury Gogotsi, and Husam N. Alsharee, *Adv. Energy Mater.*, **6**, No. 24: 1601372 (2016); <https://doi.org/10.1002/aenm.201601372>
47. Qiu Jiang, Narendra Kurra, Kathleen Maleski, Yongjiu Lei, Hanfeng Liang, Yizhou Zhang, Yury Gogotsi, and Husam N. Alsharee, *Adv. Energy Mater.*, **9**, No. 26: 1901061 (2019); <https://doi.org/10.1002/aenm.201901061>
48. You-Yu Peng, Bilen Akuzum, Narendra Kurra, Meng-Qiang Zhao, Mohamed Alhabeb, Babak Anasori, Emin Caglan Kumbur, Husam N. Alshareef, Ming-Der Ger, and Yury Gogotsi, *Energy Environ. Sci.*, **9**, No. 9: 2847 (2016); <https://doi.org/10.1039/C6EE01717G>
49. Pol Salles, Evan Quain, Narendra Kurra, Asia Sarycheva, and Yury Gogotsi, *Small*, **4**, No. 44: 1802864 (2018); <https://doi.org/10.1002/smll.201802864>
50. Evan Quain, Tyler S. Mathis, Narendra Kurra, Kathleen Maleski, Katherine L. Van Aken, Mohamed Alhabeb, Husam N. Alshareef, and Yury Gogotsi, *Adv. Mater Technol.*, **4**, No. 1: 1800256 (2019); <https://doi.org/10.1002/admt.201800256>
51. Liangzhu Zhang, Guoliang Yang, Zhiqiang Chen, Dan Liu, Jiemin Wang, Yijun

- Qian, Cheng Chen, Yuchen Liu, Lifeng Wang, Joselito Razal, and Weiwei Lei, *Journal of Materomics*, **6**, No. 1: 138 (2020);
<https://doi.org/10.1016/j.jmat.2019.12.013>
52. Qiang Li, Qizhao Wang, Linlin Li, Lijun Yang, Yang Wang, Xiaohui Wang, and Hai-Tao Fang, *Adv. Energy Mater.*, **10**, No. 24: 2000470 (2020);
<https://doi.org/10.1002/aenm.202070104>
53. Liangzhu Zhang, Guoliang Yang, Zhiqiang Chen, Dan Liu, Jiemin Wang, Yijun Qian, Cheng Chen, Yuchen Liu, Lifeng Wang, Joselito Razal, and Weiwei Le, *J. Materomics*, **6**, No. 1: 138 (2020);
<https://doi.org/10.1016/j.jmat.2019.12.013>
54. Haichao Huang, Hai Su, Haitao Zhang, Ludi Xu, Xiang Chu, Chunfeng Hu, Huan Liu, Ning jun Chen, Fangyan Liu, Wen Deng, Bingni Gu, Hepeng Zhang, and Weiqing Yang, *Adv. Electron Mater.*, **4**, No. 8: 1800179 (2018);
<https://doi.org/10.1002/aelm.201800179>
55. Aditya Sharma and Chandra Sekhar Rout, *Two-Dimensional MXene Based Materials for Micro-Supercapacitors* (IntechOpen: 2021);
[doi:10.5772/intechopen.97650](https://doi.org/10.5772/intechopen.97650)
56. Yang Yue, Nishuang Liu, Yanan Ma, Siliang Wang, Weijie Liu, Cheng Luo, Hang Zhang, Feng Cheng, Jiangyu Rao, Xiaokang Hu, Jun Su, and Yihua Gao, *ACS Nano*, **12**, No. 5: 4224; <https://doi.org/10.1021/acsnano.7b07528>
57. Haichao Huang, Xiang Chu, Hai Su, Haitao Zhang, Yanting Xie, Wen Deng, Ningjun Chen, Fangyan Liu, Hepeng Zhang, Bingni Gua, Weili Deng, and Weiqing Yang, *J. Power Sources*, **415**: 1 (2019);
<https://doi.org/10.1016/j.jpowsour.2019.01.044>
58. Cedric Couly, Mohamed Alhabeb, Katherine L. Van Aken, Narendra Kurra, Luisa Gomes, Adriana M. Navarro-Suarez, Babak Anasori, Husam N. Alshareef, and Yury Gogotsi, *Adv. Electron Mater.*, **4**, No. 1: 1700339 (2018);
<https://doi.org/10.1002/aelm.201700339>
59. Xing Chen, Siliang Wang, Junjie Shi, Xiaoyu Du, Qinghua Cheng, Rui Xue, Qi-ang Wang, Min Wang, Limin Ruan, and Wei Zeng, *Adv. Mater. Interfaces*, **6**, No. 22: 1901160 (2019); <https://doi.org/10.1002/admi.201901160>
60. Chenyang Yu, Yujiao Gong, Ruyi Chen, Mingyi Zhang, Jinyuan Zhou, Jianing An, Fan Lv, Shaojun Guo, and Gengzhi Sun, *Small*, **14**, No. 29: 1801203 (2018);
<https://doi.org/10.1002/smll.201801203>
61. Qiuyan Yang, Zhen Xu, Bo Fang, Tieqi Huang, Shengying Cai, Hao Chen, Yingjun Liu, Karthikeyan Gopalsamy, Weiwei Gao, and Chao Gao, *J. Mater. Chem. A*, **5**, No. 42: 22113 (2017); [doi:10.1039/C7TA07999K](https://doi.org/10.1039/C7TA07999K)
62. Xing Chen, Siliang Wang, Junjie Shi, Xiaoyu Du, Qinghua Cheng, Rui Xue, Qi-ang Wang, Min Wang, Limin Ruan, and Wei Zeng, *Adv. Mater. Interfaces*, **6**, No. 22: 1901160 (2019); <https://doi.org/10.1002/admi.201901160>
63. Hongpeng Li, Xiran Li, Jiajie Liang, and Yongsheng Chen, *Adv. Energy Mater.*, **9**, No. 5: 1803987 (2019); <https://doi.org/10.1002/aenm.201803987>
64. Yuanming Wang, Xue Wang, Xiaolong Li, Yang Bai, Huanhao Xiao, Yang Liu, and Guohui Yuan, *Chem. Eng. J.*, **405**: 126664 (2021);
<https://doi.org/10.1016/j.cej.2020.126664>
65. Nanfei He, Jinyun Liao, Feng Zhao, and Wei Gao, *ACS Appl. Mater. Interfaces*, **12**, No. 13: 15211-9 (2020); <https://doi.org/10.1021/acsami.0c00182>

PACS numbers: 72.80.Tm, 77.22.Ch, 77.22.Gm, 77.55.+f, 77.84.Lf, 81.07.Pr, 82.35.Np

Synthesis and Improved Dielectric Properties of PVP/TiN/Si₃N₄ Nanocomposites

Ahmed Hashim¹, Aseel Hadi², and M. H. Abbas¹

¹*College of Education for Pure Sciences,
Department of Physics,
University of Babylon,
Hilla, Iraq*

²*College of Materials Engineering,
Department of Ceramic and Building Materials,
University of Babylon,
Hilla, Iraq*

Nanocomposites of PVP/TiN/Si₃N₄ films are prepared with different concentrations to utilize in many industrial fields. The dielectric properties of PVP/TiN/Si₃N₄ nanocomposites are examined in the frequency range from 100 Hz to 5 MHz. The experimental results demonstrate that the dielectric constant, dielectric loss and electrical conductivity of PVP/TiN/Si₃N₄ nanocomposites increase with increasing concentration. In addition, the dielectric constant and dielectric loss of PVP/TiN/Si₃N₄ nanocomposites are reduced, while the conductivity is increased with rising frequency. Finally, the obtained results indicate that the PVP/TiN/Si₃N₄ nanocomposites can be considered as new nanomaterials to use in different electronics fields.

Нанокомпозити плівок полівінілпіролідон/TiN/Si₃N₄ було виготовлено з різними концентраціями для використання в багатьох галузях промисловості. Досліджено діелектричні властивості нанокомпозитів полівінілпіролідон/TiN/Si₃N₄ у діапазоні частот від 100 Гц до 5 МГц. Експериментальні результати показали, що діелектрична проникність, діелектричні втрати й електропровідність нанокомпозитів полівінілпіролідон/TiN/Si₃N₄ зростають із збільшенням концентрації. Крім того, діелектрична проникність і діелектричні втрати нанокомпозитів полівінілпіролідон/TiN/Si₃N₄ зменшилися, а провідність зросла зі збільшенням частоти. Нарешті, одержані результати показали, що нанокомпозити полівінілпіролідон/TiN/Si₃N₄ можна розглядати як нові наноматеріали для використання в різних областях електроніки.

Key words: TiN/Si₃N₄, dielectric properties, polyvinylpyrrolidone, elec-

tronics fields, nanocomposites.

Ключові слова: TiN/Si₃N₄, діелектричні властивості, полівінілпіролідон, електричні поля, нанокомпозити.

(Received 30 June, 2023; in revised form, 26 August, 2023)

1. INTRODUCTION

Polymer composites are a class of materials with prominent physicochemical properties, where a polymer acts as the matrix and micro-, macro-, or nanomaterials as the filler. Researchers have reported that nanofillers (*e.g.*, carbon nanotubes or nanosemiconductors) can improve some features of polymers, such as their electrical conductivity and mechanical behaviour. Accordingly, polymer nanocomposites (PNCs) are interesting for the industry due to their enhanced properties and have been receiving applications in fields such as environmental remediation, energy storage, and biomedicine [1].

Polymers have been widely used in various applications due to outstanding properties such as their low cost, stability, easy fabrication, *etc.*

The advantages of polymer matrix composites include their low cost and straightforward fabrication processes. Furthermore, polymer composites can be used as the primary material to create lightweight, flexible electronics, which is advantageous considering consumer demand [2].

Polyvinylpyrrolidone (PVP) has a good stable environment, easy processing, and moderate electric conductivity. It has a wide range of applications such as electrochemical devices (batteries, displays) [3].

Silicon nitride (Si₃N₄) is amid the mainly significant ceramic materials for elevated-temperature fields because of its combination of mechanical properties at room and elevated temperatures, resistance to oxidation, low thermal expansion coefficient, and low density compared of refractory metals [4].

Titanium nitride (TiN) shows excellent chemical resistance, superior electrical conductivity, and good adhesion with most materials [5].

The nanocomposites consisting of nanostructure doped with different materials have numerous applications in different fields like optical fields [6–15], energy storage [16–18], sensors [19–20], electronics and optoelectronics [21–35], antibacterial [36–41], radiation shielding and bioenvironmental [42–47].

The present work objects to prepare the PVP/TiN/Si₃N₄ nanocomposites' films to employ in many industrial applications.

2. MATERIALS AND METHODS

The used nanomaterials in this work are TiN and Si₃N₄ nanoparticles (NPs) as filler and PVP as matrix. The films of PVP/TiN/Si₃N₄ nanocomposites were prepared using casting process with various concentrations of 12.5 gm/L, 25 gm/L, and 50 gm/L with ratio of TiN/Si₃N₄ NPs (6 wt.%) and content of 50% TiN and 50% Si₃N₄. The dielectric properties of PVP/TiN/Si₃N₄ nanocomposites' films were examined at frequency ranged from 100 Hz to 5 MHz using LCR meter (HIOKI 3532-50 LCR HI TESTER). The dielectric constant (ϵ') is found by [48] as follows:

$$\epsilon' = C_p/C_0, \quad (1)$$

where C_p is the matter capacitance and C_0 is the capacitance of vacuum.

Dielectric loss (ϵ'') is calculated by [49] as follows:

$$\epsilon'' = \epsilon'D, \quad (2)$$

where D is the dispersion factor. The A.C. electrical conductivity is given by [50]:

$$\sigma_{A.C.} = 2\pi f\epsilon'D\epsilon_0. \quad (3)$$

4. RESULTS AND DISCUSSION

Figures 1–4 demonstrate the difference in the dielectric constant and dielectric loss with frequency and concentration for PVP/TiN/Si₃N₄ nanocomposites' films, respectively.

The dielectric constant and dielectric loss rise with increasing concentration; this behaviour is due to rise in number of charges' carriers. The high values of dielectric constant and dielectric loss at lower frequencies were assigned to the availability of enough time for the dipoles to interact with the fields before it changes, while the values of dielectric constant and dielectric loss decrease at higher frequencies due to the shorter time available to them [51–65].

The electrical conductivity performance with concentration and frequency for PVP/TiN/Si₃N₄ nanocomposites are shown in Figs. 5 and 6, respectively. The electrical conductivity increases with an increase in the concentration and frequency. The rise of electrical conductivity as the concentration increases due to increase in the charge-carriers' numbers. The frequency-dependent conductivity is caused by the hopping of electrons in the localized states near the Fermi level and due to the excitation of charge carriers to the

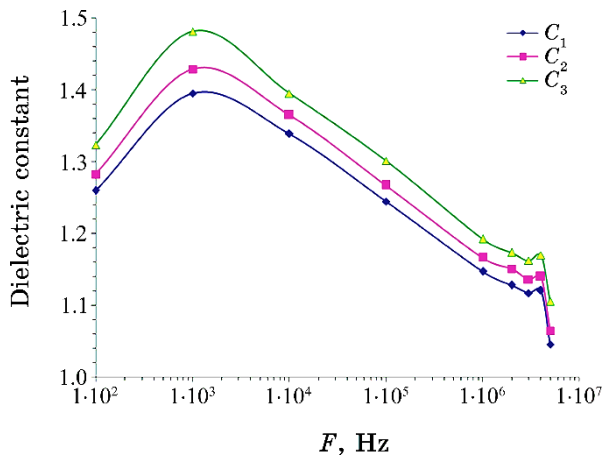


Fig. 1. Difference in the dielectric constant with frequency for PVP/TiN/Si₃N₄ nanocomposites.

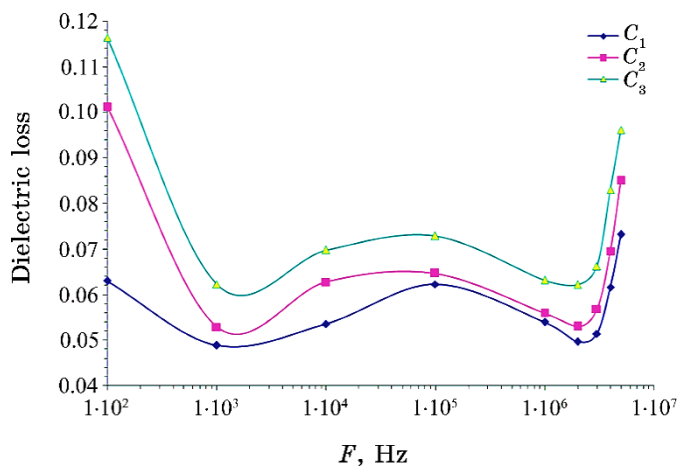


Fig. 2. Variation of dielectric loss with frequency for PVP/TiN/Si₃N₄ nanocomposites.

states in the conduction band [66–70].

5. CONCLUSIONS

This work includes fabrication of PVP/TiN/Si₃N₄ nanocomposites' films with various concentrations to utilize in different industrial applications.

The dielectric properties of PVP/TiN/Si₃N₄ nanocomposites were

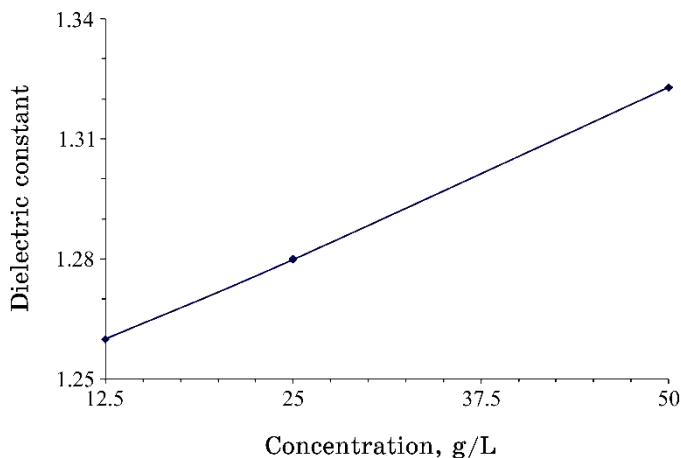


Fig. 3. Dielectric constant variation with concentration for PVP/TiN/Si₃N₄ nanocomposites.

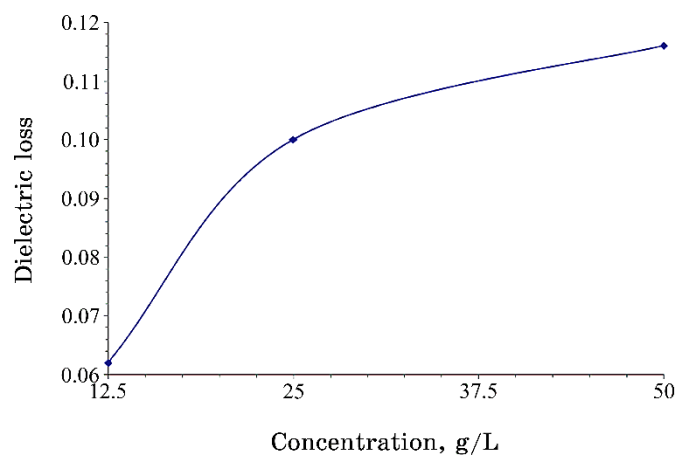


Fig. 4. Performance of dielectric loss with concentration for PVP/TiN/Si₃N₄ nanocomposites.

examined in the frequency range of 100 Hz–5 MHz. The results showed that the dielectric constant, dielectric loss and electrical conductivity of PVP/TiN/Si₃N₄ nanocomposites are increased with increasing concentration. The dielectric constant and dielectric loss of PVP/TiN/Si₃N₄ nanocomposites are reduced, while the conductivity is increased with rising frequency.

The results illustrate that the PVP/TiN/Si₃N₄ nanocomposites may be considered as new nanomaterials to employ in various electronics applications.

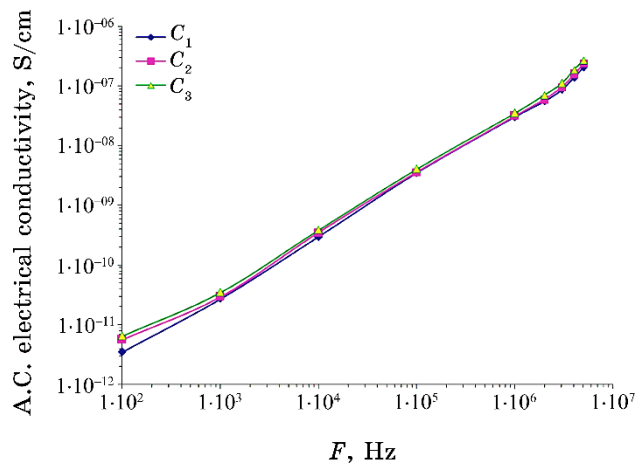


Fig. 5. Electrical conductivity performance with frequency for PVP/TiN/Si₃N₄ nanocomposites.

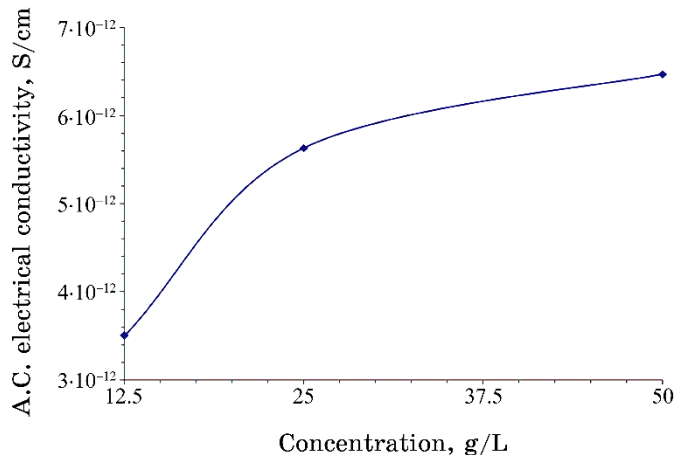


Fig. 6. Variation of electrical conductivity with concentration for PVP/TiN/Si₃N₄ nanocomposites.

REFERENCES

1. B. Jaleh, S. Hamzehi, R. Sepahvand, S. Azizian, M. Eslamipanah, R. Golbedaghi, A. Meidanchi, and R. Fausto, *Molecules*, **27**: 1 (2022); <https://doi.org/10.3390/molecules27144448>
2. A. H. Alshammari, K. Alshammari, M. Alshammari, and T. A. M. Taha, *Polymers*, **15**: 1 (2023); <https://doi.org/10.3390/polym15040871>
3. H. M. Zidan, E. M. Abdelrazek, A. M. Abdelghany, A. E. Tarabiah, *J. Mater. Res. Technol.*, **8**, Iss. 1: 904 (2019);

- <https://doi.org/10.1016/j.jmrt.2018.04.023>
- 4. L. A. Díaz, W. Solís, P. Peretyagin, A. Fernández, M. Morales, C. Pecharromán, J. S. Moya, and R. Torrecillas, *J. of Nanomaterials*, **2016**: 1 (2016); <http://dx.doi.org/10.1155/2016/3170142>
 - 5. E. Yousefi, M. Ghorbani, A. Dolati, and H. Yashiro, *Scientia Iranica F*, **24**, Iss. 6: 3481 (2017); doi:10.24200/sci.2017.4417
 - 6. H. Ahmed and A. Hashim, *Opt. Quant. Electron.*, **55**: 1 (2023); <https://doi.org/10.1007/s11082-022-04273-8>
 - 7. W. O. Obaid and A. Hashim, *Silicon*, **14**: 11199 (2022); <https://doi.org/10.1007/s12633-022-01854-w>
 - 8. O. B. Fadil and A. Hashim, *Silicon*, **14**: 9845 (2022); <https://doi.org/10.1007/s12633-022-01728-1>
 - 9. H. Ahmed and A. Hashim, *Silicon*, **15**: 2339 (2023); <https://doi.org/10.1007/s12633-022-02173-w>
 - 10. H. B. Hassan, H. M. Abduljalil, and A. Hashim, *Nanosistemi, Nanomateriali, Nanotehnologii*, **20**, Iss. 4: 941 (2022); <https://doi.org/10.15407/nnn.20.04.941>
 - 11. H. A. Jawad and A. Hashim, *Nanosistemi, Nanomateriali, Nanotehnologii*, **20**, Iss. 4: 963 (2022); <https://doi.org/10.15407/nnn.20.04.963>
 - 12. H. Ahmed and A. Hashim, *Silicon*, **14**: 6637 (2022); <https://doi.org/10.1007/s12633-021-01449-x>
 - 13. H. Ahmed and A. Hashim, *Silicon*, **13**: 4331 (2020); <https://doi.org/10.1007/s12633-020-00723-8>
 - 14. H. Ahmed and A. Hashim, *Transactions on Electrical and Electronic Materials*, **22**: 335 (2021); <https://doi.org/10.1007/s42341-020-00244-6>
 - 15. N. AH. Al-Aaraji, A. Hashim, A. Hadi, and H. M. Abduljalil, *Silicon*, **14**: 10037 (2022); <https://doi.org/10.1007/s12633-022-01730-7>
 - 16. A. S. Shareef, F. Lafta R., A. Hadi, and A. Hashim, *International Journal of Scientific & Technology Research*, **8**, Iss. 11: 1041 (2019).
 - 17. A. Hadi, A. Hashim, and D. Hassan, *Bulletin of Electrical Engineering and Informatics*, **9**, No. 1: 83 (2020); doi:10.11591/eei.v9i1.1323
 - 18. H. Ahmed and A. Hashim, *Nanosistemi, Nanomateriali, Nanotehnologii*, **20**, Iss. 4: 951 (2022); <https://doi.org/10.15407/nnn.20.04.951>
 - 19. H. Ahmed and A. Hashim, *International Journal of Scientific & Technology Research*, **8**, Iss. 11: 1014 (2019).
 - 20. B. Mohammed, H. Ahmed, and A. Hashim, *Nanosistemi, Nanomateriali, Nanotehnologii*, **20**, No. 1: 187 (2022); <https://doi.org/10.15407/nnn.20.01.187>
 - 21. H. Ahmed and A. Hashim, *Silicon*, **14**: 4907 (2022); <https://doi.org/10.1007/s12633-021-01258-2>
 - 22. A. Hashim, *Opt. Quant. Electron.*, **53**: 1 (2021); <https://doi.org/10.1007/s11082-021-08100-w>
 - 23. H. Ahmed and A. Hashim, *Trans. Electr. Electron. Mater.*, **23**: 237 (2022); <https://doi.org/10.1007/s42341-021-00340-1>
 - 24. H. Ahmed and A. Hashim, *Silicon*, **14**: 7025 (2021); <https://doi.org/10.1007/s12633-021-01465-x>
 - 25. A. Hazim, A. Hashim, and H. M. Abduljalil, *Trans. Electr. Electron. Mater.*, **21**: 48 (2019); <https://doi.org/10.1007/s42341-019-00148-0>
 - 26. A. F. Kadhim and A. Hashim, *Opt. Quant. Electron.*, **55**: 432 (2023); <https://doi.org/10.1007/s11082-023-04699-8>

27. H. Ahmed and A. Hashim, *Opt. Quant. Electron.*, **55**: 280 (2023);
<https://doi.org/10.1007/s11082-022-04528-4>
28. G. Ahmed and A. Hashim, *Silicon*, **15**: 3977 (2023);
<https://doi.org/10.1007/s12633-023-02322-9>
29. M. H. Meteab, A. Hashim, and B. H. Rabee, *Opt. Quant. Electron.*, **55**: 187 (2023); <https://doi.org/10.1007/s11082-022-04447-4>
30. B. Mohammed, H. Ahmed, and A. Hashim, *Nanosistemi, Nanomateriali, Nanotehnologii*, **21**, Iss. 1: 113 (2023);
<https://doi.org/10.15407/nnn.21.01.133>
31. A. Hashim, *Nanosistemi, Nanomateriali, Nanotehnologii*, **19**, Iss. 3: 647 (2021); <https://doi.org/10.15407/nnn.19.03.647>
32. A. Hazim, A. Hashim, and H. M. Abduljalil, *Nanosistemi, Nanomateriali, Nanotehnologii*, **18**, Iss. 4: 983 (2020);
<https://doi.org/10.15407/nnn.18.04.983>
33. A. Hashim and Z. S. Hamad, *Nanosistemi, Nanomateriali, Nanotehnologii*, **18**, Iss. 4: 969 (2020); <https://doi.org/10.15407/nnn.18.04.969>
34. A. Hazim, A. Hashim, and H. M. Abduljalil, *Egypt. J. Chem.*, **64**, No. 1: 359 (2021); <doi:10.21608/EJCHEM.2019.18513.2144>
35. H. Ahmed and A. Hashim, *Journal of Molecular Modeling*, **26**: 1 (2020);
<doi:10.1007/s00894-020-04479-1>
36. A. Hashim, I. R. Agool, and K. J. Kadhim, *Journal of Bionanoscience*, **12**, No. 5: 608 (2018); <doi:10.1166/jbns.2018.1580>
37. O. B. Fadil and A. Hashim, *Nanosistemi, Nanomateriali, Nanotehnologii*, **20**, Iss. 4: 1029 (2022); <https://doi.org/10.15407/nnn.20.04.1029>
38. W. O. Obaid and A. Hashim, *Nanosistemi, Nanomateriali, Nanotehnologii*, **20**, Iss. 4: 1009 (2022); <https://doi.org/10.15407/nnn.20.04.1009>
39. M. H. Meteab, A. Hashim, and B. H. Rabee, *Nanosistemi, Nanomateriali, Nanotehnologii*, **21**, No. 1: 199 (2023);
<https://doi.org/10.15407/nnn.21.01.199>
40. A. Hazim, A. Hashim, and H. M. Abduljalil, *International Journal of Emerging Trends in Engineering Research*, **7**, No. 8: 68 (2019);
<https://doi.org/10.30534/ijeter/2019/01782019>
41. A. Hazim, H. M. Abduljalil, and A. Hashim, *International Journal of Emerging Trends in Engineering Research*, **7**, No. 8: 104(2019);
<https://doi.org/10.30534/ijeter/2019/04782019>
42. A. Hashim and Z. S. Hamad, *Journal of Bionanoscience*, **12**, No. 4: 504 (2018); <doi:10.1166/jbns.2018.1561>
43. B. Abbas and A. Hashim, *International Journal of Emerging Trends in Engineering Research*, **7**, No. 8: 131 (2019);
<https://doi.org/10.30534/ijeter/2019/06782019>
44. K. H. H. Al-Attiyah, A. Hashim, and S. F. Obaid, *Journal of Bionanoscience*, **12**: 200 (2018); <doi:10.1166/jbns.2018.1526>
45. H. A. J. Hussien, A. Hadi, and A. Hashim, *Nanosistemi, Nanomateriali, Nanotehnologii*, **20**, Iss. 4: 1001 (2022);
<https://doi.org/10.15407/nnn.20.04.1001>
46. A. Hashim and N. Hamid, *Journal of Bionanoscience*, **12**, No. 6: 788 (2018);
<doi:10.1166/jbns.2018.1591>
47. A. Hashim and Z. S. Hamad, *Journal of Bionanoscience*, **12**, No. 4: 488 (2018); <doi:10.1166/jbns.2018.1551>
48. S. Uddin, N. Akhtar, S. Bibi, A. Zaman, A. Ali, K. Althubeiti, H. Alrobei,

- and M. Mushtaq, *Materials*, **14**: 1 (2021);
<https://doi.org/10.3390/ma14185430>
49. T. A. Abdel-Baset and A. Hassen, *Physica B*, **499**: 24 (2016);
<http://dx.doi.org/10.1016/j.physb.2016.07.002>
50. H. M. Alhusaiki-Alghamdi, *Results in Physics*, **24**: 104125 (2021);
<https://doi.org/10.1016/j.rinp.2021.104125>
51. Z. S. Hamad and A. Hashim, *Nanosistemi, Nanomateriali, Nanotehnologii*, **20**, Iss. 1: 159 (2022); <https://doi.org/10.15407/nnn.20.01.159>
52. M. H. Meteab, A. Hashim, and B. H. Rabee, *Silicon*, **15**: 251 (2023);
<https://doi.org/10.1007/s12633-022-02020-y>
53. A. Hashim, A. Hadi, and M. H. Abbas, *Opt. Quant. Electron.*, **55**: 642 (2023); <https://doi.org/10.1007/s11082-023-04929-z>
54. A. Hashim, A. Hadi, and M. H. Abbas, *Silicon*, **15**: 6431 (2023);
<https://doi.org/10.1007/s12633-023-02529-w>
55. A. Hashim and Z. S. Hamad, *Nanosistemi, Nanomateriali, Nanotehnologii*, **20**, Iss. 1: 165 (2022); <https://doi.org/10.15407/nnn.20.01.165>
56. A. Hashim and A. Jassim, *Nanosistemi, Nanomateriali, Nanotehnologii*, **20**, Iss. 1: 177 (2022); <https://doi.org/10.15407/nnn.20.01.177>
57. A. Hashim and Z. S. Hamad, *Nanosistemi, Nanomateriali, Nanotehnologii*, **20**, Iss. 2: 507(2022); <https://doi.org/10.15407/nnn.20.02.507>
58. B. Mohammed, H. Ahmed and A. Hashim, *Journal of Physics: Conference Series*, **1879**: 1(2021); doi:[10.1088/1742-6596/1879/3/032110](https://doi.org/10.1088/1742-6596/1879/3/032110)
59. D. Hassan and A. H. Ah-Yasari, *Bulletin of Electrical Engineering and Informatics*, **8**, Iss. 1: 52 (2019); doi:[10.11591/eei.v8i1.1019](https://doi.org/10.11591/eei.v8i1.1019)
60. D. Hassan, and A. Hashim, *Bulletin of Electrical Engineering and Informatics*, **7**, Iss. 4: 547 (2018); doi:[10.11591/eei.v7i4.969](https://doi.org/10.11591/eei.v7i4.969)
61. A. Hashim, M. H. Abbas, N. AH. Al-Aaraji, and A. Hadi, *J. Inorg. Organomet. Polym.*, **33**: 1 (2023); <https://doi.org/10.1007/s10904-022-02485-9>
62. A. Hashim, M. H. Abbas, N. AH. Al-Aaraji, and A. Hadi, *Silicon*, **15**: 1283 (2023); <https://doi.org/10.1007/s12633-022-02104-9>
63. M. H. Meteab, A. Hashim, and B. H. Rabee, *Silicon*, **15**: 1609 (2023);
<https://doi.org/10.1007/s12633-022-02114-7>
64. N. Al-Huda Al-Aaraji, A. Hashim, A. Hadi, and H. M. Abduljalil, *Silicon*, **14**: 4699 (2022); <https://doi.org/10.1007/s12633-021-01265-3>
65. N. Algethami, A. Rajeh, H. M. Ragab, A. E. Tarabiah, and F. Gami, *J. Mater. Sci.: Mater. Electron.*, **33**: 10645 (2022);
<https://doi.org/10.1007/s10854-022-08048-5>
66. H. A. J. Hussien and A. Hashim, *J. Inorg. Organomet. Polym.*, **33**: 2331 (2023); <https://doi.org/10.1007/s10904-023-02688-8>
67. A. Hashim, A. Hadi, N. A. H. Al-Aaraji, and F. L. Rashid, *Silicon*, **15**: 5725 (2023); <https://doi.org/10.1007/s12633-023-02471-x>
68. A. F. Kadhim and A. Hashim, *Silicon*, **15**: 4613 (2023);
<https://doi.org/10.1007/s12633-023-02381-y>
69. H. A. Jawad and A. Hashim, *Nanosistemi, Nanomateriali, Nanotehnologii*, **21**, Iss. 1: 133 (2023); <https://doi.org/10.15407/nnn.21.01.133>
70. A. M. K. Aippunny, S. M. Shamsudeen, P. Valparambil, S. Mathew, and U. N. Vishwambharan, *Inc. J. Appl. Polym. Sci.*, **133**: 43568 (2016);
doi:[10.1002/APP.43568](https://doi.org/10.1002/APP.43568)

PACS numbers: 72.80.Tm, 77.22.Ch, 77.22.Gm, 77.55.+f, 77.84.Lf, 81.07.Pr, 82.35.Np

Augmented Dielectric Properties of PVP/Si₃N₄/Al₂O₃ Nanostructures

Ahmed Hashim¹ and Aseel Hadi²

¹*College of Education for Pure Sciences,
Department of Physics,
University of Babylon,
Hilla, Iraq*

²*College of Materials Engineering,
Department of Ceramic and Building Materials,
University of Babylon,
Hilla, Iraq*

The present study aims to prepare the PVP/Si₃N₄/Al₂O₃ nanostructures to use them in different electrical and electronics fields. The dielectric properties of PVP/Si₃N₄/Al₂O₃ nanostructures are tested. The experimental results illustrate that the dielectric constant (ϵ') and dielectric loss (ϵ'') of PVP/Si₃N₄/Al₂O₃ nanostructures decrease, while the electrical conductivity ($\sigma_{A.C.}$) is rising with a rise in the frequency. The dielectric parameters (dielectric constant, dielectric loss, and electrical conductivity) are rising with a rise in the concentration. Finally, the results show that the PVP/Si₃N₄/Al₂O₃ nanostructures can be appropriate in various electronics fields.

Це дослідження спрямовано на підготовку наноструктур полівінілпролідон/Si₃N₄/Al₂O₃ для використання їх у різних галузях електротехніки й електроніки. Вивчено діелектричні властивості наноструктур полівінілпролідон/Si₃N₄/Al₂O₃. Результати експерименту показують, що діелектрична проникність (ϵ') і діелектричні втрати (ϵ'') наноструктур полівінілпролідон/Si₃N₄/Al₂O₃ зменшуються, тоді як електропровідність ($\sigma_{A.C.}$) зростає зі збільшенням частоти. Діелектричні параметри (діелектрична проникність, діелектричні втрати й електропровідність) зростають зі збільшенням концентрації. Нарешті, результати показують, що наноструктури полівінілпролідон/Si₃N₄/Al₂O₃ можуть бути дійсними в різних областях електроніки.

Key words: polyvinylpyrrolidone, Si₃N₄/Al₂O₃, nanostructures, dielectric constant, conductivity.

Ключові слова: полівінілпіролідон, $\text{Si}_3\text{N}_4/\text{Al}_2\text{O}_3$, наноструктури, діелектрична проникність, електропровідність.

(Received 28 June, 2023; in revised form, 26 August, 2023)

1. INTRODUCTION

Polymeric materials are generally insulating or nonconductive materials in nature and normally used in electric and electronic applications as insulators, but likely to accumulate the electronic discharge.

The composites are the wonder materials, which are an essential part of today's materials due to the advantages such as low weight, corrosion resistance, high fatigue strength, and faster assembly. They are extensively used as materials in making aircraft structures, electronic packaging to medical equipment, and space vehicle to home building. The composites offer unusual combinations of materials properties such as weight, strength, stiffness, permeability, electrical, biodegradability and optical properties that is difficult to attain separately by individual components [1].

As the demand for electronics and capacitor devices increases, high dielectric materials have attracted increasing attention.

Polymer materials own advantages of ease of processing, flexibility, and good mechanical properties but the dielectric properties are usually less than satisfactory. Therefore, the preparation of high dielectric composites by introducing high dielectric fillers has become a research hotspot [2]. Polyvinylpyrrolidone (PVP) has a high polar group, low toxicity, biodegradable and amorphous nature with good film properties. It has two interactive sites N atom and C=O group. It acts as a protecting agent with other surfaces of inorganic compounds [3].

Silicon nitride (Si_3N_4) is a highly stable covalent compound with great application value in many fields due to good corrosion resistance and excellent resistance to temperature change. It may be an effective filler to improve the performance of polymer materials [4]. Alumina particles act as barriers to dislocations, and the increase of its content increases hardness, compressive strength and Young's modulus, however, decreases ductility [5].

The nanocomposites have huge applications in different fields like antibacterial [6–11], energy storage [12–14], optical fields [15–24], radiation shielding and bioenvironmental [25–30], electronics and optoelectronics [31–45] sensors [46, 47].

This work deals with preparation of PVP/ $\text{Si}_3\text{N}_4/\text{Al}_2\text{O}_3$ nanostructures and investigating the A.C. electrical properties to use in various electronics applications.

2. MATERIALS AND METHODS

The materials were used in present work are PVP as matrix with Si₃N₄/Al₂O₃ nanoparticles (NPs) as additive. The PVP/Si₃N₄/Al₂O₃ nanostructures were prepared using casting method with concentrations ($C_1 = 12.5$ gm/L, $C_2 = 25$ gm/L, and $C_3 = 50$ gm/L) and constant ratio of Si₃N₄/Al₂O₃ NPs (6%) with concentration of 50% Al₂O₃ and 50% Si₃N₄. The dielectric properties of PVP/Si₃N₄/Al₂O₃ nanostructures were tested at frequency range (100 Hz–5 MHz) by LCR meter (HIOKI 3532-50 LCR HI TESTER).

The dielectric constant (ϵ') was calculated by [48]:

$$\epsilon' = C_p/C_0, \quad (1)$$

where C_p is the capacitance of matter and C_0 is the vacuum capacitance.

Dielectric loss (ϵ'') was found by [48]:

$$\epsilon'' = \epsilon'D, \quad (2)$$

where D is the dispersion factor.

The A.C. electrical conductivity was given [49]:

$$\sigma_{\text{A.C.}} = 2\pi f\epsilon'D\epsilon_0. \quad (3)$$

3. RESULTS AND DISCUSSION

Figures 1–4 show the variation of dielectric constant (ϵ') and dielectric loss (ϵ'') with frequency and concentration, respectively. The figures show that ϵ' and ϵ'' have large values at low frequencies. The interfacial effects present in the majority of the film and the electrode effects might both be responsible for the high values of ϵ' and ϵ'' . It can be observed that for all frequency ranges, the values of ϵ' and ϵ'' for PVP/Si₃N₄/Al₂O₃ nanostructures rise with increasing concentration. The increase of ϵ' and ϵ'' values can be related to raise in the number charges carriers [50–63].

The behaviour of A.C. electrical conductivity for the PVP/Si₃N₄/Al₂O₃ nanostructures with frequency and concentration are shown in Figs. 5 and 6, respectively. From these figures, the conductivity increases with rising of the concentration. The low-frequency region exhibits dispersion due to spatial charging or inter polarization.

In addition, the decrease of conductivity at lower frequency was due to decrease number of mobile ions resulting from charged cumulative at polymer interfaces. The improvement of electrical con-

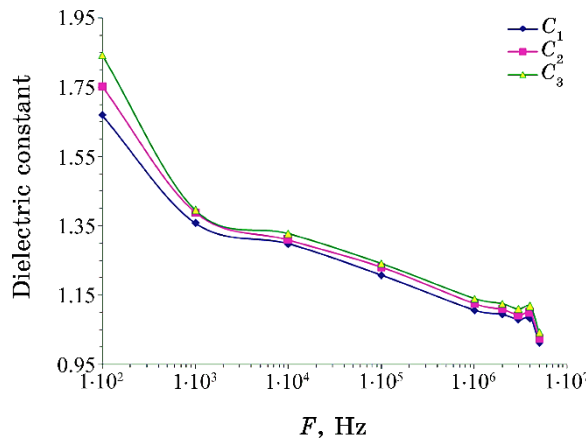


Fig. 1. Variation of dielectric constant for the PVP/Si₃N₄/Al₂O₃ nanostructures with frequency.

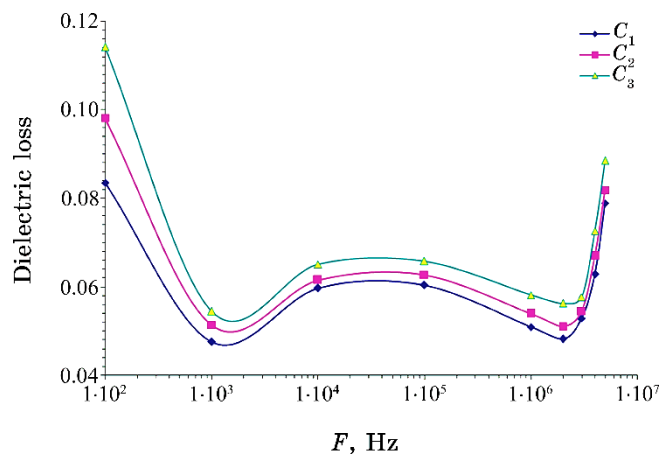


Fig. 2. Dielectric loss variation for the PVP/Si₃N₄/Al₂O₃ nanostructures with frequency.

ductivity with concentration was because of the raising the number of dopants, where the Si₃N₄/Al₂O₃NPs molecules begin to bridge the gaps between two localized states and lower potential barriers separating them; therefore, the transfer of charge carriers is easy between them, according to the percolation theory; hence, the conductivity increases as a results of increase the number of charges carriers.

Moreover, this improvement is assigned to the higher conductivity of the added Si₃N₄/Al₂O₃ NPs and increased charge mobility due to the increased amorphous degree within the doped samples [64–69].

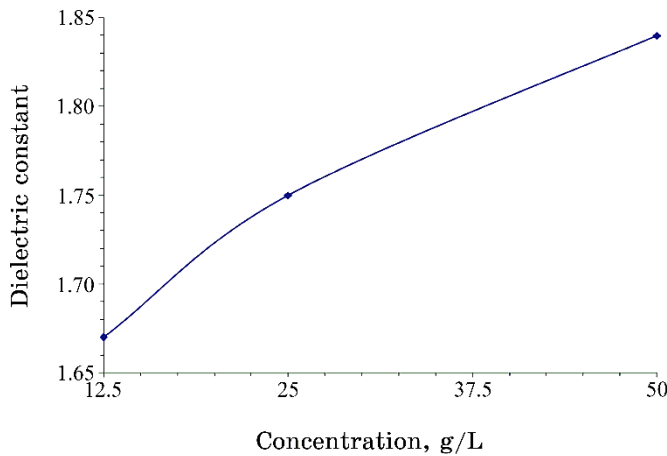


Fig. 3. Behaviour of dielectric constant for the PVP/Si₃N₄/Al₂O₃ nanostructures with concentration.

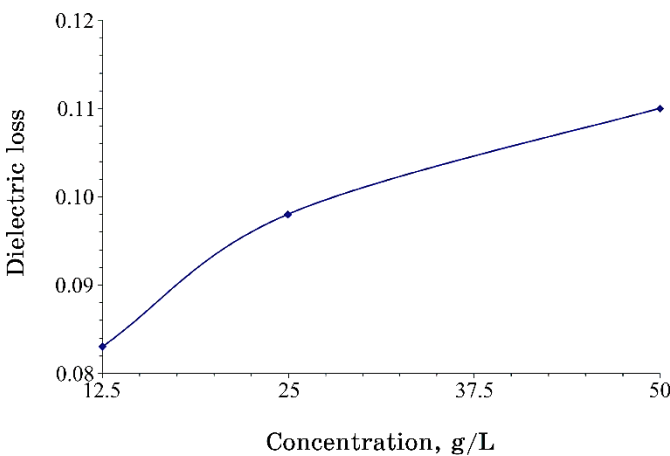


Fig. 4. Dielectric loss performance for the PVP/Si₃N₄/Al₂O₃ nanostructures with concentration.

4. CONCLUSIONS

This work involved fabrication of PVP/Si₃N₄/Al₂O₃ nanostructures to use in various electrical and electronics applications. The dielectric properties of PVP/Si₃N₄/Al₂O₃ nanostructures were examined. The results showed that the dielectric constant and dielectric loss of PVP/Si₃N₄/Al₂O₃ nanostructures decreased while the electrical conductivity was rise with a rise in the frequency. The dielectric parameters (dielectric constant, dielectric loss and electrical conductivity) were

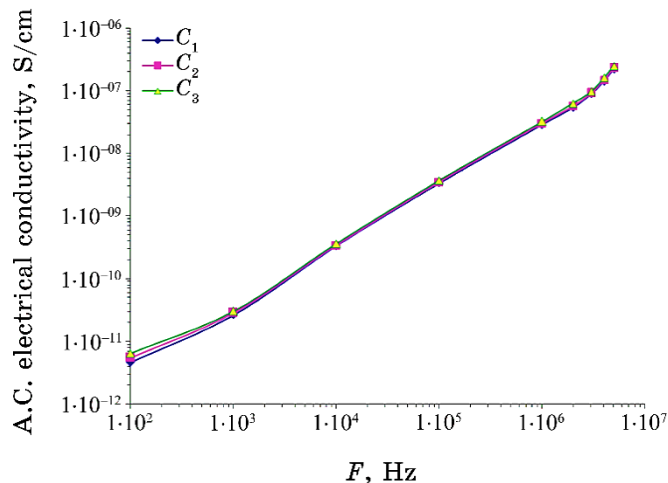


Fig. 5. Variation of A.C. electrical conductivity for the PVP/Si₃N₄/Al₂O₃ nanostructures with frequency.

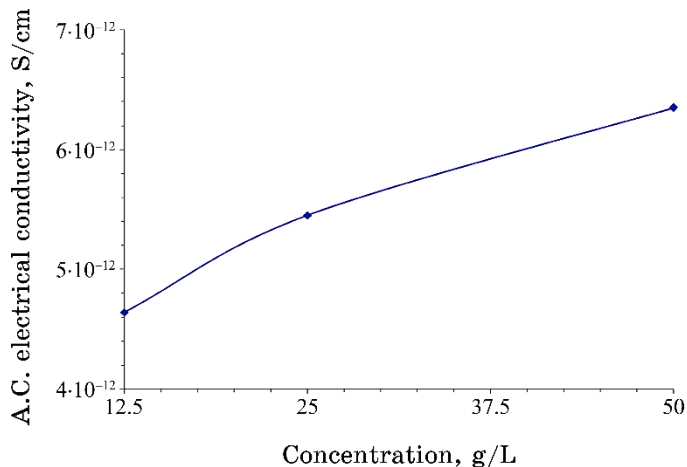


Fig. 6. Behaviour of A.C. electrical conductivity for the PVP/Si₃N₄/Al₂O₃ nanostructures with concentration.

raised with a rise in the concentration. The obtained results showed that the PVP/Si₃N₄/Al₂O₃ nanostructures could be suitable in many electronics applications.

REFERENCES

1. E. Nivrtirao, *Int. J. of Adv. Res. in Sci. and Eng.*, **6**, Iss. 1: 724 (2017).

2. Q. Wang, J. Che, W. Wu, Z. Hu, X. Liu, T. Ren, Y. Chen, and J. Zhang, *Polymer*, **15**, No. 3: 590 (2023); <https://doi.org/10.3390/polym15030590>
3. M. F. H. Abd El-Kader, Mohamed T. Elabbasy, A. A. Adeboye, and A. A. Menazea, *Polymer Bulletin*, **79**: 9779 (2022); <https://doi.org/10.1007/s00289-021-03975-5>
4. X. Wang and Y. Hu, *Polymers & Polymer Composites*, **25**, Iss. 1: 35 (2017).
5. W. S. Barakat, O. Elkady, A. Abu-Oqail, H. M. Yehya, and A. EL-Nikhaily, *Journal of Petroleum and Mining Engineering*, **22**: 1 (2020); [doi:10.21608/jpme.2020.19110.1017](https://doi.org/10.21608/jpme.2020.19110.1017)
6. O. B. Fadil and A. Hashim, *Nanosistemi, Nanomateriali, Nanotehnologii*, **20**, Iss. 4: 1029 (2022); <https://doi.org/10.15407/nnn.20.04.1029>
7. W. O. Obaid and A. Hashim, *Nanosistemi, Nanomateriali, Nanotehnologii*, **20**, Iss. 4: 1009 (2022); <https://doi.org/10.15407/nnn.20.04.1009>
8. M. H. Meteab, A. Hashim, and B. H. Rabee, *Nanosistemi, Nanomateriali, Nanotehnologii*, **21**, Iss. 1: 199 (2023); <https://doi.org/10.15407/nnn.21.01.199>
9. A. Hashim, I. R. Agool, and K. J. Kadhim, *Journal of Bionanoscience*, **12**, No. 5: 608 (2018); [doi:10.1166/jbns.2018.1580](https://doi.org/10.1166/jbns.2018.1580)
10. A. Hazim, A. Hashim, and H. M. Abduljalil, *International Journal of Emerging Trends in Engineering Research*, **7**, No. 8: 68 (2019); <https://doi.org/10.30534/ijeter/2019/01782019>
11. A. Hazim, H. M. Abduljalil, and A. Hashim, *International Journal of Emerging Trends in Engineering Research*, **7**, No. 8: 104 (2019); <https://doi.org/10.30534/ijeter/2019/04782019>
12. A. Hadi, A. Hashim, and D. Hassan, *Bulletin of Electrical Engineering and Informatics*, **9**, No. 1: 83 (2020); [doi:10.11591/eei.v9i1.1323](https://doi.org/10.11591/eei.v9i1.1323)
13. H. Ahmed and A. Hashim, *Nanosistemi, Nanomateriali, Nanotehnologii*, **20**, Iss. 4: 951 (2022); <https://doi.org/10.15407/nnn.20.04.951>
14. A. S. Shareef, F. Lafta R., A. Hadi and A. Hashim, *International Journal of Scientific & Technology Research*, **8**, Iss. 11: 1041 (2019).
15. H. Ahmed and A. Hashim, *Silicon*, **15**: 2339 (2023); <https://doi.org/10.1007/s12633-022-02173-w>
16. H. B. Hassan, H. M. Abduljalil, and A. Hashim, *Nanosistemi, Nanomateriali, Nanotehnologii*, **20**, Iss. 4: 941 (2022); <https://doi.org/10.15407/nnn.20.04.941>
17. H. A. Jawad and A. Hashim, *Nanosistemi, Nanomateriali, Nanotehnologii*, **20**, No. 4: 963 (2022); <https://doi.org/10.15407/nnn.20.04.963>
18. H. Ahmed and A. Hashim, *Silicon*, **14**: 6637 (2022); <https://doi.org/10.1007/s12633-021-01449-x>
19. H. Ahmed and A. Hashim, *Silicon*, **13**: 4331(2020); <https://doi.org/10.1007/s12633-020-00723-8>
20. H. Ahmed and A. Hashim, *Transactions on Electrical and Electronic Materials*, **22**: 335 (2021); <https://doi.org/10.1007/s42341-020-00244-6>
21. N. AH. Al-Aaraji, A. Hashim, A. Hadi, and H. M. Abduljalil, *Silicon*, **14**: 10037 (2022); <https://doi.org/10.1007/s12633-022-01730-7>
22. H. Ahmed and A. Hashim, *Opt. Quant. Electron.*, **55**: 1 (2023); <https://doi.org/10.1007/s11082-022-04273-8>
23. W. O. Obaid and A. Hashim, *Silicon*, **14**: 11199 (2022); <https://doi.org/10.1007/s12633-022-01854-w>
24. O. B. Fadil and A. Hashim, *Silicon*, **14**: 9845 (2022);

- <https://doi.org/10.1007/s12633-022-01728-1>
25. B. Abbas and A. Hashim, *International Journal of Emerging Trends in Engineering Research*, **7**, No. 8: 131 (2019);
<https://doi.org/10.30534/ijeter/2019/06782019>
26. K. H. H. Al-Attiyah, A. Hashim, and S. F. Obaid, *Journal of Bionanoscience*, **12**: 200 (2018); [doi:10.1166/jbns.2018.1526](https://doi.org/10.1166/jbns.2018.1526)
27. H. A. J. Hussien, A. Hadi, and A. Hashim, *Nanosistemi, Nanomateriali, Nanotechnologii*, **20**, No. 4: 1001 (2022); <https://doi.org/10.15407/nnn.20.04.1001>
28. A. Hashim and N. Hamid, *Journal of Bionanoscience*, **12**, No. 6: 788 (2018);
[doi:10.1166/jbns.2018.1591](https://doi.org/10.1166/jbns.2018.1591)
29. A. Hashim and Z. S. Hamad, *Journal of Bionanoscience*, **12**, No. 4: 488 (2018);
[doi:10.1166/jbns.2018.1551](https://doi.org/10.1166/jbns.2018.1551)
30. A. Hashim and Z. S. Hamad, *Journal of Bionanoscience*, **12**, No. 4: 504 (2018);
[doi:10.1166/jbns.2018.1561](https://doi.org/10.1166/jbns.2018.1561)
31. A. Hazim, A. Hashim, and H. M. Abduljalil, *Nanosistemi, Nanomateriali, Nanotechnologii*, **18**, No. 4: 983 (2020); <https://doi.org/10.15407/nnn.18.04.983>
32. A. Hashim and Z. S. Hamad, *Nanosistemi, Nanomateriali, Nanotechnologii*, **18**, No. 4: 969 (2020); <https://doi.org/10.15407/nnn.18.04.969>
33. A. Hazim, A. Hashim, and H. M. Abduljalil, *Egypt. J. Chem.*, **64**, No. 1: 359 (2021); [doi:10.21608/EJCHEM.2019.18513.2144](https://doi.org/10.21608/EJCHEM.2019.18513.2144)
34. H. Ahmed and A. Hashim, *Journal of Molecular Modeling*, **26**: 1 (2020);
[doi:10.1007/s00894-020-04479-1](https://doi.org/10.1007/s00894-020-04479-1)
35. H. Ahmed and A. Hashim, *Silicon*, **14**: 4907 (2022);
<https://doi.org/10.1007/s12633-021-01258-2>
36. H. Ahmed and A. Hashim, *Opt. Quant. Electron.*, **55**: 280 (2023);
<https://doi.org/10.1007/s11082-022-04528-4>
37. G. Ahmed and A. Hashim, *Silicon*, **15**: 3977 (2023);
<https://doi.org/10.1007/s12633-023-02322-9>
38. M. H. Meteab, A. Hashim, and B. H. Rabee, *Opt. Quant. Electron.*, **55**: 187 (2023); <https://doi.org/10.1007/s11082-022-04447-4>
39. B. Mohammed, H. Ahmed, and A. Hashim, *Nanosistemi, Nanomateriali, Nanotechnologii*, **21**, Iss. 1: 113 (2023);
<https://doi.org/10.15407/nnn.21.01.133>
40. A. Hashim, *Opt. Quant. Electron.*, **53**: 1 (2021);
<https://doi.org/10.1007/s11082-021-03100-w>
41. H. Ahmed and A. Hashim, *Trans. Electr. Electron. Mater.*, **23**: 237 (2022);
<https://doi.org/10.1007/s42341-021-00340-1>
42. H. Ahmed and A. Hashim, *Silicon*, **14**: 7025 (2021);
<https://doi.org/10.1007/s12633-021-01465-x>
43. A. Hazim, A. Hashim, and H. M. Abduljalil, *Trans. Electr. Electron. Mater.*, **21**: 48 (2019); <https://doi.org/10.1007/s42341-019-00148-0>
44. A.F. Kadhim, and A. Hashim, *Opt Quant Electron.*, **55**: 432 (2023);
<https://doi.org/10.1007/s11082-023-04699-8>
45. A. Hashim, *Nanosistemi, Nanomateriali, Nanotechnologii*, **19**, Iss. 3: 647 (2021); <https://doi.org/10.15407/nnn.19.03.647>
46. H. Ahmed and A. Hashim, *International Journal of Scientific & Technology Research*, **8**, Iss. 11: 1014 (2019).
47. B. Mohammed, H. Ahmed, and A. Hashim, *Nanosistemi, Nanomateriali, Nanotechnologii*, **20**, No. 1: 187 (2022); <https://doi.org/10.15407/nnn.20.01.187>

48. S. Uddin, N. Akhtar, S. Bibi, A. Zaman, A. Ali, K. Althubeiti, H. Alrobei, and M. Mushtaq, *Materials*, **14**: 1 (2021); <https://doi.org/10.3390/ma14185430>
49. Faiza, Z. Malik, A. Khattak, A. A. Alahmadi, and S. U. Butt, *Materials*, **15**, No. 15: 5154 (2022); <https://doi.org/10.3390/ma15155154>
50. A. Hashim, M. H. Abbas, N. AH. Al-Aaraji, and A. Hadi, *Silicon*, **15**: 1283 (2023); <https://doi.org/10.1007/s12633-022-02104-9>
51. M. H. Meteab, A. Hashim, and B. H. Rabee, *Silicon*, **15**: 1609 (2023); <https://doi.org/10.1007/s12633-022-02114-7>
52. N. Al-Huda Al-Aaraji, A. Hashim, A. Hadi, and H. M. Abduljalil, *Silicon*, **14**: 4699 (2022); <https://doi.org/10.1007/s12633-021-01265-3>
53. M. H. Meteab, A. Hashim, and B. H. Rabee, *Silicon*, **15**: 251 (2023); <https://doi.org/10.1007/s12633-022-02020-y>
54. A. Hashim, A. Hadi, and M. H. Abbas, *Opt. Quant. Electron.*, **55**: 642 (2023); <https://doi.org/10.1007/s11082-023-04929-z>
55. Z. S. Hamad and A. Hashim, *Nanosistemi, Nanomateriali, Nanotehnologii*, **20**, Iss. 1: 159 (2022); <https://doi.org/10.15407/nnn.20.01.159>
56. A. Hashim and Z. S. Hamad, *Nanosistemi, Nanomateriali, Nanotehnologii*, **20**, Iss. 1: 165 (2022); <https://doi.org/10.15407/nnn.20.01.165>
57. A. Hashim and A. Jassim, *Nanosistemi, Nanomateriali, Nanotehnologii*, **20**, Iss. 1: 177 (2022); <https://doi.org/10.15407/nnn.20.01.177>
58. A. Hashim and Z. S. Hamad, *Nanosistemi, Nanomateriali, Nanotehnologii*, **20**, Iss. 2: 507 (2022); <https://doi.org/10.15407/nnn.20.02.507>
59. B. Mohammed, H. Ahmed, and A. Hashim, *Journal of Physics: Conference Series*, **1879**: 1 (2021); doi:[10.1088/1742-6596/1879/3/032110](https://doi.org/10.1088/1742-6596/1879/3/032110)
60. D. Hassan and A. H. Ah-Yasari, *Bulletin of Electrical Engineering and Informatics*, **8**, Iss. 1: 52 (2019); doi:[10.11591/eei.v8i1.1019](https://doi.org/10.11591/eei.v8i1.1019)
61. D. Hassan and A. Hashim, *Bulletin of Electrical Engineering and Informatics*, **7**, Iss. 4: 547 (2018); doi:[10.11591/eei.v7i4.969](https://doi.org/10.11591/eei.v7i4.969)
62. A. Hashim, M. H. Abbas, N. AH. Al-Aaraji, and A. Hadi, *J. Inorg. Organomet. Polym.*, **33**: 1 (2023); <https://doi.org/10.1007/s10904-022-02485-9>
63. E. Salim and A. E. Tarabiah, *Journal of Inorganic and Organometallic Polymers and Materials*, **33**: 1638 (2023); <https://doi.org/10.1007/s10904-023-02591-2>
64. A.F. Kadhim and A. Hashim, *Silicon*, **33**: 1638 (2023); <https://doi.org/10.1007/s12633-023-02381-y>
65. H. A. Jawad and A. Hashim, *Nanosistemi, Nanomateriali, Nanotehnologii*, **21**, No. 1: 133 (2023); <https://doi.org/10.15407/nnn.21.01.133>
66. A. Hashim, A. Hadi, and M. H. Abbas, *Silicon*, **15**: 6431 (2023); <https://doi.org/10.1007/s12633-023-02529-w>
67. H. A. J. Hussien and A. Hashim, *J. Inorg. Organomet. Polym.*, **33**: 2331 (2023); <https://doi.org/10.1007/s10904-023-02688-8>
68. A. Hashim, A. Hadi, N.A. H. Al-Aaraji, and F. L. Rashid, *Silicon*, **15**: 5725 (2023); <https://doi.org/10.1007/s12633-023-02471-x>
69. M. A. Sebak, T. F. Qahtan, G. M. Asnag, and E. M. Abdallah, *Journal of Inorganic and Organometallic Polymers and Materials*, **32**: 4715 (2022); <https://doi.org/10.1007/s10904-022-02440-8>

PACS numbers: 72.80.Tm, 77.22.Ch, 77.22.Gm, 77.55.+f, 77.84.Lf, 81.07.Pr, 82.35.Np

Boosting the Dielectric Properties of PVA/In₂O₃/SiC Nanostructures for Electronics Nanodevices

Ahmed Hashim and M. H. Abbas

*College of Education for Pure Sciences,
Department of Physics,
University of Babylon,
Hilla, Iraq*

The present work aims to prepare of the indium oxide (In₂O₃)–silicon carbide (SiC) nanostructures doping the polyvinyl alcohol (PVA) to use in different electronics fields. The dielectric properties of PVA–In₂O₃–SiC nanocomposites are examined. The results demonstrate that the dielectric constant and dielectric loss of the PVA–In₂O₃–SiC nanocomposites are decreased with an increase in the frequency, while the electrical conductivity is increased as frequency is increased. The dielectric constant, dielectric loss, and electrical conductivity of PVA are increased with an increase in the In₂O₃–SiC nanoparticles' (NPs) concentration. Finally, the obtained results for the dielectric properties indicate that the PVA–In₂O₃–SiC nanocomposites can be suitable in various electronics fields.

Метою даної роботи є виготовлення наноструктур оксиду індію (In₂O₃)–карбіду кремнію (SiC), що легують полівініловий спирт (ПВС), для використання в різних галузях електроніки. Досліджено діелектричні властивості нанокомпозитів ПВС–In₂O₃–SiC. Результати показують, що діелектрична проникність і діелектричні втрати нанокомпозитів ПВС–In₂O₃–SiC зменшуються зі збільшенням частоти, тоді як електропровідність зростає зі збільшенням частоти. Діелектрична проникність, діелектричні втрати й електропровідність ПВС зростають зі збільшенням концентрації наночастинок In₂O₃–SiC. Нарешті, одержані результати стосовно діелектричних властивостей показують, що нанокомпозити ПВС–In₂O₃–SiC можуть бути придатними у різних галузях електроніки.

Key words: polyvinyl alcohol, SiC, In₂O₃, nanocomposites, dielectric properties, conductivity.

Ключові слова: полівініловий спирт, SiC, In₂O₃, нанокомпозити, діелектричні властивості, електропровідність.

(Received 30 June, 2023; in revised form, 28 July, 2023)

1. INTRODUCTION

Ongoing progress is being made toward the manufacture of more flexible dielectric nanocomposites, which can lead to distinctive designated technologies. The nanocomposites films were created by dispersing nanosize inorganic additives in an organic polymeric matrix. Those composites have been employed in a variety of implementations, such supercapacitors as well as stretchy electrodes. Composite films with distinct structural as well as dielectric properties are used as substances for electrical energy storage instruments. The composite films are important because they merge the polymers' machinability, longevity, as well as ductile qualities with the thermal stability as well as electric conductivities of the nanoadditive [1].

Silicon carbide (SiC) is used as a heat exchanger module, as it is a promising material for increasing corrosion resistance. In addition, SiC has excellent characteristics, including its low density and high specific thermal conductivity. It is well known that SiC has excellent thermal stability and corrosion resistance [2].

Indium oxide (In_2O_3) is an important functional semiconductor material, having direct band gap of ≈ 3.6 eV and indirect band gap of ≈ 2.6 eV, which has drawn much research interest in both fundamental and experimental research fields due to its ultrasensitive gas sensing characteristics, photocatalytic properties and extensive applications in sensors, flat panel displays, optoelectronic devices etc. [3].

Polyvinyl alcohol (PVA) is characterized by carbon chain backbone linked with hydroxyl groups. The hydroxyl groups, OH groups, are considered as a source of hydrogen bonding; therefore, it helps to form the polymer blends or polymer complexes. PVA is water-soluble and biocompatible polymer and is vastly used in the preparation of polymer blends due to its excellent physical and chemical properties. Therefore, the applications of PVA can be increased more and more by adding different dopant materials into PVA matrix [4].

There many studies on nanocomposites to employ in various fields like sensors [5, 6], electronics and optoelectronics [7–20], antibacterial [21–26], radiation shielding and bioenvironmental [27–32], optical fields [33–42], and energy storage [43–45].

This paper deals with fabrication of PVA– In_2O_3 –SiC nanocomposites and investigating the dielectric properties to apply in different industrial fields.

2. MATERIALS AND METHODS

Films of PVA/In₂O₃/SiC nanocomposites were prepared by casting process. The film of pure PVA was fabricated by dissolving of 1 gm of PVA in distilled water (30 ml). The In₂O₃-SiC NPs were added to the PVA with contents of 1.2%, 2.4%, 3.6%. The dielectric characteristics of PVA-In₂O₃-SiC nanocomposites were measured within the frequency (f) range from 100 Hz to $5 \cdot 10^6$ Hz by using LCR meter (HIOKI 3532-50 LCR HI TESTER). The dielectric constant, ϵ' , was determined by [46]:

$$\epsilon' = C_p d / \epsilon_0 A, \quad (1)$$

where C_p is the capacitance, d is thickness, and A in [cm²].

Dielectric loss, ϵ'' , was given by [47]:

$$\epsilon'' = \epsilon' D, \quad (2)$$

where D represents the dispersion factor.

The A.C. electrical conductivity was found by [48]:

$$\sigma_{\text{A.C.}} = 2\pi f \epsilon' D \epsilon_0. \quad (3)$$

3. RESULTS AND DISCUSSION

The behaviours of dielectric constant and dielectric loss with frequency and content of In₂O₃-SiC NPs are shown in Figs. 1–4. The

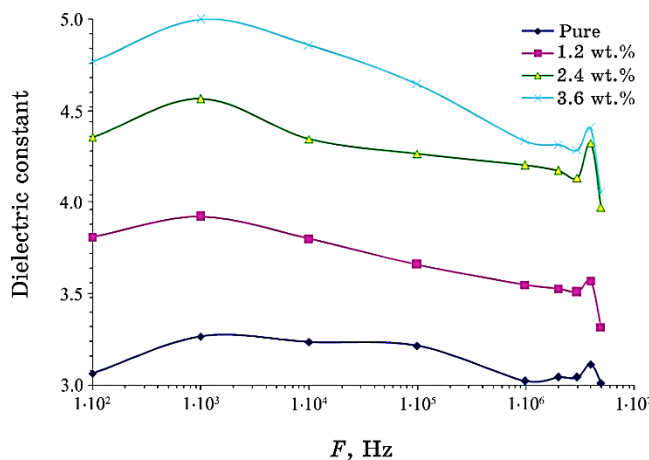


Fig. 1. Behaviour of dielectric constant with frequency for the PVA-In₂O₃-SiC nanocomposites.

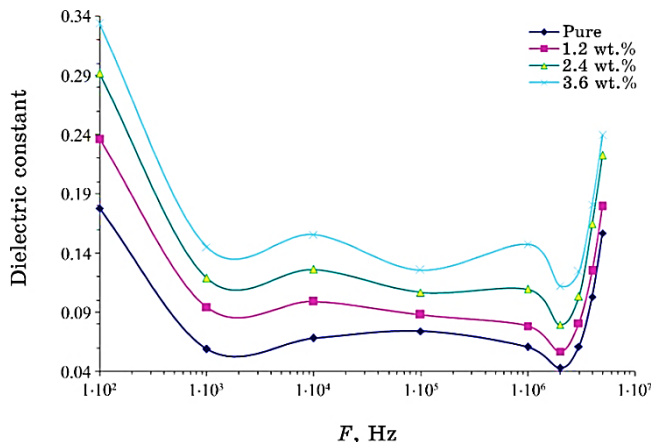


Fig. 2. Dielectric loss performance with frequency for the PVA–In₂O₃–SiC nanocomposites.

dielectric constant and dielectric loss are reduced with frequency while increased with content of In₂O₃–SiC NPs. These behaviours of both dielectric constant and dielectric loss due to the high contribution of charge accumulation in the nanocomposites assigned to the effect of polarization effect. The dielectric constant and dielectric loss are increased when the In₂O₃–SiC NPs content increases due to increase of charge-carriers' numbers [49–57].

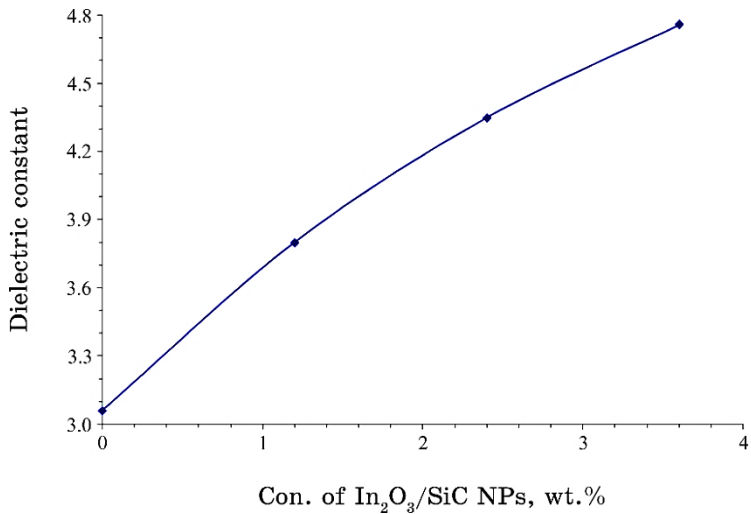


Fig. 3. Variation of dielectric constant of PVA with content of In₂O₃–SiC NPs.

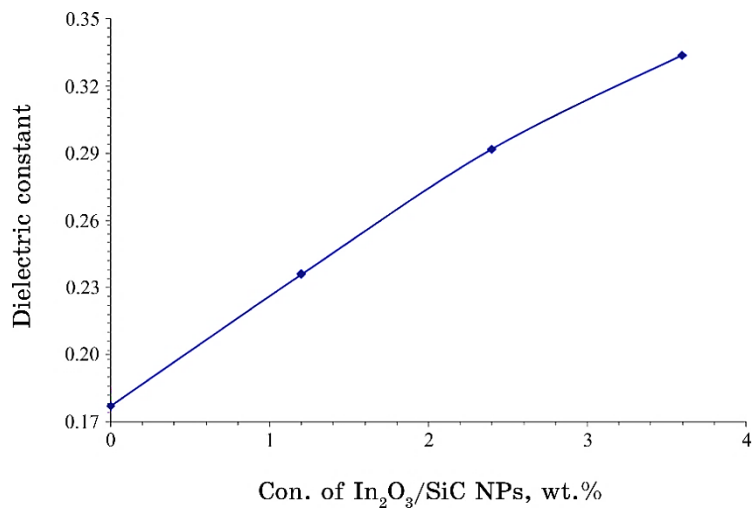


Fig. 4. Dielectric loss variation of PVA with content of In_2O_3 -SiC NPs.

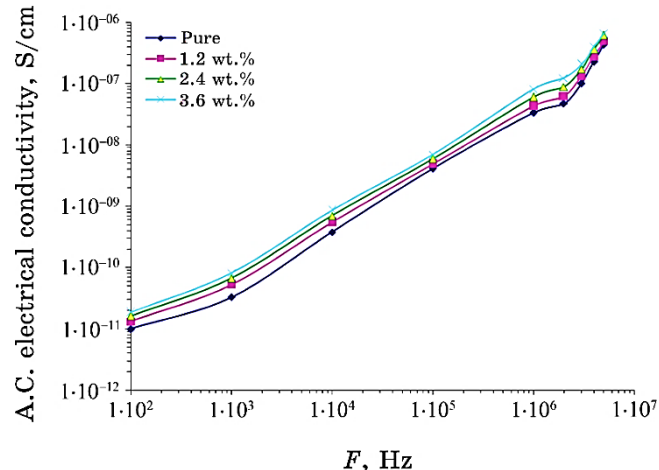


Fig. 5. Variation of A.C. electrical conductivity for PVA- In_2O_3 -SiC nanocomposites with frequency.

Figures 5 and 6 demonstrate the variation of A.C. electrical conductivity for PVA- In_2O_3 -SiC nanocomposites with frequency and content of In_2O_3 -SiC NPs. As the In_2O_3 -SiC NPs ratio is increased, the inorganic filler molecules start bridging the gap separating the two localized states and lowering the potential barrier between them, thereby, facilitating the transfer of charge carriers between two localized states; hence, the conductivity increases as a result of increase the charges carrier numbers. The frequency-dependent

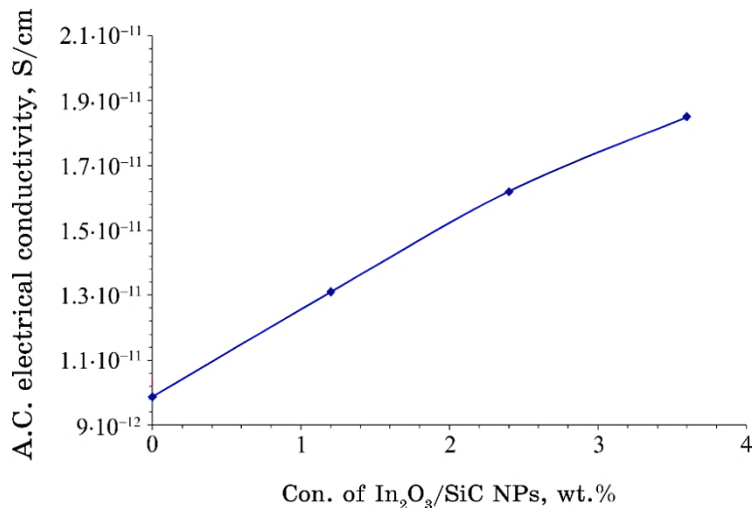


Fig. 6. Behaviour of A.C. electrical conductivity for PVA with content of In_2O_3 -SiC NPs.

conductivity is caused by the hopping of charge carriers in the localized state. The term hopping refers to the sudden displacement of charge carriers from one position to another neighbouring site and, in general, includes both jumps over a potential barrier and quantum mechanical tunnelling [58–68].

4. CONCLUSIONS

In this study, PVA– In_2O_3 –SiC nanocomposites were synthesised to utilize in various electronics approaches.

The dielectric properties of PVA– In_2O_3 –SiC nanocomposites were tested. The results showed the dielectric constant and dielectric loss of PVA– In_2O_3 –SiC nanocomposites decreased with rising frequency while the electrical conductivity increased as frequency increased. The dielectric constant, dielectric loss and electrical conductivity of PVA increased with increasing of the In_2O_3 –SiC NPs concentrations. The final results for dielectric properties showed that the PVA– In_2O_3 –SiC nanocomposites might be appropriate in many electronics approaches.

REFERENCES

1. B. M. Alotaibi, H. A. Al-Yousef, A. Atta, and F. A. Taher, *Journal of Ovonics Research*, **19**, No. 2: 175 (2023);

- <https://doi.org/10.15251/JOR.2023.192.175>
2. A. Ichinose, K. Kuwata, T. Esaki, T. Matsuda, and N. Kobayashi, *J. of Mater. Sci. and Chem. Eng.*, **8**: 23 (2020); <https://doi.org/10.4236/msce.2020.811002>
 3. M. A. M. Khan, R. Siwach, S. Kumar, J. Ahmed, and M. Ahamed, *J. of Alloys and Compounds*, **846**: 1 (2020); <https://doi.org/10.1016/j.jallcom.2020.156479>
 4. T. Fahmy, A. Sarhan, and Z. M. Elqahtani, *Int. J. of Eng. Res. and Techno.*, **13**, No. 3: 454 (2020); <https://dx.doi.org/10.37624/IJERT/13.3.2020.454-461>
 5. H. Ahmed and A. Hashim, *International Journal of Scientific & Technology Research*, **8**, Iss. 11: 1014 (2019).
 6. B. Mohammed, H. Ahmed, and A. Hashim, *Nanosistemi, Nanomateriali, Nanotehnologii*, **20**, No. 1: 187 (2022); <https://doi.org/10.15407/nnn.20.01.187>
 7. A. Hazim, A. Hashim, and H. M. Abduljalil, *Nanosistemi, Nanomateriali, Nanotehnologii*, **18**, Iss. 4: 983 (2020); <https://doi.org/10.15407/nnn.18.04.983>
 8. A. Hashim and Z. S. Hamad, *Nanosistemi, Nanomateriali, Nanotehnologii*, **18**, Iss. 4: 969 (2020); <https://doi.org/10.15407/nnn.18.04.969>
 9. A. Hazim, A. Hashim, and H. M. Abduljalil, *Egypt. J. Chem.*, **64**, No. 1: 359 (2021); [doi:10.21608/EJCHEM.2019.18513.2144](https://doi.org/10.21608/EJCHEM.2019.18513.2144)
 10. H. Ahmed and A. Hashim, *Journal of Molecular Modeling*, **26**: 1 (2020); [doi:10.1007/s00894-020-04479-1](https://doi.org/10.1007/s00894-020-04479-1)
 11. H. Ahmed and A. Hashim, *Silicon*, **14**: 4907 (2022); <https://doi.org/10.1007/s12633-021-01258-2>
 12. A. Hashim, *Opt. Quant. Electron.*, **53**: 1 (2021); <https://doi.org/10.1007/s11082-021-03100-w>
 13. H. Ahmed and A. Hashim, *Trans. Electr. Electron. Mater.*, **23**: 237 (2022); <https://doi.org/10.1007/s42341-021-00340-1>
 14. H. Ahmed and A. Hashim, *Silicon*, **14**: 7025 (2021); <https://doi.org/10.1007/s12633-021-01465-x>
 15. A. Hazim, A. Hashim, and H. M. Abduljalil, *Trans. Electr. Electron. Mater.*, **21**: 48 (2019); <https://doi.org/10.1007/s42341-019-00148-0>
 16. A. F. Kadhim and A. Hashim, *Opt. Quant. Electron.*, **55**: 432 (2023); <https://doi.org/10.1007/s11082-023-04699-8>
 17. H. Ahmed and A. Hashim, *Opt. Quant. Electron.*, **55**: 280 (2023); <https://doi.org/10.1007/s11082-022-04528-4>
 18. G. Ahmed and A. Hashim, *Silicon*, **15**: 3977 (2023); <https://doi.org/10.1007/s12633-023-02322-9>
 19. M. H. Meteab, A. Hashim, and B. H. Rabee, *Opt. Quant. Electron.*, **55**: 187 (2023); <https://doi.org/10.1007/s11082-022-04447-4>
 20. B. Mohammed, H. Ahmed, and A. Hashim, *Nanosistemi, Nanomateriali, Nanotehnologii*, **21**, Iss. 1: 113 (2023); <https://doi.org/10.15407/nnn.21.01.113>
 21. A. Hashim, I. R. Agool, and K. J. Kadhim, *Journal of Bionanoscience*, **12**, No. 5: 608 (2018); [doi:10.1166/jbns.2018.1580](https://doi.org/10.1166/jbns.2018.1580)
 22. A. Hazim, A. Hashim, and H. M. Abduljalil, *International Journal of Emerging Trends in Engineering Research*, **7**, No. 8: 68 (2019);

- <https://doi.org/10.30534/ijeter/2019/01782019>
- 23. A. Hazim, H. M. Abduljalil, and A. Hashim, *International Journal of Emerging Trends in Engineering Research*, **7**, No. 8: 104 (2019);
<https://doi.org/10.30534/ijeter/2019/04782019>
 - 24. O. B. Fadil and A. Hashim, *Nanosistemi, Nanomateriali, Nanotehnologii*, **20**, Iss. 4: 1029 (2022); <https://doi.org/10.15407/nnn.20.04.1029>
 - 25. W. O. Obaid and A. Hashim, *Nanosistemi, Nanomateriali, Nanotehnologii*, **20**, Iss. 4: 1009 (2022); <https://doi.org/10.15407/nnn.20.04.1009>
 - 26. M. H. Meteab, A. Hashim, and B. H. Rabee, *Nanosistemi, Nanomateriali, Nanotehnologii*, **21**, Iss. 1: 199 (2023);
<https://doi.org/10.15407/nnn.21.01.199>
 - 27. A. Hashim and N. Hamid, *Journal of Bionanoscience*, **12**, No. 6: 788 (2018);
[doi:10.1166/jbns.2018.1591](https://doi.org/10.1166/jbns.2018.1591)
 - 28. A. Hashim and Z. S. Hamad, *Journal of Bionanoscience*, **12**, No. 4: 488 (2018); [doi:10.1166/jbns.2018.1551](https://doi.org/10.1166/jbns.2018.1551)
 - 29. A. Hashim and Z. S. Hamad, *Journal of Bionanoscience*, **12**, No. 4: 504 (2018); [doi:10.1166/jbns.2018.1561](https://doi.org/10.1166/jbns.2018.1561)
 - 30. B. Abbas and A. Hashim, *International Journal of Emerging Trends in Engineering Research*, **7**, No. 8: 131 (2019);
<https://doi.org/10.30534/ijeter/2019/06782019>
 - 31. K. H. H. Al-Attiyah, A. Hashim, and S. F. Obaid, *Journal of Bionanoscience*, **12**: 200 (2018); [doi:10.1166/jbns.2018.1526](https://doi.org/10.1166/jbns.2018.1526)
 - 32. H. A. J. Hussien, A. Hadi, and A. Hashim, *Nanosistemi, Nanomateriali, Nanotehnologii*, **20**, Iss. 4: 1001 (2022);
<https://doi.org/10.15407/nnn.20.04.1001>
 - 33. H. Ahmed and A. Hashim, *Silicon*, **14**: 6637 (2022);
<https://doi.org/10.1007/s12633-021-01449-x>
 - 34. H. Ahmed and A. Hashim, *Silicon*, **13**: 4331 (2020);
<https://doi.org/10.1007/s12633-020-00723-8>
 - 35. H. Ahmed and A. Hashim, *Transactions on Electrical and Electronic Materials*, **22**: 335 (2021); <https://doi.org/10.1007/s42341-020-00244-6>
 - 36. N. AH. Al-Aaraji, A. Hashim, A. Hadi, and H. M. Abduljalil, *Silicon*, **14**: 10037 (2022); <https://doi.org/10.1007/s12633-022-01730-7>
 - 37. H. Ahmed and A. Hashim, *Opt. Quant. Electron.*, **55**: 1 (2023);
<https://doi.org/10.1007/s11082-022-04273-8>
 - 38. W. O. Obaid and A. Hashim, *Silicon*, **14**: 11199 (2022);
<https://doi.org/10.1007/s12633-022-01854-w>
 - 39. O. B. Fadil and A. Hashim, *Silicon*, **14**: 9845 (2022);
<https://doi.org/10.1007/s12633-022-01728-1>
 - 40. H. Ahmed and A. Hashim, *Silicon*, **15**: 2339 (2023);
<https://doi.org/10.1007/s12633-022-02173-w>
 - 41. H. B. Hassan, H. M. Abduljalil, and A. Hashim, *Nanosistemi, Nanomateriali, Nanotehnologii*, **20**, No. 4: 941 (2022);
<https://doi.org/10.15407/nnn.20.04.941>
 - 42. H. A. Jawad and A. Hashim, *Nanosistemi, Nanomateriali, Nanotehnologii*, **20**, Iss. 4: 963 (2022); <https://doi.org/10.15407/nnn.20.04.963>
 - 43. Abbas Sahi Shareef, Farhan Lafta Rashid, Aseel Hadi, and Ahmed Hashim, *International Journal of Scientific & Technology Research*, **8**, Iss. 11: 1041 (2019); https://www.researchgate.net/publication/337315854_Water-

- Polyethylene_Glycol_Sic-Wc_And_Ceo2WcNanofluids_For_Saving_Solar_Energy**
44. A. Hadi, A. Hashim, and D. Hassan, *Bulletin of Electrical Engineering and Informatics*, **9**, No. 1: 83 (2020); [doi:10.11591/eei.v9i1.1323](https://doi.org/10.11591/eei.v9i1.1323)
45. H. Ahmed and A. Hashim, *Nanosistemi, Nanomateriali, Nanotehnologii*, **20**, Iss. 4: 951 (2022); <https://doi.org/10.15407/nnn.20.04.951>
46. S. Ishaq, F. Kanwal, S. Atiq, M. Moussa, U. Azhar, and D. Losic, *Materials*, **13**: 1 (2020); [doi:10.3390/ma13010205](https://doi.org/10.3390/ma13010205)
47. T. A. Abdel-Baset and A. Hassen, *Physica B*, **499**: 24 (2016); <http://dx.doi.org/10.1016/j.physb.2016.07.002>
48. C. S. Rani and N. J. John, *Int. J. of Innovative Techno. and Exploring Eng.*, **8**, Iss. 11: 1285 (2019).
49. A. M. Ismail, Mohamed H. El-Newehy, Mehrez E. El-Naggar, A. Meera Moydeen, and A. A. Menazea, *Journal of Materials Research and Technology*, **9**, Iss. 5: 11178 (2020); <https://doi.org/10.1016/j.jmrt.2020.08.013>
50. Z. S. Hamad and A. Hashim, *Nanosistemi, Nanomateriali, Nanotehnologii*, **20**, Iss. 1: 159 (2022); <https://doi.org/10.15407/nnn.20.01.159>
51. A. Hashim and Z. S. Hamad, *Nanosistemi, Nanomateriali, Nanotehnologii*, **20**, Iss. 1: 165 (2022); <https://doi.org/10.15407/nnn.20.01.165>
52. A. Hashim and A. Jassim, *Nanosistemi, Nanomateriali, Nanotehnologii*, **20**, No. 1: 177 (2022); <https://doi.org/10.15407/nnn.20.01.177>
53. A. Hashim and Z. S. Hamad, *Nanosistemi, Nanomateriali, Nanotehnologii*, **20**, Iss. 2: 507 (2022); <https://doi.org/10.15407/nnn.20.02.507>
54. B. Mohammed, H. Ahmed, and A. Hashim, *Journal of Physics: Conference Series*, **1879**: 1 (2021); [doi:10.1088/1742-6596/1879/3/032110](https://doi.org/10.1088/1742-6596/1879/3/032110)
55. D. Hassan and A. H. Ah-Yasari, *Bulletin of Electrical Engineering and Informatics*, **8**, Iss. 1: 52 (2019); [doi:10.11591/eei.v8i1.1019](https://doi.org/10.11591/eei.v8i1.1019)
56. D. Hassan and A. Hashim, *Bulletin of Electrical Engineering and Informatics*, **7**, Iss. 4: 547 (2018); [doi:10.11591/eei.v7i4.969](https://doi.org/10.11591/eei.v7i4.969)
57. A. Hashim, M. H. Abbas, N. AH. Al-Aaraji, and A. Hadi, *J. Inorg. Organomet Polym.*, **33**: 1 (2023); <https://doi.org/10.1007/s10904-022-02485-9>
58. R. Divya, M. Meena, C. K. Mahadevan, and C. M. Padma, *Journal of Engineering Research and Applications*, **4**, Iss. 5: 1 (2014).
59. A. Hashim, M. H. Abbas, N. AH. Al-Aaraji, and A. Hadi, *Silicon*, **15**: 1283 (2023); <https://doi.org/10.1007/s12633-022-02104-9>
60. M. H. Meteab, A. Hashim, and B. H. Rabee, *Silicon*, **15**: 1609 (2023); <https://doi.org/10.1007/s12633-022-02114-7>
61. N. Al-Huda Al-Aaraji, A. Hashim, A. Hadi, and H. M. Abduljalil, *Silicon*, **14**: 4699 (2022); <https://doi.org/10.1007/s12633-021-01265-3>
62. M. H. Meteab, A. Hashim, and B. H. Rabee, *Silicon*, **15**: 251 (2023); <https://doi.org/10.1007/s12633-022-02020-y>
63. A. Hashim, A. Hadi, and M. H. Abbas, *Opt. Quant. Electron.*, **55**: 642 (2023); <https://doi.org/10.1007/s11082-023-04929-z>
64. A. Hashim, A. Hadi, and M. H. Abbas, *Silicon*, **15**: 6431 (2023); <https://doi.org/10.1007/s12633-023-02529-w>
65. H. A. J. Hussien and A. Hashim, *J. Inorg. Organomet. Polym.*, **33**: 2331 (2023); <https://doi.org/10.1007/s10904-023-02688-8>
66. A. Hashim, A. Hadi, N. A. H. Al-Aaraji, and F. L. Rashid, *Silicon*, **15**: 5725 (2023); <https://doi.org/10.1007/s12633-023-02471-x>

67. A. F. Kadhim and A. Hashim, *Silicon*, **15**: 4613 (2023);
<https://doi.org/10.1007/s12633-023-02381-y>
68. H. A. Jawad and A. Hashim, *Nanosistemi, Nanomateriali, Nanotehnologii*, **21**, No. 1: 133 (2023); <https://doi.org/10.15407/nnn.21.01.133>

PACS numbers: 72.80.Tm, 77.22.Ch, 77.22.Gm, 77.55.+f, 77.84.Lf, 81.07.Pr, 82.35.Np

Tailoring the Dielectric Properties of PS/In₂O₃/SiC Nanocomposites for Nanoelectronics Fields

Ahmed Hashim¹ and Aseel Hadi²

¹*College of Education for Pure Sciences,
Department of Physics,
University of Babylon,
Hilla, Iraq*

²*College of Materials Engineering,
Department of Ceramic and Building Materials,
University of Babylon,
Hilla, Iraq*

In this article, fabrication of polystyrene (PS)–indium oxide (In₂O₃)–silicon carbide (SiC) nanocomposites with low weight, low cost and high corrosion resistance is investigated. The dielectric properties of PS–In₂O₃–SiC nanocomposites are studied. The experimental results show that the dielectric constant and dielectric loss of PS–In₂O₃–SiC nanocomposites are decreased with an increase in the frequency, while the electrical conductivity is increased as frequency is increased. The dielectric constant, dielectric loss, and electrical conductivity of PS are increased with an increase in the In₂O₃–SiC-nanoparticles' concentration. The final results for dielectric properties show that the PS–In₂O₃–SiC nanocomposites may be useful in different electronics applications.

У цій статті було досліджено виготовлення нанокомпозитів полістирол (ПС)–оксид індію (In₂O₃)–карбід кремнію (SiC) з низькою вагою, низькою вартістю та високою корозійною стійкістю. Було досліджено діелектричні властивості нанокомпозитів PS–In₂O₃–SiC. Експериментальні результати показують, що електрична проникність і діелектричні втрати нанокомпозитів ПС–In₂O₃–SiC зменшуються зі збільшенням частоти, тоді як електропровідність зростає зі збільшенням частоти. Діелектрична проникність, діелектричні втрати й електропровідність ПС зростають зі збільшенням концентрації наночастинок In₂O₃–SiC. Остаточні результати стосовно діелектричних властивостей показують, що нанокомпозити ПС–In₂O₃–SiC можуть бути корисними в різних застосуваннях для електроніки.

Key words: In₂O₃, SiC, polystyrene, nanocomposites dielectric properties,

conductivity.

Ключові слова: In_2O_3 , SiC, полістирол, нанокомпозити, діелектричні властивості, провідність.

(Received 28 June, 2023)

1. INTRODUCTION

Polymer nanocomposites have captured the interest of many researchers owing to their high performance, remarkable mechanical and thermal properties. They possess outstanding properties, such as improved mechanical strength and dimensional stability, better optical, magnetic, and electrical properties, enhanced water and oxygen barrier, thermal stability, meaningful flame retardation, chemical resistance, increased anti-scratch and wear resistance properties, etc. [1].

Silicon carbide (SiC) is one of the main commonly utilized non-oxide ceramics for many industrial fields relating to its attention the elevated temperature characteristics like good strength, excellent hardness, and elevated resistance for thermal shock and wear. It also has a good resistance for chemical oxidation. The performance of SiC under such great conditions is projected to allow major enhancement to a multiplicity of fields. SiC nanostructures have exposed to display superior characteristics compare to the SiC bulk. It also demonstrates the potential fields in UV photodetectors and diodes relating to a higher efficiency for light emission [1].

Indium oxide (In_2O_3) is an important and well-known transparent conducting oxide of *n*-type semiconductor exhibiting a wide band gap, chemical stability, high electrical conductivity and transparency to visible light. It is frequently used for photovoltaic devices, transparent windows, liquid crystal displays (LCD), light emitting diode (LED), solar cell, gas sensors, and antireflecting coatings [2].

Polystyrene (PS) is an inexpensive, environmentally friendly polymer it is among the most popular materials which has many applications in industry, building and construction, domestic appliances and food packaging. In food packaging, polystyrene can be used in many shapes as monolayer plastic film, plastic sheet, or injection moulded and foamed. Plasticizers usually used in the industry for improving the workability of the polymers by lowering the glass transition temperature (T_g) [4].

There are several studies on nanostructured substances to make use in such fields as electronics and optoelectronics [5–19], radiation shielding and bioenvironmental [20–25], sensors [26, 27], antibacterial [28–33], energy storage [34–36], optical fields [37–46].

This work aims to prepare the PS–In₂O₃–SiC nanocomposites and to study the dielectric properties used in different electronics applications.

2. MATERIALS AND METHODS

Nanocomposites of PS–In₂O₃–SiC were prepared by using solution-casting method. The pure PS film was fabricated by dissolving of 1 gm of this polymer in chloroform (30 ml). The In₂O₃–SiC NPs were added to the PS with contents are 1.2 wt.%, 2.4 wt.%, and 3.6 wt.%. The dielectric properties of PS–In₂O₃–SiC nanocomposites were tested at frequency range (100 Hz–5·10⁶ Hz) using LCR meter (HIOKI 3532-50 LCR HI TESTER).

The dielectric constant (ϵ') was determined by [47]:

$$\epsilon' = C_p d / \epsilon_0 A, \quad (1)$$

where C_p is matter capacitance, d is the thickness, A is the area.

Dielectric loss (ϵ'') was found by [48]:

$$\epsilon'' = \epsilon' D, \quad (2)$$

where D is the dispersion factor.

The electrical conductivity was given by [49]:

$$\sigma_{A.C.} = 2\pi f \epsilon' D \epsilon_0. \quad (3)$$

3. RESULTS AND DISCUSSION

Figures 1–4 show the variations of dielectric constant and dielectric loss with frequency and content of In₂O₃–SiC NPs, respectively. The performances of dielectric constant and dielectric loss in the given frequency range as the following, the strong frequencies dispersion of the permittivity is seen at low range of frequency.

The values of dielectric constant and dielectric loss are decreased with increase of frequency due to the relaxation process and may be due to charge accumulation inside the nanocomposites attributed to influence of interfacial polarization on permittivity.

With addition of the filler In₂O₃–SiC, the values of both dielectric constant and dielectric loss increases at the range of lower frequency and nearly the same at the range of the higher frequency attributed to the filler cause more localization of charge carriers along with mobile ions causing higher ionic conductivity. Also, the rise of dielectric constant and dielectric loss with increasing content

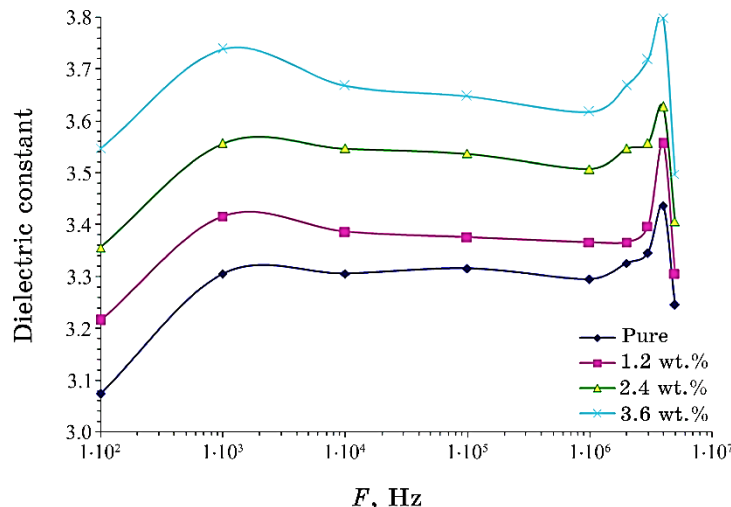


Fig. 1. Variation of dielectric constant for the PS-In₂O₃-SiC nanocomposites with frequency.

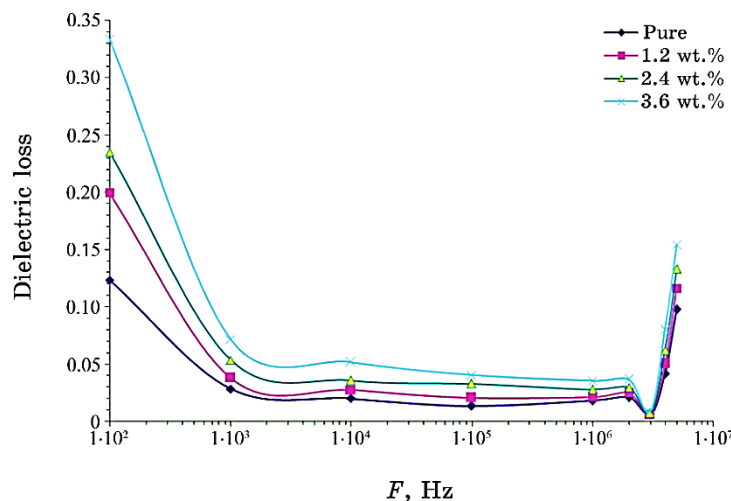


Fig. 2. Behaviour of dielectric loss for the PS-In₂O₃-SiC nanocomposites with frequency.

of In₂O₃-SiC NPs due to increase in the numbers of charges carriers [50-61].

Figures 5 and 6 demonstrate the behaviour of A.C. electrical conductivity with frequency and In₂O₃-SiC NPs content, respectively. As shown in these figures, the A.C. electrical conductivity rises with an increase in the frequency and In₂O₃-SiC NPs content. It

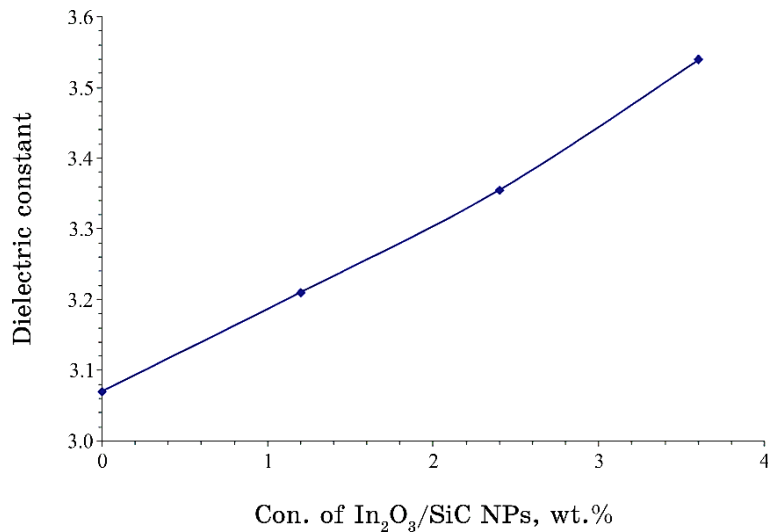


Fig. 3. Behaviour of dielectric constant for PS with content of In_2O_3 -SiC NPs.

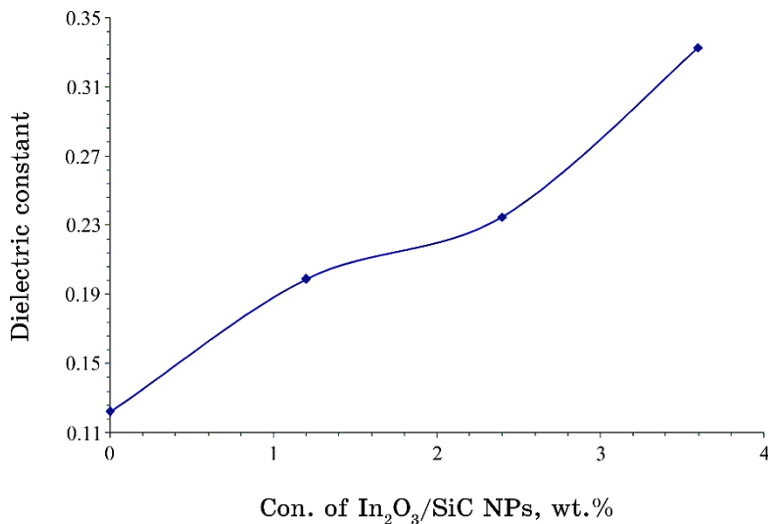


Fig. 4. Dielectric loss performance for PS with content of In_2O_3 -SiC NPs.

was also observed that the values of AC electrical conductivity are increased as the concentration of In_2O_3 -SiC NPs increased into PS matrix. The increase of conductivity due to increase the mobility and charge-carriers' numbers. Furthermore, these observations could be assigned to space-charge polarization [62–69].

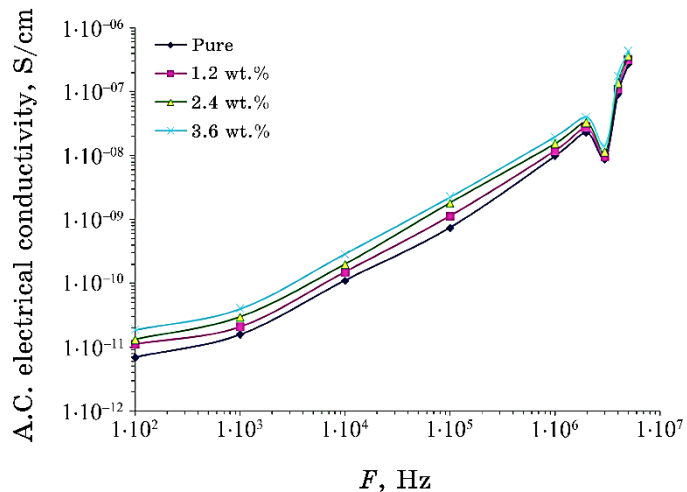


Fig. 5. Behaviour of A.C. electrical conductivity for the PS–In₂O₃–SiC nanocomposites with frequency.

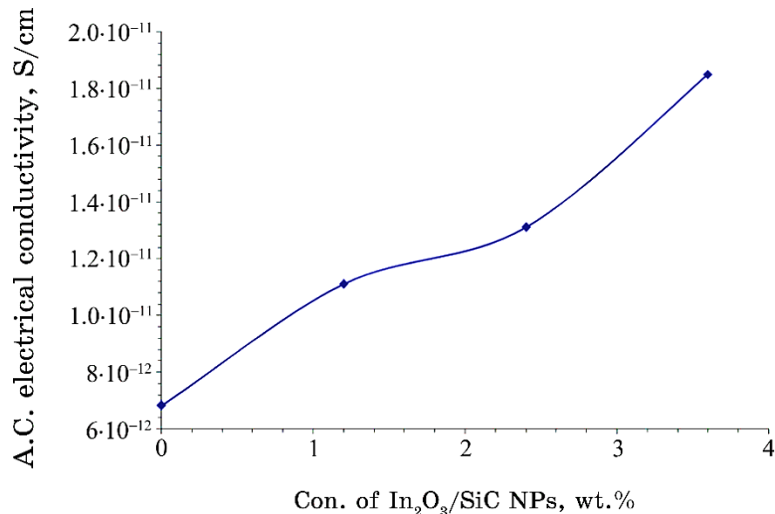


Fig. 6. Performance of A.C. electrical conductivity for PS with In₂O₃–SiC NPs content.

4. CONCLUSIONS

The present work includes manufacture of PS–In₂O₃–SiC nanocomposites with low weight, low cost and high corrosion resistance. The dielectric properties of PS–In₂O₃–SiC nanocomposites were tested. The results showed that the dielectric constant and dielectric loss of

PS–In₂O₃–SiC nanocomposites decreased with an increase in the frequency while the electrical conductivity increased as frequency increased. The dielectric constant, dielectric loss and electrical conductivity of PS increased with an increase in the In₂O₃–SiC nanoparticles concentrations. The final results for dielectric properties showed that the PS–In₂O₃–SiC nanocomposites might be suitable in many electronics fields.

REFERENCES

1. S. U. Rehman, S. Javaid, M. Shahid, I. H. Gul, B. Rashid, C. R. Szczepanski, M. Naveed, and S. J. Curley, *Polymers*, **14**: 1 (2022); <https://doi.org/10.3390/polym14173576>
2. K. W. Mas'udah, M. Diantoro, and A. Fuad, *IOP Conf. Series: Journal of Physics: Conf. Series.*, **1093**: 1 (2018); [doi:10.1088/1742-6596/1093/1/012033](https://doi.org/10.1088/1742-6596/1093/1/012033)
3. A. Attaf, A. Bouhdjar, H. Saidi, Y. Benkhetta, H. Bendjedidi, M. Nouadji, and N. Lehraki, *AIP Conf. Proc.*, **1653**: 1 (2014); [doi:10.1063/1.4914207](https://doi.org/10.1063/1.4914207)
4. N. A. Kamel, M. A. Saied, R. M. Ramadan, and S. L. Abd El-Messieh, *Egypt. J. Chem.*, **64**: 3111(2021); [doi:10.21608/EJCHEM.2021.61000.3309](https://doi.org/10.21608/EJCHEM.2021.61000.3309)
5. H. Ahmed and A. Hashim, *Silicon*, **14**: 7025 (2021); <https://doi.org/10.1007/s12633-021-01465-x>
6. A. Hazim, A. Hashim, and H. M. Abduljalil, *Trans. Electr. Electron. Mater.*, **21**: 48 (2019); <https://doi.org/10.1007/s42341-019-00148-0>
7. A.F. Kadhim and A. Hashim, *Opt. Quant. Electron.*, **55**: 432 (2023); <https://doi.org/10.1007/s11082-023-04699-8>
8. H. Ahmed and A. Hashim, *Opt. Quant. Electron.*, **55**: 280 (2023); <https://doi.org/10.1007/s11082-022-04528-4>
9. G. Ahmed and A. Hashim, *Silicon*, **15**: 3977 (2023); <https://doi.org/10.1007/s12633-023-02322-9>
10. M. H. Meteab, A. Hashim, and B. H. Rabee, *Opt. Quant. Electron.*, **55**: 187 (2023); <https://doi.org/10.1007/s11082-022-04447-4>
11. B. Mohammed, H. Ahmed, and A. Hashim, *Nanosistemi, Nanomateriali, Nanotehnologii*, **21**, Iss. 1: 113 (2023); <https://doi.org/10.15407/nnn.21.01.113>
12. A. Hashim, *Nanosistemi, Nanomateriali, Nanotehnologii*, **19**, Iss. 3: 647 (2021); <https://doi.org/10.15407/nnn.19.03.647>
13. A. Hazim, A. Hashim, and H. M. Abduljalil, *Nanosistemi, Nanomateriali, Nanotehnologii*, **18**, Iss. 4: 983 (2020); <https://doi.org/10.15407/nnn.18.04.983>
14. A. Hashim and Z. S. Hamad, *Nanosistemi, Nanomateriali, Nanotehnologii*, **18**, Iss. 4: 969 (2020); <https://doi.org/10.15407/nnn.18.04.969>
15. A. Hazim, A. Hashim, and H. M. Abduljalil, *Egypt. J. Chem.*, **64**, No. 1: 359 (2021); [doi:10.21608/EJCHEM.2019.18513.2144](https://doi.org/10.21608/EJCHEM.2019.18513.2144)
16. H. Ahmed and A. Hashim, *Journal of Molecular Modeling*, **26**: 1 (2020); [doi:10.1007/s00894-020-04479-1](https://doi.org/10.1007/s00894-020-04479-1)
17. H. Ahmed and A. Hashim, *Silicon*, **14**: 4907 (2022); <https://doi.org/10.1007/s12633-021-01258-2>

18. A. Hashim, *Opt. Quant. Electron.*, **53**: 1 (2021);
<https://doi.org/10.1007/s11082-021-03100-w>
19. H. Ahmed and A. Hashim, *Trans. Electr. Electron. Mater.*, **23**: 237 (2022);
<https://doi.org/10.1007/s42341-021-00340-1>
20. A. Hashim and Z. S. Hamad, *Journal of Bionanoscience*, **12**, No. 4: 504 (2018); [doi:10.1166/jbns.2018.1561](https://doi.org/10.1166/jbns.2018.1561)
21. B. Abbas and A. Hashim, *International Journal of Emerging Trends in Engineering Research*, **7**, No. 8: 131 (2019);
<https://doi.org/10.30534/ijeter/2019/06782019>
22. K. H. H. Al-Attiyah, A. Hashim, and S. F. Obaid, *Journal of Bionanoscience*, **12**: 200 (2018); [doi:10.1166/jbns.2018.1526](https://doi.org/10.1166/jbns.2018.1526)
23. H. A. J. Hussien, A. Hadi, and A. Hashim, *Nanosistemi, Nanomateriali, Nanotehnologii*, **20**, No. 4: 1001 (2022);
<https://doi.org/10.15407/nnn.20.04.1001>
24. A. Hashim and N. Hamid, *Journal of Bionanoscience*, **12**, No. 6: 788 (2018);
[doi:10.1166/jbns.2018.1591](https://doi.org/10.1166/jbns.2018.1591)
25. A. Hashim and Z. S. Hamad, *Journal of Bionanoscience*, **12**, No. 4: 488 (2018); [doi:10.1166/jbns.2018.1551](https://doi.org/10.1166/jbns.2018.1551)
26. H. Ahmed and A. Hashim, *International Journal of Scientific & Technology Research*, **8**, Iss. 11: 1014 (2019).
27. B. Mohammed, H. Ahmed, and A. Hashim, *Nanosistemi, Nanomateriali, Nanotehnologii*, **20**, Iss. 1: 187 (2022);
<https://doi.org/10.15407/nnn.20.01.187>
28. A. Hazim, H. M. Abduljalil, and A. Hashim, *International Journal of Emerging Trends in Engineering Research*, **7**, No. 8: 104 (2019);
<https://doi.org/10.30534/ijeter/2019/04782019>
29. O. B. Fadil and A. Hashim, *Nanosistemi, Nanomateriali, Nanotehnologii*, **20**, Iss. 4: 1029 (2022); <https://doi.org/10.15407/nnn.20.04.1029>
30. W. O. Obaid and A. Hashim, *Nanosistemi, Nanomateriali, Nanotehnologii*, **20**, No. 4: 1009 (2022); <https://doi.org/10.15407/nnn.20.04.1009>
31. M. H. Meteab, A. Hashim, and B. H. Rabee, *Nanosistemi, Nanomateriali, Nanotehnologii*, **21**, Iss. 1: 199 (2023);
<https://doi.org/10.15407/nnn.21.01.199>
32. A. Hashim, I. R. Agool, and K. J. Kadhim, *Journal of Bionanoscience*, **12**, No. 5: 608 (2018); [doi:10.1166/jbns.2018.1580](https://doi.org/10.1166/jbns.2018.1580)
33. A. Hazim, A. Hashim, and H. M. Abduljalil, *International Journal of Emerging Trends in Engineering Research*, **7**, No. 8: 68 (2019);
<https://doi.org/10.30534/ijeter/2019/01782019>
34. A. Hadi, A. Hashim, and D. Hassan, *Bulletin of Electrical Engineering and Informatics*, **9**, No. 1: 83 (2020); [doi:10.11591/eei.v9i1.1323](https://doi.org/10.11591/eei.v9i1.1323)
35. H. Ahmed and A. Hashim, *Nanosistemi, Nanomateriali, Nanotehnologii*, **20**, Iss. 4: 951 (2022); <https://doi.org/10.15407/nnn.20.04.951>
36. A. S. Shareef, F. Lafta R., A. Hadi, and A. Hashim, *International Journal of Scientific & Technology Research*, **8**, Iss. 11: 1041 (2019).
37. H. Ahmed and A. Hashim, *Silicon*, **15**: 2339 (2023);
<https://doi.org/10.1007/s12633-022-02173-w>
38. H. B. Hassan, H. M. Abduljalil, and A. Hashim, *Nanosistemi, Nanomateriali, Nanotehnologii*, **20**, Iss. 4: 941(2022);
<https://doi.org/10.15407/nnn.20.04.941>

39. H. A. Jawad and A. Hashim, *Nanosistemi, Nanomateriali, Nanotehnologii*, **20**, Iss. 4: 963 (2022); <https://doi.org/10.15407/nnn.20.04.963>
40. H. Ahmed and A. Hashim, *Silicon*, **14**: 6637 (2022); <https://doi.org/10.1007/s12633-021-01449-x>
41. H. Ahmed and A. Hashim, *Silicon*, **13**: 4331 (2020); <https://doi.org/10.1007/s12633-020-00723-8>
42. H. Ahmed and A. Hashim, *Transactions on Electrical and Electronic Materials*, **22**: 335 (2021); <https://doi.org/10.1007/s42341-020-00244-6>
43. N. AH. Al-Aaraji, A. Hashim, A. Hadi, and H. M. Abduljalil, *Silicon*, **14**: 10037 (2022); <https://doi.org/10.1007/s12633-022-01730-7>
44. H. Ahmed and A. Hashim, *Opt. Quant. Electron.*, **55**: 1 (2023); <https://doi.org/10.1007/s11082-022-04273-8>
45. W.O. Obaid and A. Hashim, *Silicon*, **14**: 11199 (2022); <https://doi.org/10.1007/s12633-022-01854-w>
46. O. B. Fadil and A. Hashim, *Silicon*, **14**: 9845 (2022); <https://doi.org/10.1007/s12633-022-01728-1>
47. T. A. Abdel-Baset and A. Hassen, *Physica B*, **499**: 24 (2016); <http://dx.doi.org/10.1016/j.physb.2016.07.002>
48. E. Elbayoumy, N. A. El-Ghamaz, F. Sh. Mohamed, M. A. Diab, and T. Nakano, *Polymers*, **13**, No. 17: 3005 (2021); <https://doi.org/10.3390/polym13173005>
49. P. Beena and H. S. Jayanna, *Polymers and Polymer Composites*, **27**, No. 9: 619 (2019); <doi:10.1177/0967391119856140>
50. M. H. Meteab, A. Hashim, and B. H. Rabee, *Silicon*, **15**: 251 (2023); <https://doi.org/10.1007/s12633-022-02020-y>
51. A. Hashim, A. Hadi, and M. H. Abbas, *Opt. Quant. Electron.*, **55**: 642 (2023); <https://doi.org/10.1007/s11082-023-04929-z>
52. A. Hashim, A. Hadi, and M. H. Abbas, *Silicon*, **15**: 6431 (2023); <https://doi.org/10.1007/s12633-023-02529-w>
53. A. Hashim, M. H. Abbas, N. AH. Al-Aaraji, A. Hadi, *J. Inorg. Organomet Polym.*, **33**: 1 (2023); <https://doi.org/10.1007/s10904-022-02485-9>
54. A. Hashim, M. H. Abbas, N. AH. Al-Aaraji, and A. Hadi, *Silicon*, **15**: 1283 (2023); <https://doi.org/10.1007/s12633-022-02104-9>
55. M. H. Meteab, A. Hashim, and B. H. Rabee, *Silicon*, **15**: 1609 (2023); <https://doi.org/10.1007/s12633-022-02114-7>
56. N. Al-Huda Al-Aaraji, A. Hashim, A. Hadi, and H. M. Abduljalil, *Silicon*, **14**: 4699 (2022); <https://doi.org/10.1007/s12633-021-01265-3>
57. H. A. J. Hussien and A. Hashim, *J. Inorg. Organomet. Polym.*, **33**: 2331 (2023); <https://doi.org/10.1007/s10904-023-02688-8>
58. A. Hashim, A. Hadi, N. A. H. Al-Aaraji, and F. L. Rashid, *Silicon*, **15**: 5725 (2023); <https://doi.org/10.1007/s12633-023-02471-x>
59. A. F. Kadhim and A. Hashim, *Silicon*, **15**: 4613 (2023); <https://doi.org/10.1007/s12633-023-02381-y>
60. A. A. Menazea, A. M. Ismail, and I. S. Elashmawi, *Journal of Materials Research and Technology*, **9**, Iss. 3: 5689 (2020); <https://doi.org/10.1016/j.jmrt.2020.03.093>
61. H. A. Jawad and A. Hashim, *Nanosistemi, Nanomateriali, Nanotehnologii*, **21**, Iss. 1: 133 (2023); <https://doi.org/10.15407/nnn.21.01.133>
62. Z. S. Hamad and A. Hashim, *Nanosistemi, Nanomateriali, Nanotehnologii*,

- 20, Iss. 1: 159 (2022); <https://doi.org/10.15407/nnn.20.01.159>
63. A. Hashim and Z. S. Hamad, *Nanosistemi, Nanomateriali, Nanotehnologii*, 20, Iss. 1: 165 (2022); <https://doi.org/10.15407/nnn.20.01.165>
64. A. Hashim and A. Jassim, *Nanosistemi, Nanomateriali, Nanotehnologii*, 20, Iss. 1: 177 (2022); <https://doi.org/10.15407/nnn.20.01.177>
65. A. Hashim and Z. S. Hamad, *Nanosistemi, Nanomateriali, Nanotehnologii*, 20, Iss. 2: 507(2022); <https://doi.org/10.15407/nnn.20.02.507>
66. B. Mohammed, H. Ahmed, and A. Hashim, *Journal of Physics: Conference Series*, 1879: 1 (2021); doi:[10.1088/1742-6596/1879/3/032110](https://doi.org/10.1088/1742-6596/1879/3/032110)
67. D. Hassan and A. H. Ah-Yasari, *Bulletin of Electrical Engineering and Informatics*, 8, Iss. 1: 52 (2019); doi:[10.11591/eei.v8i1.1019](https://doi.org/10.11591/eei.v8i1.1019)
68. D. Hassan and A. Hashim, *Bulletin of Electrical Engineering and Informatics*, 7, Iss. 4: 547 (2018); doi:[10.11591/eei.v7i4.969](https://doi.org/10.11591/eei.v7i4.969)
69. A. M. Ismail, Mohamed H. El-Newehy, Mehrez E. El-Naggar, A. Meera Moydeen, and A. A. Menazea, *Jounral of Materials Research and Technology*, 9, Iss. 5: 11178 (2020); <https://doi.org/10.1016/j.jmrt.2020.08.013>

PACS numbers: 72.80.Tm, 77.22.Ch, 77.22.Gm, 77.55.+f, 77.84.Lf, 81.07.Pr, 82.35.Np

Exploring the Dielectric Properties of PVP/Ag/SiC Nanostructures to Use in Various Electronics Fields

Ahmed Hashim and M. H. Abbas

*College of Education for Pure Sciences,
Department of Physics,
University of Babylon,
Hilla, Iraq*

This work objects to fabrication of PVP/Ag/SiC nanostructures and investigation of the dielectric properties to use them in various electronics applications with lightweight and low cost. The results demonstrate that the dielectric constant and dielectric loss of PVP/Ag/SiC nanostructures are reduced, while the electrical conductivity is increased with an increase in the frequency. The dielectric constant, dielectric loss, and electrical conductivity are increased with an increase of the concentration. Finally, the results of dielectric properties indicate that the PVP/Ag/SiC nanostructures can be suitable in different electronics fields.

Цю роботу спрямовано на виготовленняnanoструктур полівінілпіролідон/Ag/SiC та дослідження діелектричних властивостей для використання їх у різних електронних застосуваннях з легкою вагою та низькою ціною. Результати показують, що діелектрична проникність і діелектричні втрати nanoструктур полівінілпіролідон/Ag/SiC зменшуються, а електропровідність зростає зі збільшенням частоти. Діелектрична проникність, діелектричні втрати та електропровідність зростають зі збільшенням концентрації. Нарешті, результати стосовно діелектричних властивостей показують, що nanoструктури полівінілпіролідон/Ag/SiC можуть бути придатними у різних галузях електроніки.

Key words: polyvinylpyrrolidone, Ag/SiC, nanostructures, dielectric properties, electronics fields.

Ключові слова: полівінілпіролідон, Ag/SiC, nanoструктури, діелектричні властивості, галузі електроніки.

(Received 30 June, 2023; in revised form, 26 August, 2023)

1. INTRODUCTION

Polymer nanocomposites are one of the most important materials in the academic and industrial areas, and are produced by dispersing nanofillers with one or more dimensions at nanoscale into the polymeric matrix.

Recently, researchers have been attracted to polymer nanocomposites over conventional microcomposites due to their wide applications in electromechanical systems and their large interfacial area per unit volume of the dispersion medium [1].

Organic/inorganic nanocomposites are extremely promising for applications in light-emitting diodes, photodiodes, photovoltaic cells, smart microelectronic device, and gas sensors among others. The properties of nanocomposites' films can be adjusted by varying the composition. Their fabrication shares the same advantages of organic device technology, such as low cost production and the possibility of device fabrication on large area and flexible substrates [2].

Among noble metal nanoparticles, silver has been extensively studied due to the possibilities for their use in different areas of nonlinear optics, optoelectronics, and laser physics. Silver nanoparticles are advantageous compared with nanoparticles of other noble metals (in particular, gold and copper) as the energy of the surface plasmon resonance lies far from the energy corresponding to interband transitions. This allows one to distinguish clearly the effect of surface plasmons on different optical properties.

Therefore, nanocomposites, in which the silver nanoparticles are dispersed in a dielectric matrix, have some advantages in this regard [3].

Silicon carbide (SiC) nanoparticles have high thermal conductivity, stability, purity, good wear resistance, and a low thermal expansion coefficient. At high temperatures, these particles are also resistant to oxidation [4].

Polyvinylpyrrolidone (PVP) has chosen because it has excellent characteristics such as optical, mechanical and electrical properties. PVP has ad-chive nature. Thus, it may be used in electronic circuit boards and display device applications. PVP has good compatibility and can easily form films with large internal area [5].

The nanocomposites materials were suggested to utilize in different applications such as optical fields [6–15], antibacterial [16–21], sensors [22, 23], radiation shielding and bioenvironmental [24–29], energy storage [30–32], electronics and optoelectronics [33–46].

This article aims to prepare of PVP/Ag/SiC nanostructures and studying the dielectric properties to utilize in different electronics fields.

2. MATERIALS AND METHODS

Nanocomposites films of PVP doped with Ag/SiC nanoparticles were fabricated using casting process with different concentrations ($C_1 = 12.5$ gm/L, $C_2 = 25$ gm/L, and $C_3 = 50$ gm/L). Ag–SiC nanoparticles (NPs) with a ratio of 6% were added to polymer with content of 50% Ag and 50% SiC. The dielectric properties of PVP/Ag/SiC nanostructures films were measured at frequency range 100 Hz– $5 \cdot 10^6$ Hz by LCR meter (HIOKI 3532-50 LCR HI TESTER).

The dielectric constant (ϵ') was determined by [47]:

$$\epsilon' = C_p/C_0, \quad (1)$$

where C_p is the matter capacitance and C_0 is the vacuum capacitance.

Dielectric loss (ϵ'') was given by [47]:

$$\epsilon'' = \epsilon'D, \quad (2)$$

where D is the dispersion factor.

The A.C. electrical conductivity was found [48] as follows:

$$\sigma_{A.C.} = 2\pi f\epsilon'D\epsilon_0. \quad (3)$$

4. RESULTS AND DISCUSSION

The behaviours of dielectric constant and dielectric loss with frequency and concentration are shown in Figs. 1–4, respectively. It can be seen that with increasing frequency dielectric constant (ϵ'), dielectric loss (ϵ'') decreases. This is because of the available relaxation time of the polymer. At low frequencies, polymer molecules get sufficient time to orient themselves according to the applied field. However, as the frequency increases, molecules are not getting sufficient time to orient themselves according to the direction of the electrical field.

Therefore, the overall polarization effect decreases and, consequently, the value of dielectric constant decreases too, as it is directly proportional to the value of polarization. At high frequencies, as the polarization decreases, the dielectric loss and dissipation factor, also decreases as sufficient time is not provided to the polymer chain to generate phase angle. Thus, at high frequencies, the contribution of orientational or dipole polarization vanishes and the effect is only for electronic polarization, which is instantaneous. The dielectric constant and dielectric loss increase with rising concentration that relates to increase in charge carriers [49–60].

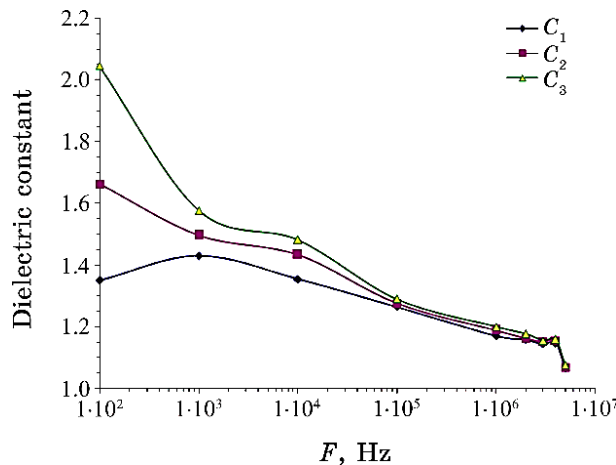


Fig. 1. Behaviour of dielectric constant with frequency for the PVP/Ag/SiC nanostructures.

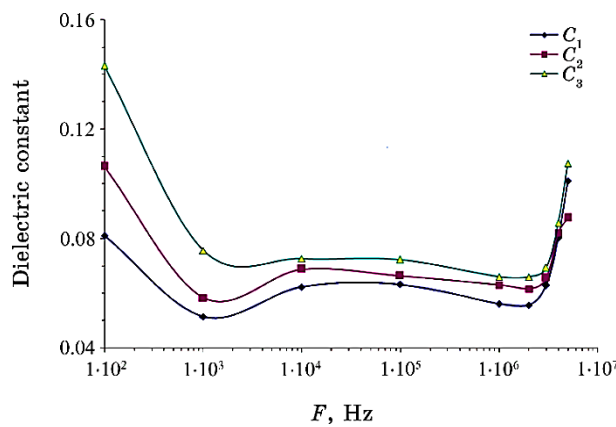


Fig. 2. Dielectric loss performance with frequency for the PVP/Ag/SiC nanostructures.

Figures 5 and 6 show the variation of A.C. conductivity for PVP/Ag/SiC nanostructures films with frequency for varied concentrations. As shown in these figures, the electrical conductivity increases with increasing the concentration, because the distributed Ag/SiC NPs in the polymer matrix has increased the number of conductive pathways and rise in the charge-carriers' numbers. In addition, the conductivity of PVP/Ag/SiC nanostructures films increases with rising of the frequency. The dependence of conductivity with the frequency is caused by the hopping of carriers of charge in the localized levels [61–68].

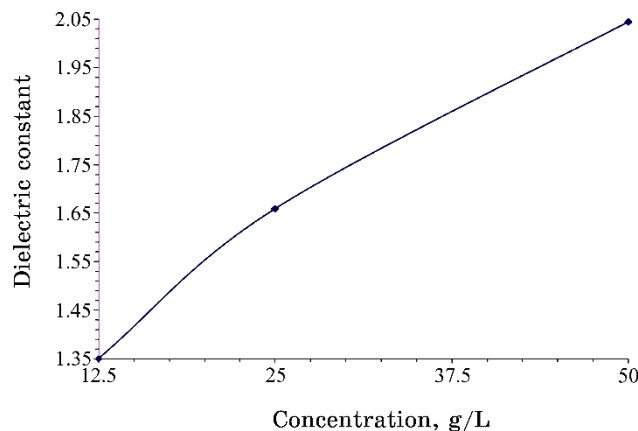


Fig. 3. Dielectric constant variation for the PVP/Ag/SiC nanostructures with concentration.

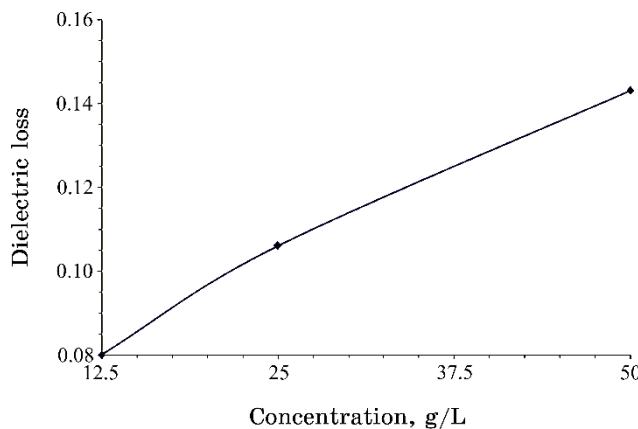


Fig. 4. Variation of dielectric loss for the PVP/Ag/SiC nanostructures with concentration.

5. CONCLUSIONS

This study comprises preparation of PVP/Ag/SiC nanostructures and examining the dielectric properties to use them in different electronics fields with lightweight and low cost. The results showed that the dielectric constant and dielectric loss of PVP/Ag/SiC nanostructures reduced while the electrical conductivity increased with an increase in the frequency. The dielectric constant, dielectric loss and electrical conductivity rise with increasing of the concentration. The final results indicated that the dielectric properties indicated that the PVP/Ag/SiC nanostructures could be suitable in

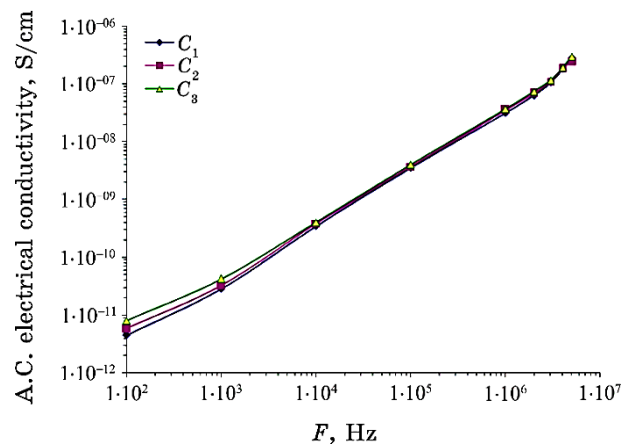


Fig. 5. Variation of A.C. conductivity for the PVP/Ag/SiC nanostructures with frequency.

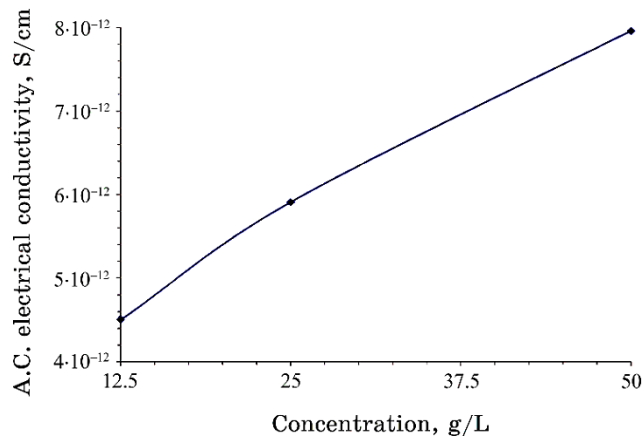


Fig. 6. Behaviour of A.C. conductivity for the PVP/Ag/SiC nanostructures with concentration.

various electronics applications.

REFERENCES

1. D. A. Nasrallah and M. A. Ibrahim, *J. of Polym. Res.*, **29**: 1 (2022); <https://doi.org/10.1007/s10965-022-02943-5>
2. E. Sheha, H. Khoder, T. S. Shanap, M. G. El-Shaarawy, M. K. El Mansy, *Optik*, **123**, Iss. 13: 1161 (2012); <https://doi.org/10.1016/j.ijleo.2011.06.066>
3. P. B. Anand, C. S. Suchand Sandeep, Kishore Sridharan, T. N. Narayanan,

- Senoy Thomas, Reji Philip, and M. R. Anantharaman, *Adv. Sci. Eng. Med.*, **4**: 33 (2012); doi:[10.1166/asem.2012.111533](https://doi.org/10.1166/asem.2012.111533)
4. S. C. R. Modugu, J. Schuster, and Y. P. Shaik, *J. Compos. Sci.*, **6**: 1 (2022); <https://doi.org/10.3390/jcs6100312>
 5. S. K. Shahenoor Basha, K. Vijay Kumar, G. Sunita Sundari, and M. C. Rao, *Adv. in Mater. Sci. and Eng.*, **2018**: 1 (2018); <https://doi.org/10.1155/2018/4372365>
 6. W. O. Obaid and A. Hashim, *Silicon*, **14**: 11199 (2022); <https://doi.org/10.1007/s12633-022-01854-w>
 7. O. B. Fadil and A. Hashim, *Silicon*, **14**: 9845 (2022); <https://doi.org/10.1007/s12633-022-01728-1>
 8. H. Ahmed and A. Hashim, *Silicon*, **15**: 2339 (2023); <https://doi.org/10.1007/s12633-022-02173-w>
 9. H. B. Hassan, H. M. Abduljalil, and A. Hashim, *Nanosistemi, Nanomateriali, Nanotehnologii*, **20**, Iss. 4: 941 (2022); <https://doi.org/10.15407/nnn.20.04.941>
 10. H. A. Jawad and A. Hashim, *Nanosistemi, Nanomateriali, Nanotehnologii*, **20**, Iss. 4: 963 (2022); <https://doi.org/10.15407/nnn.20.04.963>
 11. H. Ahmed and A. Hashim, *Silicon*, **14**: 6637 (2022); <https://doi.org/10.1007/s12633-021-01449-x>
 12. H. Ahmed and A. Hashim, *Silicon*, **13**: 4331 (2020); <https://doi.org/10.1007/s12633-020-00728-8>
 13. H. Ahmed and A. Hashim, *Transactions on Electrical and Electronic Materials*, **22**: 335 (2021); <https://doi.org/10.1007/s42341-020-00244-6>
 14. N. AH. Al-Aaraji, A. Hashim, A. Hadi, and H. M. Abduljalil, *Silicon*, **14**: 10037 (2022); <https://doi.org/10.1007/s12633-022-01730-7>
 15. H. Ahmed and A. Hashim, *Opt. Quant. Electron.*, **55**: 1(2023); <https://doi.org/10.1007/s11082-022-04273-8>
 16. A. Hazim, H. M. Abduljalil and A. Hashim, *International Journal of Emerging Trends in Engineering Research*, **7**, No. 8: 104 (2019); <https://doi.org/10.30534/ijeter/2019/04782019>
 17. O. B. Fadil and A. Hashim, *Nanosistemi, Nanomateriali, Nanotehnologii*, **20**, Iss. 4: 1029 (2022); <https://doi.org/10.15407/nnn.20.04.1029>
 18. W. O. Obaid and A. Hashim, *Nanosistemi, Nanomateriali, Nanotehnologii*, **20**, Iss. 4: 1009 (2022); <https://doi.org/10.15407/nnn.20.04.1009>
 19. M. H. Meteab, A. Hashim, and B. H. Rabee, *Nanosistemi, Nanomateriali, Nanotehnologii*, **21**, Iss. 1: 199 (2023).
 20. A. Hashim, I. R. Agool, and K. J. Kadhim, *Journal of Bionanoscience*, **12**, No. 5: 608 (2018); doi:[10.1166/jbns.2018.1580](https://doi.org/10.1166/jbns.2018.1580)
 21. A. Hazim, A. Hashim, and H. M. Abduljalil, *International Journal of Emerging Trends in Engineering Research*, **7**, No. 8: 68 (2019); <https://doi.org/10.30534/ijeter/2019/01782019>
 22. H. Ahmed and A. Hashim, *International Journal of Scientific & Technology Research*, **8**, Iss. 11: 1014 (2019).
 23. B. Mohammed, H. Ahmed, A. Hashim, *Nanosistemi, Nanomateriali, Nanotehnologii*, **20**, No. 1: 187 (2022); <https://doi.org/10.15407/nnn.20.01.187>
 24. B. Abbas and A. Hashim, *International Journal of Emerging Trends in Engineering Research*, **7**, No. 8: 131 (2019); <https://doi.org/10.30534/ijeter/2019/06782019>

25. K. H. H. Al-Attiyah, A. Hashim, and S. F. Obaid, *Journal of Bionanoscience*, **12**: 200 (2018); [doi:10.1166/jbns.2018.1526](https://doi.org/10.1166/jbns.2018.1526)
26. H. A. J. Hussien, A. Hadi, and A. Hashim, *Nanosistemi, Nanomateriali, Nanotehnologii*, **20**, Iss. 4: 1001 (2022);
<https://doi.org/10.15407/nnn.20.04.1001>
27. A. Hashim and N. Hamid, *Journal of Bionanoscience*, **12**, No. 6: 788 (2018);
[doi:10.1166/jbns.2018.1591](https://doi.org/10.1166/jbns.2018.1591)
28. A. Hashim and Z. S. Hamad, *Journal of Bionanoscience*, **12**, No. 4: 488 (2018); [doi:10.1166/jbns.2018.1551](https://doi.org/10.1166/jbns.2018.1551)
29. A. Hashim and Z. S. Hamad, *Journal of Bionanoscience*, **12**, No. 4: 504 (2018); [doi:10.1166/jbns.2018.1561](https://doi.org/10.1166/jbns.2018.1561)
30. H. Ahmed and A. Hashim, *Nanosistemi, Nanomateriali, Nanotehnologii*, **20**, 4: 951 (2022); <https://doi.org/10.15407/nnn.20.04.951>
31. Abbas Sahi Shareef, Farhan Lafta Rashid, Aseel Hadi, and Ahmed Hashim, *International Journal of Scientific & Technology Research*, **8**, Iss. 11: 1041 (2019); https://www.researchgate.net/publication/337315854_Water-Polyethylene_Glycol_Sic-Wc_And_Ceo2WcNanofluids_For_Saving_Solar_Energy
32. A. Hadi, A. Hashim, and D. Hassan, *Bulletin of Electrical Engineering and Informatics*, **9**, No. 1: 83(2020); [doi:10.11591/eei.v9i1.1323](https://doi.org/10.11591/eei.v9i1.1323)
33. A. Hazim, A. Hashim, and H. M. Abduljalil, *Nanosistemi, Nanomateriali, Nanotehnologii*, **18**, Iss. 4: 983 (2020);
<https://doi.org/10.15407/nnn.18.04.983>
34. A. Hashim and Z. S. Hamad, *Nanosistemi, Nanomateriali, Nanotehnologii*, **18**, Iss. 4: 969 (2020); <https://doi.org/10.15407/nnn.18.04.969>
35. A. Hazim, A. Hashim and H. M. Abduljalil, *Egypt. J. Chem.*, **64**, No. 1: 359 (2021); [doi:10.21608/EJCHEM.2019.18513.2144](https://doi.org/10.21608/EJCHEM.2019.18513.2144)
36. H. Ahmed and A. Hashim, *Journal of Molecular Modeling*, **26**: 1 (2020);
[doi:10.1007/s00894-020-04479-1](https://doi.org/10.1007/s00894-020-04479-1)
37. A. Hazim, A. Hashim, and H. M. Abduljalil, *Trans. Electr. Electron. Mater.*, **21**: 48 (2019); <https://doi.org/10.1007/s42341-019-00148-0>
38. A. F. Kadhim, and A. Hashim, *Opt. Quant. Electron.*, **55**: 432 (2023);
<https://doi.org/10.1007/s11082-023-04699-8>
39. H. Ahmed and A. Hashim, *Opt. Quant. Electron.*, **55**: 280 (2023);
<https://doi.org/10.1007/s11082-022-04528-4>
40. G. Ahmed and A. Hashim, *Silicon*, **15**: 3977 (2023);
<https://doi.org/10.1007/s12633-023-02322-9>
41. M. H. Meteab, A. Hashim, and B. H. Rabee, *Opt. Quant. Electron.*, **55**: 187 (2023); <https://doi.org/10.1007/s11082-022-04447-4>
42. B. Mohammed, H. Ahmed, and A. Hashim, *Nanosistemi, Nanomateriali, Nanotehnologii*, **21**, Iss. 1: 113 (2023);
<https://doi.org/10.15407/nnn.21.01.113>
43. H. Ahmed and A. Hashim, *Silicon*, **14**: 4907 (2022);
<https://doi.org/10.1007/s12633-021-01258-2>
44. A. Hashim, *Opt. Quant. Electron.*, **53**: 1 (2021);
<https://doi.org/10.1007/s11082-021-03100-w>
45. H. Ahmed and A. Hashim, *Trans. Electr. Electron. Mater.*, **23**: 237 (2022);
<https://doi.org/10.1007/s42341-021-00340-1>
46. H. Ahmed and A. Hashim, *Silicon*, **14**: 7025 (2021);

- <https://doi.org/10.1007/s12633-021-01465-x>
47. A. H. Selçuk, E. Orhan, S. Bilge Ocak, A. B. Selçuk, and U. Gökmen, *Materials Science-Poland*, **35**, Iss. 4: 885 (2017); doi:10.1515/msp-2017-0108
48. H. Bouaamlat, N. Hadi, N. Belghiti, H. Sadki, M. N. Bennani, F. Abdi, T.-D. Lamcharfi, M. Bouachrine, and M. Abarkan, *Advances in Materials Science and Engineering*, **2020**: 1 (2020);
<https://doi.org/10.1155/2020/8689150>
49. A. Hashim, M. H. Abbas, N. AH. Al-Aaraji, and A. Hadi, *J. Inorg. Organomet. Polym.*, **33**: 1 (2023); <https://doi.org/10.1007/s10904-022-02485-9>
50. A. Hashim, M. H. Abbas, N. AH. Al-Aaraji, and A. Hadi, *Silicon*, **15**: 1283 (2023); <https://doi.org/10.1007/s12633-022-02104-9>
51. M. H. Meteab, A. Hashim, and B. H. Rabee, *Silicon*, **15**: 1609 (2023);
<https://doi.org/10.1007/s12633-022-02114-7>
52. H. A. J. Hussien and A. Hashim, *J. Inorg. Organomet. Polym.*, **33**: 2331 (2023); <https://doi.org/10.1007/s10904-023-02688-8>
53. A. Hashim, A. Hadi, N. A. H. Al-Aaraji, and F. L. Rashid, *Silicon*, **15**: 5725 (2023); <https://doi.org/10.1007/s12633-023-02471-x>
54. A.F. Kadhim and A. Hashim, *Silicon*, **15**: 4613 (2023);
<https://doi.org/10.1007/s12633-023-02381-y>
55. H. A. Jawad and A. Hashim, *Nanosistemi, Nanomateriali, Nanotehnologii*, **21**, Iss. 1: 133 (2023); <https://doi.org/10.15407/nnn.21.01.133>
56. N. Al-Huda Al-Aaraji, A. Hashim, A. Hadi, and H. M. Abduljalil, *Silicon*, **14**: 4699 (2022); <https://doi.org/10.1007/s12633-021-01265-3>
57. M. H. Meteab, A. Hashim, and B. H. Rabee, *Silicon*, **15**: 251 (2023);
<https://doi.org/10.1007/s12633-022-02020-y>
58. A. Hashim, A. Hadi, and M. H. Abbas, *Opt. Quant. Electron.*, **55**: 642 (2023); <https://doi.org/10.1007/s11082-023-04929-z>
59. A. Hashim, A. Hadi, and M. H. Abbas, *Silicon*, **15**: 6431 (2023);
<https://doi.org/10.1007/s12633-023-02529-w>
60. M. Singhi and M. Fahim, *International Journal of Scientific Research*, **3**, Iss. 11: 45 (2014).
61. Z. S. Hamad and A. Hashim, *Nanosistemi, Nanomateriali, Nanotehnologii*, **20**, Iss. 1: 159 (2022); <https://doi.org/10.15407/nnn.20.01.159>
62. B. Mohammed, H. Ahmed and A. Hashim, *Journal of Physics: Conference Series*, **1879**: 1 (2021); doi:10.1088/1742-6596/1879/3/032110
63. D. Hassan and A. H. Ah-Yasari, *Bulletin of Electrical Engineering and Informatics*, **8**, Iss. 1: 52 (2019); doi:10.11591/eei.v8i1.1019
64. D. Hassan and A. Hashim, *Bulletin of Electrical Engineering and Informatics*, **7**, Iss. 4: 547 (2018); doi:10.11591/eei.v7i4.969
65. A. Hashim and Z. S. Hamad, *Nanosistemi, Nanomateriali, Nanotehnologii*, **20**, Iss. 1: 165 (2022); <https://doi.org/10.15407/nnn.20.01.165>
66. A. Hashim and A. Jassim, *Nanosistemi, Nanomateriali, Nanotehnologii*, **20**, Iss. 1: 177 (2022); <https://doi.org/10.15407/nnn.20.01.177>
67. A. Hashim and Z. S. Hamad, *Nanosistemi, Nanomateriali, Nanotehnologii*, **20**, No. 2: 507 (2022); <https://doi.org/10.15407/nnn.20.02.507>
68. E. Salim and A. E. Tarabiah, *Journal of Inorganic and Organometallic Polymers and Materials*, **33**: 1638 (2023); <https://doi.org/10.1007/s10904-023-02591-2>

PACS numbers: 68.37.Hk, 68.37.Ps, 82.35.Np, 82.45.Yz, 87.64.Dz, 87.80.Dj, 87.85.Rs

Preparation and Characterization of Nanofilm-Coated Modified Electrodes and Their Use in Valsartan Drug Analysis

Ahmed Filayih Hassan^{1,2}

¹*Education Directorate of Dhi Qar,
Dhi Qar, Iraq*

²*College of Pharmacy,
Department of Pharmacy,
National University of Science and Technology,
Dhi Qar, Iraq*

The use of nanomaterials is a modern trend in electrochemical analysis because of the ease and accuracy of the analysis that, in addition, being non-destructive to the samples, gives the possibility of repeating the analysis to obtain better results. In this research, films of a co-conductive polymer of pyrrole and one of its derivatives are fabricated by docking on a graphite substrate. The film and the substrate form a modified electrode described by EIS and CV in the presence and absence of valsartan. Using a modified electrode, the concentration of valsartan is determined in titres and blood samples of patients with a standard deviation ($SD = 0.6$). The quantitative and detection limit are $LOQ = 6 \mu\text{M}$ and $LOD = 1.8 \mu\text{M}$, respectively. DPV with standard addition method has standard deviation ($SD = 0.34$). The new method succeeds in being more accurate with $LOQ = 3.4 \mu\text{M}$ and $LOD = 1.1 \mu\text{M}$, respectively. *F*-test proves that the HPLC method is not better than DPV and DPV with modified standard addition methods in determining the drug concentration of valsartan. The modified standard addition method is probably the best.

Використання наноматеріалів є сучасною тенденцією в електрохемічній аналізі через легкість і точність аналізу; крім того, вони не руйнують зразки, що дає можливість повторної аналізу для одержання ліпших результатів. У цьому дослідженні плівки провідного полімеру піролу й одного з його похідних були виготовлені шляхом стикування на графітовій підкладинці. Плівка та підкладинка утворили модифіковану електроду, описану електрохемічною імпедансною спектроскопією та циклічною вольтамперометрією, у присутності та за відсутності валсартану. За допомогою модифікованої електроди визначено концентрацію валсартану в титрах і зразках крові пацієнтів зі стандартним відхиленням ($SD = 0,6$). Кількісна межа та межа виявлення становлять $LOQ = 6 \mu\text{M}$ і

LOD = 1,8 μM відповідно. Диференційна імпульсна вольтамперометрія з методом стандартного додавання має стандартний відхил ($SD = 0,34$). Новий метод став більш точним із LOQ = 3,4 μM і LOD = 1,1 μM відповідно. *F*-тест довів, що метод високоефективної рідинної хроматографії не є кращим, аніж диференційна імпульсна вольтамперометрія та диференційна імпульсна вольтамперометрія з модифікованими стандартними методами додавання у визначені концентрації препарату валсартану. Модифікований стандартний метод додавання, ймовірно, є найліпшим.

Key words: polymer thin films, anchoration, modified electrode, differential pulse voltammetry, valsartan.

Ключові слова: полімерні тонкі плівки, анкерування, модифікована електродна, диференційна імпульсна вольтамперометрія, валсартан.

(Received 7 June, 2023; in revised form, 24 June, 2023)

1. INTRODUCTION

Electrochemical analysis is a modern, accurate, non-destructive sampling technique [1], which can be used on water-soluble solid or liquid samples [2]. Electrochemical analysis has many characteristics and advantages [3]. All methods work through the contact of the sample solution with a working electrode, and the circuit is completed with an auxiliary electrode and the potential is measured with respect to a comparator electrode within the triple cell [4].

Electrochemical analysis involves measuring current (ampere), potential (volt), or amount of electricity (charge) (coulombs) against time, potential, or current [3]. During the analysis, precise electrical devices measure the very slight changes in the analytical signal values against the changes of the corresponding factor in the experiment. The analysis depends mostly on electrical conductivity and oxidation-reduction reactions within the cell, in which the measurement is made [5]. Working electrodes are the base for cell used in an analytical or chemical application [6].

Electrodes are often composed of a surface of a chemically inert material that is a good conductor of electric current; this material forms the main body of the electrode in electrical operations and transfers the electric current to the circuit outside the solution [5]. Many layers can be added to the surface of the electrode for work [6]. Recently, there is a tendency to use nanofilms on electrodes in many applications, such as electrolysis, electrolysis, and photoelectrolysis [7]. The thickness of the film, the size of its particles, the type of its constituent material, and the electrode material affect the application of the film and the method of its manufacture on

the surface of the electrode [8]. Nanofilms are made chemically by anchoring and electrodeposition and physically by dipcoting and spincoting. Dipcoting and spincoting were preferred for fabrication of films, which are used for analytical applications, due to the ease of fabrication of very thin, well-covered, homogeneous films [9].

Films in analytical applications are very thin and easily damaged; so, we need to renew constantly them to reuse them again [10]. Conductive polymers can form thin films by an anchoring method. Concentration, temperature and time all affect the film thickness and particle size [11]. Electrodeposition is used in the preparation of many thin films of metal oxides and conductive polymers. The potential and current of deposition and the film material often affect the thickness of the film, the size of its particles and its stability. Many researchers made thin films by electrodeposition and studied their analytical properties [12].

The drug valsartan is widely used in patients with chronically elevated arterial pressure at different doses that suit the patient's condition alone or in synergy with one or more other drugs. Many researchers have developed analysis methods that meet the need, but need more development [13]. In this research, we present a method for analysing the valsartan in both pure samples and capsules and in blood samples, based on measurements of the cyclic potential of the aqueous solution on a working electrode, whose surface is covered with a film of poly(pyrrole-formylpyrrol) by anchoring.

2. EXPERIMENTAL

2.1. Materials

Pyrrole-2-carboxaldehyde 98% sigma, pyrrole > 98% sigma trichloroacetic acid sigma, and graphite electrodes sigma.

2.2. Measurements

Thin films were characterized by electrochemical impedance spectroscopy (EIS) applied using in KClO_4 (1 M) solution, 1 mA/cm^2 and 0.58 V in the range of 0.1 Hz–10 kHz, cycle voltammetry (CV) method at a scan rate of $100 \text{ mV}\cdot\text{s}^{-1}$ within the potential range of -0.2–1 V (AMEL model 2550). Thin film morphologies were examined with AFM (Nanosurf model eseyscan2) and SEM (TESCAN model MIRA3).

2.3. Analysis Protocol

The differential pulse voltammetry (DPV) was in a potential range

of 0.01 to 0.6 V at scan rate of $5 \text{ mV}\cdot\text{s}^{-1}$ and the DPV input data are as follow: step potential of 0.004 V, modulation amplitude of 0.08 V, modulation time of 0.2 s, and interval time 0.5 s. The DPV oxidation peaks of valsartan were at $227 \pm 5 \text{ mV}$ against the Ag/AgCl electrode. HPLC [13] used mobile phase acetonitrile and water in the ratio 55:45 (*v/v*), and the pH adjusted to 3.6 with 88% orthophosphoric acid with a flow rate of $1.0 \text{ ml}\cdot\text{min}^{-1}$ and C18 column ($250\times4.6 \text{ mm id}, 5 \mu\text{m}$ particle size).

2.4. Thin Films Fabrication

The film was fabricated by anchoration in the reaction solution (pyrrole and 2-formyl pyrrole (10 mmol)) was dissolved in the 25 ml of ethanol, and 3 g of trichloroacetic acid was added [14]. The electrodes were immersed in the solution of reaction, and left in the solution for 30 min and removed from the solution. The films (on electrodes) were washed with deionized water and alcohol (do not touch the film surface).

2.5. Film Deposition

Graphite electrodes were sanded to great fineness. Electrode was isolated with electrical insulator coating except for a precisely defined surface (1 cm^2). The films were fabricated by docking: the electrode was immersed completely in the reaction solution to prepare a polymer.

2.6. Sample Analysis

The valsartan samples were analysed in two methods for comparison; the first method is by HPLC as the reference method, and the second method is by DPV. Standard series were prepared from standard analysis using the same method. Samples from three sources of valsartan were obtained for the purpose of the study.

2.6.1. Capsule Sample

The capsule was obtained from the pharmacy outlets in the city of Baghdad for a drug produced by a national company. According to the attached leaflet, it contains a substance containing (160 mg) an active substance loaded with excipients and film-coated. Ten capsules were taken and finely ground. Transfer to a 1000 ml volumetric flask and add water to the mark. A solution of theoretical con-

centration of 100 mg/L was prepared from the mother liquor.

2.6.2. Pure Substance Sample

The active substance of the valsartan drug was taken from the manufacturing laboratory; the data sheet for the substance was reviewed, and the data of the substance was verified before working on it. From the material, weigh accurately, transfer to a beach, add the solution to it, stir until dissolution, transfer to a volumetric flask, and complete the volume to the mark.

2.6.3. Patient Blood Sample

A blood sample (5 ml) was taken from a patient's left hand vein after the patient's consent by a medical specialist with sterile instruments after 2, 4 and 6 hours of taking the drug. Samples were subjected to primary treatment to obtain blood serum and sedimentation of soluble proteins. The treated serum sample was transferred to a 25 mL calibrated flask and filled with distilled water to the mark.

3. RESULTS AND DISCUSSION

3.1. SEM of Polymer

Electron microscopy images give information about the shape and size of nanoparticles. Figure 1 shows pictures of the electronic microscope of the polymer. Polymer particles are bacillus in close sizes and the size of the particles is of around 70 nm. The particles on a rough surface are clogged to be coral.

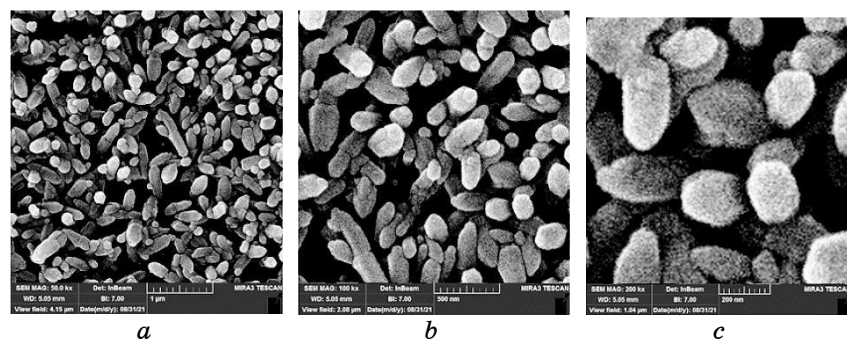


Fig. 1. Scanning electron microscopy images of polymer.

3.2. AFM of Polymer Thin Films

Figure 2 shows the atomic force microscopy images for two areas of the film.

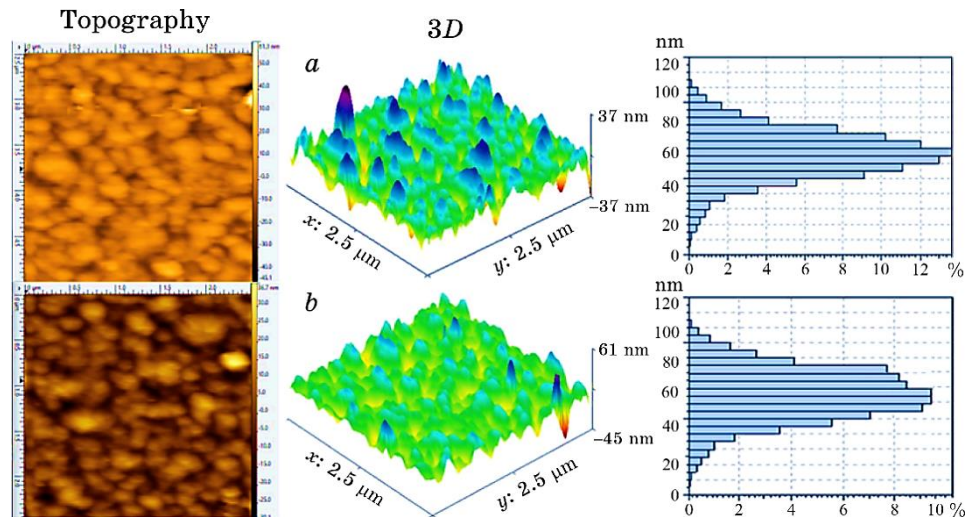


Fig. 2. The atomic force microscopy images for two areas of the film.

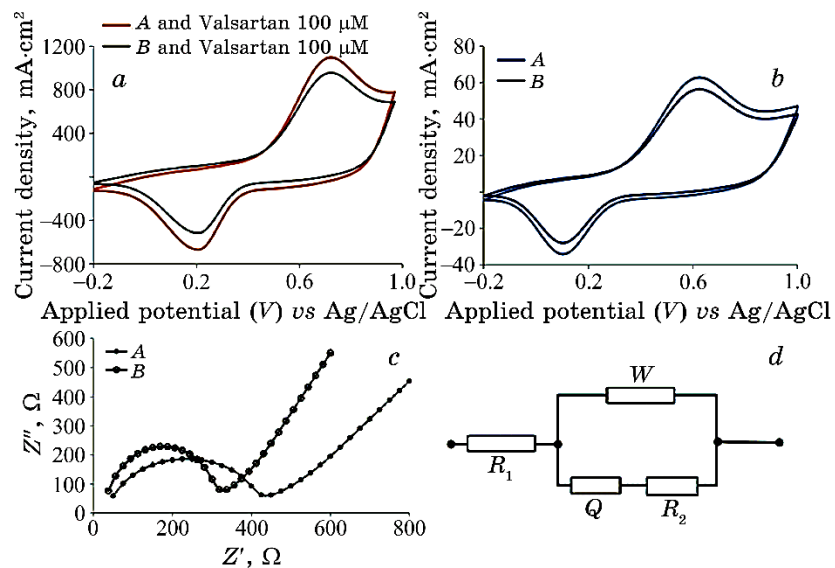


Fig. 3. (a) Cyclic voltammetry of the electrodes with valsartan 100 μM ; (b) cyclic voltammetry of the electrodes without valsartan; (c) Nyquist plot for films; (d) equivalent electrical circuits for the films.

From the comparison of Fig. 2, *a* and *b*, it appears that there is a good homogeneity in the structure of the films forming the surface of the electrode, the peaks are close in height up to 80 nm, the surface is rough, and the particle size is of about 60 nm in both images. This approximates the particle size in electron microscopy images, and the particle shape is similar too.

3.3. CV and EIS of Polymer Thin Films

The cyclic voltammetry of the electrodes (Fig. 3, *b*) shows two clear return oxidation peaks on two electrodes, the peak around 0.582 V, when using the electrodes (Fig. 3, *b*) valsartan solution. The oxidation peak differs, which becomes at 0.679 V.

Figure 3, *c* shows the electrochemical impedance spectrum for electrodes. The curves consist of two parts. Semi-circular at high frequencies is the first part, and the other one is linear at low frequencies. In order to analyse the EIS results, we fitted the impedance data to equivalent electrical circuits (Fig. 3, *d*), which consist of resistance (solution resistance R_1) of 46 ± 5 Ohm. Warburg Impedance (noted W) or capacitance is, therefore, ascribed to the diffusive capacitance (*a*: 54 ± 7 and *B*: 43 ± 5 (m·Ohm) $^{-2}$). Warburg Impedance is analogous to resistance (R_2) and capacitance (Q). Resistance (R_2) is (*a*: 154 ± 18 and *b*: 185 ± 42 Ohm), while Q is the double-layer capacitance (*a*: 0.23 ± 0.02 and *b*: 0.183 ± 0.02 $\mu\text{F}/\text{cm}^2$).

3.4. Valsartan Analysis by HPLC

A standard method was used to determine the valsartan using HPLC according to Ref. [13], where a titre series (100–600 μM) was prepared and analysed according to the conditions of the aforementioned method. Figure 4 shows: the peak area *versus* valsartan concentration, ($y = 898870x + 1 \cdot 10^6$)-regression equation with noise rate (0.013) and LOD = 0.039 μM and LOQ = 0.132 μM .

3.5. Valsartan Analysis by DPV

Figure 5 shows the current measurement curves in DPV and the linear regression curve of current density *versus* concentration. In Figure 5, *a*, the current density increases exponentially with increasing valsartan concentration. The linear regression equation is ($y = 0.0368x + 6.99$) with a correlation coefficient ($R_2 = 0.998$), with a standard deviation (SD = 0.6). The limit of detection (LOD) and limit of quantification (LOQ) were calculated by standard deviation (signal to SD ratio of 3:1) and quantified (signal to SD ratio of

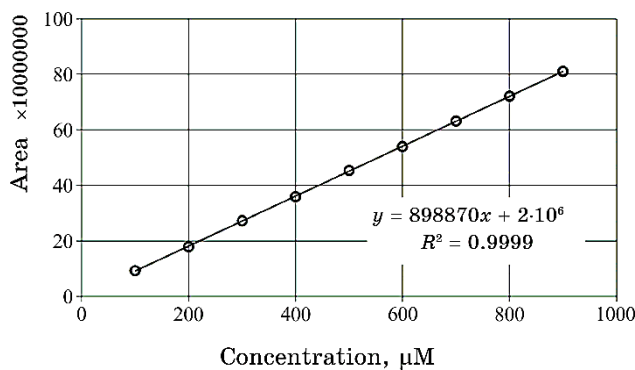


Fig. 4. The peak area *versus* valsartan concentration.

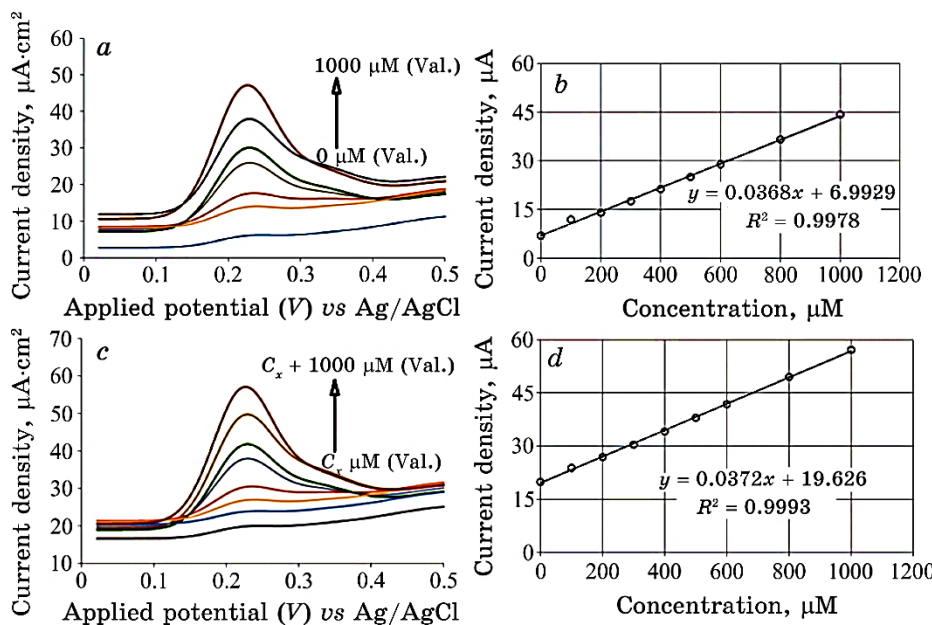


Fig. 5. (a) current measurement curves in DPV; (b) current density *vs* valsartan concentration; (c) current measurement curves in DPV by the modified standard addition method; (d) current density *vs* valsartan concentration.

10:1), respectively: LOD = 1.8 μM and LOQ = 6.0 μM.

Tables 1 and 2 show the results of valsartan analysis. Retrospective titre samples reached (58.1 μM) blood samples gave results with good reproducibility.

Figure 5 shows the current measurement curves in DPV by the modified standard addition method, where a concentrated titre solu-

TABLE 1. The results of the analysis of samples of valsartan.

Level, %	<i>n</i>	Concentration, μM	Found concentration, μM	Recovery	RSD
50	5	150	147.9	99.2	0.584
100	5	300	298.5	99.5	0.486
150	5	450	449.1	99.8	0.569

TABLE 2. Shows the results of valsartan analysis by DPV and DPV-S.A.M.

Method	Level, %	<i>n</i>	Concentration, μM	Found concentration, μM	Recovery	RSD
PDV	50	5	175	177.6	101.5	0.459
	100	5	350	349.3	99.8	0.658
	150	5	525	519.2	98.9	0.662
PDV-S.A.M.	50	5	175	173.8	99.3	0.349
	100	5	350	344.8	98.5	0.417
	150	5	525	528.2	100.6	0.394

tion of valsartan ($525 \mu\text{M}$) was used as an unknown solution, and an amount of a high-concentration titre solution was added to it according to the titre series. The concentration was calculated from the regression equation. The linear regression equation is ($y = 0.0372x + 19.63$) with a correlation coefficient ($R^2 = 0.998$), with a standard deviation ($SD = 0.34$). The limit of detection (LOD) and limit of quantification (LOQ) were calculated by standard deviation (signal to SD ratio of 3:1) and quantified (signal to SD ratio of 10:1), respectively: $LOD = 1.0 \mu\text{M}$ and $LOQ = 3.4 \mu\text{M}$.

Table 2 shows the results of valsartan analysis retrieved from titre samples ($58.2 \mu\text{M}$) in blood samples; the concentration of valsartan was determined by the modified standard addition method, and we got good results with a good reproducibility.

The concentration of valsartan was determined by three methods: HPLC, DPV, and DPV with modified standard addition. The methods were compared with a paired *F*-test to determine the most accurate method. The *F*-value for (0.05, 9, 9) is of 3.117. Table 3 shows F_{exp} for comparison of methods. From this table, HPLC method is not better than DPV and DPV with modified standard addition.

4. CONCLUSIONS

Conductive polymer thin film was fabricated on a graphite substrate and characterized by SEM and AFM. The film and substrate formed

TABLE 3. F_{exp} shown for comparison of methods.

Method <i>vs</i> Method	<i>n</i>	F_{exp}
DPV <i>vs</i> HPLC	9	2.250
DPV-S.A. <i>vs</i> HPLC	9	0.723
DPV <i>vs</i> DPV-S.A.	9	3.114

a modified electrode. The modified electrode was described by CV and EIS in the presence and absence of valsartan. Using a modified electrode, the concentration of valsartan was determined in titres and blood samples of patients, with a standard deviation ($SD = 0.6$). The quantitative and detection limit are $LOQ = 6 \mu\text{M}$ and $LOD = 1.8 \mu\text{M}$, respectively; DPV with standard addition method has been modified to suit the use of limited volume samples such as human blood samples and non-destructive measurement methods. The new method has standard deviation ($SD = 0.34$). The new method succeeded in being more accurate with $LOQ = 3.4 \mu\text{M}$ and $LOD = 1.1 \mu\text{M}$ respectively. Fisher's test proved that the HPLC method is not superior to the electrochemical methods in determining the drug concentration of valsartan; by comparing the two methods, it was found that the modified standard addition method is more accurate, especially with its ability to exclude the effect of the matrix.

5. HIGHLIGHTS

A nanofilm of a carrier polymer was fabricated and characterized by SEM and AFM.

Preparation of a conducting electrode, characterization by electrical impedance spectrum, and study by CV are used to determine the possibility of using it for the analysis of valsartan.

It is introduced a modified standard addition method for limited-source samples and non-destructive analytical methods.

ACKNOWLEDGEMENTS

The author offers great thanks and gratitude to the spirit of his late father, Professor Dr. Filayih Hassan Aziz Aal-Sahalani.

REFERENCES

1. A. Vali, H. Z. Malayeri, M. Azizi, and H. Choi, *Applied Catalysis B*, **266**, Iss. 1: 118 (2020); <https://doi.org/10.1016/j.apcatb.2020.118646>
2. T. Hazhir, B. Abbas, and W. Joseph, *Chemical Society Reviews*, **1**, Iss. 1:

- 127 (2020); [doi:10.1089/D0CS00304B](https://doi.org/10.1089/D0CS00304B)
- 3. Sriparna Dutta and R. K. Sharma, *Separation Science and Technology*, **11**: 371 (2019); <https://doi.org/10.1016/B978-0-12-815730-5.00015-6>
 - 4. A. R. Harris, D. B. Grayden, and S. E. John, *Micromachines*, **14**, Iss. 1: 722 (2023); [doi:10.3390/mi14040722](https://doi.org/10.3390/mi14040722)
 - 5. A. Sulciute, K. Nishimura, E. Gilshtein, F. Cesano, G. Viscardi, A. G. Nasibulin, Y. Ohno, and S. J. Rackauskas, *Phys. Chem. C*, **1**, Iss. 125: 1472 (2021); [doi:10.1021/acs.jpcc.0c08459](https://doi.org/10.1021/acs.jpcc.0c08459)
 - 6. C. Steinem, A. Janshoff, H. J. Galla, and M. Sieber, *Bioelectrochemistry and Bioenergetics*, **42**, Iss. 2: 213 (1997); [doi:10.3390/s80314000](https://doi.org/10.3390/s80314000)
 - 7. A. Al-Hamdan, A. Al-Falah, and F. Al-Deri, *Kuwait Journal of Science*, **48**, Iss. 3: 1 (2021); [doi:10.48129/kjs.v48i3.9624](https://doi.org/10.48129/kjs.v48i3.9624)
 - 8. A. Al-Hamdan, A. Al-Falah, and F. Al-Deri, *Int. J. Thin. Fil. Sci. Tec.*, **10**, No. 2: 101 (2021); [doi:10.18576/ijtfst/100205](https://doi.org/10.18576/ijtfst/100205)
 - 9. A. Al-Hamdan, A. Al-Falah, F. Al-Deri, and I. Al-ghoraibi, *Nanosistemi, Nanomateriali, Nanotehnologii*, **20**, Iss. 1: 195 (2022); <https://doi.org/10.15407/nnn.20.01.195>
 - 10. A. Al-Hamdan, A. Al-Falah, and F. Al-Deri, *Int. J. Thin. Fil. Sci. Tec.*, **11**, Iss. 2: 153 (2022); [doi:10.18576/ijtfst/110201](https://doi.org/10.18576/ijtfst/110201)
 - 11. A. Al-Hamdan, A. Al-Falah, F. Al-Deri, and M. Al-Kheder, *Nanosistemi, Nanomateriali, Nanotehnologii*, **19**, Iss. 4: 913 (2021); <https://doi.org/10.15407/nnn.19.04.913>
 - 12. S. Saha, M. Johnson, F. Altayaran, Y. Wang, D. Wang, and Q. Zhang, *Electrochem.*, **1**, Iss. 3: 286 (2020); [doi:10.3390/electrochem1030019](https://doi.org/10.3390/electrochem1030019)
 - 13. K. S. Lakshmi and L. Sivasubramanian, *J. Chil. Chem. Soc.*, **55**, Iss. 2: 223 (2010); [doi:10.4067/S0717-97072010000200017](https://doi.org/10.4067/S0717-97072010000200017)
 - 14. Y. Hoshina and T. Kobayashi, *Engineering*, **4**, Iss. 3: 139 (2012); [doi:10.4236/eng.2012.43018](https://doi.org/10.4236/eng.2012.43018)

PACS numbers: 78.40.-q, 79.20.Eb, 87.64.Cc, 87.64.Ee, 87.19.xb, 87.50.W-, 87.85.Rs

Characterization and Evaluation of the Antimicrobial Activity of CuO Nanoparticles Prepared by Pulse Laser Ablation in Double-Distilled Water

Khalaf Ajaj, Abdullah M. Ali, and Mushtaq Abed Al-Jubbori

*College of Education for Pure Sciences,
Department of Physics,
University of Tikrit,
41001 Mosul, Iraq*

In the current research, Q-switched Nd:YAG-laser ablation is used to create the copper-oxide nanoparticles (NPs). A disc-shaped copper target is subjected to the ablation procedure, while it is submerged in double-distilled water. The ablation is carried out with pulse counts ranging from 100, 200, 300, 400, and 500 with two different energy levels, namely, 200 mJ and 400 mJ. Transmission electron microscopy (TEM), x-ray diffraction analysis (XRD), and UV-vis spectrophotometry are used to determine the morphological and optical properties of nanoparticles. An increase in the absorbance spectrum with an increase in the number of pulses indicates an increase in the concentration of copper-oxide nanoparticles. The peaks of surface-plasmon resonance at 217 nm are seen in the absorption spectra as the laser pulses increased. A slight reduction in the optical band gap is occurred too. CuO-NPs' formation is verified by XRD analysis, which also reveals that the copper-oxide NPs' structure is a monoclinic lattice. Further, the results of the TEM and UV-vis analyses show that there are presented CuO nanoparticles. CuO nanoparticles, which are nearly spherical, are found, according to the findings of the TEM and UV-vis analyses. When 200 mJ and 400 mJ of energy are used, it is discovered that the average diameters of these nanoparticles are of about 46 nm and 52 nm, respectively. Additionally, our study results show that CuO NPs at 200 mJ are more effective for inhibiting *S. aureus* and *E. coli* than they are at 400 mJ with the same number of pulses.

У поточному дослідженні аблляція лазером Nd:YAG із модуляцією добробутності використовували для створення наночастинок оксиду Купруму. Дископодібну мідну мішень піддавали процедурі аблляції, занурюючи її у двічі дистильовану воду. Аблляцію проводили з підрахунком імпульсів у діапазоні від 100, 200, 300, 400 і 500 з двома різними рівнями енергії, а саме, 200 мДж і 400 мДж. Для визначення морфологіч-

них та оптических властивостей наночастинок використовували просвітлювальну електронну мікроскопію (ПЕМ), рентгенівську дифракційну аналізу (РДА) та спектрофотометричну аналізу у видимій та ультрафіолетовій областях світла. Збільшення спектру поглинання зі збільшеннем кількості імпульсів свідчить про збільшення концентрації наночастинок оксиду Купруму. Піки поверхневого плазмонного резонансу біля 217 нм були помітні в спектрах поглинання, коли лазерні імпульси збільшувалися. Також відбулося незначне зменшення оптичної забороненої смуги. Утворення CuO-наночастинок було підтверджено РДА, яка також показала, що структура наночастинок оксиду Купруму була моноклінною ґратицею. Крім того, результати ПЕМ та спектрофотометричної аналізи показали наявність наночастинок CuO. Наночастинки CuO, які були майже сферичними, було знайдено згідно з результатами ПЕМ і спектрофотометричної аналізи. Коли було використано рівні енергії у 200 мДж і 400 мДж, було виявлено, що середні діаметри цих наночастинок становили приблизно 46 нм і 52 нм відповідно. Крім того, результати нашого дослідження показують, що CuO-наночастинки за умови 200 мДж були ефективнішими для інгібування *S. aureus* і *E. coli*, ніж за умови рівня 400 мДж з такою ж кількістю імпульсів.

Key words: copper-oxide nanoparticles, UV-visible laser ablation, XRD, TEM, particle size, antibacterial activity.

Ключові слова: наночастинки оксиду Купруму, УФ-видима лазерна абляція, РДА, ПЕМ, розмір частинок, антибактеріальна активність.

(Received 18 May, 2023; in revised form, 27 May, 2023)

1. INTRODUCTION

The nanoparticles (NPs) offer significant scientific benefits as they serve as a crucial intermediary between macroscopic materials and atomic or molecular structures. The physical properties of bulk materials are required to remain constant and independent of size, while at the nanoscale, the physical properties of nanomaterials exhibit size-dependent characteristics, such as quantum size effect and quantum confinement in semiconductor nanoparticles, as well as surface plasmon resonance in certain metal nanoparticles [1]. The optimal methods for synthesizing metallic nanoparticles should exhibit reproducibility and the capacity to regulate particle shape while achieving uniform yields. In addition, the method exceptional qualities include the exclusion of toxic precursors, utilization of eco-friendly solvents, maintenance of reaction temperature in proximity to ambient temperature, and reduction of by-product production [2].

Pulse laser ablation in liquid (PLAL) presents distinct advantages for the synthesis of nanostructured particles, such as high purity, simplicity, rapidity, and the absence of the need for sophisticated

vacuum equipment or chemicals, which may contaminate the final product and pollute the environment [3, 4]. The PLAL technique, despite its experimental simplicity, is distinguished by intricate and rapid mechanisms that can be succinctly described as a series of four phases. Upon impact with a solid target, the foremost portion of the laser pulse causes the evaporation of a slender stratum of substance, thereby instigating the creation of plasma. The plasma generated at the outset gives rise to a region of elevated optical absorption, which subsequently absorbs the remainder of the laser pulse and undergoes ionization to attain a state of high pressure. The isotropic propagation of a shock wave into the surrounding medium is driven by the expansion of high-pressure plasma [5]. Throughout the duration of the laser pulse, the plasma undergoes growth and consistently accompanies and reinforces the expansion of the shock. Subsequent to the cessation of the laser pulse, the shock wave propagates outward by utilizing the internal energy present within the shock front; the decay process occurs rapidly and results in the generation of an acoustic wave within a few 100 ns [6].

The transfer of energy from plasma to liquid results in the generation of a slender gaseous envelope encircling the plasma, thereby initiating the formation of a cavitation bubble. The elevated internal pressure of the bubble propels it to expand externally. Because of the fluid mass inertia, the bubble surpasses its state of equilibrium and attains its utmost radius at the point where the temperature of the bubbles' interior matches that of the adjacent liquid [7, 8]. Upon reaching a certain stage, the vapour pressure within the bubble decreases to the saturation pressure corresponding to the temperature of the liquid, which is approximately one hundred times less than the hydrostatic pressure [9, 10].

Following this, the bubble undergoes contraction, and the inward movement persists until the gas reaches a level of compression that is sufficient to cause a reversal of the motion. Upon rebound, the bubble releases surplus energy in the form of a secondary shock. The ejected matter is usually captured by the bubble and eventually delivered into the water after the bubble collapses. This provides a relatively straightforward and feasible method for creating nanoparticles with desirable structures and properties [11–13]. Furthermore, the mechanism of nanostructuring surface is contingent upon various laser parameters, including limited to the number of laser pulses, energy per pulse, pulse width, and wavelength, as well as ambient conditions. The technique high level of confinement of plasma pressure, precise and efficient cooling and ease of use render it highly advantageous and valuable. The successful application of this technique is of significant importance in the production of oxides that are synthesized through chemical reactions occurring at

the liquid–solid interface [14, 15].

It's also through various physical parameters of laser radiation, including laser pulse energy, repetition rates, laser wavelength, focal spot size, and focusing conditions, that efficient NPs size control can be achieved [16, 17]. PLAL is used to create a variety of novel materials, including nanodiamond and related nanocrystals, metallic nanocrystals, nanocrystal alloys, and metal oxides [18, 19]. The PLAL present methodology exhibits several benefits in comparison to alternative techniques, such as its straightforwardness, lack of by-products, absence of post-synthesis washing requirements, economic feasibility, and adjustable experimental parameters. Quantum dots (QD) are a type of semiconductor nanoparticle characterized by their zero-dimensional structure. They exhibit distinct optical properties such as narrow emission peaks and a broad excitation range. The wavelengths of emission and energy gap of quantum dots are significantly influenced by the particle size, which is a result of the confinement effect [20, 21].

Copper is a widely used material due to its plentiful availability, low cost, thermal and electrical conductivity and antimicrobial characteristics. Colloidal copper-oxide nanoparticles (CuO NPs) are synthesized using pulsed laser ablation technology on a copper target in a liquid medium. CuO nanoparticles have shown potential for biomedical applications due to their antibacterial activity. Moreover, CuO nanostructured materials show utility in diverse applications, including biosensors, gas sensors, lithium-ion battery electrode materials, photo detectors, and supercapacitors [22, 23]. The phenomenon of surface plasmon resonance (SPR) is contingent upon the morphology and dimensions of the particle, in addition to the optical characteristics of the nanoparticles their distinctive, particularly their sharp plasmon absorption peak, make them highly appealing for biophysical, biochemical, and biotechnological applications [24]. Additionally, the copper oxide nanoparticles exhibited inhibitory properties against two bacterial groups, namely gram-positive bacteria such as *B. subtilis* and *S. aureus*, and gram-negative bacteria such as *E. coli* and *P. aeruginosa*. The inhibitory effects were observed to be dependent on the size of the particles [25, 26].

The present research pertains to the production of copper oxide nanoparticles through the employment of the PLAL method, where, by the manipulation of ablated energies and pulse counts, it is exercised for the purpose of control. The study examined the optical and morphological characteristics of the samples through the utilization of various analytical techniques, including UV-visible spectrophotometry, x-ray diffraction analysis, and transmission electron microscopy. Furthermore, the study employed CuO NPs to assess their antibacterial effectiveness against *Staphylococcus aureus* and *Escherichia coli*.

2. EXPERIMENTAL SETUP

2.1. Method for Preparation of CuO Nanoparticles

The colloidal solutions of CuO nanoparticles were synthesized in a liquid medium by the pulsed laser ablation technique (PLAL). A disc-shaped target made of high-purity copper (99.99%) with a diameter = 20 mm and a thickness = 2 mm was positioned 10 cm away from the laser source. The target was placed in a beaker containing 5 ml of double-distilled water (DDW).

Figure 1 illustrates the experimental setup for PLAL. The Q-switched Nd:YAG is a mechanism to generate high-intensity, short-duration pulses of light. The experimental setup employed Nd:YAG laser operating at a repetition rate of 6 Hz, emitting at a wavelength of 1064 nm and with a pulse width of 10 ns. Under standard conditions of temperature and pressure, the laser source changed two distinct energy levels 200 and 400 mJ. The number of pulses was systematically altered between 100 and 500, with increments of 100 pulses for each energy level.

Figure 2 shows the effects of laser pulses on the copper metal surface. Before to ablation, the target underwent a series of cleaning procedures involving deionized water, acetone, and ethanol to eliminate any oxide layer that may have formed due to exposure to air. Additionally, the target was subjected to ultrasonic treatment to remove any mechanical impurities. In the course of the ablation procedure, the beaker underwent a gradual rotation to prevent the formation of craters on the target surface due to the focused beam and to facilitate the dispersion of the NPs generated through the

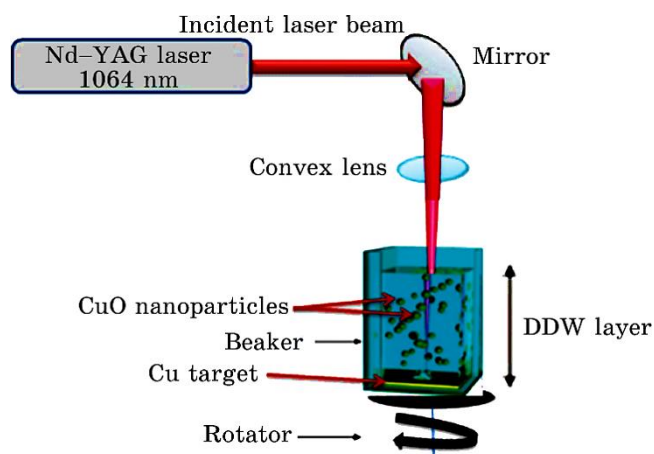


Fig. 1. PLAL system schematic diagram.

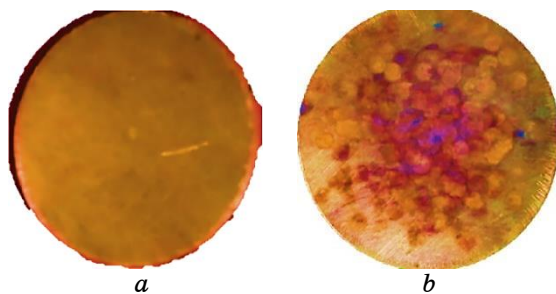


Fig. 2. Copper-metal surface ((a) before (b) after) ablated.

movement of the liquid.

2.2. Antibacterial Activity of CuO NPs

The medium was prepared by dissolving 37 grams of Mueller–Hinton agar (MHA) in one litre of distilled water. The pH of the medium was regulated to 7.2 and subsequently sterilized in an autoclave. Subsequently, into single-use petri dishes and positioned on a flat plane with a thickness of roughly 5 mm, followed by refrigeration at a temperature of 4 degrees Celsius until employment. The well was made in the MHA with a sterile micropipette tip. In this study, the antibacterial activity of copper-oxide nanoparticles (CuO NPs) at two different energy levels of 200 mJ and 400 mJ and with 500 pulses was evaluated using two bacterial strains, namely *Staphylococcus aureus* (gram-positive) and *Escherichia coli* (gram-negative). In this procedure, the bacteria were inoculated onto the media of the plates (MHA) using sterile cotton swabs and were evenly spread. Subsequently, a volume of 150 µl of a colloidal solution of CuO nanoparticles was introduced to each of the previously arranged bacterial. Subsequently, the plates housing both the test organism and CuO NPs were subjected to incubation at a temperature of 37°C for duration of 24 hours. Following incubation, the impact of CuO NPs on bacterial growth was assessed through the observation of the inhibition zone and the transformation of the surface into a transparent layer, indicative of the suppression of bacterial growth.

3. RESULTS AND DISCUSSION

3.1. The Optical Properties of Copper-Oxide NPs

The investigation of spectroscopic absorption in a synthesized collo-

dal solution of copper oxide nanoparticles in double distilled water was conducted using a Shimadzu (UV-1800) UV-vis spectrophotometer. The absorbance of colloidal nanoparticles varies with the wavelength of their absorption spectra. The findings depicted in Fig. 3 show a favourable relationship between the number of laser pulses and the level of CuO-NPs' concentration, as evidenced by the observed increase in absorption. The presence of CuO nanoparticles is indicated by the elevation of the surface-plasmon resonance peak (SPRP). Furthermore, with an increase in the number of laser pulses, the peak exhibited a reduction in width, while the dimensions of CuO NPs experienced an increase. Spherical copper oxide NPs were synthesized based on the detection of a plasmon single peak. The alteration in hue of colloidal CuO nanoparticles to a pale green, as depicted in Fig. 4, can be attributed to plasmon absorption.

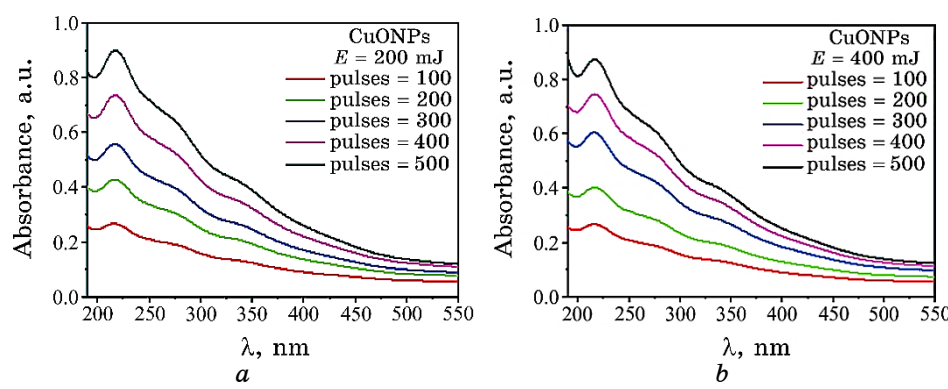


Fig. 3. Absorption spectra of CuO NPs in double distilled water at various numbers of pulses and different pulse energies.

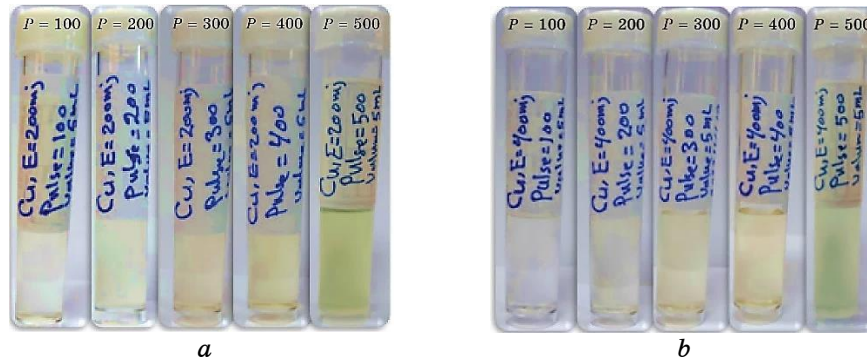


Fig. 4. Photograph of the copper-oxyde NPs prepared by PLAL using number of laser pulses and different energies (a) 200 mJ and (b) 400 mJ.

The SPRP is subject to modification by the size of the particles, resulting in a red shift towards longer wavelengths within the spectrum. Furthermore, it can be observed that the nanoparticles demonstrate a diminished absorption coefficient, resulting in elevated transmission values on the longer wavelength end of the spectrum, encompassing the visible range and wavelengths measuring up to 500 nm. The low absorption phenomenon can be elucidated by the reduction in energy of the incident photon as the wavelength increases, which results in the photon's inability to interact with the atoms present in the colloidal medium. Hence, the photons will undergo transmission instead of absorption.

The optical band gap was calculated using linear extrapolation of the equation's $(\alpha h\nu)$ versus $(h\nu)$ curve by fitting Tauc's relation [27]. The direct optical band gap is determined using the absorption coefficient calculated as a function of the incident photon energy. CuO nanoparticles were generated using 100 to 500 numbers of pulses at various laser energies of 200 mJ and 400 mJ:

$$(ah\nu)^{1/2} = D(h\nu - E_q^{opt.}), \quad (1)$$

where D is a constant and $h\nu$ represents the photon energy.

The absorption coefficient (α) is influenced by both the incident photon energy and the material's properties. This relationship has been utilized to calculate the absorption coefficient, which is contingent on the absorbance (A) and the thickness (d) [28]:

$$\alpha = \frac{2.303A}{d}. \quad (2)$$

Figures 5 and 6 show the optical band gap of copper oxide nanoparticles decreased as the number of pulses has increased. This result could be due to the quantum confinement effect. This increase is a result of quantum confinement.

Figure 7 as the number of laser pulses increases, the concentration of CuO NPs causes an increase in the absorption coefficient.

From the surface-plasmon resonance peak, copper oxide nanoparticles optical constants can be evaluated their values. The refractive index (n) is directly proportional to the concentration of CuO NPs. The refractive index can be calculated by [29, 30]:

$$n = \sqrt{\frac{4R}{(R-1)^2} - K^2} - \left(\frac{R+1}{R-1}\right), \quad (3)$$

where R and K , the reflectance and extinction coefficient, respectively. The extinction coefficient can be calculated from the relationship [31]:

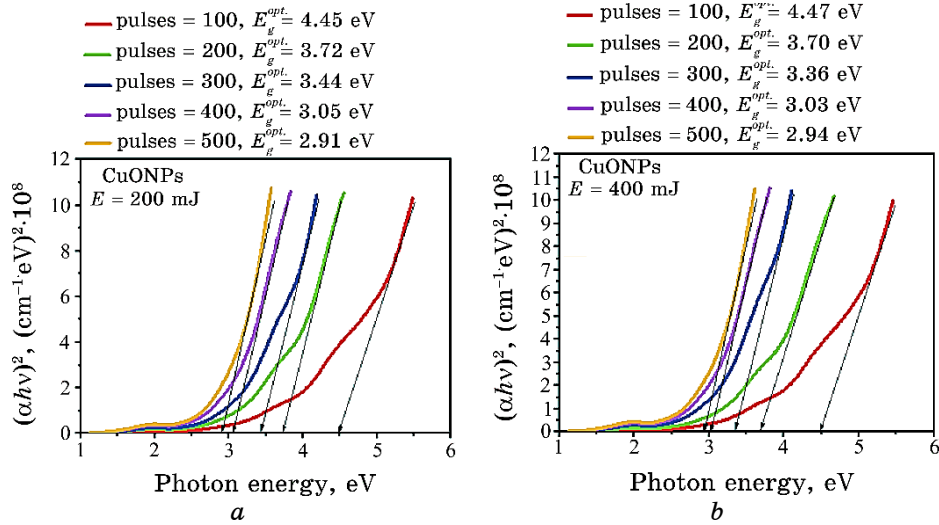


Fig. 5. Tauc plots of the CuO NPs prepared with various laser pulse energies of (a) 200 mJ and (b) 400 mJ.

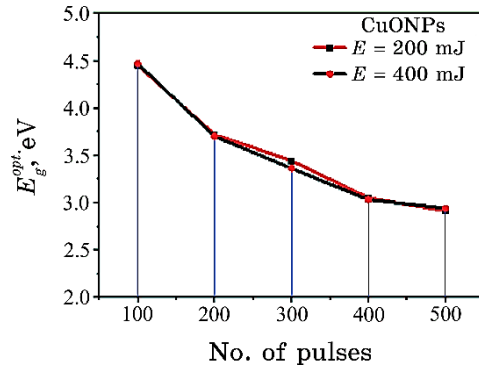


Fig. 6. Optical band gap values for prepared CuO NPs at various energies as a function of the number of pulses.

$$K = \frac{\alpha\lambda}{4\pi}. \quad (4)$$

The electric field of light interacts with the electrons in the nanoparticle in a way that is different from the way it interacts with electrons in bulk materials. This effect is more pronounced for smaller particles because the surface area-to-volume ratio increases as the particle size decreases. In particular, the electric field near the surface of a nanoparticle is enhanced, leading to an increase in

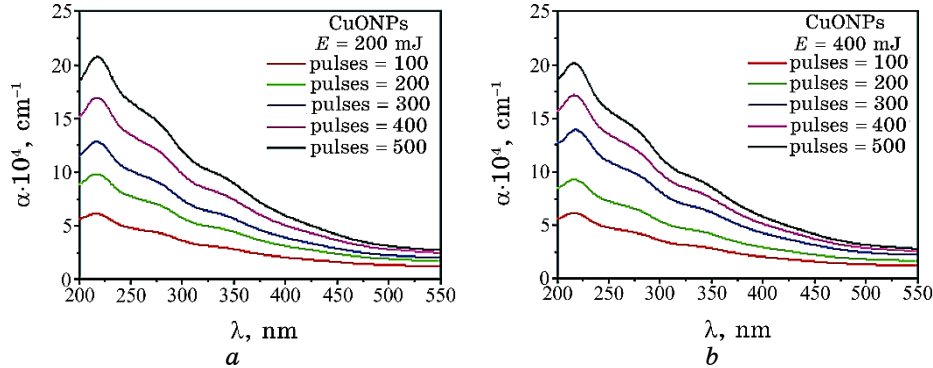


Fig. 7. Absorption coefficient *versus* wavelength of CuO NPs.

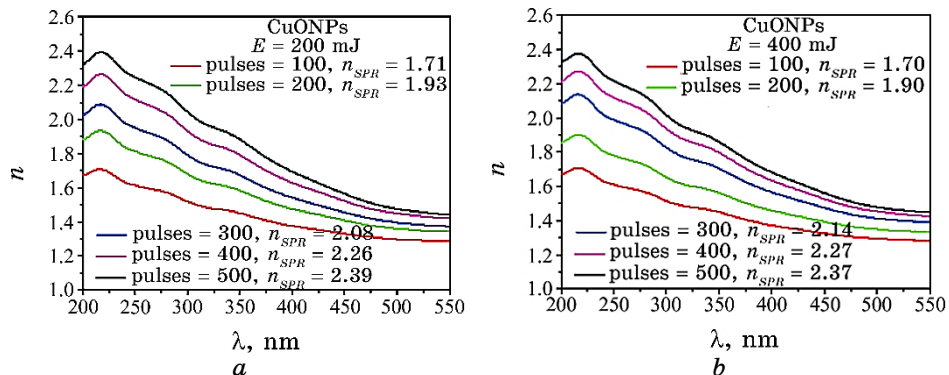


Fig. 8. Refractive index *versus* wavelength for copper-oxide NPs.

the refractive index and extinction coefficient with the number of laser pulses an increase as shown in Figs. 8 and 9.

Evaluation of the real and imaginary parts of the dielectric constant is done using the complex dielectric constant $\epsilon = \epsilon_r - i\epsilon_i = (n + iK)^2$. The real (ϵ_r) and imaginary (ϵ_i) parts of the dielectric constant are related to the refractive index and extinction coefficient by the following relationships [32]:

$$\epsilon_r = n^2 - K^2, \quad (5)$$

$$\epsilon_i = 2nk. \quad (6)$$

Figure 10 the increase in the real and imaginary dielectric constants of copper oxide nanoparticles with increasing laser pulse number can be attributed to the enhanced polarization and increased scattering and absorption of light, respectively.

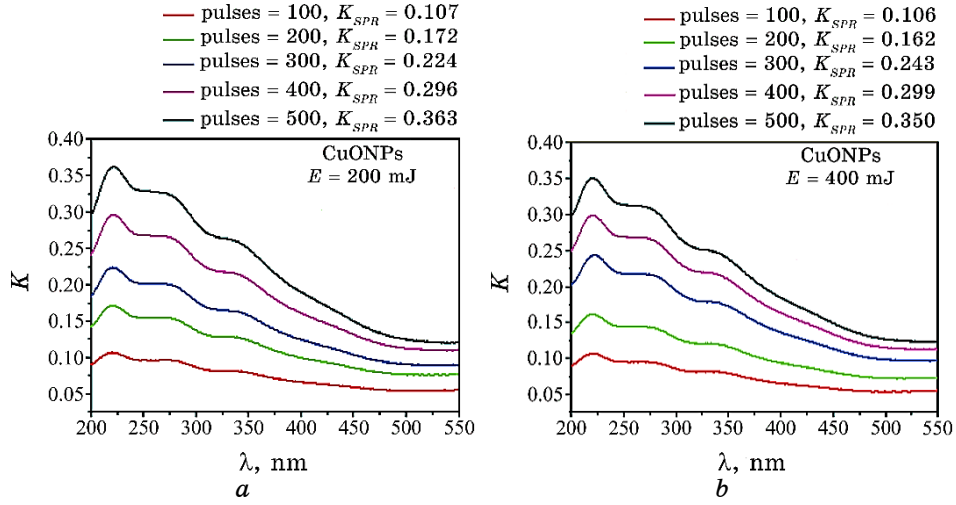


Fig. 9. Extinction coefficient *versus* wavelength for copper-oxide NPs.

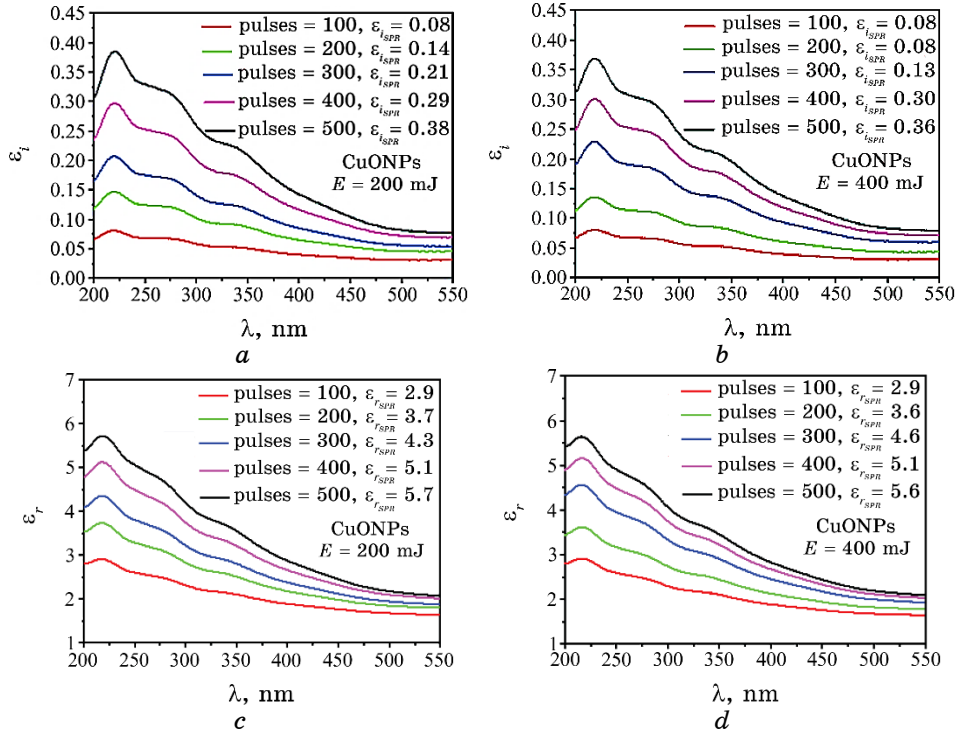


Fig. 10. Imaginary dielectric constants ((a) 200 mJ, (b) 400 mJ) and real dielectric constants ((c) 200 mJ, (d) 400 mJ) as functions of laser-pulse number.

The relationship between the linear refractive index and the linear absorption coefficient can be used to determine the optical conductivity of CuO NPs [31]:

$$\sigma_{opt.} = \frac{anc}{4\pi}, \quad (7)$$

where c is the speed of light in a vacuum. The increase in optical conductivity can be attributed to the greater number of excited electrons with increasing concentrations of CuO NPs, as shown in Fig. 11.

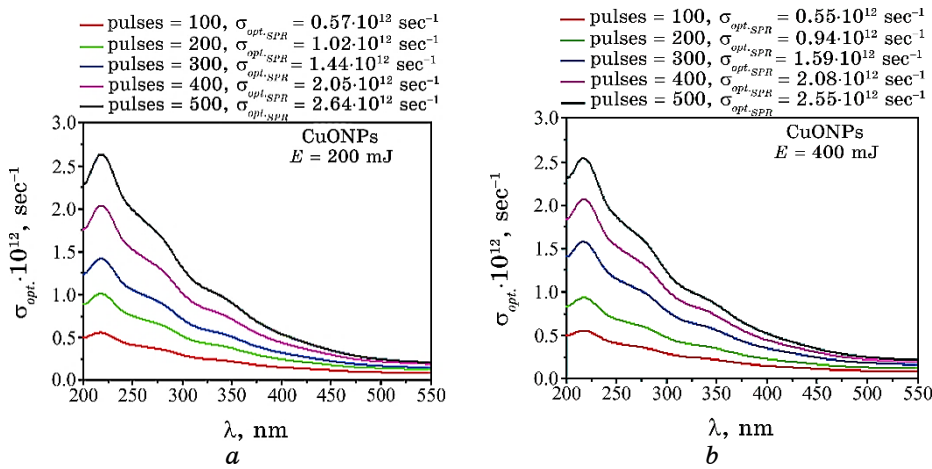


Fig. 11. Optical conductivity *versus* wavelength of CuO NPs as a function number of laser pulses.

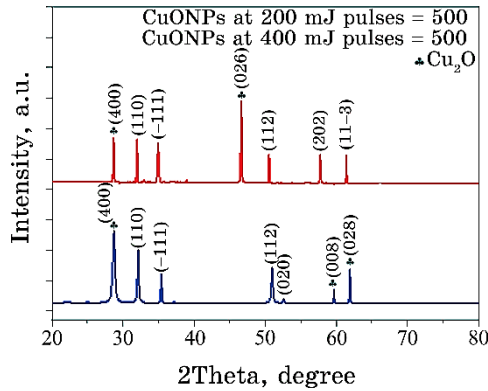


Fig. 12. XRD patterns of the samples prepared by laser ablation in DDW.

3.2. Morphology and Particle Size Analysis for CuO NPs

3.2.1. X-Ray Diffraction Patterns

The XRD patterns of CuO NPs in DDW laser-ablated at 200 mJ and 400 mJ with same number of pulses (500) are shown in Fig. 12. The average crystallite size was computed using the Debye–Scherrer equation [33]:

$$D_{av} = \frac{k\lambda_{x-ray}}{\beta \cos \theta}, \quad (3)$$

where the shape factor constant k is of 0.9, λ_{x-ray} the x-ray wavelength is of 0.15406 nm, β is the full width at half-maximum FWHM intensity in radians, and θ is the diffraction angle (Bragg angle). The calculated average crystallite size for CuO nanoparticles is found to be between 50 nm and 73 nm for 200 mJ and 400 mJ, respectively. The analysis of x-ray diffraction patterns revealed that CuO NPs have the crystallographic planes of monoclinic (1 1 0), (1 1 0), (-1 1 1), (1 1 2), (0 2 0), (0 2 0) and (1 1 -3) can be indexed to the diffraction peaks at about $2\theta = 32, 35, 51, 58$ and 61° conformed to the ICSD standard No. 98-004-3181; 01-089-2531. Furthermore, the diffraction peaks at around $2\theta = 28, 46, 59$ and 61° can be assigned to the crystallographic planes (4 0 0), (0 2 6), (0 0 8), and (0 2 8) which can be regarded as an orthorhombic crystal system. This is consistent with the standard ICSD No. 98-008-5080. The XRD results also corroborate the absence of impurities in the ablated nanoparticles, as the XRD patterns do not contain any peaks other than CuO nanoparticles. Using Scherrer's equation, the mean crystallite size of each sample was determined.

As shown in Table, the mean crystallite size of laser-ablated nanoparticles increases marginally with increasing pulse energy, according to the literature [34, 35].

CuO nanoparticles may be formed by two common processes, the thermal evaporation of atomic (and ionic) species from the liquid–solid interface and the thermally-induced discharge of nanometer-size molten droplets from the target. At the interface of liquid and target, the adiabatic expansion of the created plasma confines the surrounding double distilled water. The presence of PLAL in DDW solution results in an oxygen-rich cavitation bubble environment. Plasma's high temperature and pressure create the chemical conditions for the formation of CuO. Therefore, species within the plasma plume can interact to produce CuO nanoparticles. Eventually, the plasma is extinguished, and the CuO structures solidify [36, 37]. In addition, DDW can react with molten particles, and molten Cu oxidation contributes to the formation of CuO. Consequently, both of these phenomena may be responsible for the formation of CuO structures [38, 39].

TABLE. X-ray diffraction of samples prepared.

(200 mJ, pulses = 500) CuO NPs				(400 mJ, pulses = 500) CuO NPs			
Exp. 2θ, degree	FWHM, degree	<i>h k l</i>	Compound name	Exp. 2θ, degree	FWHM, degree	<i>h k l</i>	Compound name
28.728	0.492	4 0 0	CuO ₂	16.667	28.672	0 161	4 0 0
32.091	0.314	1 1 0	CuO	26.325	31.924	0.105	1 1 0
35.397	0.136	-1 1 1	CuO	61.316	34.941	0.246	-1 1 1
51.979	0.281	1 1 2	CuO	31.452	46.972	0.217	0 2 6
52.554	0.235	0 2 0	CuO	37.701	50.559	0.092	1 1 2
59.679	0.103	0 0 8	CuO ₂	88.917	57.741	0.089	2 0 2
61.902	0.105	0 2 8	CuO ₂	88.223	61.338	0.083	1 1 -3
Average crystallite size, nm				Average crystallite size, nm			
50.8				73.1			

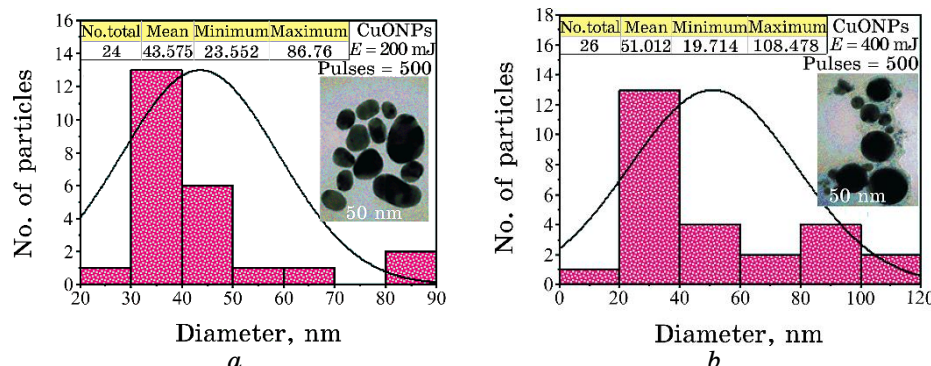


Fig. 13. TEM images and the particle size distribution of copper-oxide NPs with (a) 200 mJ (b) 400 mJ at 500 pulses.

3.2.2. Transmission Electron Microscopy (TEM)

Transmission EM analysis was used to confirm the average particle size, size distribution, and morphology of individual CuO nanoparticles prepared by the PLAL technique under 200 mJ and 400 mJ with 500 pulses. Analysis of TEM images uses the Image J program. The TEM image in Fig. 13 clearly shows that the aforementioned NPs have morphology, which is almost spherical. Copper oxide NPs diameters between 44 and 51 nm were confirmed by the TEM image. Using TEM analysis, which is consistent with that obtained from x-ray diffraction, On the other hand, because CuO nanoparticles tend to agglomerate, the agglomeration of nanoparticles can be attributed to the absence of antiagglomeration agents in the colloidal aqueous solution.

4. ANTIBACTERIAL ACTIVITY OF COPPER-OXIDE NPs

The diameter of inhibition zones was estimated using a meter ruler, and the mean value for each organism was recorded for two types of bacteria. The samples of CuO NPs with 500 pulses and laser energies of 200 mJ and 400 mJ were poured into wells on plates. DDW was used as a negative control to determine the antibacterial activity. According to our investigation, the CuO NPs produced did not significantly suppress the growth of the bacteria *S. aureus* G(+ve) and *E. coli* G(-ve). A surge in bacterial resistance may be to blame for this. Additionally, efficiency of nanoparticle synthesis by the PLAL technique is low compared with other synthesis techniques [34]. The copper-oxide NPs prepared by PLAL have inhibitory areas that can be seen in Figs. 14, 15 for both the energy and pulse con-



Fig. 14. Photograph of the antibacterial activity test of CuO NPs prepared for *Staphylococcus aureus* and *Escherichia coli*.

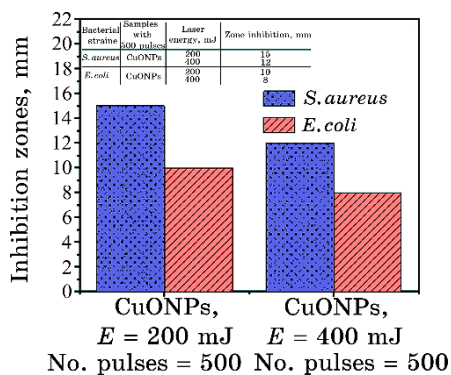


Fig. 15. Histogram of antibacterial activity for CuO NPs at 200 mJ and 400 mJ with the same number of 500 pulses.

figurations indicated. For the same number of pulses, the 200-mJ nanoparticles were more effective than the 400-mJ ones. In many instances, it is still unclear whether the death of the bacterium was caused by a single mechanism or a mixture of mechanisms. Negatively charged bacterial cell surfaces and positively charged nanoparticles may attract each other electrostatically. In contact with bacterial cells, copper oxide nanoparticles can pierce the cell wall and break the cell membrane, causing the release of cellular contents and ultimately cell death.

5. CONCLUSIONS

Copper-oxide nanoparticles can be easily produced by using the laser ablation technique on a copper target in double-distilled water. After several analyses were performed to investigate and characterize

the Cu NPs, according to UV-visible spectroscopy, the absorbance increased as the number of pulses increased. As the number of laser pulses increased, the plasmon peak at 217 nm redshifted. The compounds associated with the oxidation of Cu NPs into CuO NPs were produced by the reaction of dissolved oxygen in water with the Cu NPs. At the same number of pulses, copper-oxide NPs prepared at 400 mJ have a larger size than samples prepared at 200 mJ. CuO nanoparticles have a spherical shape and diameters ranging from 46 nm to 52 nm for 200 mJ and 400 mJ, respectively. However, compared to *Escherichia coli* (gram -ve) bacteria, the tested *Staphylococcus aureus* (gram +ve) bacteria demonstrated a higher sensitivity to copper-oxide NPs. This is due to variations in the molecular makeup of the cell walls of these bacterial strains. The results of our study show that when the laser energy is low and the same number of pulses, copper oxide nanoparticles have a stronger antibacterial effect against *S. aureus* and *E. coli*, respectively.

ACKNOWLEDGEMENTS

The authors would like to express their warmest thanks to University of Mosul, College of Education for Pure Science, Department of Physics for supporting this work.

REFERENCES

1. I. Khan, K. Saeed, and I. Khan, *Arabian Journal of Chemistry*, **12**, Iss. 7: 908 (2019); <https://doi.org/10.1016/j.arabjc.2017.05.011>
2. A. Abedini, A. A. Bakar, F. Larki, P. S. Menon, M. S. Islam, and S. Shaari, *Nanoscale Research Letters*, **11**: 1 (2016); <https://doi.org/10.1186/s11671-016-1500-z>
3. D. Zhang, B. Gulkce, and S. Barcikowski, *Chemical Reviews*, **117**, No. 5: 3990 (2017); <https://doi.org/10.1021/acs.chemrev.6b00468>
4. S. M. Arakelyan, V. P. Veiko, S. V. Kutrovskaya, A. O. Kucherik, A. V. Osipov, T. A. Vartanyan, and T. E. Itina, *Journal of Nanoparticle Research*, **18**, Iss. 6: 1 (2016); <https://doi.org/10.1007/s11051-016-3468-0>
5. T. T. P. Nguyen, R. Tanabe, and Y. Ito, *Optics & Laser Technology*, **100**: 21 (2018); <https://doi.org/10.1016/j.optlastec.2017.09.021>
6. T. T. P. Nguyen, R. Tanabe, and Y. Ito, *Applied Physics A*, **116**: 1109 (2013); <https://doi.org/10.1007/s00339-013-8193-2>
7. I. Akhatov, O. Lindau, A. Topolnikov, R. Mettin, N. Vakhitova, and W. Lauterborn, *Physics of Fluids*, **13**, Iss. 10: 2805 (2001); <https://doi.org/10.1063/1.1401810>
8. S. Ibrahimkutty, P. Wagener, A. Menzel, A. Plech, and S. Barcikowski, *Applied Physics Letters*, **101**, Iss. 10: 103104 (2012); <https://doi.org/10.1063/1.4750250>
9. I. Akhatov, N. Vakhitova, A. Topolnikov, K. Zakirov, B. Wolfrum, T. Kurz,

- O. Lindau, R. Mettin, and W. Lauterborn, *Experimental Thermal and Fluid Science*, **26**, Iss. 6–7: 731 (2002); [https://doi.org/10.1016/S0894-1777\(02\)00182-6](https://doi.org/10.1016/S0894-1777(02)00182-6)
10. A. Letzel, B. Gökce, P. Wagener, S. Ibrahimkutty, A. Menzel, A. Plech, and S. Barcikowski, *The Journal of Physical Chemistry C*, **121**: 5356 (2017); <https://doi.org/10.1021/acs.jpcc.6b12554>
 11. M. Q. Jiang, X. Q. Wu, Y. P. Wei, G. Wilde, and L. H. Dai, *Extreme Mechanics Letters*, **11**: 24 (2017); <https://doi.org/10.1016/j.eml.2016.11.014>
 12. H. Zeng, X. Du, S. C. Singh, S. A. Kulinich, S. Yang, J. He, and W. Cai, *Advanced Functional Materials*, **22**, Iss. 7: 1333 (2012); <https://doi.org/10.1002/adfm.201102295>
 13. J. Xiao, P. Liu, C. X. Wang, and G. W. Yang, *Progress in Materials Science*, **87**: 140 (2017); <https://doi.org/10.1016/j.pmatsci.2017.02.004>
 14. S. Bashir, M. S. Rafique, C. S. Nathala, and W. Husinsky, *Applied Surface Science*, **290**: 53 (2014); <https://doi.org/10.1016/j.apsusc.2013.10.187>
 15. M. Curcio, A. De Bonis, A. Santagata, A. Galasso, and R. Teghil, *Optics & Laser Technology*, **138**: 106916 (2021); <https://doi.org/10.1016/j.optlastec.2021.106916>
 16. A. Baladi and R. S. Mamoory, *Applied Surface Science*, **256**, Iss. 24: 7559 (2010); <https://doi.org/10.1016/j.apsusc.2010.05.103>
 17. S. A. Al-Mamun, R. Nakajima, and T. Ishigaki, *Journal of Colloid and Interface Science*, **392**: 172 (2013); <https://doi.org/10.1016/j.jcis.2012.10.027>
 18. S. Besner, A. V. Kabashin, and M. Meunier, *Applied Physics A*, **88**, No. 2: 269 (2007); <https://doi.org/10.1007/s00339-007-4001-1>
 19. G. W. Yang, *Progress in Materials Science*, **52**, Iss. 4: 648 (2007); <https://doi:10.1016/j.pmatsci.2006.10.016>
 20. R. C. Ashoori, *Nature*, **379**: 413 (1996); <https://doi.org/10.1038/379413a0>
 21. A. P. Alivisatos, *Science*, **271**, Iss. 5251: 933 (1996); <https://doi.org/10.1126/science.271.5251.933>
 22. A. S. Zoolfakar, R. A. Rani, A. J. Morfa, A. P. O'Mullane, and K. Kalantar-Zadeh, *Journal of Materials Chemistry C*, **2**, Iss. 27: 5247 (2014); <https://doi.org/10.1039/C4TC00345D>
 23. H. Azadi, H. D. Aghdam, R. Malekfar, and S. M. Bellah, *Results in Physics*, **15**: 102610 (2019); <https://doi.org/10.1016/j.rinp.2019.102610>
 24. J. Prikulis, F. Svedberg, M. Käll, J. Enger, K. Ramser, M. Goksör, and D. Hanstorp, *Nano Letters*, **4**, No. 1: 115 (2004); <https://doi.org/10.1021/nl0349606>
 25. A. Azam, A. S. Ahmed, M. Oves, M. S. Khan, and A. Memic, *International Journal of Nanomedicine*, **7**: 3527 (2012); <http://dx.doi.org/10.2147/IJN.S29020>
 26. A. F. Halbus, T. S. Horozov, and V. N. Paunov, *ACS Applied Materials & Interfaces*, **11**, No. 13: 12232 (2019); <https://doi.org/10.1021/acsami.8b21862>
 27. J. Tauc, R. Grigorvici, and A. Vancu, *physica status solidi (b)*, **15**, Iss. 2: 627 (1966); <https://doi.org/10.1002/pssb.19660150224>
 28. Triloki, R. Rai, and B. K. Singh, *Nuclear Instruments and Methods in Physics Research Section A: Accelerators, Spectrometers, Detectors and Associated Equipment*, **785**: 70 (2013); <http://dx.doi.org/10.1016/j.nima.2015.02.059>

29. M. D. Migahed and H. M. Zidan, *Current Applied Physics*, **6**, Iss. 1: 91 (2006); <https://doi:10.1016/j.cap.2004.12.009>
30. I. Saini, J. Rozra, N. Chandak, S. Aggarwal, P. K. Sharma, and A. Sharma, *Materials Chemistry and Physics*, **139**, Iss. 2–3: 802 (2013); <https://doi:10.1016/j.matchemphys.2013.02.035>
31. D. Babu, P. Philominathan, and K. Murali, *Optik*, **186**: 350 (2019); <https://doi.org/10.1016/j.ijleo.2019.03.048>
32. V. R. Kumar, P. R. S. Wariar, and J. Koshy, *Crystal Research and Technology*, **45**, Iss. 6: 619 (2010); <https://doi.org/10.1002/crat.201000048>
33. A. A. Menazea, *Radiation Physics and Chemistry*, **168**: 108616 (2020); <https://doi.org/10.1016/j.radphyschem.2019.108616>
34. *Laser Ablation in Liquids: Principles and Applications in the Preparation of Nanomaterials* (Ed. G. Yang) (New York: Jenny Stanford Publishing: 2012); <https://doi.org/10.1201/b11623>
35. J. Zhang, J. Claverie, M. Chaker, and D. Ma, *Chem. Phys. Chem.*, **18**, Iss. 9: 986 (2017); <https://doi.org/10.1002/cphc.201601220>
36. H. Zeng, W. Cai, Y. Li, J. Hu, and P. Liu, *The Journal of Physical Chemistry B*, **109**, No. 39: 18260 (2005); <https://doi.org/10.1021/jp052258n>
37. H. Zeng, X. Xu, Y. Bando, U. K. Gautam, T. Zhai, X. Fang, B. Liu, and D. Golberg, *Advanced Functional Materials*, **19**, Iss. 19: 3165(2009); <https://doi.org/10.1002/adfm.200900714>
38. K. Y. Niu, J. Yang, S. A. Kulinich, J. Sun, H. Li, and X. W. Du, *Journal of the American Chemical Society*, **132**, No. 28: 9814 (2010); <https://doi.org/10.1021/ja102967a>
39. M. A. Gondal, T. F. Qahtan, M. A. Dastageer, T. A. Saleh, Y. W. Maganda, and D. H. Anjum, *Applied Surface Science*, **286**: 149 (2013); <https://doi.org/10.1016/j.apsusc.2013.09.038>

Наукове видання

НАНОСИСТЕМИ, НАНОМАТЕРІАЛИ, НАНОТЕХНОЛОГІЇ

ЗБІРНИК НАУКОВИХ ПРАЦЬ ТОМ 22 випуск 1 (2024)

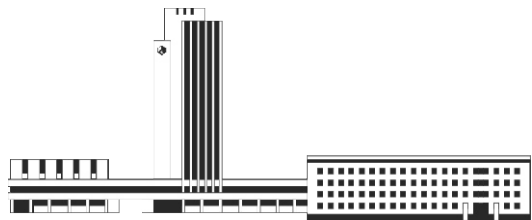
Підписано до друку **30.04.2024**. Формат 70×100/16.

Папір офсетний. Друк різографічний.

Ум. друк. арк. **19,99**. Обл.-вид. арк. **18,39**.

Наклад **58** прим. Зам. № **1**

Поліграфічно-розмножувальна дільниця РВВ ІМФ ім. Г. В. Курдюмова НАН України
бульв. Акад. Вернадського, 36; 03142 Київ, Україна



НАЦІОНАЛЬНА АКАДЕМІЯ НАУК УКРАЇНИ



НАНОСИСТЕМИ
НАНОМАТЕРІАЛИ
НАНОТЕХНОЛОГІЇ

NANOSYSTEMS
NANOMATERIALS
NANOTECHNOLOGIES

Редакція щоквартального збірника наукових праць

«НАНОСИСТЕМИ, НАНОМАТЕРІАЛИ, НАНОТЕХНОЛОГІЙ»

(CODEN: NNNAAAT; ISSN (Print): 1816-5230, ISSN (Online): 2617-3794;

у «Каталозі видань України» передплатний індекс: 94919)

повідомляє про передплату (починаючи з поточного кварталу випуску).

Рекомендуємо оформити передплату безпосередньо перерахуванням оплати

у гривнях:

«ОТРИМУВАЧУ»: Інститут металофізики ім. Г. В. Курдюмова НАН України на розрахунковий рахунок № UA058201720313291001201001901 в банку ГУДКСУ в м. Києві код банку 820172

код ЗКПО: 05417331

для «ПОСТАЧАЛЬНИКА» — Інституту металофізики ім. Г. В. Курдюмова НАН України

Свідоцтво платника податку № 36283185

ППН 054173326066

Код призначення платежу: 25010100

Призначення платежу: за збірник «Наносистеми, наноматеріали, нанотехнології» для РВВ

ІМФ НАНУ

ПІДСТАВА: передоплата 100%

в іноземній валюті (доларах США, євро) через відповідні банки-кореспонденти АТ «Державний експортно-імпортний банк України»:

«Отримувач»: Філія АТ «Державний експортно-імпортний банк України» в м. Києві (Україна, 04053 Київ, вул. Бульварно-Кудрявська, 11^б)

на розрахунковий рахунок № UA603223130000025308000000067

МФО 322313

для «ПОСТАЧАЛЬНИКА» — Інституту металофізики ім. Г. В. Курдюмова НАН України

Призначення платежу: за збірник «Наносистеми, наноматеріали, нанотехнології» для РВВ

ІМФ НАНУ

ПІДСТАВА: передоплата 100%

За цього способу передплати необхідно сповістити редакцію збірника за поштовою адресою:

РВВ (№ 83) ІМФ НАНУ,

бульв. Акад. Вернадського, 36,

03142 Київ, Україна

e-mail: tatar@imp.kiev.ua; факс: +380 44 4242561; телефон: +380 44 4241221, +380 44 4249042

дату сплати, називу установи або найменування передплатника, адресу для поштової доставки, а за потреби — свої реквізити для податкової накладної.

Періодичність — том з 4 випусків у рік.

Із врахуванням поштової пересилки

для передплатників в Україну передплатна ціна: одного примірника випуску — 312 грн., тому

— 1248 грн.;

для передплатників у країні СНД передплатна ціна: одного примірника випуску — 36 US\$, тому

— 144 US\$;

для іноземних передплатників назовні СНД передплатна ціна: одного примірника випуску — 40

US\$ (36 EUR), тому — 160 US\$ (144 EUR).

×

Зразок для оплати річної передплати

Рахунок-фактура

«ПОСТАЧАЛЬНИК»: Інститут металофізики ім. Г. В. Курдюмова НАН України

«ОТРИМУВАЧ»: Філія АТ «Державний експортно-імпортний банк України» в м. Києві

(Україна, 04053 Київ, вул. Бульварно-Кудрявська, 11^б)

на розрахунковий рахунок № UA603223130000025308000000067, МФО 322313

Призначення платежу: за збірник «Наносистеми, наноматеріали, нанотехнології» для ІМФ НАНУ

«ПЛАТНИК»:

ПІДСТАВА: передоплата 100%

№	Назва	Од. вим.	Кількість	Ціна	Сума
1	збірник «Наносистеми, наноматеріали, нанотехнології» (включаючи доставку поштою)	прим.	4	36 US\$	144 US\$
Сума до сплати					144 US\$

